

Université Pierre et Marie Curie

École Doctorale SMAER, specialité Mécanique


Università degli Studi di Roma "Tor Vergata"

Corso di Dottorato in Ingegneria Civile, XXIX ciclo

DOCTORAL THESIS

in partial fulfilment of the requirements for the degrees of

Docteur de l'Université Pierre et Marie Curie

Dottore di Ricerca in Ingegneria Civile, indirizzo Strutture e Geotecnica

---

Strength properties of nanoporous materials: Theoretical analyses and Molecular Dynamics computations

---

by Stella Brach

under the joint supervision of Profs. Djimédo KONDO and Giuseppe VAIRO

Public dissertation on November 29, 2016

Prof. A. MOLINARI	University of Lorraine, France	President
Prof. F. AURICCHIO	University of Pavia, Italy	Reviewer
Prof. V. TVERGAARD	Technical University of Denmark, Denmark	Reviewer
Prof. J. YVONNET	University Paris-Est, France	Reviewer
Prof. R. BRENNER	University Pierre and Marie Curie, France	Examiner
Prof. A. CORIGLIANO	Politecnico di Milano, Italy	Examiner
Prof. F. MACERI	University of Rome "Tor Vergata", Italy	Invited professor
Prof. D. KONDO	University Pierre and Marie Curie, France	PhD co-advisor
Prof. G. VAIRO	University of Rome "Tor Vergata", Italy	PhD co-advisor

Acknowledgements

This thesis has been written during my position as a joint-supervised doctoral candidate at the University Pierre and Marie Curie, and at the University of Rome "Tor Vergata".

I would express my deeply-felt gratitude to my PhD advisors, Giuseppe Vairo and Djimédo Kondo, for their expertise, invaluable advice and continuous support throughout my studies, as well as to made research in mechanics fascinating to me. I sincerely treasure their precious remarks about academic writing, research and future perspectives, and I am honoured to acknowledge their mentoring along the way. They listened to me whenever I was excited about a new idea, sharing their enthusiasm and investing their time in any stage of this three-years-long period of personal growth. I look forward to continue our collaboration in both research and life.

My heartfelt appreciation also extends to Prof. Franco Maceri, who expertly guided me through my higher education by encouraging my passion in learning, and whose truly inspiring example turned me towards teaching and academics. I am extremely grateful for his wisdom in pushing me further than I thought I could go.

I would like to express my sincere gratitude to the members of the dissertation committee: Profs. F. Auricchio, V. Tvergaard and J. Yvonnet, who have kindly accepted to review the thesis, as well as Profs. R. Brenner, A. Corigliano, F. Maceri and A. Molinari. I am extremely grateful for their willingness to take part in my doctoral examination, as well as for precious comments and insightful questions they provide on the present research work.

PhD is not a lonely task. I was given the valuable opportunity to work in two different countries, and I would express my deep appreciation to Italian and French colleagues, for helpful discussions and priceless teaching experience.

Résumé

Dans les deux dernières décennies, grâce au développement de nouvelles nanotechnologies, les matériaux nano-structurés ont suscité l'intérêt de nombreux groupes de recherche académiques ou industriels, donnant lieu à la mise en place d'essais expérimentaux, à la formulation de modèles analytiques, et à des simulations numériques dédiées.

Parmi les différents types de matériaux nano-structurés, un rôle important est tenu par les matériaux nanoporeux, constitués d'une matrice solide contenant des pores dont la dimension caractéristique est de l'ordre de quelques nanomètres à quelques dizaines de nanomètres. En effet, en raison de leurs excellentes propriétés mécaniques et chimiques, les nanoporeux ont récemment fait l'objet de nombreuses applications novatrices dans différents domaines techniques, permettant ainsi la conception de dispositifs à ultra-haute performance et aux propriétés multi-fonctionnelles inhabituelles.

Afin de répondre à ces exaltantes perspectives, une des voies de recherche les plus prometteuses réside dans la compréhension, la caractérisation et la prédiction des effets de taille des nanopores sur les propriétés mécaniques du matériau. Malgré cela, la plus parte des études actuellement disponibles dans la littérature, concernant les effets de taille sur la réponse mécanique des nanoporeux, ont essentiellement porté sur l'estimation des propriétés élastiques effectives. Au contraire, très peu d'attention a été accordée à l'influence de la taille des nanopores dans le régime plastique.

L'objectif principal de cette thèse a donc été d'étudier les propriétés de résistance des matériaux nanoporeux ductiles à l'aide d'approches théoriques et numériques. En particulier, dans le contexte des méthodes d'homogénéisation, visant à construire un milieu homogène aux propriétés effectives équivalentes, des critères de résistance macroscopiques ont été établis par des approches analytiques (homogénéisation non-linéaire et analyse limite). Dans ce cadre, les surfaces des nanopores ont été modélisées comme des interfaces imparfaites cohérentes. Les critères de résistance ainsi obtenus ont permis de tenir en compte les effets de taille, tout en améliorant les formulations déjà existantes.

En outre, dans le but de comprendre les mécanismes de déformation à l'œuvre dans les matériaux nanoporeux et de constituer une base de référence pour la calibration et/ou la validation des modèles analytiques disponibles, ainsi que pour le développement de nouvelles approches de modélisation, des simulations numériques basées sur la Dynamique Moléculaire ont été conduites, sous des conditions de chargements multiaxiaux en vitesse de déformation. Par rapport aux simulations actuellement disponibles dans la littérature, considérant généralement des conditions de chargement particulières (essais de traction

mono-axiale ou sous pression uniforme), les résultats obtenus ont permis une identification du domaine multiaxial de résistance, en établissant clairement l'influence de trois invariants de contrainte ainsi que les effets de taille sur les surfaces de résistance du nanoporeux.

Dans le but de mettre à profit les indications fournies par les simulations numériques, le cas d'un matériau nanoporeux constitué d'une matrice ductile sensible aux trois invariants isotropes a été étudié. L'état limite d'une sphère creuse, avec une interface imparfaite cohérente à la surface du nanopore, a été identifié de façon exacte dans le cas d'un chargement isotrope, en établissant des expressions analytiques pour les champs locaux de vitesse de déformation et de contrainte, et pour la résistance hydrostatique du matériau nanoporeux. Finalement, à partir des résultats ainsi obtenus, une approche d'analyse limite cinématique a été mise en place pour le modèle d'une sphère creuse sous chargement axisymétrique et au comportement plastique sensible aux trois invariants isotropes de contrainte. Un critère de résistance du matériau rendant compte des effets de taille des nanopores et de l'influence des trois invariants de contrainte a été analytiquement dérivé, en résolvant un problème de minimisation sous contrainte non-linéaire d'inégalité.

Mots clés: Matériaux nanoporeux, propriétés de résistance, effets de taille des nanopores, Dynamique Moléculaire, analyse limite cinématique, homogénéisation non linéaire.

Sommario

Negli ultimi anni, lo sviluppo di nuove nanotecnologie ha portato ad un crescente interesse nei confronti dei materiali cosiddetti *nano-strutturati*, progettati al fine di garantire proprietà e prestazioni generalmente superiori o comunque non assimilabili a quelle esibite dai materiali convenzionali. Tra gli altri, grande interesse hanno suscitato i materiali nanoporosi, costituiti da una matrice solida contenente dei pori la cui dimensione caratteristica è dell'ordine di alcuni nanometri. Generalmente contraddistinti da un ridotto peso specifico, da elevate energie superficiali e da significative proprietà fisico-chimiche, i materiali nanoporosi sono impiegati nella progettazione di dispositivi ultra-efficienti per applicazioni innovative in differenti ambiti industriali, tra cui l'ingegneria meccanica e civile, il settore petrolchimico e geotecnico, la biomeccanica e la sensoristica.

Uno degli attuali aspetti di ricerca più affascinanti consiste nell'identificazione e nella descrizione delle proprietà meccaniche del materiale in funzione della taglia caratteristica dei pori, assegnato che sia un valore di porosità. Una tale dipendenza, non esibita dai materiali porosi convenzionali, è strettamente correlata alla dimensione nanometrica dei pori, consentendo di alterare deliberatamente la risposta meccanica del materiale al fine di prescrivere specifiche funzionalità di interesse progettuale.

A fronte di una risposta meccanica così complessa e rispetto alla letteratura esistente, l'obiettivo della presente tesi è consistito nella formulazione di approcci analitici e numerici per la caratterizzazione delle proprietà di resistenza dei materiali nanoporosi, identificandone la dipendenza dagli effetti di taglia.

In particolare, nel contesto degli approcci di omogeneizzazione non lineare e di analisi limite, dei criteri di resistenza sono stati analiticamente determinati, tenendo conto della dipendenza dalla taglia dei nanopori tramite l'introduzione di un modello d'interfaccia imperfetta coerente. Le stime di resistenza così ottenute hanno permesso di migliorare significativamente i più recenti modelli disponibili in letteratura, fornendo una descrizione consistente degli effetti associati sia alla porosità che alla taglia dei nanopori.

Inoltre, al fine di fornire delle evidenze numeriche utili alla calibrazione e/o alla validazione di formulazioni analitiche esistenti, oltre che per lo sviluppo di nuovi modelli teorici, delle simulazioni di Dinamica Molecolare sono state condotte considerando una varietà di condizioni al contorno multiassiali in velocità di deformazione. Rispetto agli approcci numerici disponibili in letteratura, riferiti generalmente a delle condizioni di carico estremamente esemplificative, la procedura computazionale proposta ha permesso un'identificazione tridimensionale del dominio di resistenza del materiale nanoporoso,

mettendone in evidenza la dipendenza dagli invarianti isotropi nonché i significativi effetti di taglia.

Sulla base delle indicazioni fisiche fornite dalle simulazioni di Dinamica Molecolare, lo stato limite di un materiale nanoporoso con una matrice plastica dipendente dai tre invarianti isotropi è stato risolto in modo esatto. I campi locali di tensione e di velocità di deformazione, nonché la resistenza idrostatica effettiva, sono stati determinati in forma esplicita e validati rispetto alla letteratura esistente.

Infine, a partire dai risultati analitici così ottenuti, un approccio cinematico all'analisi limite è stato proposto, considerando come dominio di riferimento una sfera cava soggetta a delle condizioni al contorno assial-simmetriche in velocità di deformazione. La superficie del nanoporo è stata descritta tramite un modello d'interfaccia coerente imperfetta, al fine di tenere conto delle tensioni superficiali auto-equilibrate dovute alla nanoscala del poro. Un criterio di resistenza per il materiale nanoporoso espresso in termini dei tre invarianti isotropi è stato esplicitamente determinato, risolvendo un problema di minimizzazione non-lineare vincolata.

Parole chiave: Materiali nanoporosi, proprietà di resistenza, effetti di taglia, Dinamica Molecolare, analisi limite cinematica, omogeneizzazione non lineare.

Contents

Abstract

Since the recent arising of advanced nano-technologies, as well as of innovative engineering design approaches, nanoporous materials have been extensively studied in the last two decades, leading to a considerable worldwide research interest in both industrial and academic domains. Generally characterised by high specific surface area, uniform pore size and rich surface chemistry, nanoporous materials have allowed for the development of challenging ultra-high performance devices with tailorable properties, finding widespread application in several technical fields, including civil and environmental engineering, petroleum and chemical industries, aeronautics and biomechanics.

In order to fulfil to these promising applications, one of the most fundamental research aspect consists in characterising and predicting the strength properties of these materials, as dependent on the size of voids. Since the current lack of an exhaustive benchmarking evidence, as well as of a comprehensive theoretical modelling, the central purpose of the present thesis consisted in:

- investigating strength properties of in-silico nanoporous samples via Molecular Dynamics computations. In detail, a parametric analysis with respect to the void radius and for different porosity levels has been carried out, by considering different loading paths with a wide range of triaxiality scenarios. As a result, the influence of void-size effects on the computed strength properties has been clearly quantified, also highlighting the dependence of the predicted material strength domain on the three stress invariants;

- establishing engineering-oriented theoretical models able to predict macroscopic strength properties of nanoporous materials, by properly accounting for void-size effects. To this end, theoretical approaches based on both non-linear homogenization techniques and kinematic limit-analysis strategies have been proposed. As a result, closed-form macroscopic strength criteria have been derived, allowing for a consistent description of void-size effects and taking into account different local plastic behaviours.

Keywords: Nanoporous materials, strength properties, void-size effects, Molecular Dynamics, kinematic limit analysis, non-linear homogenization.

Introduction

In the last decades, the development of novel and challenging nano-technologies has led to unprecedented opportunities in materials design. As a matter of fact, instead of coming upon new materials with trial-and-error research processes, the core focus of current engineering design approaches consists in manipulating material microstructure at the atomic level in order to deliberately prescribe specific properties at the continuum scale. As a result, a new generation of customer-oriented devices, based on the so-called *nanostructured materials*, has recently attracted a keen research interest in both industrial and academic domains, opening towards groundbreaking multifunctional applications in several technical fields.

An important class of nanostructured materials consists in *nanoporous media*, whose microstructure comprises an organic or inorganic solid matrix embedding long-range orderly- or disorderly-distributed pores (see Fig. 1). According to the International Union of Pure and Applied Chemistry nomenclature, and depending on pores characteristic length, nanoporous media can be divided into three subcategories: *microporous* (with pore size smaller than 2 nanometers), *mesoporous* (with pore size in the range of 2 to 50 nanometers), and *macroporous* (with pore size larger than 50 nanometers). Nevertheless, for the sake of clarity and in agreement with the most extensively adopted terminology in literature, in this thesis the term *nanoporous* is used to refer to materials presenting structural features in between those of atomic arrangements and bulk solids, with characteristic pore size ranging from 1 to 100 nanometers.

Generally characterised by high specific surfaces area, uniform pore size and rich surface energy, nanoporous materials present a wide variety of chemical compositions and physical features, which are often dramatically different from those of the same material at a larger lengthscale. Such an intriguing combination of electro-chemical-mechanical properties has represented the driving force behind the ever-growing research interest in nanoporous materials, opening towards cutting-edge technological uses (Ding and Zhang, 2016; Jenkins, 2010; Lu and Zhao, 2004; Pinnavaia and Thorpe, 2006; Valiev et al., 2013). As a matter of fact, due to the presence of nanosized cavities, these materials possess a high capability to interact, absorb and cooperate with atoms, ions and molecules, thereby finding widespread application as catalysts or adsorbents in petroleum and chemical industries (Roque-Malherbe, 2007). Moreover, by combining advantages due to high surface-to-volume ratio and uniform pore size, nanoporous-based devices have been conceived for size-selective adsorption purposes, allowing to sensibly improve the efficiency of several

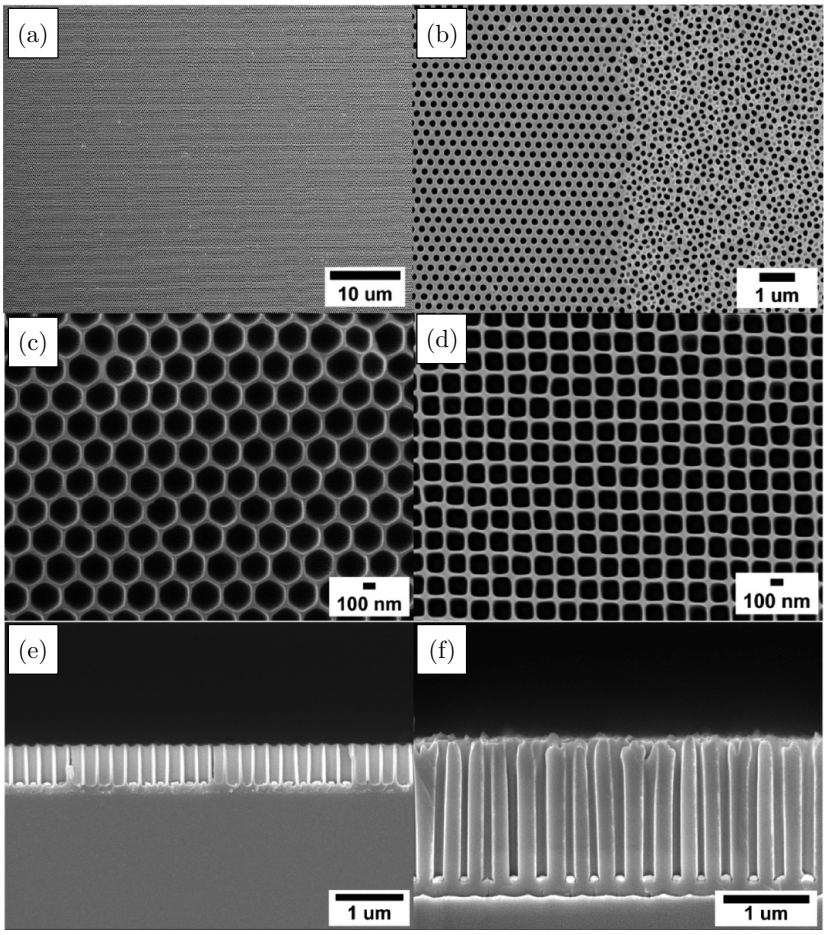

Figure 1 – Scanning Electron Microscopy images of a near-perfect ordered nanoporous alumina (Kustandi et al., 2010): (a)-(d) Top views. (e)-(f) Cross-sectional views.

catalytic processes (Kärger et al., 2012). Since the ever-more stringent regulatory limits on environmental emissions, innovative nanoporous filters with sizeable pore space and high surface energy have been recently developed, aiming to remove contaminants and pollutants from waste gas and water streams (Kumeria et al., 2014; Lu and Zhao, 2004). Due to their high sensitivity to detect slight changes in the surrounding environment, mainly associated to temperature, humidity and light, nanoporous materials have been extensively used as sensors and actuators in several practical applications, such as for detecting combustible gases, ethanol, oxygen, and hydrocarbons (Lee, 2009; Ozdemir and Gole, 2007). By opportunely conceiving material morphology and pores spatial distribution, biocompatible nanoporous devices have been engineered to mimic natural filtration processes, for uses in smart implantable drug-delivery systems and bioartificial organs, as well as to allow for biosensoring and molecular sieving (Adiga et al., 2009; Dai and Ju, 2012; Sotiropoulou et al., 2005). In detail, some examples of nanoporous implants for therapeutic purposes are reported in Fig. 2. Ductile plastic behaviour and high strength properties make nanoporous metallic foams excellent choices for many structural applica-

tions, as well as for designing lightweight devices in automotive, aeronautic and construction industries. Finally, in the fields of clean energy production and storage, nanoporous metals have been recognized as an alternative type of electrode materials, which exhibit some very unique structural properties not commonly expected from carbon-based electrodes (Ding and Zhang, 2016; Lang et al., 2011).

To date, two basic and complementary methods have been developed for the synthesis of nanoporous materials, generally known as *bottom-up* and *top-down* approaches (Gleiter, 2000; Zehetbauer and Zhu, 2009). In the first case, advanced microstructural nanotechnologies afford to fabricate nanoporous solid frameworks by assembling individual atomic structures or by consolidating nanosized molecular arrangements. Extensively-used bottom-up techniques include inert gas condensation (Gleiter, 2000; Zehetbauer and Zhu, 2009), electro-deposition (Erb et al., 1993; Shin et al., 2003), ball milling with subsequent consolidation (Koch and Cho, 1992; Chen et al., 1999), and mechanical milling in a liquid nitrogen environment (Luton et al., 1988; Witkin and Lavernia, 2006). On the other hand, top-down approaches consists in obtaining nanoporous materials via the structural decomposition of originally-bulk solid samples. Among other top-down techniques, dealloying represents the most exploited method for fabricating nanoporous metals (Sun et al., 2004; Senior and Newman, 2006; Weissmüller et al., 2009), consisting in the selective corrosion of less-noble elements in alloy-based solid specimens.

Interest in conceiving and developing engineering devices based on nanoporous materials with respect to conventional porous ones (i.e., with relatively larger characteristic sizes) arose from the discovery that, by opportunely calibrating pore dimension at the nanoscale, it is possible to deliberately prescribe specific size-related effects at the macroscale. Accordingly, and with particular reference on mechanical features, one of the core research focus consists in identifying and describing the strength properties of nanoporous materials as dependent on the size of voids.

Experimental tests performed on nanoporous foams (e.g., Biener et al., 2005, 2006; Cheng and Hodge, 2013; Fan and Fang, 2009; Hakamada and Mabuchi, 2007; Hodge et al., 2007) revealed that, for a fixed porosity level, a reduction in the void size induces a significant increase in the yield strength, which results higher than characteristic values observed for conventional porous metals. As an illustrative example, evidence-based data provided by Fan and Fang (2009) and obtained via nanoindentation tests on nanoporous gold foams are reported in Fig.3a, highlighting the strengthening effect associated to the reduction of the ligament size (the latter being proportional to the characteristic void length). However, apart from these qualitative indications of the void-size influence on the material yield stress, available experimental literature does not furnish either an exhaustive description of the three-dimensional material strength domain (i.e., in the space of principal stresses) or a proper characterization of the impact of void-size effects under arbitrary loading conditions.

In this light, numerical simulations can be considered as effective methods to provide benchmarking evidence, allowing also to separately control a number of possible coupled effects. Nevertheless, computational approaches usually employed for modelling macro-

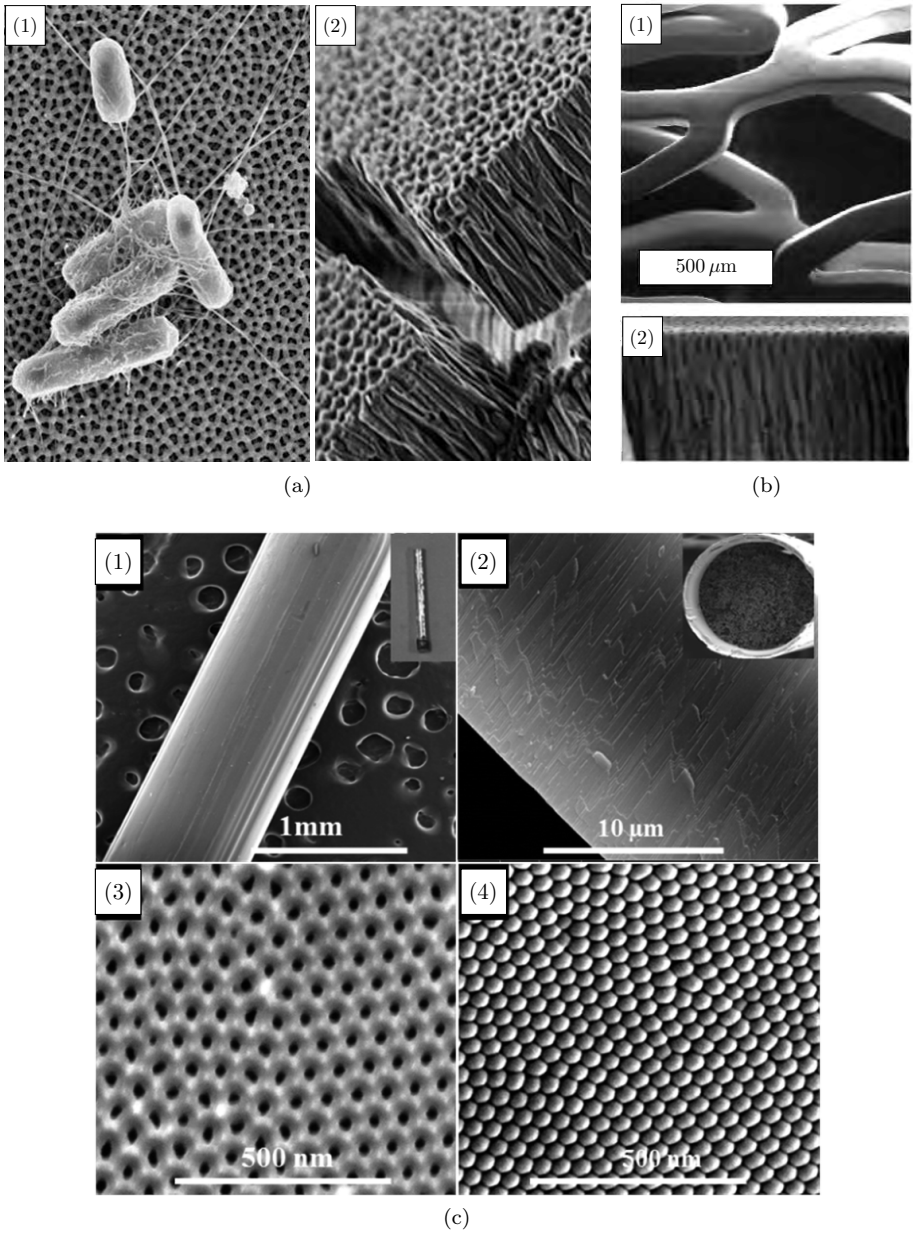

Figure 2 – Scanning Electron Microscopy images of nanoporous-based devices for therapeutic purposes. (a) Anodic surfaces with cylindrical nanopores, able to reduce microbial attachment and biofilm development (Feng et al., 2014): a-1) nanopores induce a perturbation of both the electrical charge and the surface energy of a metal, exerting a repulsive force on bacterial cells; a-2) cross-sectional view of the nanoporous surface alumina. (b) Stent with a nanoporous alumina layer filled with anti-inflammatory drugs (Jenkins, 2010): b-1) stainless-steel active stent, coated with a nanoporous alumina oxide; b-2) cross section of the nanoporous alumina layer. (c) Nanoporous alumina-aluminium wire implants for localized therapy (Rahman et al., 2015): c-1) low-resolution image of a portion of the nanoporous wire depicted in the inset figure (total length 10 mm); c-2) cross-sectional view of the nanoporous layer; c-3) top-surface view of the nanoporous layer, showing nanopores to be filled with therapeutic drugs; c-4) bottom-surface view of the nanoporous layer, showing closed ends of nanopores.

and/or micro-mechanical response are not able to automatically provide helpful insights on dominant size-related effects, since they do not include an adequately rich description of the material structure at the nanoscale. For instance, this is the case of finite elements-based calculations (e.g., Morin et al., 2015), in which the dependence of nanoporous material strength properties on the void size is enforced by a priori defining a specific yield criterion for surface elements at cavity boundaries. On the contrary, allowing to describe the material arrangement at the atomic level, Molecular-Dynamics computational approaches can be considered as a promising candidate to numerically investigate the mechanical response of nanoporous materials, automatically providing helpful insights on dominant size-induced effects. Specifically, available Molecular Dynamics calculations mainly addressed the identification and the characterization of atomistic mechanisms underlying failure processes related to void growth and coalescence (e.g., Farrissey et al., 2000; Lubarda et al., 2004; Lubarda, 2011; Marian et al., 2004, 2005; Pogorelko and Mayer, 2016; Ruestes et al., 2013; Tang et al., 2010; Traiviratana et al., 2008). On the other hand and at the best of the author's knowledge, a limited number of studies has been devoted to the definition of engineering-oriented strength measures for nanoporous materials. For instance, mention can be made to results provided by Mi et al. (2011), Traiviratana et al. (2008) and Zhao et al. (2009), predicting a significant enhancement of the computed strength measure as the void size reduces (see Fig. 3b). Nonetheless, current Molecular Dynamics computations are generally limited to the analysis of particular strength states only, obtained under uniaxial (Farrissey et al., 2000; Tang et al., 2010), volumetric or shear conditions (Marian et al., 2004, 2005), and therefore defining only few discrete points on the a-priori unknown material strength surface. In fact, no numerical analysis has been provided addressing more exhaustive multiaxial loading cases, thereby resulting in a lack of a comprehensive characterization of void-size effects on material strength domain.

As regards theoretical modelling, although size-related effects have been extensively investigated in the elastic regime (e.g., Brisard et al., 2010a,b; Duan et al., 2005a,b; Le Quang and He, 2007), limited attention has been paid so far to the dependence of effective strength properties on the void size, classical plasticity theories for porous materials being generally conceived to predict porosity effects only (e.g., Gurson, 1977; Ponte Castañeda, 1991). Referring to limit-analysis approaches, a macroscopic yield function accounting for void-size effects has been recently proposed by Dormieux and Kondo (2010), who extended the well-known criterion established by Gurson (1977) to nanoporous materials, by describing cavities boundary via a plastic generalization of stress-interface laws (Gurtin and Murdoch, 1975, 1978; Monchiet and Bonnet, 2010). An analogous modelling strategy has been adopted by Monchiet and Kondo (2013), who addressed the combined influence of void size and void shape on nanoporous materials plastic response. Void-size dependent strength criteria have also been established in the framework of non-linear homogenization approaches (Dormieux and Kondo, 2013; Goudarzi et al., 2010; Moshtaghin et al., 2012; Zhang and Wang, 2007; Zhang et al., 2008, 2010). However, as it will be shown in the following, the most recent non-linear homogenization strength criterion (Dormieux

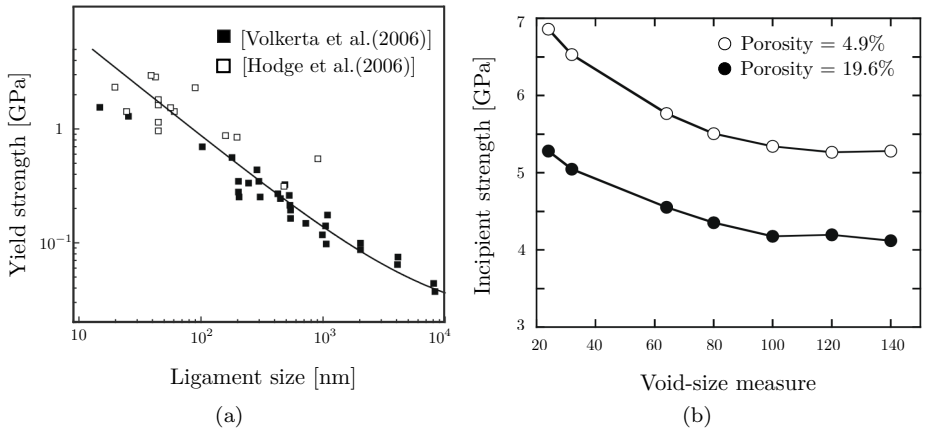

Figure 3 – Void-size effects on strength properties of nanoporous materials. (a) Experimental evidence provided by (Fan and Fang, 2009), obtained via nanoindentation tests on nanoporous foams, the ligament size being a measure of the characteristic length of voids. (b) Molecular-Dynamics results by Zhao et al. (2009) for an in-silico nanovoided single-crystal copper undegoing an uniaxial tension loading.

and Kondo, 2013) strongly overrates available numerical evidence (Trillat and Pastor, 2005; Morin et al., 2015), resulting inaccurate especially for high stress-traxiality levels. Moreover, afore-mentioned strength models have been obtained by considering a plastic solid matrix obeying to a von Mises yield criterion, that is by assuming the local plastic response to be independent from both the hydrostatic stress and the stress Lode angle. The effectiveness of this modelling choice needs to be assessed, eventually opening towards the possibility to consider different local plastic behaviours.

Motivated by above observations, the central purpose of the present thesis consists in investigating strength properties of nanoporous materials via both analytical and numerical approaches. The thesis is organized as follows, each chapter corresponding to a submitted or a published research work with a self-consistent notation:

- in Chapter 1, aiming to enhance the model recently provided by Dormieux and Kondo (2013), a non-linear homogenization approach is proposed, delivering a novel macroscopic strength criterion for ductile nanoporous materials. A 3-layered description is adopted, accounting for surface-stress effects at cavities boundary via an imperfect-coherent interface law. The effectiveness of the proposed strength criterion is assessed with respect to available numerical benchmarking data (Trillat and Pastor, 2005; Morin et al., 2015);

- in Chapter 2 [Mec Mater; 101: 102-117 (2016)], strength properties of in-silico nanoporous samples are investigated via a Molecular-Dynamics computational approach. A parametric analysis with respect to the void radius and for different porosity levels is carried out, by considering different loading paths with a wide range of triaxiality scenarios. As a result, the influence of void-size effects on the computed strength properties is quantified, also highlighting the dependence of the predicted material strength domain on the three stress invariants;

- in Chapter 3 [Int J Plasticity; DOI: 10.1016/j.ijplas.2016.10.007 (2016)], the limit-state problem of a nanovoided hollow sphere is exactly solved, in the case of isotropic loading conditions. In agreement with Molecular-Dynamics indications concerning bulk nanosized samples in Chapter 2, the hollow sphere is assumed to be comprised of a rigid-ideal-plastic material obeying to a general isotropic yield criterion. The latter being defined as a simplified form of the yield function proposed by Bigoni and Piccolroaz (2004), a broad class of pressure-sensitive, frictional and ductile local plastic responses are taken into account, allowing also for an extremely flexible description of the stress-Lode-angle influence. Void-size effects are modelled by describing the cavity boundary as a coherent-imperfect homogeneous interface. The exact solution of the limit-state problem is fully determined, providing closed-form relationships for stress, strain-rate and velocity fields, as well as for the macroscopic hydrostatic strength;

- in Chapter 4, a macroscopic general strength criterion accounting for void-size effects is established, by referring to a nanovoided hollow-sphere model undergoing axialsymmetric strain-rate boundary loadings. The general yield function introduced in Chapter 3 is considered, allowing for an extreme flexibility in describing the stress-Lode-angle influence on the local plastic behaviour. In the framework of a kinematic limit-analysis approach, relationships provided in Chapter 3 are used to construct an effective trial velocity field. A parametric closed-form expression of the macroscopic strength criterion is obtained as the physically-consistent solution of a constrained minimization problem, this latter being faced via the Lagrangian method combined with Karush-Kuhn-Tucker conditions. Illustrative computations highlight the impact of the local plastic behaviour on the macroscopic one, as well as the strengthening effect induced on macroscopic yield surfaces by a reduction in the void size for a fixed porosity level.

- in Appendix A [Springer Series in Solid and Structural Mechanics; DOI: 10.1007/978-3-319-48884-4 (2016)], as a complement of the model proposed in Chapter 1, an estimate for the deviatoric strength of nanoporous materials is proposed, by addressing the limit state of a nanovoided hollow sphere undergoing axialsymmetric deviatoric loading conditions. The hollow sphere is assumed to be comprised of a rigid-ideal-plastic matrix obeying to a von Mises strength criterion. A kinematic limit analysis is performed by referring to a suitable trial velocity field (Budiansky et al., 1982). The resulting closed-form expression for the macroscopic deviatoric strength enhances the corresponding estimate provided by Dormieux and Kondo (2010) via a kinematic limit-analysis procedure.

Finally, some conclusions are traced by summarizing main outcomes of proposed theoretical and numerical approaches, as well as by highlighting the contribution of the present thesis to the current literature on nanoporous materials. Possible future research directions are also traced, by furnishing preliminary studies and indications towards more advanced modelling strategies.

CHAPTER 1

A 3-layered based non-linear homogenization approach with interface effects

Abstract

In this Chapter, the strength properties of a ductile nanoporous material are investigated by means of a non-linear homogenization approach based on the modified secant method. The material is described as a rigid ideal-plastic solid matrix, obeying to a von Mises strength criterion, and containing isotropically-distributed spherical nanovoids. Aiming to properly account for local strain-rate heterogeneities, a 3-layered model is adopted. A novel closed-form macroscopic strength criterion is established, and successfully compared with available numerical data. Proposed approach results in an effective enhancement of the non-linear homogenization-based model recently proposed by Dormieux and Kondo [Int J Eng Sci 2013; 71: 102-110].

Present Chapter corresponds to the submitted research paper (Brach et al., 2016a).
A self-consistent notation is adopted.

Keywords: Nanoporous materials, void-size effects, non-linear homogenization, n-layered based approach, modified secant method.

1.1 Introduction

The development of materials characterised by a nanosized microstructure has recently given rise to a growing research interest, involving experimental tests, numerical simulations and theoretical models, aiming to investigate the influence of nano-inclusions or nanopores on the overall material response (Arico et al., 2005; Lu et al., 2004; Jenkins, 2010).

An important class of nanostructured materials consists in nanoporous media, characterised by reduced mass density, high surface-to-volume ratio, good levels of both stiffness and strength, and generally exhibiting a ductile behaviour. Furthermore, due to the nanosize of cavities, these challenging materials are chemically active, exhibiting a high capability to interact with ions and molecules. Through these attractive properties, nanoporous materials are of the most interest in several technical fields, including civil and environmental engineering, geophysics, petroleum industry, biomechanics and chemistry, opening towards groundbreaking multifunctional applications (Jenkins, 2010).

From a mechanical point of view, one of the most important aspect concerns the influence, for a fixed porosity value, of the size of voids on the macroscopic material properties. As a matter of fact, with reference to strength features, recent nano-indentation tests (Biener et al., 2005, 2006; Hakamada and Mabuchi, 2007) have proven a significant increase of the yield stress when the void size decreases. The same dependency has been shown in numerical studies based on Molecular Dynamics approaches (Brach et al., 2016a; Traiviratana et al., 2008; Mi et al., 2011; Zhao et al., 2009), where strength predictions decrease towards asymptotic values when the void size increases.

The physical origin of such a phenomenon has been addressed in literature by analysing the solid-void interphase regions at the atomic length-scale (Gibbs, 1906; Cammarata, 1994; Murr, 1975; Orowan, 1970; Shuttleworth, 1950). Indeed, it has been well recognized that, due to the nanovoid presence, a local perturbation in the atomic arrangement occurs close to the void surface, leading to self-equilibrated interactions which can be interpreted as surface stresses (Needs et al., 1991). Surface-induced effects, usually negligible for classical porous materials, become relevant for nanoporous ones (Duan et al., 2005b), resulting in the experimentally- or numerically-observed void-size dependency of effective mechanical properties.

In the framework of a continuum approach, surface-induced stress fields have been generally addressed by introducing interface models (e.g., Duan et al., 2005a; Gurtin and Murdoch, 1975, 1978; Wang et al., 2011), defined in the zero-thickness limit of the transition zone affected by the perturbation of the atomic arrangement. Reference is usually made to coherent and imperfect interface laws, resulting in the continuity (resp., discontinuity) of the displacement field (resp., stress vector) across the interface (Duan et al., 2005b; Gurtin and Murdoch, 1975, 1978; Povstenko and Yu, 1993).

Early works involving surface-stress effects have been focused on the effective elastic properties of nanoporous or nanocomposite materials (Brisard et al., 2010a,b; Duan et al., 2005a,b; Le Quang and He, 2007; Sharma et al., 2003; Sharma and Ganti, 2004). In contrast, few attention has been paid so far to the influence of surface stresses (and

thereby of void-size effects) on the material plastic behaviour.

Referring to limit-analysis approaches (Salençon, 1983), the well-established yield function proposed by Gurson (1977) for ductile classical porous media has been extended to nanoporous ones by Dormieux and Kondo (2010), taking advantage of a plastic generalization of a two-dimensional stress-interface model (Monchiet and Bonnet, 2010). The same interface description has been used by Monchiet and Kondo (2013) for deriving a nanoporous strength criterion in the case of spheroidal cavities, incorporating then both void-shape and void-size effects.

An alternative to limit-analysis models consists in non-linear homogenization (NLH) methods based on the so-called modified secant-moduli approach (Suquet, 1995, 1997), which have been proven to be equivalent to the variational procedure proposed by Ponte Castañeda (1991). Referring to the linear formulation by Herve and Zaoui (1993) and addressing a n-layered spherical composite assembly, semi-analytical strength criteria for classical porous materials have been derived by Bilger et al. (2002) and by Vincent et al. (2009), numerically-experiencing more accurate strength estimates higher the number n of layers. As regards nanoporous materials and by adopting imperfect-coherent interfaces approaches, some void-size dependent strength criteria have been recently proposed by Goudarzi et al. (2010), Moshtaghin et al. (2012), Zhang and Wang (2007), Zhang et al. (2008), and Zhang et al. (2010). Nevertheless, in these cases, the corresponding macroscopic yield functions are questionably expressed in terms of surface elastic properties, in contrast with the proper definition of limit-stress states. A consistent generalization to nanoporous materials of the porous strength criterion by Ponte Castañeda (1991) has been proposed by Dormieux and Kondo (2013), including surface-induced effects via an interface stress model. However, as it will be shown in the following, such a strength model (denoted as DK) strongly overrates available numerical evidence (Trillat and Pastor, 2005; Morin et al., 2015), especially for high stress-traxiality levels.

Such an occurrence is mainly due to a rough description of local strain-rate heterogeneity in the limit state, and it clearly highlights the need of a further research effort to enhance non-linear homogenization-based strength estimates for nanoporous materials.

In this light, present Chapter aims to establish a consistent and accurate strength model for nanoporous media, properly accounting for void-size effects and able to recover available benchmarking evidence. In detail, strength properties of ductile nanoporous materials are investigated via a non-linear homogenization procedure based on a 3-layered description and including surface-stress effects by means of an imperfect-coherent interface model. The Chapter is organized as follows. In Section 1.2 basic elements of the adopted theoretical framework are presented. Section 1.3 is devoted to the derivation of a novel analytical strength criterion for nanoporous materials, whose effectiveness and accuracy is discussed in Section 1.4. Finally, some conclusions are traced in Section 1.5.

1.2 Preliminary background

1.2.1 Problem statement

Aiming to investigate strength properties of a nanoporous material via a non-linear homogenization (NLH) approach, let Ω be a material representative volume element (RVE), whose exterior boundary is $\partial\Omega$. Let the RVE be comprised of internal isotropically-distributed spherical cavities of radius a and of a rigid-ideal-plastic solid matrix Ω^{s} (Fig. 1.1). Therefore, material strength properties are straight identified by referring to the yield limit state.

It is observed that the rigid-ideal-plastic assumption on the local mechanical response is a fundamental requirement of the limit analysis theory. Such an hypothesis has been widely adopted in both classical and more recent literature focusing on porous and nanoporous materials (see for instance limit-analysis-based approaches by Gurson (1977), Guo et al. (2008), Dormieux and Kondo (2010), Monchiet and Kondo (2013), Anoukou et al. (2016), and Brach et al. (2016b), as well as variational non-linear homogenization techniques by Ponte Castañeda (1991), Zhang and Wang (2007), Zhang et al. (2008), Zhang et al. (2010) and Dormieux and Kondo (2013)), and it is recognized to be particularly effective for metallic solid matrices.

Denoting by $|\Omega|$ and $|\Omega^{\mathrm{v}}|$ the volume measures of the RVE and of the voided region $\Omega^{\mathrm{v}} = \Omega \setminus \Omega^{\mathrm{s}}$, respectively, the porosity p results in $p = |\Omega^{\mathrm{v}}|/|\Omega|$. Moreover, let $\partial\Omega^{\mathrm{v}}$ be the overall cavities boundary, $\mathbf{n}^{\mathrm{v}}$ being the corresponding normal unit vector (see Fig. 1.1).

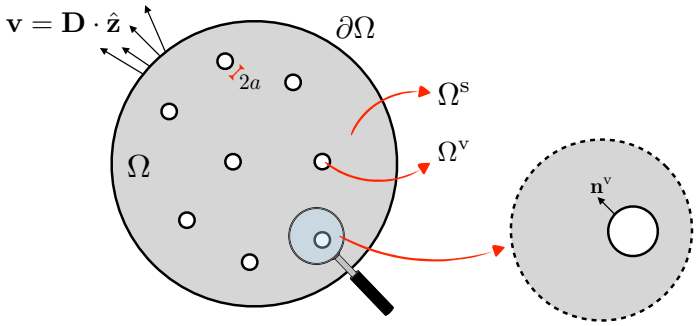

Figure 1.1 – Representative volume element. Notation. Solid matrix and the overall region occupied by voids are respectively denoted as Ω^{s} and Ω^{v}, such that $\Omega = \Omega^{\mathrm{s}} \cup \Omega^{\mathrm{v}}$. Vector $\hat{\mathbf{z}}$ identifies a position at the RVE exterior boundary $\partial\Omega$.

As a notation rule, vectors (e.g., $\mathbf{z}$) and tensors (e.g., second-order $\boldsymbol{\sigma}$ and $\mathbf{d}$, and fourth-order $\boldsymbol{\mathcal{C}}$) are denoted by bold letters; ∇ is the nabla operator, ${}^{\mathrm{t}}\nabla$ indicating its transpose; symbols $\cdot$ and $:$ respectively denote dot and double contraction product operators, component-wise defined in an orthonormal frame as $(\mathbf{d}\cdot\mathbf{z})_i = \sum_j d_{ij} z_j$, $\boldsymbol{\sigma} : \mathbf{d} = \sum_{i,j} \sigma_{ij} d_{ij}$ and $(\boldsymbol{\mathcal{C}} : \mathbf{d})_{ij} = \sum_{k,\ell} \mathcal{C}_{ijk\ell} d_{k\ell}$.

Moreover, let Ω-based and Ω^{s}-based averages of a certain space-dependent field $q(\mathbf{z})$ be defined as:

$$\overline{q} = \frac{1}{|\Omega|} \int_{\Omega} q(\mathbf{z})\, d\Omega, \qquad \overline{q}^{\mathrm{s}} = \frac{1}{|\Omega^{\mathrm{s}}|} \int_{\Omega^{\mathrm{s}}} q(\mathbf{z})\, d\Omega\,, \tag{1.1}$$

where vector $\mathbf{z}$ identifies the position of a point in Ω. Furthermore, let $\boldsymbol{\sigma}(\mathbf{z})$ and $\mathbf{d}(\mathbf{z})$ (resp., $\boldsymbol{\Sigma}$ and $\mathbf{D}$) be the microscopic (resp., macroscopic) stress and strain-rate tensor measures.

The RVE is assumed to undergo homogeneous strain-rate boundary conditions, prescribed in terms of the second-order symmetric constant tensor $\mathbf{D}$. Accordingly, the set of kinematically-admissible microscopic velocity fields $\mathbf{v}(\mathbf{z})$ is defined as

$$\mathcal{V}(\mathbf{D}) = \left\{ \mathbf{v}(\mathbf{z}) \,|\, \mathbf{v} = \mathbf{D} \cdot \hat{\mathbf{z}} \quad \text{with } \hat{\mathbf{z}} \in \partial\Omega \right\}. \tag{1.2}$$

Considering an equilibrated stress field $\boldsymbol{\sigma}(\mathbf{z})$ in Ω, such that $\boldsymbol{\Sigma} = \overline{\boldsymbol{\sigma}}$, and a compatible strain-rate field $\mathbf{d} = (\nabla\mathbf{v} + {}^{\mathrm{t}}\nabla\mathbf{v})/2$ with $\mathbf{v} \in \mathcal{V}(\mathbf{D})$, the Hill's lemma holds (e.g., Salençon, 1983):

$$|\Omega|\boldsymbol{\Sigma} : \mathbf{D} = \int_{\Omega} \boldsymbol{\sigma} : \mathbf{d}\, d\Omega \tag{1.3}$$

stating the equivalence between the exterior and interior powers.

Let the convex set of the admissible stress states in a certain material point of the solid matrix be introduced as

$$G^{\mathrm{s}}(\mathbf{z}) = \left\{ \boldsymbol{\sigma} \,\middle|\, f^{\mathrm{s}}(\mathbf{z}, \boldsymbol{\sigma}) \leq 0 \right\} \tag{1.4}$$

where $f^{\mathrm{s}}(\mathbf{z}, \boldsymbol{\sigma})$ identifies the matrix yield function, possibly accounting for local heterogeneous strength properties.

Since the exterior power associated to the prescribed strain-rate boundary conditions has to be lower or at the most equal to the maximum plastic dissipation that can be afforded in Ω, by combining Eqs. (1.3) and (1.4) the following inequality is obtained

$$|\Omega|\boldsymbol{\Sigma} : \mathbf{D} \leq \int_{\Omega} \pi^{\mathrm{s}}(\mathbf{z}, \mathbf{d}(\mathbf{z}))\, d\Omega \tag{1.5}$$

where π^{s} identifies the local support function for G^{s} and it represents the maximum plastic dissipation that can be locally achieved, thereby resulting in

$$\pi^{\mathrm{s}}(\mathbf{z}, \mathbf{d}(\mathbf{z})) = \sup_{\boldsymbol{\sigma} \in G^{\mathrm{s}}} \left\{ \boldsymbol{\sigma}(\mathbf{z}) : \mathbf{d}(\mathbf{z}) \right\}. \tag{1.6}$$

Therefore, for a certain material point, $\pi^{\mathrm{s}}(\mathbf{d})$ is the hyperplane tangent to the yield surface $f^{\mathrm{s}}(\boldsymbol{\sigma}) = 0$ (i.e., such that $\boldsymbol{\sigma} = \partial\pi^{\mathrm{s}}/\partial\mathbf{d}$) in the space of microscopic stresses.

Accordingly, the inequality (1.5) can be recast as

$$\boldsymbol{\Sigma} : \mathbf{D} \leq \Pi^{\mathrm{hom}}(\mathbf{D}) \tag{1.7}$$

where Π^{hom} is the macroscopic maximum plastic dissipation, defined as

$$\Pi^{\mathrm{hom}}(\mathbf{D}) = \inf_{\mathbf{v} \in \mathcal{V}(\mathbf{D})} \left\{ \overline{\pi} \right\} \qquad \text{with} \quad \pi = \begin{cases} \pi^{\mathrm{s}}\,, & \text{in } \Omega^{\mathrm{s}} \\ 0\,, & \text{in } \Omega^{\mathrm{v}} \end{cases} \tag{1.8}$$

π^{s} being a function of the velocity field $\mathbf{v}$ via the above-introduced compatibility condition $\mathbf{d} = (\nabla\mathbf{v} + {}^{\mathrm{t}}\nabla\mathbf{v})/2$. It can be shown (e.g., de Buhan, 1986) that the stress state

$$\boldsymbol{\Sigma} = \frac{\partial \Pi^{\mathrm{hom}}}{\partial \mathbf{D}} \tag{1.9}$$

belongs to the boundary $\partial G^{\mathrm{hom}}$ of the macroscopic strength domain, at the stress point where $\mathbf{D}$ is normal to $\partial G^{\mathrm{hom}}$, thereby Π^{hom} identifying the support function for the convex set G^{hom} of the admissible macroscopic stress states.

It is worth observing that, when Π^{hom} is estimated by means of a particular microscopic velocity field $\mathbf{v} \in \mathcal{V}(\mathbf{D})$, Eq. (1.9) furnishes an upper bound of the macroscopic limit stress.

The following boundary-value problem is introduced (e.g., Dormieux et al., 2006).

Problem 1 *For a given* $\mathbf{D}$, *find* $\{\boldsymbol{\sigma}(\mathbf{z}), \mathbf{d}(\mathbf{z}), \mathbf{v}(\mathbf{z})\}$ *s.t.*

$$\operatorname{div}\boldsymbol{\sigma} = \mathbf{0} \qquad \textit{in } \Omega \tag{1.10a}$$

$$\boldsymbol{\sigma} = \frac{\partial \pi(\mathbf{z}, \mathbf{d}(\mathbf{z}))}{\partial \mathbf{d}} \qquad \textit{in } \Omega \tag{1.10b}$$

$$\mathbf{d} = \frac{1}{2}(\nabla\mathbf{v} + {}^{t}\nabla\mathbf{v}) \qquad \textit{in } \Omega \tag{1.10c}$$

$$\boldsymbol{\sigma}\cdot\mathbf{n}^{v} = \mathbf{0} \qquad \textit{on } \partial\Omega^{v} \tag{1.10d}$$

$$\mathbf{v} = \mathbf{D}\cdot\hat{\mathbf{z}} \qquad \textit{on } \partial\Omega \tag{1.10e}$$

In the framework of non-linear homogenization (NLH) techniques, Problem 1 is faced by referring to the secant-moduli approach, proven by Suquet (Suquet, 1995) to be equivalent to the Ponte-Castañeda's non-linear variational procedure (Ponte Castañeda, 1991).

1.2.2 Non-linear homogenization: the secant-moduli approach

Equation (1.10b) can be thought as representative of a fictitious non-linear behaviour described by the following fictitious constitutive relationship

$$\boldsymbol{\sigma}(\mathbf{z}) = \begin{cases} \boldsymbol{\mathcal{C}}\big(\mathbf{z}, \mathbf{d}(\mathbf{z})\big) : \mathbf{d}(\mathbf{z}) & \text{if} \quad \mathbf{z} \in \Omega^{\mathrm{s}} \\ \mathbf{0} & \text{if} \quad \mathbf{z} \in \Omega^{\mathrm{v}} \end{cases} \tag{1.11}$$

where the fourth-order secant stiffness tensor $\boldsymbol{\mathcal{C}}$ is well defined from the support function $\pi^{\mathrm{s}}(\mathbf{z}, \mathbf{d}(\mathbf{z}))$, considered as the potential of the corresponding fictitious viscous material.

Let $I_1^{\sigma} = \operatorname{tr}\boldsymbol{\sigma}$ (resp., $I_1^{\mathrm{d}} = \operatorname{tr}\mathbf{d}$) be the first stress (resp., strain-rate) invariant, and $J_2^{\sigma} = \boldsymbol{\sigma}_{\mathrm{dev}} : \boldsymbol{\sigma}_{\mathrm{dev}}/2$ (resp., $J_2^{\mathrm{d}} = \mathbf{d}_{\mathrm{dev}} : \mathbf{d}_{\mathrm{dev}}/2$) the second deviatoric stress (resp., strain-rate) invariant, with $\boldsymbol{\sigma}_{\mathrm{dev}} = \boldsymbol{\sigma} - I_1^{\sigma}\mathbf{1}/3$ (resp., $\mathbf{d}_{\mathrm{dev}} = \mathbf{d} - I_1^{\mathrm{d}}\mathbf{1}/3$) the stress (resp., strain-rate) deviatoric part, $\mathbf{1}$ being the second-order identity tensor such that $(\mathbf{1})_{ij} = \delta_{ij}$, with δ_{ij} the Kronecker delta. By assuming the local strength function f^{s} to be representative of an isotropic plastic response, and defined in terms of the first and the second-order deviatoric invariants I_1^{σ} and J_2^{σ} only, π^{s} depends in turn on strain-rate invariants I_1^{d} and J_2^{d} only. Accordingly, $\boldsymbol{\mathcal{C}}$ describes an isotropic non-linear behaviour for a fictitious

heterogeneous material, characterised by

$$\boldsymbol{\mathcal{C}}\big(\mathbf{z},\mathbf{d}(\mathbf{z})\big) = 3k\big(\mathbf{z},\mathbf{d}(\mathbf{z})\big)\boldsymbol{\mathcal{J}} + 2\mu\big(\mathbf{z},\mathbf{d}(\mathbf{z})\big)\boldsymbol{\mathcal{K}} \tag{1.12}$$

where $\boldsymbol{\mathcal{J}}$ and $\boldsymbol{\mathcal{K}} = \mathbf{I} - \boldsymbol{\mathcal{J}}$ are spherical and deviatoric fourth-order isotropic projector tensors, respectively, component-wise defined by $3\mathcal{J}_{ijk\ell} = \delta_{ij}\delta_{k\ell}$ and $2I_{ijk\ell} = \delta_{ik}\delta_{j\ell} + \delta_{i\ell}\delta_{jk}$. Moreover, volumetric (namely, k) and shear (μ) secant moduli read as:

$$k\big(\mathbf{z},\mathbf{d}(\mathbf{z})\big) = \frac{1}{I_1^{\mathrm{d}}}\frac{\partial\pi^{\mathrm{s}}}{\partial I_1^{\mathrm{d}}}, \qquad \mu\big(\mathbf{z},\mathbf{d}(\mathbf{z})\big) = \frac{1}{2}\frac{\partial\pi^{\mathrm{s}}}{\partial J_2^{\mathrm{d}}}\,. \tag{1.13}$$

The case of a solid matrix obeying to a von Mises strength criterion is herein addressed. Therefore, G^{s} is defined in terms of $f^{\mathrm{s}}(\mathbf{z},\boldsymbol{\sigma}) = 3J_2^{\sigma}(\boldsymbol{\sigma}) - \hat{\sigma}^2(\mathbf{z})$, where $\hat{\sigma}(\mathbf{z})$ is the von Mises strength, and the local support function π^{s} reads as

$$\pi^{\mathrm{s}}(\mathbf{z}, I_1^{\mathrm{d}}, J_2^{\mathrm{d}}) = \begin{cases} 2\hat{\sigma}(\mathbf{z})\sqrt{\dfrac{J_2^{\mathrm{d}}}{3}} & \text{if } I_1^{\mathrm{d}} = 0 \\ +\infty & \text{if } I_1^{\mathrm{d}} \neq 0 \end{cases} \tag{1.14}$$

It is worth pointing out that π^{s} provided in Eq. (1.14) is not differentiable due to the singularity for $I_1^{\mathrm{d}} \neq 0$. Nevertheless, secant moduli in Eqs. (1.13) can be derived by using an asymptotic approach, resulting in (e.g., Dormieux et al., 2006):

$$k \to +\infty, \qquad \mu(\mathbf{z},\mathbf{d}(\mathbf{z})) = \frac{\hat{\sigma}(\mathbf{z})}{2\sqrt{3}}\frac{1}{\sqrt{J_2^{\mathrm{d}}(\mathbf{d}(\mathbf{z}))}}\,. \tag{1.15}$$

Accordingly, Problem 1 can be considered associated to a fictitious incompressible material, whose constitutive law (1.11) is representative of a non-linear (owing to the dependency of $\boldsymbol{\mathcal{C}}$ on the strain rate $\mathbf{d}$ by means of J_2^{d}) and heterogeneous response (due to the space dependency of $\hat{\sigma}$ and $\mathbf{d}$, and formally equivalent to a pointwise homogeneous behaviour).

1.2.3 n-layered modelling

In order to obtain an analytical solution, a simplified version of the Problem 1 is introduced, by describing $\boldsymbol{\mathcal{C}}$ as a piecewise-constant (in space) tensor. With reference to the n-layered model proposed by Herve and Zaoui (1993), a suitable partition of Ω is considered, as shown in Fig. 1.2a. In detail, in agreement with previous studies (Ponte Castañeda and Suquet, 1998; Dormieux and Kondo, 2013), Ω is decomposed as $\Omega = \Omega^{\mathrm{c}} \cup \Omega_{\mathrm{n}+1}$, where Ω^{c} identifies the overall region occupied by the collection of $\mathcal{N}$ identical non-intersecting spheres Ω_i^{c}, each of them concentric to a void (namely, $\Omega^{\mathrm{c}} = \cup_{i=1}^{\mathcal{N}}\Omega_i^{\mathrm{c}}$, with $\Omega_i^{\mathrm{c}} \cap \Omega_j^{\mathrm{c}} = \emptyset$ when $i \neq j$), and $\Omega_{\mathrm{n}+1}$ is the complementary part. Each spherical subdomain Ω_i^{c} is in turn assumed to be identically partitioned via n confocal spherical layers, such that $\Omega_i^{\mathrm{c}} = \cup_{\alpha=1}^{n}\Omega_{i,\alpha}$, where $\Omega_{i,1}$ is the i-th void region. The normal vector at the separation surface $\partial\Omega_{i,\alpha}$ between layers $\Omega_{i,\alpha}$ and $\Omega_{i,\alpha+1}$, outward-oriented with respect to $\Omega_{i,\alpha}$ (see Fig. 1.2b), is denoted as $\mathbf{n}_{i,\alpha}$, with $\mathbf{n}_{i,1}$ coincident to the unit vector $\mathbf{n}^{\mathrm{v}}$ normal to the void

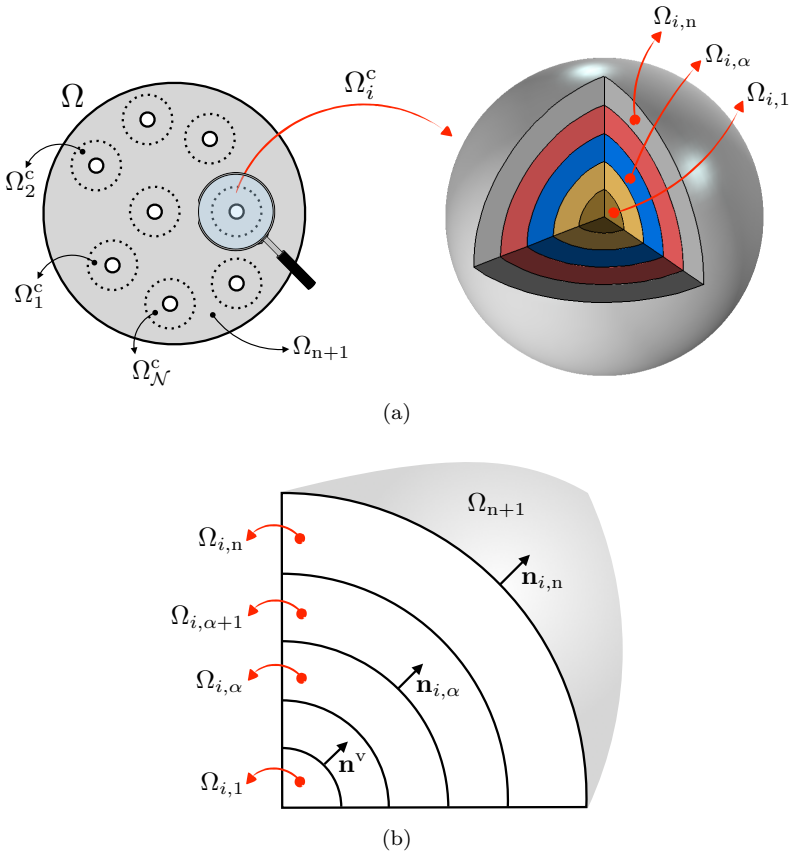

Figure 1.2 – (a) n-layered sub-partition adopted in Problem 2 for treating the fictitious constitutive response described by Eqs. (1.12) and (1.15). (b) Normal unit vectors on separation surfaces $\partial\Omega_{i,\alpha}$.

surface. The following partition rules apply: $\Omega = \cup_{\alpha=1}^{n+1}\Omega_\alpha$, where $\Omega_\alpha = \cup_{i=1}^{\mathcal{N}}\Omega_{i,\alpha}$ (with $\alpha \neq n+1$) is the overall volume region occupied by spherical layers of type α, having the boundary part $\partial\Omega_\alpha = \cup_{i=1}^{\mathcal{N}}\partial\Omega_{i,\alpha}$ with $\mathbf{n}_\alpha$ being the corresponding normal unit vector (such that $\mathbf{n}_\alpha = \mathbf{n}_{i,\alpha}$ on $\partial\Omega_{i,\alpha}$). For what follows and for a certain spherical subdomain $\Omega_i^{\rm c}$, it is useful to introduce the spherical coordinate system (θ, φ, r), with the origin at the center of $\Omega_i^{\rm c}$ and whose corresponding orthonormal basis is denoted as $(\mathbf{e}_\theta, \mathbf{e}_\varphi, \mathbf{e}_{\rm r})$, such that $\mathbf{e}_{\rm r} \equiv \mathbf{n}^{\rm v}$.

In each subregion Ω_α, both the von Mises parameter and the second-order strain-rate invariant are assumed to be constant in space, namely $\hat{\sigma}(\mathbf{z}) = \hat{\sigma}_\alpha$ (with $\hat{\sigma}_1 = 0$), and $J_2^{\rm d}(\mathbf{d}(\mathbf{z})) = J_{2\alpha}^{\rm d}$. Thereby, owing to Eqs. (1.11), (1.12) and (1.15), the fictitious material occupying the region Ω is described as a $(n+1)$-phases composite medium (consisting in composite spheres $\Omega_i^{\rm c}$ embedded in a homogeneous solid matrix $\Omega_{\rm n+1}$) with constant (in space) secant moduli in each phase Ω_α.

Accordingly, a piecewise homogeneous representation (i.e., corresponding to a finite number of phases) of the heterogeneous fictitious response in Eq. (1.11) (formally related to a pointwise homogeneous behaviour, that is corresponding to infinite phases) is obtained.

It is worth observing that the adopted partition, depending on the number of phases $(n+1)$, allows to furnish a certain description of the local strain-rate heterogeneity, whose occurrence is widely documented (e.g., Marian et al., 2004, 2005; Traiviratana et al., 2008; Zhao et al., 2009).

This partition strategy has been adopted in other NLH-based models. For instance, the analytical criterion by Dormieux and Kondo (2013), for nanoporous materials and accounting for void-size effects, is deduced by considering three phases (corresponding to a 2-layered model). Referring to a partition involving two phases, Suquet (1995) established a macroscopic criterion for porous materials (i.e., without any surface-stress effects) which coincides with the variational-based one provided by Ponte-Castañeda (Ponte Castañeda, 1991). Finally, again in the case of porous materials, semi-analytical results are provided by Bilger et al. (2002) and Vincent et al. (2009) for different values of n. Corresponding computational evidence showed that the predicted hydrostatic strength tends to its exact value (Gurson, 1977) by increasing the number of spherical layers in each composite sphere. For instance, considering $p = 1\%$, the exact hydrostatic limit stress has been accurately estimated by assuming $n = 21$, (Bilger et al., 2002).

Due to previous assumptions, Problem 1 simplifies as follows.

Problem 2 *For a given* $\mathbf{D}$ *and for an assigned integer number* n*, find* $\left\{\boldsymbol{\sigma}_\alpha(\mathbf{z}), \mathbf{d}_\alpha(\mathbf{z}), \mathbf{v}_\alpha(\mathbf{z})\right\}$ *for any* $\alpha \in \{1, \ldots, n+1\}$*, s.t.*

$$\operatorname{div} \boldsymbol{\sigma}_\alpha = \mathbf{0} \qquad \text{in } \Omega_\alpha \tag{1.16a}$$

$$\boldsymbol{\sigma}_\alpha = \begin{cases} \boldsymbol{\mathcal{C}}_\alpha : \mathbf{d}_\alpha & \text{in } \Omega_\alpha \quad \text{for } \alpha \neq 1 \\ \mathbf{0} & \text{in } \Omega_1 \equiv \Omega^v \end{cases} \tag{1.16b}$$

$$\mathbf{d}_\alpha = \frac{1}{2}(\nabla \mathbf{v}_\alpha + {}^t\nabla \mathbf{v}_\alpha) \qquad \text{in } \Omega_\alpha \tag{1.16c}$$

$$(\boldsymbol{\sigma}_\alpha - \boldsymbol{\sigma}_{\alpha+1}) \cdot \mathbf{n}_\alpha = \mathbf{0} \qquad \text{on } \partial\Omega_\alpha \quad \text{for } \alpha \neq n+1 \tag{1.16d}$$

$$\mathbf{v}_\alpha = \mathbf{v}_{\alpha+1} \qquad \text{on } \partial\Omega_\alpha \quad \text{for } \alpha \neq n+1 \tag{1.16e}$$

$$\mathbf{v}_{n+1} = \mathbf{D} \cdot \hat{\mathbf{z}} \qquad \text{on } \partial\Omega \tag{1.16f}$$

where $\boldsymbol{\mathcal{C}}_\alpha$ *(when* $\alpha \neq 1$*) is defined as in Eqs.* (1.12) *and* (1.15)*, with* $\mu = \mu_\alpha$ *in* Ω_α*,* μ_α *being*

$$\mu_\alpha = \frac{\hat{\sigma}_\alpha}{2\sqrt{3}} \frac{1}{\sqrt{J^d_{2\alpha}}}\,. \tag{1.17}$$

It is worth observing that the constitutive law expressed by Eq. (1.16b) (when $\alpha \neq 1$) is non linear due to the dependency of $J^{\mathrm{d}}_{2\alpha}$ on the local strain-rate field $\mathbf{d}(\mathbf{z})$.

As a matter of fact, assuming for a while that $J^{\mathrm{d}}_{2\alpha}$ is known for each phase, Problem 2 reduces to a standard linearly-viscous problem defined on a piecewise homogeneous medium, referred to as a linear comparison composite (LCC) (Suquet, 1997). In this case, an estimate of the macroscopic limit stress is

$$\boldsymbol{\Sigma} = \boldsymbol{\mathcal{C}}^{\mathrm{hom}}(\mathbf{D}) : \mathbf{D} \tag{1.18}$$

where $\boldsymbol{\mathcal{C}}^{\text{hom}}$ is the homogenized fictitious constitutive tensor, which can be computed starting from $\boldsymbol{\mathcal{C}}_\alpha$, by means of a suitable linear homogenization scheme. It is pointed out that, since the composite spherical inclusions in Ω are isotropically-distributed and each phase α is isotropic, $\boldsymbol{\mathcal{C}}^{\text{hom}}$ is in turn isotropic and characterised by effective moduli μ^{hom} and k^{hom}.

The non linearity involved in Eqs. (1.16b) and (1.18), associated to the determination of $J^{\text{d}}_{2\alpha}$ (equivalently, μ_α), is faced by referring to the first variation with respect to μ_α of the Hill's equality (1.3), when $\boldsymbol{\sigma}$ and $\boldsymbol{\Sigma}$ are expressed by Eqs. (1.16b) and (1.18), respectively. In detail, the following equalities are provided (see Ponte Castañeda and Suquet (1998), Buryachenko (1993), Kreher (1990), and Dormieux et al. (2006))

$$\mathcal{F}: \qquad F_\alpha J^{\text{d}}_{2\alpha} = \frac{1}{4}\left(\frac{\Sigma_{\text{m}}}{k^{\text{hom}}}\right)^2 \frac{\partial k^{\text{hom}}}{\partial \mu_\alpha} + \frac{1}{12}\left(\frac{\Sigma_{\text{eq}}}{\mu^{\text{hom}}}\right)^2 \frac{\partial \mu^{\text{hom}}}{\partial \mu_\alpha} \tag{1.19}$$

where $F_\alpha = |\Omega_\alpha|/|\Omega|$ is the volume fraction of the phase α, and where hydrostatic and deviatoric macroscopic stress measures are introduced as $\Sigma_{\text{m}} = I^\Sigma_1/3$ and $\Sigma_{\text{eq}} = \sqrt{3J^\Sigma_2}$, respectively.

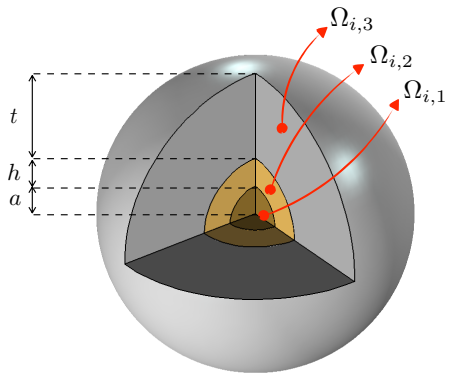

Figure 1.3 – Sketch of the adopted 3-layered model ($n = 3$). Notation.

1.3 A novel NLH-based strength criterion

With the aim to provide a novel analytical strength criterion for nanoporous materials, an approach based on a 3-layered model is employed to treat the non-linear homogenization underlying Problem 2. With reference to Fig. 1.3, the adopted domain partition consists in four phases ($n = 3$): pore regions (phase Ω_1), spherical layers $\Omega_{i,2} \equiv \mathcal{L}_i$ of thickness h (phase Ω_2), $\mathcal{L}_i$-to matrix transition zones $\Omega_{i,3}$ of thickness t (phase Ω_3), and solid matrix (phase $\Omega_4 \equiv \Omega_{\text{n+1}}$).

Each subregion $\mathcal{L}_i$ allows to take into account surface-stress effects due to the possible nanosize of voids. To this end, the length-scale parameter $\chi = h/a$ is assumed such that $\chi = \text{O}(\epsilon)$ for any dimensionless $\epsilon > 0$ however small. By integrating the equilibrium equation (1.16a) written for $\alpha = 2$ over $a \le r \le a(1+\chi)$, and by neglecting contributions

scaling as χ, the following relationship holds (see Dormieux and Kondo, 2013)

$$(\boldsymbol{\sigma}_2^+ - \boldsymbol{\sigma}_2^-) \cdot \mathbf{e}_\mathrm{r} = \frac{1}{a}(\tau_\mathrm{r}\mathbf{e}_\mathrm{r} + \tau_\theta \mathbf{e}_\theta + \tau_\varphi \mathbf{e}_\varphi) \tag{1.20}$$

$\boldsymbol{\sigma}_2^+$ (resp., $\boldsymbol{\sigma}_2^-$) indicating $\boldsymbol{\sigma}_2$ on $\partial\Omega_2$ (resp., on $\partial\Omega_1$), with τ_r, τ_θ and τ_φ resulting in

$$\begin{aligned}
\tau_r &= \sigma^{\mathcal{L}}_{\theta\theta} + \sigma^{\mathcal{L}}_{\varphi\varphi} \\
\tau_\theta &= (\sigma^{\mathcal{L}}_{\varphi\varphi} - \sigma^{\mathcal{L}}_{\theta\theta}) \cot\theta - \frac{\partial \sigma^{\mathcal{L}}_{\theta\theta}}{\partial\theta} - \frac{1}{\sin\theta}\frac{\partial \sigma^{\mathcal{L}}_{\theta\varphi}}{\partial\varphi} \\
\tau_\varphi &= -\left(\frac{\partial \sigma^{\mathcal{L}}_{\theta\varphi}}{\partial\theta} + \frac{1}{\sin\theta}\frac{\partial \sigma^{\mathcal{L}}_{\varphi\varphi}}{\partial\varphi} + 2\sigma^{\mathcal{L}}_{\theta\varphi}\cot\theta\right)
\end{aligned} \tag{1.21}$$

where the unknown stress components $\sigma^{\mathcal{L}}_{\theta\theta}$, $\sigma^{\mathcal{L}}_{\varphi\varphi}$ and $\sigma^{\mathcal{L}}_{\theta\varphi}$ have the meaning of surface stresses, namely $\sigma^{\mathcal{L}}_*(\theta,\varphi) = \int_a^{a(1+\chi)} \sigma_* dr \simeq a\chi\sigma_*|_{r=a}$. Accordingly, due to Eq. (1.20) and under the smallness assumption $\chi = \mathrm{O}(\epsilon)$, each spherical layer $\mathcal{L}_i$ plays the physical role of an interface, characterized by a discontinuous stress vector and, owing to Eq. (1.16e), by a continuous velocity field across $\mathcal{L}_i$. Thereby, the latter corresponds to an imperfect-coherent interface (e.g., Monchiet and Bonnet, 2010).

In agreement with the domain partition depicted in Fig. 1.3, phase volume fractions introduced in Eq. (1.19) are expressed in terms of the porosity p, as

$$F_1 = p, \qquad F_2 = p\left(\frac{1}{f} - 1\right), \qquad F_3 = \varphi - \frac{p}{f}, \qquad F_4 = 1 - \varphi \tag{1.22}$$

where the following volume ratios are introduced

$$\begin{aligned}
f &= \frac{|\Omega_1|}{|\Omega_1| + |\Omega_2|} = 1 - 3\chi + \mathrm{o}(\epsilon) \\
\varphi &= \frac{|\Omega_1| + |\Omega_2| + |\Omega_3|}{|\Omega|} = \frac{|\Omega^\mathrm{c}|}{|\Omega|}
\end{aligned} \tag{1.23}$$

with φ a dimensionless parameter representing the volume fraction of composite inclusions in Ω.

It is worth pointing out that the transition phase Ω_3 has been introduced in order to refine the local strain-rate description with respect to the approach provided by Dormieux and Kondo (2013). Furthermore, since numerical evidence on nanoporous materials (e.g., Brach et al., 2016a; Marian et al., 2004, 2005; Traiviratana et al., 2008; Zhao et al., 2009) shows that high strain-rate inhomogeneities occur in thin regions surrounding nanovoids, a satisfactory description of the local strain-rate distribution is expected to be provided by considering small values of the thickness t. Hence, the dimensionless ratio $\xi = t/a$ is assumed to satisfy the smallness condition $\xi = \mathrm{O}(\epsilon)$ and, since φ can be expressed as $\varphi = p(1+\chi^3+\xi^3)$, the volume fraction of the solid part of composite inclusions $\psi = \varphi - p$ (with $\psi \geq 0$) results in $\psi = \mathrm{O}(\epsilon)$.

The von Mises phase strength $\hat{\sigma}_\alpha$, introduced in Eq. (1.17), is defined as

$$\hat{\sigma}_\alpha = \begin{cases} 0 & \text{in } \Omega_1 \\ \sigma_{\mathcal{L}}/(a\chi) & \text{in } \Omega_2 \\ \sigma_0 & \text{in } \Omega_\alpha \quad \text{with } \alpha \in \{3,4\} \end{cases} \tag{1.24}$$

where $\sigma_{\mathcal{L}}$ has the physical dimension of a surface stress. Accordingly, the fictitious shear moduli in Eq. (1.17) result in

$$\mu_1 = 0, \qquad \mu_2 = \frac{\sigma_0 \kappa}{2\chi\sqrt{3J_{22}^{\mathrm{d}}}}, \qquad \mu_3 = \frac{\sigma_0}{2\sqrt{3J_{23}^{\mathrm{d}}}}, \qquad \mu_4 = \frac{\sigma_0}{2\sqrt{3J_{24}^{\mathrm{d}}}} \tag{1.25}$$

where the dimensionless parameter κ is introduced as

$$\kappa = \frac{\sigma_{\mathcal{L}}}{a\sigma_0} \tag{1.26}$$

allowing to describe the influence of surface-induced effects, as strictly related to the void size. As a matter of fact, an increase in κ corresponds, for a fixed value of the strength parameter σ_0, to an increase in the ratio $\sigma_{\mathcal{L}}/a$, and it results from a reduction in the void size. Consequently, the case of porous materials (associated to negligible interface effects as a result of suitably large values of a) can be recovered by setting $\kappa \to 0^+$.

Finally, in agreement with the modified secant-moduli approach proposed by Suquet (1995), the kinematical descriptors $J_{2\alpha}^{\mathrm{d}}$ occurring in Eqs. (1.25) are defined as the average of the local strain-rate invariant $J_2^{\mathrm{d}}(\mathbf{d}(\mathbf{z}))$ on Ω_α:

$$J_{2\alpha}^{\mathrm{d}} = \frac{1}{|\Omega_\alpha|} \int_{\Omega_\alpha} J_2^{\mathrm{d}}(\mathbf{d}(\mathbf{z}))\, d\Omega\,. \tag{1.27}$$

1.3.1 LCC effective moduli

The effective moduli μ^{hom} and k^{hom} involved in Eqs. (1.18) and (1.19), and associated to the above-introduced four-phases linear comparison composite (LCC), are obtained by means of a generalized Mori-Tanaka homogenization scheme. To this aim, the following auxiliary Eshelby-type problem is defined.

Let $\Omega^E \equiv \Omega_i^{\mathrm{c}}$ be a three-phases composite hollow sphere, embedded in an isotropic linearly-elastic solid medium Ω^∞, whose stiffness tensor is assumed equal to $\boldsymbol{\mathcal{C}}_4$ (see Eq. (1.16b)).

Isotropic and shear homogeneous strain-rate boundary conditions are singularly prescribed, by assigning constant strain-rate tensors $\mathbf{D}_\infty^{\mathrm{iso}}$ and $\mathbf{D}_\infty^{\mathrm{shr}}$ at infinity, these latter being characterized by null deviatoric and hydrostatic parts, respectively (that is, $\boldsymbol{\mathcal{K}} : \mathbf{D}_\infty^{\mathrm{iso}} = \mathbf{0}$, and allowing to straight determine k^{hom}; $\boldsymbol{\mathcal{J}} : \mathbf{D}_\infty^{\mathrm{shr}} = \mathbf{0}$, and allowing to straight determine μ^{hom}). Reference is herein made to infinity strain-rate tensors ($\mathbf{D}_\infty^{\mathrm{iso}}$ and $\mathbf{D}_\infty^{\mathrm{shr}}$) and to the corresponding exact velocity fields ($\mathbf{v}_\alpha^{\mathrm{iso}}$ and $\mathbf{v}_\alpha^{\mathrm{shr}}$, for the α-subdomain in Ω^{E}) provided by Love (1944) and by Herve and Zaoui (1993).

In agreement with the approach proposed by Herve and Zaoui (1993), the velocity

field $\mathbf{v}_\alpha^w$ (which solves the equilibrium problem when $\mathbf{D}_\infty^w$ is considered, with $w = \text{iso}$ or $w = \text{shr}$) is adopted to compute the corresponding compatible strain-rate field $\mathbf{d}_\alpha^w$ and the equilibrated stress field $\boldsymbol{\sigma}_\alpha^w$ in each α-subdomain within Ω^{E} (see Eqs. (1.16)). Thereby, stress and strain-rate average measures on Ω^{E} result in (with $w = \text{iso}$ or $w = \text{shr}$)

$$\begin{aligned} \overline{\boldsymbol{\sigma}_w}^E &= \frac{1}{|\Omega^E|}\int_{\Omega^E} \boldsymbol{\sigma}_\alpha^w \, d\Omega = \boldsymbol{\mathcal{A}}_w : \mathbf{D}_\infty^w \\ \overline{\mathbf{d}_w}^E &= \frac{1}{|\Omega^E|}\int_{\Omega^E} \mathbf{d}_\alpha^w \, d\Omega = \boldsymbol{\mathcal{B}}_w : \mathbf{D}_\infty^w \end{aligned} \tag{1.28}$$

$\boldsymbol{\mathcal{A}}_w$ and $\boldsymbol{\mathcal{B}}_w$ being fourth-order localization tensors, herein not detailed for the sake of compactness and straight recoverable by referring to results provided by Herve and Zaoui (1993).

In the framework of Problem 2 formulated for $n = 3$, and as an extension of the Mori-Tanaka scheme, the homogeneous strain-rate tensor $\mathbf{D}_\infty^w$ is assumed to describe the strain-rate state for the region Ω_4. Accordingly, the macroscopic stress and strain rate are obtained as

$$\begin{aligned} \boldsymbol{\Sigma}_w &= \overline{\boldsymbol{\sigma}_w} = \left[\varphi\boldsymbol{\mathcal{A}}_w + (1-\varphi)\boldsymbol{\mathcal{C}}_4\right] : \mathbf{D}_\infty^w \\ \mathbf{D}_w &= \overline{\mathbf{d}_w} = \left[\varphi\boldsymbol{\mathcal{B}}_w + (1-\varphi)\mathbf{I}\right] : \mathbf{D}_\infty^w \end{aligned} \tag{1.29}$$

resulting, from Eq. (1.18), in

$$\left[\varphi\boldsymbol{\mathcal{A}}_w + (1-\varphi)\boldsymbol{\mathcal{C}}_4\right] : \left[\varphi\boldsymbol{\mathcal{B}}_w + (1-\varphi)\mathbf{I}\right]^{-1} = \begin{cases} 3k^{\text{hom}}\boldsymbol{\mathcal{J}}\,, & \text{if} \quad w = \text{iso} \\ 2\mu^{\text{hom}}\boldsymbol{\mathcal{K}}\,, & \text{if} \quad w = \text{shr} \end{cases} \tag{1.30}$$

Thereby, the effective moduli describing the homogenized fictitious constitutive tensor $\boldsymbol{\mathcal{C}}^{\text{hom}}$ are expressed by

$$k^{\text{hom}} = \frac{4}{3}\left(\frac{1-f}{p}\mu_2 + \frac{p-\varphi f}{\varphi p}\mu_3 + \frac{\varphi-1}{\varphi}\mu_4\right) \tag{1.31a}$$

$$\mu^{\text{hom}} = -3\,\frac{\mu_4\left(\Theta_1{\mu_4}^2 + \Theta_2\mu_3\mu_4 + \Theta_3{\mu_3}^2\right)}{\Theta_4\mu_4^2 + \Theta_5\mu_3\mu_4 + \Theta_6\mu_3^2} \tag{1.31b}$$

where $\Theta_i = \Theta_i(\mu_2, \mu_3, p, \varphi, f)$, with $i \in \{1, \ldots, 6\}$, are

$$\Theta_1 = \eta_1\,{\mu_3}^2 + \eta_2\,\mu_2\,\mu_3 + \eta_3\,{\mu_2}^2 \qquad \Theta_2 = \eta_4\,{\mu_3}^2 + \eta_5\,\mu_2\,\mu_3 + \eta_6\,{\mu_2}^2 \tag{1.32a}$$

$$\Theta_3 = \eta_7\,{\mu_3}^2 + \eta_8\,\mu_2\,\mu_3 + \eta_9\,{\mu_2}^2 \qquad \Theta_4 = \varrho_1\,{\mu_3}^2 + \varrho_2\,\mu_2\,\mu_3 + \varrho_3\,{\mu_2}^2 \tag{1.32b}$$

$$\Theta_5 = \varrho_4\,{\mu_3}^2 + \varrho_5\,\mu_2\,\mu_3 + \varrho_6\,{\mu_2}^2 \qquad \Theta_6 = \varrho_7\,{\mu_3}^2 + \varrho_8\,\mu_2\,\mu_3 + \varrho_9\,{\mu_2}^2 \tag{1.32c}$$

coefficients $\eta_j = \eta_j(p, \varphi, f)$ and $\varrho_j = \varrho_j(p, \varphi, f)$ (with $j \in \{1, \ldots, 9\}$) being detailed in 1.A.

Due to Eqs. (1.49) and (1.50) (see 1.A), by enforcing the dimensionless ratio χ to comply with $\chi = \text{O}(\epsilon)$, as well as by prescribing the further smallness condition $\psi = (\varphi - p) = \text{O}(\epsilon)$, effective moduli in Eqs. (1.31) can be expressed in the following linearized

form

$$k^{\mathrm{hom}} = \frac{4}{3p}\left[\mu_4(1-p) + 3(\mu_2-\mu_3)\chi + \frac{\mu_3-\mu_4}{p}(\varphi-p)\right] + \mathrm{o}(\epsilon) \tag{1.33a}$$

$$\mu^{\mathrm{hom}} = \frac{3}{2p+3}\left[\mu_4(1-p) + \frac{15p(\mu_2-\mu_3)}{2p+3}\chi + \frac{5(\mu_3-\mu_4)}{2p+3}(\varphi-p)\right] + \mathrm{o}(\epsilon) \tag{1.33b}$$

1.3.2 A perturbative approach

A closed-form macroscopic strength criterion for nanoporous materials is herein deduced by considering Eq. (1.19) written for $\alpha \in \{2,3,4\}$, and in the unknowns μ_2, μ_3 and μ_4, the case $\alpha = 1$ resulting trivial.

In detail, Eq. (1.19) for $\alpha = 4$ (namely, $\mathcal{F}|_{\alpha=4}$) reads as

$$F_4 = 3\left(\frac{\Sigma_{\mathrm{m}}}{\sigma_0}\frac{\mu_4}{k^{\mathrm{hom}}}\right)^2\frac{\partial k^{\mathrm{hom}}}{\partial \mu_4} + \left(\frac{\Sigma_{\mathrm{eq}}}{\sigma_0}\frac{\mu_4}{\mu^{\mathrm{hom}}}\right)^2\frac{\partial \mu^{\mathrm{hom}}}{\partial \mu_4} \tag{1.34}$$

and, by employing Eqs. (1.25), the ratios $\mathcal{F}|_{\alpha=2}/\mathcal{F}|_{\alpha=3}$ and $\mathcal{F}|_{\alpha=3}/\mathcal{F}|_{\alpha=4}$ can be introduced:

$$\begin{aligned}
\mathcal{G}(\mu_2,\mu_3,\mu_4) &= \frac{F_2}{F_3}\left(\frac{\kappa}{\chi}\frac{\mu_3}{\mu_2}\right)^2 - \frac{3T^2\left(\dfrac{\mu^{\mathrm{hom}}}{k^{\mathrm{hom}}}\right)^2\dfrac{\partial k^{\mathrm{hom}}}{\partial \mu_2} + \dfrac{\partial \mu^{\mathrm{hom}}}{\partial \mu_2}}{3T^2\left(\dfrac{\mu^{\mathrm{hom}}}{k^{\mathrm{hom}}}\right)^2\dfrac{\partial k^{\mathrm{hom}}}{\partial \mu_3} + \dfrac{\partial \mu^{\mathrm{hom}}}{\partial \mu_3}} = 0 \\
\mathcal{H}(\mu_2,\mu_3,\mu_4) &= \frac{F_3}{F_4}\left(\frac{\mu_4}{\mu_3}\right)^2 - \frac{3T^2\left(\dfrac{\mu^{\mathrm{hom}}}{k^{\mathrm{hom}}}\right)^2\dfrac{\partial k^{\mathrm{hom}}}{\partial \mu_3} + \dfrac{\partial \mu^{\mathrm{hom}}}{\partial \mu_3}}{3T^2\left(\dfrac{\mu^{\mathrm{hom}}}{k^{\mathrm{hom}}}\right)^2\dfrac{\partial k^{\mathrm{hom}}}{\partial \mu_4} + \dfrac{\partial \mu^{\mathrm{hom}}}{\partial \mu_4}} = 0
\end{aligned} \tag{1.35}$$

$T = \Sigma_{\mathrm{m}}/\Sigma_{\mathrm{eq}}$ being the stress-triaxiality parameter.

The non-null shear moduli in Eqs. (1.25) can be recast as

$$\mu_2 = \frac{\kappa}{\chi}\,\rho_{23}\,\rho_{34}\,\mu_4\,, \qquad \mu_3 = \rho_{34}\,\mu_4 \tag{1.36}$$

where

$$\rho_{23} = \sqrt{\frac{J^{\mathrm{d}}_{23}}{J^{\mathrm{d}}_{22}}}, \qquad \rho_{34} = \sqrt{\frac{J^{\mathrm{d}}_{24}}{J^{\mathrm{d}}_{23}}}\,. \tag{1.37}$$

Therefore, for a given p, the effective moduli result in $\mu^{\mathrm{hom}} = \mu^{\mathrm{hom}}(\mathcal{P},\rho_{23},\rho_{34},\mu_4)$ and $k^{\mathrm{hom}} = k^{\mathrm{hom}}(\mathcal{P},\rho_{23},\rho_{34},\mu_4)$, where $\mathcal{P}$ is the set of variables defined as $\mathcal{P} = \{\chi,\psi,\kappa\}$. It is worth observing that, by enforcing positions (1.36) and (1.37), k^{hom} and μ^{hom} in Eqs. (1.31) linearly depend on μ_4. Correspondingly, Eqs. (1.34) and (1.35) do not depend on μ_4, that is $\mathcal{G} = \mathcal{G}(\mathcal{P},\rho_{23},\rho_{34})$ and $\mathcal{H} = \mathcal{H}(\mathcal{P},\rho_{23},\rho_{34})$. Hence, once solved parameters ρ_{23} and ρ_{34} from Eqs. (1.35), the relationship (1.34) allows to identify macroscopic limit stress states $(\Sigma_{\mathrm{m}},\Sigma_{\mathrm{eq}})$.

In order to compute ρ_{23} and ρ_{34}, let the following problem be introduced.

Problem 3 *Find* $\{\rho_{23}, \rho_{34}\}$ *s.t.*

$$\begin{aligned} \mathcal{G}\big(\mathcal{P}, \rho_{23}, \rho_{34}\big) = 0 \\ \mathcal{H}\big(\mathcal{P}, \rho_{23}, \rho_{34}\big) = 0 \end{aligned} \tag{1.38}$$

Since Eqs. (1.38) are non linear in ρ_{23} and ρ_{34}, the exact solution of Problem 3 can not be simply obtained. An estimate for $\{\rho_{23}, \rho_{34}\}$ is deduced by adopting a perturbative approach with respect to κ. In detail, by enforcing $\kappa = \mathrm{O}(\epsilon)$, the interface effects are assumed to produce a perturbation with respect to the case of porous materials (namely, corresponding to $\kappa = 0$). Accordingly, due also to the previously-introduced smallness assumptions, Eqs. (1.38) can be linearised with respect to χ, ψ and κ. Thereby, neglecting higher-order terms, the following simplified problem can be stated.

Problem 4 *Find* $\{\rho_{23}, \rho_{34}\}$ *s.t.*

$$\begin{aligned} \hat{\mathcal{G}}(\mathcal{P}, \rho_{23}, \rho_{34}) = \mathcal{G}(\mathcal{P}_0, \rho_{23}, \rho_{34}) + \left.\frac{\partial \mathcal{G}}{\partial \chi}\right|_{\mathcal{P}=\mathcal{P}_0} \chi + \left.\frac{\partial \mathcal{G}}{\partial \psi}\right|_{\mathcal{P}=\mathcal{P}_0} \psi + \left.\frac{\partial \mathcal{G}}{\partial \kappa}\right|_{\mathcal{P}=\mathcal{P}_0} \kappa = 0 \\ \hat{\mathcal{H}}(\mathcal{P}, \rho_{23}, \rho_{34}) = \mathcal{H}(\mathcal{P}_0, \rho_{23}, \rho_{34}) + \left.\frac{\partial \mathcal{H}}{\partial \chi}\right|_{\mathcal{P}=\mathcal{P}_0} \chi + \left.\frac{\partial \mathcal{H}}{\partial \psi}\right|_{\mathcal{P}=\mathcal{P}_0} \psi + \left.\frac{\partial \mathcal{H}}{\partial \kappa}\right|_{\mathcal{P}=\mathcal{P}_0} \kappa = 0 \end{aligned} \tag{1.39}$$

where $\mathcal{P}_0 = \mathcal{P}|_{\chi=\psi=\kappa=0}$.

Solution $\{\rho_{23}, \rho_{34}\}$ can be expressed in the form

$$\begin{aligned} \rho_{23} = \rho_{23}^0 + \Delta\rho_{23} \\ \rho_{34} = \rho_{34}^0 + \Delta\rho_{34} \end{aligned} \tag{1.40}$$

where $\{\rho_{23}^0, \rho_{34}^0\}$ is the solution of Problem 4 when $\kappa = 0$, and $\{\Delta\rho_{23}, \Delta\rho_{34}\}$ identifies the perturbation induced by nanoscale effects, under the condition $\Delta\rho_\cdot/\rho_\cdot^0 = \mathrm{O}(\epsilon)$. In detail, the following perturbative correction problem is introduced.

Problem 5 *Find* $\{\Delta\rho_{23}, \Delta\rho_{34}\}$ *s.t.*

$$\begin{aligned} \hat{\mathcal{G}}\big(\mathcal{P}, \rho_{23}^0 + \Delta\rho_{23}, \rho_{34}^0 + \Delta\rho_{34}\big) = 0 \\ \hat{\mathcal{H}}\big(\mathcal{P}, \rho_{23}^0 + \Delta\rho_{23}, \rho_{34}^0 + \Delta\rho_{34}\big) = 0 \end{aligned} \tag{1.41}$$

The solution of the porous problem (that is, Problem 4 for $\kappa = 0$) can be straight determined as

$$\rho_{23}^0 = 1\,, \qquad \rho_{34}^0 = \sqrt{\frac{27pT^2 + 8p + 12}{20 + 27T^2}} \tag{1.42}$$

resulting in $\rho_\cdot^0 = \mathrm{O}(1)$. A first-order solution of Problem 5 is obtained by linearising Eqs. (1.41) with respect to $\Delta\rho_\cdot$, delivering the following perturbative corrections

$$\Delta\rho_{23} = \mathcal{T}\,\frac{\psi}{p} = \mathrm{O}(\epsilon), \qquad \Delta\rho_{34} = \mathcal{S}\,\kappa + \frac{\mathcal{S}}{3}\left(1 - \frac{1}{2\rho_{34}^0}\right)\frac{\psi}{p} = \mathrm{O}(\epsilon) \tag{1.43}$$

with

$$\mathcal{S} = \frac{4}{3}\,\frac{135pT^2 + 729T^2 + 40p + 600}{(20 + 27T^2)^2}\,, \qquad \mathcal{T} = -\frac{1}{18}\,\frac{243T^2 + 200}{(20 + 27T^2)}\,. \tag{1.44}$$

Finally, by recasting effective moduli in Eqs. (1.31) via the solution $\{\rho_{23}, \rho_{34}\}$ expressed by Eqs. (1.42) and (1.43), and by enforcing resulting expressions into Eq. (1.34), the following closed-form macroscopic strength criterion is obtained

$$\frac{20\Sigma_{\rm eq}^2 + 27\Sigma_{\rm m}^2}{12(1-p)^3}\left[(1-p)(\rho_{34}^0)^2 + (1-2\rho_{34}^0)\psi - (6p\rho_{34}^0)\kappa\right] = \sigma_0^2 \tag{1.45}$$

where, since Eq. (1.42), $\rho_{34}^0 = \rho_{34}^0(\Sigma_{\rm m}, \Sigma_{\rm eq})$.

In the stress plane $(\Sigma_{\rm m}, \Sigma_{\rm eq})$, Eq. (1.45) results in a symmetric (with respect to both $\Sigma_{\rm m}$ and $\Sigma_{\rm eq}$ axes) and convex strength profile, expressed in terms of the porosity p, the volume fraction $\varphi = \psi + p$ of composite inclusions, and the parameter κ accounting for interface effects.

1.3.3 Optimization on φ

The volume fraction φ of composite inclusions represents a free model parameter, in the framework of the consistency conditions $\psi \geq 0$ and $\psi = \mathrm{O}(\epsilon)$. Since choosing a value for φ corresponds to identify a class of kinematical descriptors $J_{2\alpha}^{\rm d}$ via Eq. (1.27), φ is herein employed to furnish a certain minimization, in the sense of Eq. (1.8), for estimating $\Pi^{\rm hom}$.

It is worth observing that a rough description of $\Pi^{\rm hom}$ generally leads to a significant overestimate of material strength, especially for high levels of stress triaxiality (for instance, this is the case of the DK strength criterion). As shown in Fig. 1.4 for fixed values of p and κ, model parameter φ mainly affects limit-stress states characterised by a significant hydrostatic condition, resulting in a reduction of the predicted material strength when φ increases. Accordingly, aiming to furnish an accurate strength prediction, φ is herein chosen by prescribing, as an optimality condition, the equality between the hydrostatic strength predicted via Eq. (1.45) (corresponding to $\Sigma_{\rm eq} = 0$) and the expected value $\Sigma_{\rm m}^{\rm (ex)}/\sigma_0 = -(2/3)\ln p + 2\kappa$, furnished by Dormieux and Kondo (2010) as a generalization of the Gurson's result (Gurson, 1977).

Thereby, in the framework of a first-order approach in κ, the optimal value for φ results in

$$\varphi^{\rm opt} = \phi_0 + \phi_1\,\kappa \tag{1.46}$$

with

$$\begin{aligned} \phi_0 &= \frac{p\,\left(p - 2\sqrt{p}\right)}{1 - 2\sqrt{p}} + \frac{4}{9}\,\frac{(1-p)^3}{\left(1 - 2\sqrt{p}\right)(\ln p)^{4/3}}\,, \\ \phi_1 &= 6\,\frac{p^{3/2}}{1 - 2\sqrt{p}} - \frac{16}{9}\,\frac{(1-p)^3}{(\ln p)^2\left(1 - 2\sqrt{p}\right)}\,. \end{aligned} \tag{1.47}$$

It is simple to prove that, owing to the definition of φ (see Eq. (1.23)), the consistency condition $\psi = \varphi^{\rm opt} - p \geq 0$ is surely verified for any value of κ when $p < 25\%$, fully in

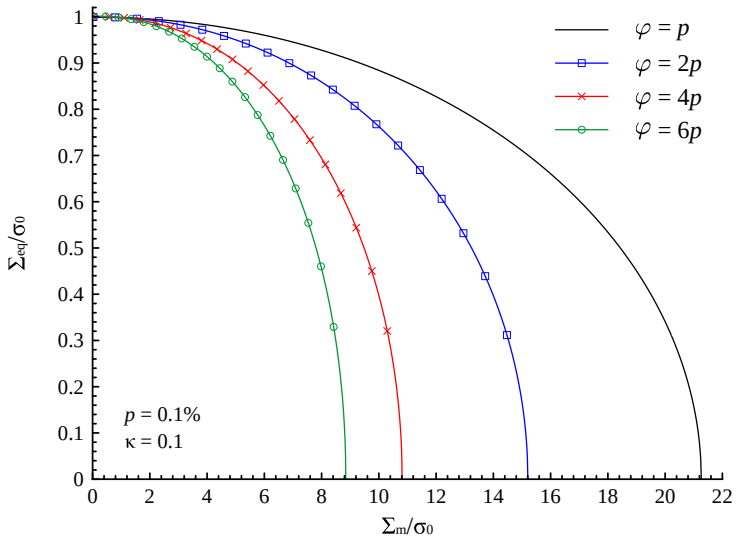

Figure 1.4 – Strength profiles obtained via Eq. (1.45) for different values of the model parameter φ ($\kappa = 0.1$ and $p = 0.1\%$).

agreement with porosity values generally characterising nanoporous materials. Furthermore, in the framework of small values of p, and assuming $p^\eta = \mathrm{O}(\epsilon)$ for any $\eta < 1$, consistency condition $\psi = \mathrm{O}(\epsilon)$ is straight verified.

Therefore, by combining Eqs. (1.45) and (1.46), the optimized version (denoted in the following as BDKV) of the proposed strength criterion results in

$$\frac{20\Sigma_{\mathrm{eq}}^2 + 27\Sigma_{\mathrm{m}}^2}{12(1-p)^3}\left\{(1-p)(\rho_{34}^0)^2 + (1-2\rho_{34}^0)(\phi_0 - p) - \left[6p\rho_{34}^0 - \phi_1(1-2\rho_{34}^0)\right]\kappa\right\} = \sigma_0^2 \quad (1.48)$$

where ρ_{34}^0 depends on the macroscopic stress state $(\Sigma_{\mathrm{m}}, \Sigma_{\mathrm{eq}})$ via Eq. (1.42).

1.4 Criterion assessment

Model sensitivity to parameters p and κ is addressed in Figs. 1.5. Proposed results show that, in the framework of small values for p and κ, slight effects occur for small stress-triaxiality levels. Results shown in Fig. 1.5a highlight also that the macroscopic strength properties reduce when p increases, mainly for high hydrostatic stress components. As regards the parameter κ, introduced in Eq. (1.26), the results in Fig. 1.5b indicate that such a parameter allows to effectively account for void-size effects. As a matter of fact, when strength values for interfaces (namely, $\sigma_{\mathcal{L}}$) and for solid phases (σ_0) are fixed, a reduction in the void size a corresponds to an increase κ. As depicted in Fig. 1.5b, such an occurrence leads to an improvement of strength features, qualitatively in agreement with aforementioned experimental and numerical evidence (Biener et al., 2005, 2006; Hakamada and Mabuchi, 2007; Zhao et al., 2009; Brach et al., 2016a).

A description of strength properties for porous materials comprising cavities with large

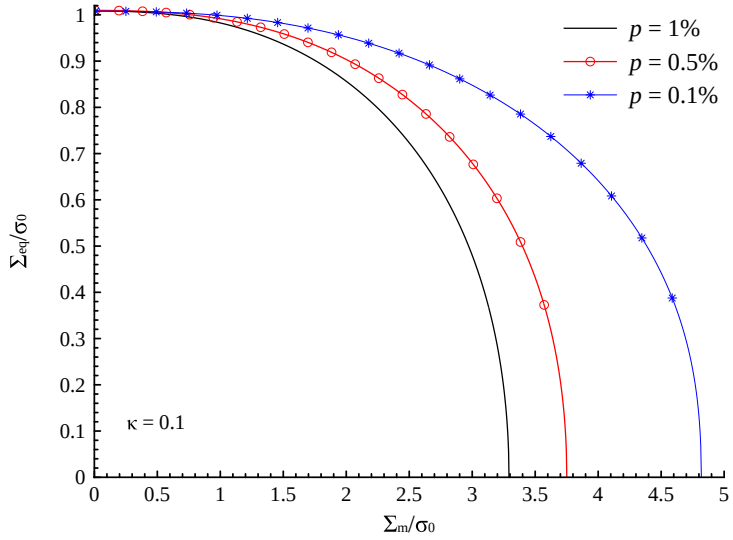

(a)

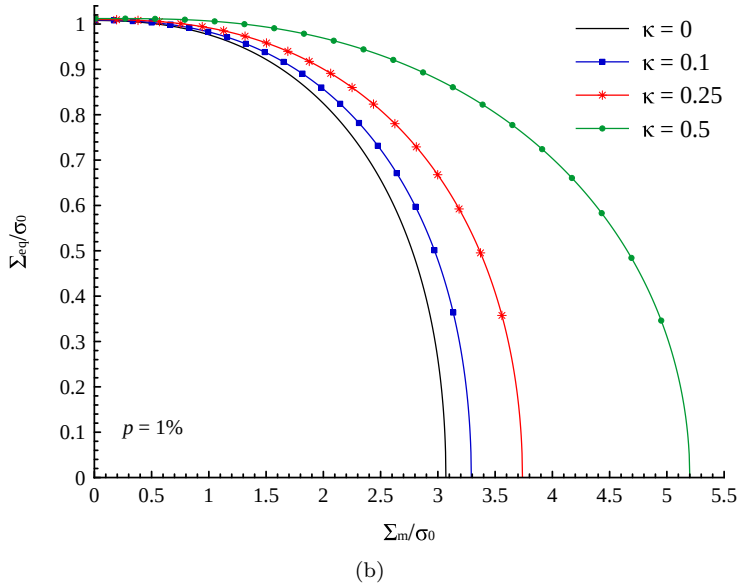

(b)

Figure 1.5 – Strength profiles obtained via the proposed BDKV criterion in Eq. (1.48) for different values of: (a) porosity p (with $\kappa = 0.1$); (b) interface parameter κ (with $p = 1\%$).

values of a is furnished by enforcing $\kappa = 0$ in Eq. (1.48), namely by assuming as negligible the surface-induced effects.

The effectiveness of the proposed BDKV strength criterion is assessed in Fig. 1.6. In detail, comparisons with both theoretical and numerical benchmarks are provided for different values of the interface parameter κ. By addressing the case $p = 1\%$, reference is made to the theoretical predictions obtained via the DK model (Dormieux and Kondo, 2013) and to finite-element-based limit analysis calculations provided by Morin et al. (2015) when $\kappa = 0.25$ and by Trillat and Pastor (2005) when $\kappa = 0$. It can be noted that the DK criterion significantly overestimates strength properties predicted by numerical simulations. In particular, addressing a pure hydrostatic case, the DK model predicts a strength limit greater of about 100% (respectively, 110%) than the numerical one for $\kappa = 0.25$ (resp., for $\kappa = 0$). On the contrary, BDKV-based results are proven in very good agreement with benchmarking calculations (with relative errors always lower than 10%), resulting in a significant improvement with respect to the DK case.

As a matter of fact, proposed strength criterion for nanoporous materials allows also to recover the well-known model proposed by Ponte Castañeda (1991), simply considering the case $\psi = \kappa = 0$ in Eq. (1.45). Moreover, the nanoporous criterion DK is recovered by setting $\psi = 0$ (with $\kappa \geq 0$), corresponding to a domain partition based on three phases: pore regions, interfaces $\mathcal{L}$, and solid matrix. In particular, by comparing Eq. (1.45) for $\psi = 0$ and Eq. (1.48), corrective terms $(1 - 2\rho_{34}^0)(\phi_0 - p)$ and $\phi_1(1 - 2\rho_{34}^0)\kappa$ allow to enhance the DK-based strength predictions both accounting or not for interface effects. Such additional terms straight results from the proposed optimization approach on φ, entirely absent in the developments already provided by Dormieux and Kondo (2013), and strictly related to the herein adopted 3-layered (that is, four phases) modelling strategy.

1.5 Concluding remarks

In this Chapter, strength properties of nanoporous materials are investigated by means of a 3-layered model formulated in the framework of a non-linear homogenization (NLH) approach. To this end, a representative volume element which comprises a rigid ideal-plastic solid matrix, obeying to a von Mises strength criterion and containing isotropically-distributed spherical voids, has been considered.

At the local level, and by regarding the microscopic support function as the potential for a viscous material, a fictitious non-linear isotropic constitutive equation has been introduced. Following the modified secant method (Suquet, 1995) and by referring to the multiphase modelling technique proposed by Herve and Zaoui (1993), a linear comparison composite material has been considered.

The present approach has been developed by referring to the theoretical background recently provided by Dormieux and Kondo (2013), based on a 2-layered modelling strategy. The latter has been proven in Section 1.4 to strongly overestimate available numerical benchmarking strength evidence for both porous and nanoporous media. Aiming to develop a more accurate NLH technique, a refined description of the local strain-rate heterogeneity at the limit state has been herein proposed, by introducing a four phases

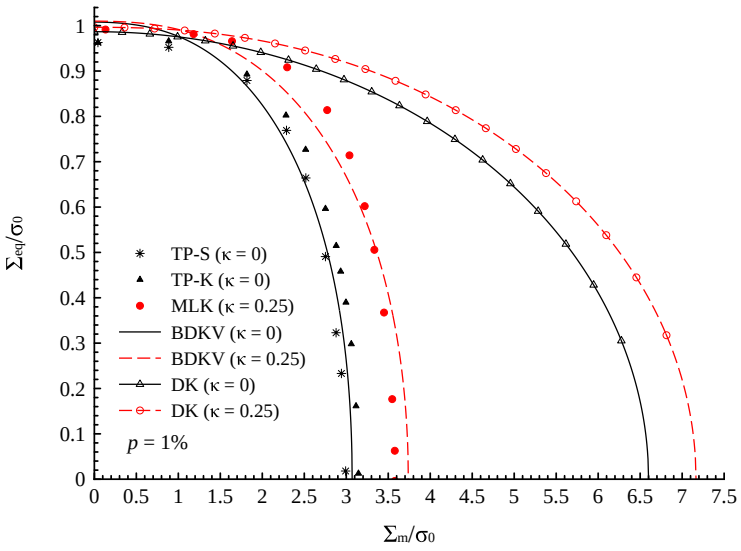

Figure 1.6 – Strength profiles for different values of κ and for $p = 1\%$. Comparisons among: proposed model (BDKV), theoretical predictions by Dormieux and Kondo (2013) (DK), numerical data provided by Morin et al. (2015) (denoted as MLK), kinematic (TP-K) and static (TP-S) numerical bounds proposed by Trillat and Pastor (2005).

comparison composite material. In detail, a sub-domain partition consisting in 3-layered composite spheres, confocal to nanovoids and embedded into the solid matrix, has been employed. Each composite sphere comprises the void region, an imperfect-coherent interface and an interface-to-matrix transition phase. The microscopic strain-rate fields entering the proposed procedure have been accounted for by introducing piecewise descriptors in agreement with Buryachenko (1993), Kreher (1990), Ponte Castañeda and Suquet (1998), and Dormieux et al. (2006). Thereby, the non-linear problem underlying the determination of strength properties for nanoporous materials has been reduced to a non-linear viscous one defined on a fictitious piecewise homogenenous medium. By solving via a perturbative procedure the constitutive fictitious moduli, a novel analytical closed-form strength criterion (BDKV) has been derived. A suitable value for the volume fraction of the composite spheres has been determined, aiming to optimize the criterion performance at pure hydrostatic stress states. In agreement with well-posed strategies (e.g., Duan et al., 2005a,b; Dormieux and Kondo, 2010, 2013), the void-solid interface has been successfully introduced in order to take into account for surface-stress effects.

It is worth observing that the additional layer introduced with respect to the approach by Dormieux and Kondo (2013) (namely, the transition phase) allowed on one hand for a finer estimate of the fictitious constitutive description, and on the other hand to recast the NLH problem in terms of an optimization procedure (not possible in the framework of the developments provided by Dormieux and Kondo (2013)), solved via an original perturbation approach, and resulting in a novel effective engineering-oriented strength criterion.

As a consistency indication and as special cases, present criterion recovers previously-

established NLH-based analytical strength estimates both accounting (Dormieux and Kondo, 2013) or not (Ponte Castañeda, 1991) for surface-stress effects.

Results obtained via BDKV highlight that a suitable description of void-size effects can be experienced, resulting in an increase of the predicted strength features as the void length decreases, especially for high triaxiality levels. Furthermore, comparisons with respect to both theoretical predictions (Dormieux and Kondo, 2013) and finite-element-based calculations (Trillat and Pastor, 2005; Morin et al., 2015) have shown consistency and accuracy of the proposed formulation, resulting in a significant improvement of the benchmarking NLH-based model by Dormieux and Kondo (2013).

It is worth pointing out that, in the framework of a n-layered approach and in the case of classical porous materials (namely, neglecting surface-induced effects), suitable estimates have been provided by Bilger et al. (2002) and by Vincent et al. (2009), by adopting semi-analytical strategies with different values of n up to $n = 21$. Nevertheless, although the proposed formulation (based on $n = 3$) results in a less accurate description of local kinematics, it allows for deriving an accurate analytical closed-form strength criterion, useful for engineering purposes and able to properly describe limit stress-states both accounting or not for surface-induced effects.

1.A LCC effective moduli: coefficients in Eqs. (1.31)

Coefficients introduced in Eqs. (1.31) are computed from localization tensors $\boldsymbol{\mathcal{A}}_w$ and $\boldsymbol{\mathcal{B}}_w$ (see Eqs.(1.28), with $w = \text{iso}$ or $w = \text{shr}$) as

$$
\begin{aligned}
&\eta_1+\eta_2+\eta_3=(1-\varphi)\,\lambda_1 && \varrho_1+\varrho_2+\varrho_3=-\,(3+2\,\varphi)\,\lambda_1\\
&\eta_1=(1-\varphi)\,\lambda_2\lambda_3 && \varrho_1=-\,(3+2\,\varphi)\,\lambda_2\lambda_3\\
&\eta_3=(1-\varphi)\,\lambda_4\lambda_5 && \varrho_3=-\,(3+2\,\varphi)\,\lambda_4\lambda_5\\
&\eta_4+\eta_5+\eta_6=\lambda_6\varphi+\lambda_7 && \varrho_4+\varrho_5+\varrho_6=2\lambda_6\varphi-3\lambda_7\\
&\eta_4=[\lambda_8\varphi+\lambda_9]\lambda_3 && \varrho_4=[2\lambda_8\varphi-3\lambda_9]\lambda_3\\
&\eta_6=[\lambda_{10}\varphi+\lambda_{11}]\lambda_5 && \varrho_6=[2\lambda_{10}\varphi-3\lambda_{11}]\lambda_5\\
&\eta_7+\eta_8+\eta_9=(2+3\varphi)\lambda_{12} && \varrho_7+\varrho_8+\varrho_9=6\lambda_{12}(\varphi-1)\\
&\eta_7=(2+3\,\varphi)\,\lambda_{13}\lambda_3 && \varrho_7=6(\varphi-1)\lambda_3\lambda_{13}\\
&\eta_9=(2+3\,\varphi)\,\lambda_{14}\lambda_5 && \varrho_9=6(\varphi-1)\lambda_5\lambda_{14}
\end{aligned}
\tag{1.49}
$$

with

$$
\begin{aligned}
\lambda_1&=175\,\left(38\,\omega^{11/3}f^{10/3}+225\,\omega^{8/3}f^{7/3}-336\,\omega^2f^{5/3}+200\,\omega^{4/3}f+48\,\omega^{1/3}\right)\\
\lambda_2&=38\,\omega^{11/3}+225\,\omega^{8/3}-336\,\omega^2+200\,\omega^{4/3}+48\,\omega^{1/3}\\
\lambda_3&=38\,f^{10/3}+225\,f^{7/3}-336\,f^{5/3}+200\,f+48\\
\lambda_4&=24\,\left(4\,\omega^{11/3}-25\,\omega^{8/3}+42\,\omega^2-25\,\omega^{4/3}+4\,\omega^{1/3}\right)\\
\lambda_5&=19\,f^{10/3}-75\,f^{7/3}+112\,f^{5/3}-75\,f+19\\
\lambda_6&=1575\left(-\frac{19}{9}\,\omega^{11/3}f^{10/3}+50\,\omega^{8/3}f^{7/3}-\frac{224}{3}\,\omega^2f^{5/3}+\frac{250}{9}\,\omega^{4/3}f-\omega^{1/3}\right)\\
\lambda_7&=8750\left(-\frac{38}{25}\,\omega^{11/3}f^{10/3}-3/2\,\omega^{8/3}f^{7/3}+\frac{56}{25}\,\omega^2f^{5/3}-\omega^{4/3}f+\frac{89}{50}\,\omega^{1/3}\right)\\
\lambda_8&=-19\,\omega^{11/3}+450\,\omega^{8/3}-672\,\omega^2+250\,\omega^{4/3}-9\,\omega^{1/3}\\
\lambda_9&=-76\,\omega^{11/3}-75\,\omega^{8/3}+112\,\omega^2-50\,\omega^{4/3}+89\,\omega^{1/3}\\
\lambda_{10}&=-48\,\omega^{11/3}-1200\,\omega^{8/3}+2016\,\omega^2-750\,\omega^{4/3}-18\,\omega^{1/3}\\
\lambda_{11}&=-192\,\omega^{11/3}+200\,\omega^{8/3}-336\,\omega^2+150\,\omega^{4/3}+178\,\omega^{1/3}\\
\lambda_{12}&=3325\left(\omega^{11/3}f^{10/3}-\frac{75}{19}\,\omega^{8/3}f^{7/3}+\frac{112}{19}\,\omega^2f^{5/3}-\frac{75}{19}\,\omega^{4/3}f+\omega^{1/3}\right)\\
\lambda_{13}&=19\,\omega^{11/3}-75\,\omega^{8/3}+112\,\omega^2-75\,\omega^{4/3}+19\,\omega^{1/3}\\
\lambda_{14}&=48\,\omega^{11/3}+200\,\omega^{8/3}-336\,\omega^2+225\,\omega^{4/3}+38\,\omega^{1/3}
\end{aligned}
\tag{1.50}
$$

where $\omega = p/(\varphi f)$.

References

Anoukou, K., Pastor, F., Dufrenoy, P., & Kondo, D. (2016). Limit analysis and homogenization of porous materials with Mohr–Coulomb matrix. Part I: Theoretical formulation. *Journal of the Mechanics and Physics of Solids*, 91, 145-171.

Arico, A. S., Bruce, P., Scrosati, B., Tarascon, J. M., & Van Schalkwijk, W. (2005). Nanostructured materials for advanced energy conversion and storage devices. *Nature materials*, 4, 366-377.

Bilger, N., Auslender, F., Bornert, M., & Masson, R. (2002). New bounds and estimates for porous media with rigid perectly plastic matrix. *Compte Rendu Mécanique*, 330, 127-132.

Biener, J., Hodge, A.M., Hamza, A.V., Hsiung, L.M., & Satcher, J.H. (2005). Nanoporous Au: A high yield strength material. *Journal of Applied Physics*, 97, 024301.

Biener, J., Hodge, A.M., Hayes, J.R., Volkert, C.A., Zepeda-Ruiz, L.A., Hamza, A.V., & Abraham, F.F. (2006). Size Effects on the Mechanical Behaviour of Nanoporous Au. *Nano Letters*, 6, 2379-2382.

Brach, S., Dormieux, L., Kondo, D., & Vairo, G. (2016). A computational insight into void-size effects on strength properties of nanoporous materials. *Mechanics of Materials*, 101, 102-117.

Brach, S., Dormieux, L., Kondo, D., & Vairo, G. (2016). Nanoporous materials with a general isotropic plastic matrix: exact limit state under isotropic loadings. *International Journal of Plasticity*, DOI: 10.1016/j.ijplas.2016.10.007.

Brisard, S., Dormieux, L., & Kondo, D. (2010). Hashin-Shtrikman bounds on the bulk modulus of a nanocomposite with spherical inclusions and interface effects. *Computational Materials Science*, 48, 589-596.

Brisard, S., Dormieux, L., & Kondo, D. (2010). Hashin-Shtrikman bounds on the shear modulus of a nanocomposite with spherical inclusions and interface effects. *Computational Materials Science*, 50, 403-410.

Buryachenko, V. (1993). Effective strength properties of elastic physically nonlinear composites. *Mecamat*, 93, 567-578.

Cammarata, R.C. (1994). Surface and interface stress effects in thin films. *Progress in Surface Science*, 46, 1-38.

de Buhan, P. (1986). Approach fondamentale du calcul à la rupture des ouvrages en sols renforcés. Thèse d'État. Paris VI.

Dormieux, L., & Kondo, D. (2010). An extension of Gurson model incorporating interface stress effects. *International Journal of Engineering Science*, 48, 575-581.

Dormieux, L., & Kondo, D. (2013). Non linear homogenization approach of strength of nanoporous materials with interface effects. *International Journal of Engineering Science*, 71, 102-110.

Dormieux, L., Kondo, D., & Ulm, F.-J. (2006). *Microporomechanics*. Chichester: J. Wiley & Sons.

Duan, H.L., Wang, J., Huang, Z.P., & Luo, Z.Y. (2005). Stress concentration tensors of inhomogeneities with interface effects. *Mechanics of Materials*, 37, 723-736.

Duan, H.L., Wang, J., Huang, Z.P., & Karihaloo, B.L. (2005). Size-dependent effective elastic constants of solids containing nano-inhomogeneities with interface stress. *Journal of the Mechanics and Physics of Solids*, 53, 1574-1596.

Gibbs, J W. (1906). *The scientific papers of J. Willard Gibbs* (Vol.1). London, New York & Bombay: Longmans, Green and Company.

Goudarzi, T., Avazmohammadi, R., & Naghdabadi, R. (2010). Surface energy effects on the yield strength of nanoporous materials containing nanoscale cylindrical voids. *Mechanics of Materials*, 42, 852-862.

Guo, T., Faleskog, J., & Shih, C., (2008). Continuum modelling of a porous solid with pressure-sensitive dilatant matrix. *Journal of Mechanics and Physics of Solids*, 56, 2188-2212.

Gurson, A.L. (1977). Continuum theory of ductile rupture by void nucleation and growth: Part I. - Yield criterion and flow rules for porous ductile media. *Journal of Engineering Materials and Technology*, 99, 2-15.

Gurtin, M.E., & Murdoch, A.I. (1975). A continuum theory of elastic material surfaces. *Archive for Rational Mechanics and Analysis*, 57, 291-323.

Gurtin, M.E., & Murdoch, A.I. (1978). Surface stress in solids. *International Journal of Solids and Structures*, 14, 431-440.

Hakamada, M., & Mabuchi, M. (2007). Mechanical strength of nanoporous gold fabricated by dealloying. *Scripta Materalia*, 56, 1003-1006.

Herve, E., & Zaoui, A. (1993). n-Layered inclusion-based micromechanical modelling. *International Journal of Engineering Science*, 31, 1-10.

Jenkins, S.B. (2010). *Nanoporous Materials: Types, Properties, and Uses*. New York: Nova Science Publishers.

Kreher, W. (1990). Residual stresses and stored elastic energy of composites and polycrystals. *Journal of the Mechanics and Physics of Solids*, 38, 115-128.

Le Quang, H., & He, Q.-C. (2007). Size-dependent effective thermoelastic properties of nanocomposites with spherically anisotropic phases. *Journal of the Mechanics and Physics of Solids*, 55, 1899-1931.

Love, A.E.H. (1944). *A Treatise on the Mathematical Theory of Elasticity*. Dover, New York.

Lu, G.Q., Zhao, X.S., & Wei, T.K. (2004). *Nanoporous materials: science and engineering*. London: Imperial College Press.

Marian, J., Knap, J., & Ortiz, M. (2004). Nanovoid Cavitation by Dislocation Emission in Aluminum. *Physical Review*, 93, 165503.

Marian, J., Knap, J., & Ortiz, M. (2005). Nanovoid deformation in aluminum under simple shear. *Acta Materialia*, 53, 2893-2900.

Mi, C., Buttry, D.A., Sharma, P., & Kouris, D.A. (2011). Atomistic insights into dislocation-based mechanisms of void growth and coalescence. *Journal of the Mechanics and Physics of Solids*, 59, 1858-1871.

Monchiet, V., & Bonnet, G. (2010). Interfacial models in viscoplastic composites materials. *International Journal of Engineering Science*, 48, 1762-1768.

Monchiet, V., & Kondo, D. (2013). Combined voids size and shape effects on the macroscopic criterion of ductile nanoporous materials. *International Journal of Plasticity*, 43, 20-41.

Morin, L., Kondo, D., & Leblond, J.-B. (2015). Numerical assessment, implementation and application of an extended Gurson model accounting for void size effects. *European Journal of Mechanics A/Solids*, 51, 183-192.

Moshtaghin, A.F., Naghdabadi, R., & Asghari, M. (2008). Effects of surface residual stress and surface elasticity on the overall yield surfaces of nanoporous materials with cylindrical nanovoids. *Mechanics of Materials*, 51, 74-87.

Murr, L.E. (1975). *Interfacial Phenomena in Metals and Alloys*. London: Addison-Wesley.

Needs, R.J., Godfrey, M.J., & Mansfield, M. (1991). Theory of surface stress and surface reconstruction. *Surface Science*, 242, 215-221.

Orowan, E. (1970). Surface energy and surface tension in solids and liquids. *Proceedings of the Royal Society of London A*, 316, 473-491.

Ponte Castañeda, P. (1991). The effective mechanical properties of nonlinear isotropic composites. *Journal of the Mechanics and Physics of Solids*, 39, 45-71.

Ponte Castañeda, P., & Suquet, P. (1998). Nonlinear Composites. *Advances in Applied Mechanics*, 34, 171-302.

Povstenko, Yu. Z. (1993). Theoretical investigation of phenomena caused by heterogeneous surface tension in solids. *Journal of the Mechanics and Physics of Solids*, 41, 1499-1514.

Salençon, J. (1983). Calcul à la rupture et analyse limite, *Presses de l'ENPC*.

Sharma, P., Ganti, S., & Bhate, N. (2003). Effect of surfaces on the size-dependent elastic states of nano-inhomogeneities. *Applied Physics Letters*, 82, 535-537.

Sharma, P., & Ganti, S. (2004). Size-Dependent Eshelby's Tensor for Embedded Nano-Inclusions Incorporating Surface/Interface Energies. *Journal of Applied Mechanics*, 71, 663-671.

Shuttleworth, R. (1950). The surface tension of solids. *Proceedings of the Physical Society A*, 63, 444-457.

Suquet, P. (1995). Overall properties of nonlinear composites: a modified secant moduli theory and its link with Ponte Castañeda's non linear variational procedure. *Comptes Rendus Académie de Science de Paris*, II B, 320, 11, 563-571.

Suquet, P. (1997). *Continuum micromechanics*. New York: Springer-Verlag.

Traiviratana, S., Bringa, E.M., Benson, D.J., & Meyers, M.A. (2008). Void growth in metals: Atomistic calculations. *Acta Materalia*, 56, 3874-3886.

Trillat, M., & Pastor, J. (2005). Limit analysis and Gurson's model. *European Journal of Mechanics A/Solids*, 24, 800-819.

Vincent, P.-G., Monerie, Y., & Suquet, P. (2009). Porous materials with two populations of voids under internal pressure: I. instantaneous constitutive relations. *International Journal of Solids and Structures*, 46, 480-506.

Wang, J., Huang, Z., Duan, H., Yu, S., Feng, X., Wang, G., Zhang, W., & Wang, T. (2011). Surface stress effect in mechanics of nanostructured materials. *Acta Mechanica Solida Sinica*, 52-82.

Zhang, W., & Wang, T.J (2007). Effect of surface energy on the yield strength of nanoporous materials. *Applied Physics Letters*, 90, 063104.

Zhang, W., Wang, T.J., & Chen, X. (2008). Effect of surface stress on the asymmetric yield strength of nanowires. *Journal of Applied Physics*, 103, 123527.

Zhang, W., Wang, T.J., & Chen, X. (2010). Effect of surface/interface stress on the plastic deformation of nanoporous materials and nanocomposites. *International Journal of Plasticity*, 26, 957-975.

Zhao, K.J., Chen, C.Q., Shen, Y.P., & Lu, T.J. (2009). Molecular dynamics study on the nano-void growth in face-centered cubic single crystal copper. *Computational Materials Science*, 46, 749-754.

CHAPTER 2

Void-size effects on strength properties of nanoporous materials: A Molecular Dynamics approach

Abstract

In this Chapter, strength properties of nanoporous materials are addressed aiming to establish novel insights into the influence of void-size effects. To this end, a virtual spherically-nanovoided sample of an aluminium single crystal is investigated by adopting a Molecular-Dynamics computational approach. Elasto-plastic mechanical response, under triaxial strain-based conditions and including axisymmetric and shear states, are numerically experienced, identifying the corresponding limit stresses. Computed strength measures are used to furnish estimates of strength domains, described in terms of meridian and deviatoric profiles. The influence of void-size effects on the computed strength properties is clearly quantified for different porosity levels, numerical results confirming a strengthening of the sample when the void radius reduces. Moreover, it is shown that the occurrence and the amount of void-size effects are strongly dependent on the Lode angle, resulting in a shape transition of both meridian and deviatoric strength profiles when the void radius is varied. Finally, present results suggest porosity-dependent threshold values for the void radius above which void-size effects tend to disappear. With respect to the actual state-of-the-art, useful benchmarks for assessing the effectiveness of available theoretical models are provided, resulting in a novel incremental contribution towards the definition of advanced modelling strategies for describing strength properties of nanoporous materials.

Present Chapter corresponds to the published research paper (Brach et al., 2016b) [Mec Mater; 101: 102-117 (2016)].
A self-consistent notation is adopted.

Keywords: Nanoporous materials, strength properties, void-size effects, Lode angle influence, Molecular Dynamics.

2.1 Introduction

In the last decades, since the development of novel and challenging nano-technologies, nanostructured materials have yielded a growing research interest, involving experimental tests, theoretical formulations and numerical models (Arico et al., 2005; Lu et al., 2004; Jenkins, 2010). An important class of nanostructured materials consists in nanoporous media, characterized by very fascinating properties or combination of properties in terms of mechanical, chemical and electromagnetic features. In particular, due to the presence of nanoscale cavities, these materials exhibit a high capability to interact, absorb and cooperate with atoms, ions and molecules. Moreover, they are characterised by reduced mass density, high surface-to-volume ratio, good levels of both stiffness and strength, and they generally exhibit a ductile behaviour. Accordingly, nanoporous materials open towards groundbreaking functional applications in several technical fields, including civil and environmental engineering, geophysics, petroleum industry, biomechanics, chemistry. For instance, they are used to conceive multifunctional devices for aerospace/automotive applications, energy storage, ion-exchange, molecular biosensing and bioseparation, drug delivery, catalysis, filtration, sensoring (Jenkins, 2010).

From a mechanical point of view, one of the most fundamental aspect consists in identifying and describing the constitutive response and the strength properties of these materials, as dependent on the size of voids (which is in the order of some nanometres), as well as on their shape and arrangement (Dormieux and Kondo, 2010, 2013; Huang et al., 2005; Li and Huang, 2005; Monchiet et al., 2008; Monchiet and Kondo, 2013). As regards void-size effects, well-established experiments (usually based on nano-indentation tests) have shown that a reduction in the length-scale of nanovoids induces an improvement of the material strength (Biener et al., 2005, 2006; Hakamada and Mabuchi, 2007). Such an effect cannot be theoretically described by classical approaches for porous materials (e.g., Gurson, 1977; Ponte Castaneda, 1991), that are generally conceived to predict porosity effects only, and thereby resulting in void-size-independent strength criteria.

The influence of void size on the mechanical behaviour of nanoporous materials are related to the presence, at the cavity boundaries, of self-equilibrated surface stresses (Needs et al., 1991). These latter can be modelled via interface laws (Gurtin and Murdoch, 1975) and they reveal fundamental in describing the mechanical response of nanoscale structures (Amelang and Kochmann, 2015) and nano-structured materials (e.g., Duan et al., 2005a,b), as well as for modelling strength properties of nanoporous media (e.g., Dormieux and Kondo, 2010, 2013; Goudarzi et al., 2010; Monchiet and Kondo, 2013; Moshtaghin et al., 2012). As an example, by applying a limit-analysis approach on a hollow spherical domain, Dormieux and Kondo (2010) extended the well-known strength criterion proposed by Gurson (1977) for ductile porous media to the case of nanoporous materials, aiming to predict void-size effects. The void-size-dependent strength criterion by Dormieux and Kondo (2010), as well as the porous model by Gologanu et al. (1993, 1994), have been successively extended by Monchiet and Kondo (2013) to the case of nanoscale spheroidal cavities, thereby incorporating both void-shape and void-size effects. Other analytical formulations have been proposed by Dormieux and Kondo (2013),

Goudarzi et al. (2010), Zhang and Wang (2007) and Zhang et al. (2010), by combining non-linear homogenization techniques and variational arguments, and resulting in a generalization of the Ponte-Castaneda's strength criterion (Ponte Castaneda, 1991) to nanoporous materials.

It is worth observing that available strength models for nanoporous materials are based on a number of a priori assumptions. In fact, they generally include a very simple limit behaviour of the bulk matrix, as well as a simplified representation of the physics underlying nanoscale effects (usually faced by introducing fictitious plastic interfaces). Nevertheless, available experimental results are not sufficient to support these assumptions, so that current theoretical models can be neither properly validated nor suitably calibrated. As a matter of fact, apart from some qualitative indications of the void-size influence on the material strength level, no further information can be deduced from the experimental literature either on the three-dimensional material strength domain or on the influence of the void size as a function of the loading state. In this context, numerical methods may be considered as an effective alternative to provide comparative benchmarks, allowing also to successfully control a number of possible coupled effects, and thereby resulting in useful indications towards advanced modelling strategies.

Computational methods usually employed for modelling macro- and/or micro-mechanical response are not able to automatically provide helpful insights on nanoscale effects, since they do not include a satisfactory description of the material structure at that length-scale. On the contrary, and as confirmed by recent investigations (e.g., Bringa et al., 2010; Borg et al., 2008; Mi et al., 2011; Tang et al., 2010; Traiviratana et al., 2008; Zhao et al., 2009), numerical methods based on Molecular Dynamics (MD) approaches allow to describe the material arrangement at the atomistic level, and thereby they can be considered as promising tools for investigating the elasto-plastic behaviour of nanoporous materials.

As a matter of fact, available studies based on MD approaches mainly address the identification and the characterization of atomistic mechanisms underlying failure processes related to void growth and coalescence (e.g., Farrissey et al., 2000; Lubarda et al., 2004; Lubarda, 2011; Marian et al., 2004, 2005; Pogorelko and Mayer, 2016; Ruestes et al., 2013; Tang et al., 2010; Traiviratana et al., 2008). On the other hand and at the best of the authors' knowledge, very few attempts have been provided in order to employ these numerical strategies to furnish indications towards the definition of engineering strength measures for nanoporous materials. For instance, an attempt to put in relationship strength properties at the macroscale with MD-based evidence has been provided by Mi et al. (2011) and Traiviratana et al. (2008), referring to the void-size-independent Gurson model. Nevertheless, current MD studies are generally limited to the analysis of particular admissible stress states only, computed under uniaxial (Farrissey et al., 2000; Tang et al., 2010), volumetric or shear conditions (Marian et al., 2004, 2005), and therefore defining only few discrete points on the a-priori unknown material strength surface, without considering more complete multiaxial scenarios. In fact, a comprehensive three-dimensional characterization of material strength properties requires

a proper investigation of failure mechanisms under multiaxial loading conditions. Furthermore, no numerical evidence has been yet provided concerning the influence of void size on material strength domains. Accordingly, with respect to the previously-discussed state-of-the-art, a parametric multiaxial loading strategy is expected to pave the way for a number of original contributions, such as: (i) complete identification of failure surfaces and of the influence of stress invariants on material strength properties; (ii) analysis of void-size effects on strength domains; (iii) assessment of novel and effective comparative benchmarks for validating and calibrating available theoretical formulations, as well as for drawing advanced modelling strategies.

It must be pointed out that porous and nanoporous materials may be generally characterised by irregular patterns and randomly-distributed voids. Nevertheless, as it is customary in classical elasto-plastic theoretical approaches for micro/nano-structured materials, simple geometrical descriptions are often considered. This is the case of single-voided domains and of hollow sphere models (Gurson, 1977), widely adopted in porous metal plasticity and limit analysis approaches (Dormieux and Kondo, 2010; Monchiet and Kondo, 2013; Tvergaard and Needleman, 1984). Corresponding results are strictly valid for the particular, but realistic, considered microstructure (in the case of hollow sphere models, the microstructure is the so-called Hashin Composite Sphere Assemblage, (Hashin, 1962; Leblond et al., 1994; Michel and Suquet, 1992)), but they generally furnish also helpful indications on statistically-equivalent arrangements. In this framework, domains embedding a single spherical nanovoid have been adopted in many recent MD-based computational studies (e.g. Farrissey et al., 2000; Marian et al., 2004, 2005; Traiviratana et al., 2008), addressing plastic mechanisms in nanoporous materials.

In this Chapter, strength properties of an aluminium single crystal containing a spherical nanovoid are addressed via a Molecular Dynamics approach. A parametric analysis with respect to the void radius and for different porosity levels is carried out, by considering different strain paths (shear, triaxial expansion and triaxial compression) and a wide range of triaxiality scenarios (from pure deviatoric conditions to pure hydrostatic ones). The computational model is defined in Section 2.2, drawing also basic elements of the adopted numerical procedure. With the aim to present simulation results in the framework of a customary notation in plasticity, and by referring to average stress and strain measures, the Haigh-Westergaard (HW) coordinates are introduced. Section 2.3 is devoted to analyse some preliminary results, in terms of both stress-strain relationships and dominant atomistic mechanisms, in order to identify suitable strength measures for estimating limit stress conditions for the in-silico samples. Analyses of numerically-experienced strength properties are provided in Section 2.4, wherein meridian and deviatoric representations of computed strength domains are proposed, highlighting and discussing the influence of void-size effects. Finally, main concluding remarks are traced in Section 2.5.

2.2 Problem statement and computational methods

Let a material neighbourhood of a nanoporous medium be considered (Fig. 2.1), characterized by a periodic nanostructure along the global Cartesian directions X, Y and Z, and whose representative cell consists in a nano-single crystal embedding a single spherical void. In the following, reference is made to a single crystal of aluminium, whose ideal crystallographic arrangement is based on a face-centred cubic lattice (FCC). Let the local Cartesian frame (x, y, z) be introduced, with axes parallel to the global ones and with $\{\mathbf{e}_\mathrm{x}, \mathbf{e}_\mathrm{y}, \mathbf{e}_\mathrm{z}\}$ the corresponding orthonormal basis. Moreover, referring to the Miller's notation (Hull and Bacon, 2001), let the orientation of FCC lattices be assumed such that crystallographic directions [100], [010] and [001] line up with axes x, y and z, respectively.

A numerical approach based on a MD strategy and implemented in LAMMPS (Large-scale Atomic/Molecular Massively Parallel Simulator) (Plimpton, 1995) is adopted, by considering a cubic simulation box (Fig.2.1) undergoing periodic boundary conditions. The simulation domain is defined by: the edge length L; a centred spherical void of radius R; the atomic arrangement $\mathcal{C}^0$, resulting from the bulk FCC-based cubic box by suppressing all atoms belonging to the centred spherical region. Different values of the box length L are herein considered, such that:

$$\frac{L}{B} = 10\big(1+n\big) \tag{2.1}$$

n being an integer number ranging from 1 to 10, $B = a_0/2$ being the length-scale of the Burgers vector $\mathbf{b} = B < 110 >$ associated to perfect dislocations along slip directions of type $< 110 >$, and a_0 being the lattice constant (equal to 4.04 Å for aluminium at room temperature (Mishin et al., 1999)). Accordingly, for a fixed material porosity p, defined as $p = 4\pi R^3/3L^3$, varying the box length L corresponds to proportionally vary the void radius R. For instance, referring to the case $p = 1\%$, R varies from 0.541 nm to 2.977 nm when L/B varies from 20 ($n = 1$) to 110 ($n = 10$). It is worth observing that, since the cut-off distance r_c for the aluminium is equal to 0.628 nm (Mishin et al., 1999), assumption in Eq. (2.1) allows to satisfy the minimum image convention (Allen and Tildesley, 1991), resulting in the consistency requirement $L > 2r_c$ for any $n \geq 1$.

Vector velocities $\mathbf{v}_i$ $(i = 1 \dots N)$ of the N atoms in $\mathcal{C}^0$ are initialized as non-physical random vectors. In order to obtain a physically-consistent simulation domain at the temperature $T^* = 300\,\mathrm{K}$ and with zero pressure at the domain boundaries, a preliminary equilibration step is performed by simulating 30 picoseconds via a Nose-Hoover time-integration scheme (e.g., Plimpton, 1995). As a result, the statistically-equilibrated configuration $\mathcal{C}^*$ is obtained, consisting in a cubic simulation domain with the edge length equal to L^*. For the sake of compactness, values of L^* obtained from this preliminary equilibration step are omitted, consisting however in percentage differences with respect to L always less then 0.3%.

Afterwards, considering $\mathcal{C}^*$ as the reference configuration at the time $t = 0$, an incremental strain-driven deformation process is simulated, considering a fixed time-step Δt. Denoting with $\bar{t}$ the actual value of the time variable, a measure of the actual strain

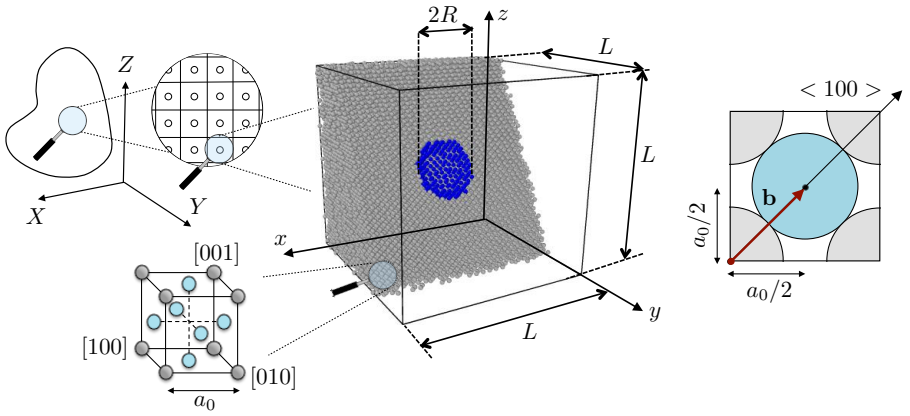

Figure 2.1 – Computational model herein adopted for describing an aluminium nanovoided single crystal. Notation.

tensor for the overall simulation domain is assumed to be expressed by:

$$\mathbf{D}(\bar{t}) = \chi \bar{t}\left(D_{\mathrm{x}}\mathbf{e}_{\mathrm{x}} \otimes \mathbf{e}_{\mathrm{x}} + D_{\mathrm{y}}\mathbf{e}_{\mathrm{y}} \otimes \mathbf{e}_{\mathrm{y}} + D_{\mathrm{z}}\mathbf{e}_{\mathrm{z}} \otimes \mathbf{e}_{\mathrm{z}}\right) \tag{2.2}$$

where χ is a positive strain-rate constant parameter, and D_{x}, D_{y} and D_{z} are assigned dimensionless quantities. Accordingly, the prescribed increments of the box lengths at each time-step result in $\Delta L_q = L^* D_q \, \chi \, \Delta t$, with $q = x, y, z$.

As a notation rule, the following three strain invariants are introduced: $I_1^{\mathrm{D}} = \mathrm{tr}\,\mathbf{D}$, $J_2^{\mathrm{D}} = \mathbf{D}_{\mathrm{d}} : \mathbf{D}_{\mathrm{d}}/2$ and $J_3^{\mathrm{D}} = \det \mathbf{D}_{\mathrm{d}}$, where $\mathbf{D}_{\mathrm{d}} = \mathbf{D} - (I_1^{\mathrm{D}}/3)\mathbf{1}$ is the deviatoric strain tensor and $\mathbf{1}$ is the second-order unit tensor ($1_{\mathrm{ij}} = \delta_{\mathrm{ij}}$, with δ_{ij} the Kronecker symbol). Moreover, referring to a strain-based Haigh-Westergaard notation (see for instance Menetrey and Willam, 1995), the strain Lode angle $\theta_{\mathrm{D}} \in [0, \pi/3]$ is defined such that: $\cos 3\theta_{\mathrm{D}} = 3\sqrt{3} J_3^{\mathrm{D}}/[2(J_2^{\mathrm{D}})^{3/2}]$. When necessary, reference is also made to the following invariant strain measures: $D_{\mathrm{m}} = I_1^D/3$ and $D_{\mathrm{eq}} = \sqrt{J_2^D}$.

In order to analyse the sample response under a broad range of triaxial strain-based conditions, three deformation paths are simulated, corresponding to $\theta_{\mathrm{D}} = 0$ (triaxial strain expansion, denoted as $\mathrm{TXE_D}$), $\theta_{\mathrm{D}} = \pi/3$ (triaxial strain compression, denoted as $\mathrm{TXC_D}$), and $\theta_{\mathrm{D}} = \pi/6$ (shear strain conditions, denoted as $\mathrm{SHR_D}$). Furthermore, the following choices of the dimensionless quantities D_{x}, D_{y} and D_{z} are considered:

$$\begin{aligned} \mathrm{TXE_D} \quad &: \quad D_{\mathrm{x}} = D_{\mathrm{y}} = \lambda, \quad D_{\mathrm{z}} = 1 \\ \mathrm{TXC_D} \quad &: \quad D_{\mathrm{y}} = D_{\mathrm{z}} = 1, \quad D_{\mathrm{x}} = \eta \\ \mathrm{SHR_D} \quad &: \quad D_{\mathrm{x}} = 1, \quad D_{\mathrm{y}} = (1+\mu)/2, \quad D_{\mathrm{z}} = \mu \end{aligned} \tag{2.3}$$

For any choice in Eq. (2.3), and referring to the case of a non-negative first invariant I_1^{D}, different scenarios are simulated. In detail, several strain-based triaxiality levels, ranging from a pure deviatoric condition ($D_{\mathrm{m}} = 0$) to a pure hydrostatic one ($D_{\mathrm{eq}} = 0$), are accounted for by varying the dimensionless coefficients λ, η and μ, as summarised in Table 2.1.

Table 2.1 – Values adopted for parameters λ, η and μ introduced in Eq. (2.3) to describe different triaxiality levels, ranging from a pure deviatoric condition ($D_{\mathrm{m}} = 0$) to a pure hydrostatic one ($D_{\mathrm{eq}} = 0$).

	$D_{\mathrm{m}} = 0$								$D_{\mathrm{eq}} = 0$
λ ($\mathrm{TXE_D}$)	-0.5	-0.4	-0.3	-0.2	-0.1	0	0.25	0.5	1
η ($\mathrm{TXC_D}$)	-2	-1.8	-1.6	-1.4	-1.2	-1	-0.5	0	1
μ ($\mathrm{SHR_D}$)	-1	$-0.8\overline{6}$	$-0.7\overline{3}$	-0.6	$-0.4\overline{6}$	$-0.\overline{3}$	0	$0.\overline{3}$	1

In order to achieve effective results with a reasonable computational time, numerical simulations are performed by considering $\chi = 5 \cdot 10^9$ s^{-1}. Such a strain-rate value is consistent with those usually adopted in the recent MD-based literature, ranging from 10^7 to 10^{12} s^{-1} (Bringa et al., 2010; Horstemeyer et al., 2001; Mi et al., 2011; Pogorelko and Mayer, 2016; Ruestes et al., 2013; Seppala et al., 2004; Shabib and Miller, 2009; Tang et al., 2010; Traiviratana et al., 2008; Zhao et al., 2009), and it can be experimentally obtained via laser-shock techniques (Lubarda et al., 2004). As a further consistency indication for such a choice, Horstemeyer et al. (2001) numerically proved that the yield strength for FCC metals becomes practically insensitive to the strain rate for values lower than $10^{10}\,\mathrm{s}^{-1}$.

Adopting a time-step equal to $\Delta t = 1$ femtosecond, trajectories of atoms are determined by integrating the Newton's second law via the Verlet algorithm (Verlet, 1967). As a result, the actual average stress tensor is computed as the superposition of atomistic kinetic contributions and pairwise interactions, and it is described via the following virial formula (e.g., Subramaniyan and Sun, 2008):

$$\boldsymbol{\Sigma}(\bar{t}) = -\frac{1}{V_{\mathrm{at}}} \sum_{i=1}^{N} \left(m_i \mathbf{v}_i \otimes \mathbf{v}_i + \sum_{j \neq i, j=1}^{N} f_{ij} \frac{\mathbf{r}_{ij} \otimes \mathbf{r}_{ij}}{r_{ij}} \right) \tag{2.4}$$

where V_{at} is the total atomic volume, m_i is the mass of the atom i, and $f_{ij} = \partial \mathcal{E} / \partial r_{ij}$ is the modulus of the interaction force between atoms i and j. The total energy $\mathcal{E}$ of the system is defined in agreement with the Embedded Atom Method (Daw and Baskes, 1984) as:

$$\mathcal{E} = \sum_{i=1}^{N} F_i(\overline{\rho}_i) + \frac{1}{2} \sum_{i=1}^{N} \sum_{\mathrm{j}=1 \neq \mathrm{i}}^{N} \Phi_{ij}(r_{ij}), \quad \text{with} \quad \overline{\rho}_i = \sum_{\mathrm{j}=1 \neq \mathrm{i}}^{N} \rho_j(r_{ij}) \tag{2.5}$$

where r_{ij} is the modulus of the separation vector $\mathbf{r}_{ij} = \mathbf{r}_j - \mathbf{r}_i$, with $\mathbf{r}_i$ identifying the position of the atom i. Accordingly, $\mathcal{E}$ is defined as the superposition of two terms. The first is the sum of cohesive embedding energies F_i (required to include the atom i into the electron cloud), expressed in terms of the electron-cloud density $\overline{\rho}_i$ (defined as the linear superposition of the neighbouring atomic electron densities ρ_j). The second contribution is associated to the repulsive pairwise potential function Φ_{ij} between the atom i and its neighbours j.

In this study, the Haigh-Westergaard (HW) representation is adopted for giving a three-dimensional description of the computed strength states. Accordingly, denoting with $\theta_\Sigma \in [0, \pi/3]$ the stress Lode angle, a given stress state $\mathbf{\Sigma}$ is uniquely determined by referring to the following stress-invariant quantities (e.g., Khan and Huang, 1995; Lubliner, 2008):

$$\zeta = \frac{I_1^\Sigma}{\sqrt{3}}, \qquad r = \sqrt{2J_2^\Sigma}, \qquad \cos 3\theta_\Sigma = \frac{3\sqrt{3}J_3^\Sigma}{2{J_2^\Sigma}^{3/2}} \tag{2.6}$$

where $I_1^\Sigma = \operatorname{tr}\mathbf{\Sigma}$, $J_2^\Sigma = \mathbf{\Sigma}_\mathrm{d} : \mathbf{\Sigma}_\mathrm{d}/2$ and $J_3^\Sigma = \det\mathbf{\Sigma}_\mathrm{d}$ are the isotropic stress invariants, and where $\mathbf{\Sigma}_\mathrm{d} = \mathbf{\Sigma} - (I_1^\Sigma/3)\mathbf{1}$ is the deviatoric part of the stress measure introduced in Eq.(2.4).

For what follows, notation TXE_Σ, TXD_Σ and SHR_Σ is introduced to indicate triaxial stress expansion (i.e., $\theta_\Sigma = 0$), triaxial stress compression (i.e., $\theta_\Sigma = \pi/3$) and shear (i.e., $\theta_\Sigma = \pi/6$) stress states. Furthermore, when necessary, reference is made to the following invariant stress measures: $\Sigma_\mathrm{m} = I_1^\Sigma/3$ and $\Sigma_\mathrm{eq} = \sqrt{J_2^\Sigma}$.

The HW representation defines a cylindrical coordinate system $(\zeta, r, \theta_\Sigma)$ within the space of the principal stresses $(\Sigma_1, \Sigma_2, \Sigma_3)$, with ζ and r being the magnitudes of the orthogonal projections of the stress tensor $\mathbf{\Sigma}$ on the hydrostatic axis (i.e., $\Sigma_1 = \Sigma_2 = \Sigma_3$, $r = 0$) and on the deviatoric plane (or π-plane, that is $\zeta = \text{const}$), respectively. It is worth to remark that, for a given stress state $(\zeta, r, \theta_\Sigma)$ it is always possible to recover the corresponding stress tensor $\mathbf{\Sigma}$, allowing for possible alternative representations (based for instance on anisotropic stress invariants, (Hill, 1948; Monchiet et al., 2008)). Nevertheless, aiming to furnish possible indications towards the characterization of material strength properties in the framework of a continuum description, and since actual strength models for nanoporous media are generally expressed in terms of isotropic stress invariants, the HW representation is herein considered as useful for such purposes.

2.3 Strength measure and atomistic mechanisms

Strength properties of the herein-considered aluminium nanovoided single crystal are identified by defining, for each deformation scenario, a limit stress state. With reference to stress and strain measures previously introduced, typical stress-strain responses computed via the present approach are shown in Figs. 2.2 and 2.3. They refer to the case $p = 1\,\%$ and $L/B = 50$ (corresponding to $R = 1.353\,\mathrm{nm}$) and address the deformation path TXE_D. Aiming to furnish some indications on temperature effects related to elasto-plastic mechanisms, two different cases are simulated: an isothermal process (denoted as IP), and a non-isothermal one (NIP, no temperature control is used during the loading process). Stress-strain relationships presented in Fig. 2.2 are obtained for three different deformation scenarios ($\lambda = -0.5$, pure deviatoric condition; $\lambda = 0$, traction test corresponding to a mixed hydrostatic/deviatoric condition; $\lambda = 1$, pure hydrostatic condition). Moreover, addressing the case $\lambda = -0.5$, Fig. 2.3a depicts stress-strain responses computed in the IP case for different temperature values (Fig. 2.3a), and Fig. 2.3b shows the temperature evolution numerically-experienced in the NIP-based simulation.

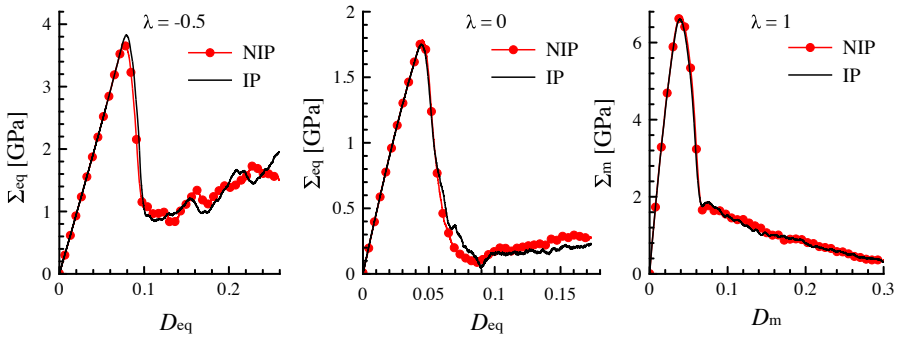

Figure 2.2 – Stress-strain relationships computed for the deformation path $\mathrm{TXE_D}$ with: $\lambda = -0.5$ (pure deviatoric state), $\lambda = 0$ (traction test) and $\lambda = 1$ (pure hydrostatic state). $L/B = 50$, $R = 1.353\,\mathrm{nm}$, $p = 1\%$. IP: isothermal process (at 300 K). NIP: non-isothermal process.

As main features of the resulting stress-strain responses, stress peaks are clearly identified, indicating a critical condition for the sample, followed by a stress-relaxation phase. Stress-strain relationships obtained by considering all the other deformation paths and different triaxiality levels (see Eqs.(2.3) and Table 2.1), as well as in the case of a bulk sample (i.e., $p = 0$), exhibit the same characteristics and they are herein omitted for the sake of compactness. With reference to the IP case and mainly resulting from the temperature influence on the atomic mobility, Fig. 2.3a shows that if the temperature increases then the stress peak reduces, and the latter is attained at a lower strain level. Furthermore, for high strains, material response is proven to become smoother as temperature is higher, sequences of rises and falls tending to disappear. On the other hand, addressing the NIP deformation process, Fig. 2.3b reveals that the occurrence of the stress peak corresponds to a significant change in the slope of the monotonically-increasing temperature evolution. Nevertheless, as it is highlighted by comparing IP- and NIP-based results (Fig. 2.2), such a heating does not significantly affect either the values of the stress peaks or the strain levels at which they occur. On the contrary, some heating-induced effects appear for higher strains values.

As previously stated, very few experimental tests have been performed so far in order to characterise the mechanical response of nanoporous materials, and the corresponding evidence is thereby not sufficient to provide a proper validation benchmarking for MD-based results. Nevertheless, present numerically-experienced stress-strain features are fully in agreement with those obtained by other well-established MD studies (e.g., Mi et al., 2011; Ruestes et al., 2013; Traiviratana et al., 2008; Zhao et al., 2009).

The occurrence of the stress peak is assumed to identify the limit stress state of the sample (as also assumed, for instance, by Mi et al., 2011; Ruestes et al., 2013; Traiviratana et al., 2008; Zhao et al., 2009), and the corresponding values of stress invariants I_1^Σ, J_2^Σ and J_3^Σ allow to define a strength point $(\zeta, r, \theta_\Sigma)$ in the HW coordinate system. In the following, strength features are computed by referring to IP-based simulations.

It is worth pointing out that, when the deviatoric strain level is significant, the limit stress state of the sample is straight identified by referring to stress-strain curves expressed

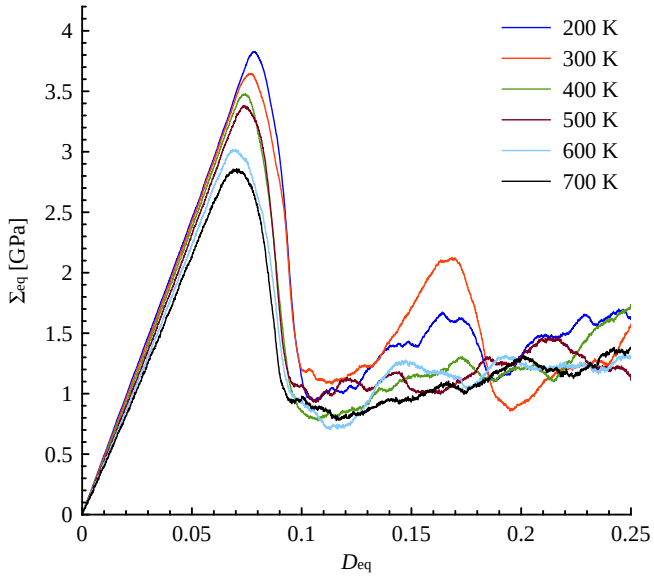

(a)

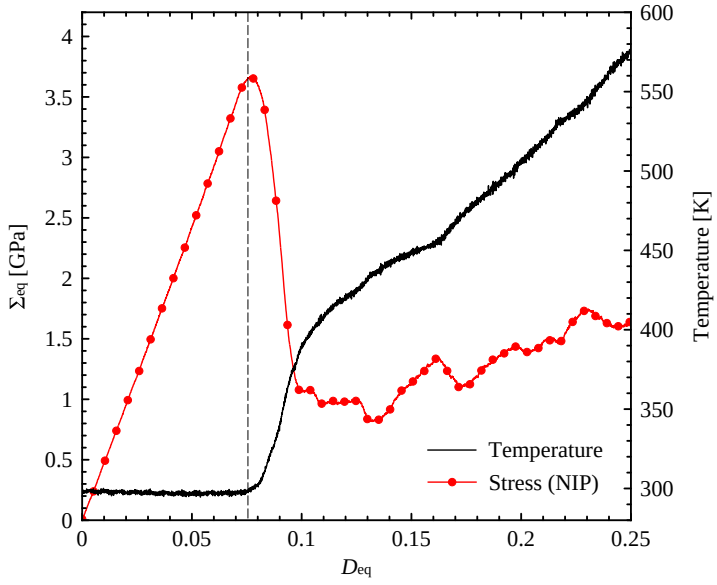

(b)

Figure 2.3 – Deformation path $\mathrm{TXE_D}$ with $\lambda = -0.5$ in the case $L/B = 50$ and for $p = 1\,\%$. (a) Stress-strain responses computed considering an isothermal process (IP) and for different temperature values. (b) Stress and temperature vs. strain in the case of a non-isothermal process (NIP).

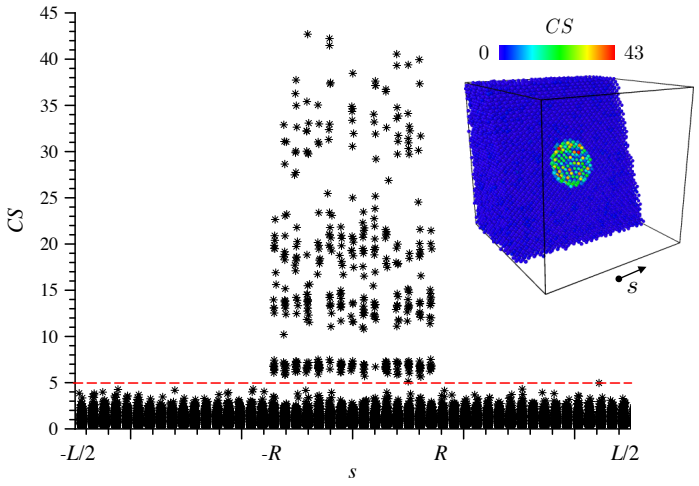

Figure 2.4 – Centro-symmetry distribution (CS), represented as one-data point per atom, relevant to the reference configuration $\mathcal{C}^*$. $L/B = 50$, $R = 1.353\,\mathrm{nm}$, $p = 1\%$.

in terms of Σ_{eq} versus D_{eq}. On the other hand, when a pure hydrostatic deformation scenario is considered, numerical computations reveal that the stress measure Σ_{eq} is practically equal to zero, and thereby reference is made to the stress-strain response in terms of Σ_{m} versus D_{m} (Fig. 2.2).

Aiming to furnish indications for relating the numerically-experienced stress-strain behaviour with some basic atomistic mechanisms, MD-based results relevant to the deformation path $\mathrm{TXE_D}$ with $\lambda = -0.5$ (for $L/B = 50$, $p = 1\,\%$ and considering a NIP case) are post-processed in the OVITO environment (Stukowski, 2010), by carrying out two different analyses. The first one allows to estimate the centro-symmetry deviation parameter CS. This latter is defined in agreement with Kelchner et al. (1998), Stukowski (2010), and Plimpton (1995), resulting in $CS = 0$ for ideal FCC lattices (i.e., neglecting any disturbance effects induced by thermal fluctuations, (Stukowski, 2012)) and $CS > 0$ when defects, crystallographic disorder, or different lattice structures appear. The second atomistic investigation is based on the Common Neighbour Analysis (CNA) (Honeycutt and Andemen, 1987) that allows to detect the lattice nature of each atom, distinguishing among face-centered cubic (FCC), hexagonal close-packed (HCP), body-centered cubic (BCC) lattices, icosahedral (ICO) and cubic diamond (DIA) arrangements, or other assemblies with an unknown coordination structure (thereby exhibiting an amorphous nature, and denoted as "Others").

As shown in Fig. 2.4, due to the void presence and as a result of the preliminary equilibration step, the CS instantaneous measure in the reference configuration $\mathcal{C}^*$ is significantly different from 0 at the void surface, and it is characterised by values ranging from 0 to 5 elsewhere (due to thermal fluctuations).

At each simulation step, the CNA post-processing phase is performed in order to investigate the evolution of the atomistic arrangement induced by the simulated deformation path, possibly associated to plastic mechanisms. Nevertheless, aiming to focus on

dominant atomistic processes, the centro-symmetry parameter CS is used to filter regions where atomic patterns significantly differ from the FCC lattices. In detail, in agreement with previous observations, CNA post-processing is applied to atoms characterised by $CS > 5$.

The atomistic-based results obtained from the post-processing phase and depicted in the bottom part of Fig. 2.5, highlight that a number of dislocation mechanisms, theoretically expected for FCC-based nanovoided single crystals (as briefly summarised in 2.A), are properly caught by the proposed simulations in the case of a pure deviatoric deformation scenario. Observed evidence is in agreement with other well-established numerical studies (e.g., Bringa et al., 2010; Marian et al., 2004, 2005; Tang et al., 2010; Traiviratana et al., 2008; Zhao et al., 2009). For instance, Marian and co-workers have obtained similar results studying the void growth of an aluminium nanovoided specimen, in terms of both volume expansion (Marian et al., 2004) and applied shear angle (Marian et al., 2005). Moreover, the herein observed dislocation nucleation and propagation mechanisms are comparable with results proposed by Traiviratana et al. (2008) and relevant to the case of an uniaxial expansion of monocrystalline and bicrystalline copper.

As a matter of fact, the analysis of Fig. 2.5 reveals that for small values of the equivalent strain measure D_{eq}, the sample is almost totally composed by FCC lattices and the temperature is practically constant, resulting in the elastic behaviour observed in the zone z1. At the end of this phase, for greater values of D_{eq}, proposed results show that Shockley partial dislocations are nucleated, leading to the occurrence of HCP atoms (see 2.A). Correspondingly, a plastic regime is activated (zone z2) and the temperature slope significantly changes, in agreement with (Ruestes et al., 2013). Once nucleated at the end of the zone z1, leading Shockley partials glide away from the surface of the void until they intersect along a crystallographic direction belonging to $< 110 >$ (see Fig.2.5a), resulting in a Lomer-Cottrell dislocation. The latter is sessile and it acts as a barrier with respect to trailing partials (the so-called Lomer-Cottrell lock (Hull and Bacon, 2001)). Contemporaneously, secondary slipping systems are activated in other regions of the void surface. At the end of the zone z2 a stress peak is observed when the sessile arrangement breaks up (Fig.2.5e), realising potential hotbeds for further dislocations slipping (Fig.2.5f) and leading to complex dislocations interactions. In the zone z3, the stress-strain relationship experiences a relaxation phase, characterized by a steep dropping off of the stress, followed by further rises and falls associated to the formation, interaction and subsequent unlocking of other sessile assemblies, out of the current concern. Correspondingly, a significant irreversible heating appears, as both experimental (e.g., Rittel et al., 2006) and computational (e.g., Higginbotham et al., 2011) evidence widely confirms.

It is worth pointing out that plastic deformation can be accompanied at the nanoscale by a number of other complex atomistic interacting processes, related to void growth and collapse mechanisms, dislocations emission, and shear loops (Bringa et al., 2010; Marian et al., 2004, 2005; Traiviratana et al., 2008). Nevertheless, aiming to support the choice of a suitable strength measure via a basic description of atomistic mechanisms only, the detailed analysis of such phenomena does not fall in the purposes of the present study.

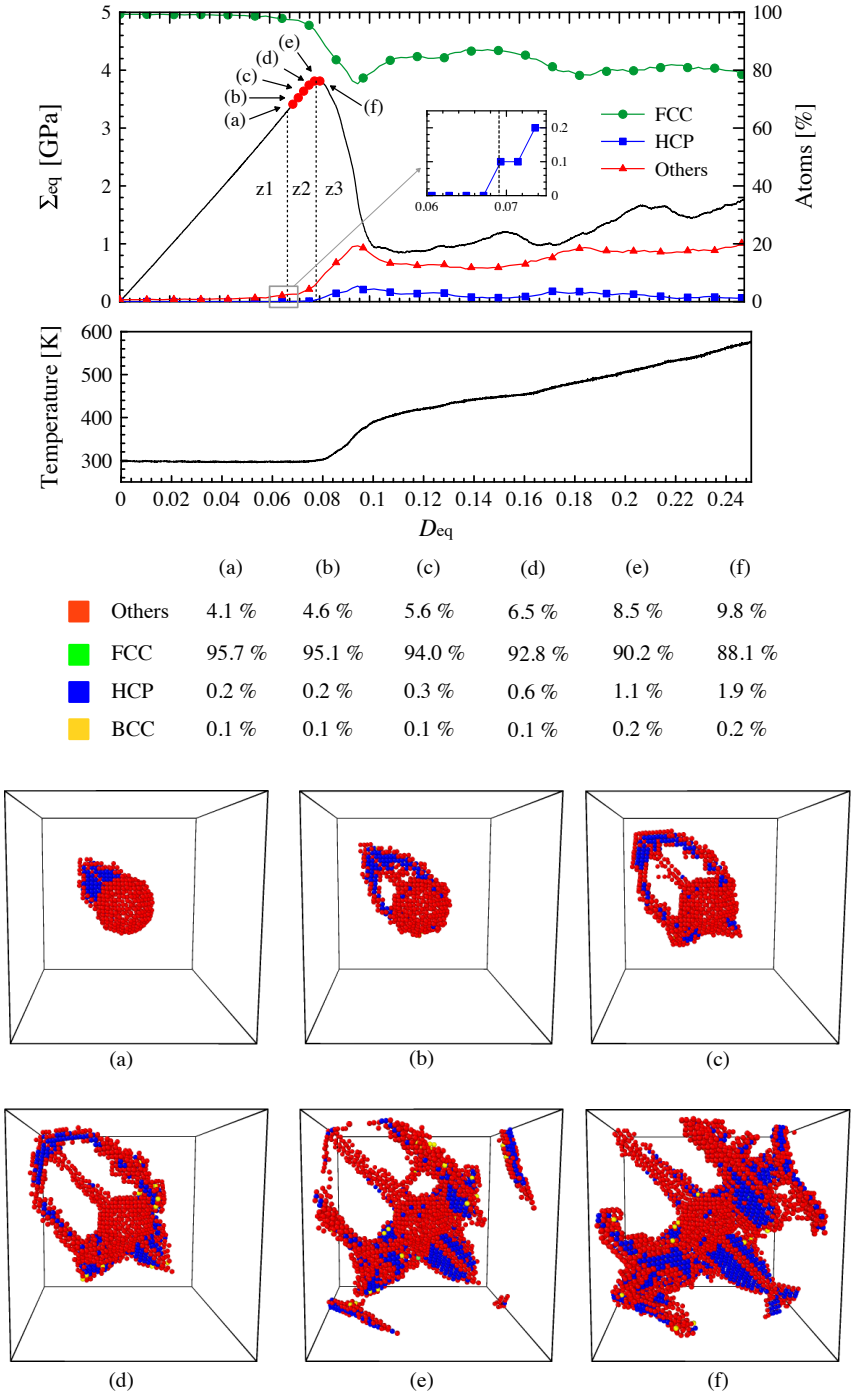

	(a)	(b)	(c)	(d)	(e)	(f)
Others	4.1 %	4.6 %	5.6 %	6.5 %	8.5 %	9.8 %
FCC	95.7 %	95.1 %	94.0 %	92.8 %	90.2 %	88.1 %
HCP	0.2 %	0.2 %	0.3 %	0.6 %	1.1 %	1.9 %
BCC	0.1 %	0.1 %	0.1 %	0.1 %	0.2 %	0.2 %

Figure 2.5 – (Top) Stress-strain relationship, temperature-strain relationship, and CNA results computed under a pure strain-based deviatoric condition corresponding to a non-isothermal deformation path $\mathrm{TXE_D}$ ($\lambda = -0.5$, $L/B = 50$, $R = 1.353\,\mathrm{nm}$, $p = 1\%$). z1: elastic zone; z2: activation of plastic mechanisms; z3: stress-relaxation zone. (Bottom) Atomic patterns and CNA results corresponding to different states within zones z2 and z3. Percentages of icosahedral (ICO) and cubic diamond (DIA) atomic arrangements are equal to zero.

2.4 Strength analyses

Strength points computed in agreement with considerations traced in Section 2.3 are used to furnish meridian (i.e., in the plane (ζ, r), with $\theta_\Sigma = \text{const}$) and deviatoric (i.e., in the plane (r, θ_Σ), with $\zeta = \text{const}$) representations of the strength domain. To this aim, a non-linear least-squares fitting based on the algorithm proposed by Levenberg (1944) and Marquardt (1963) is employed.

With reference to the simulation cell introduced in Fig. 2.1, the presence of the nanovoid is expected to induce a perturbation on the mechanical behaviour with respect to the bulk sample (namely, corresponding to $p = 0$). Accordingly, as an useful comparative benchmark, strength properties of the in-silico bulk specimen are preliminarily investigated. Furthermore, the influence of the nanovoid on both strength-domain shape and strength values is analysed, highlighting and discussing void-size effects, when different porosity levels are accounted for.

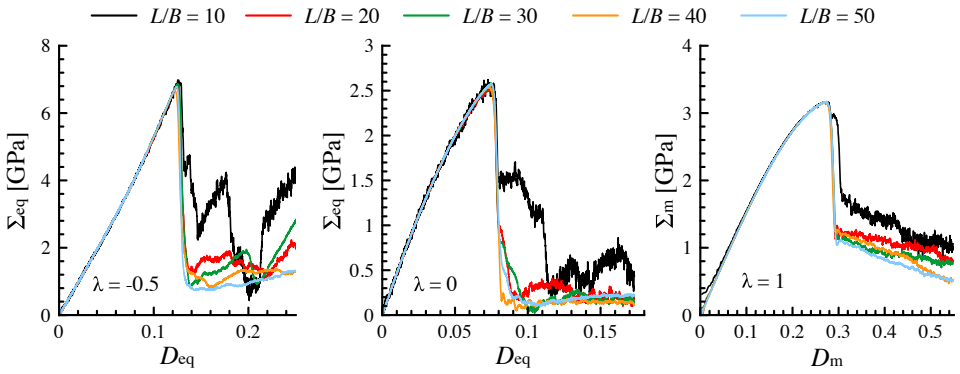

Figure 2.6 – Bulk sample. Influence of the simulation box length L/B on the stress-strain response for the deformation path TXE_D.

2.4.1 Bulk sample

Stress-strain curves obtained in the case of a bulk domain and for different values of the simulation box length L/B are depicted in Fig. 2.6, addressing the deformation path TXE_D and different triaxiality levels.

As a matter of fact, the long-range nature of dislocation fields results in the interaction of dislocations through the cell boundaries, leading to possibly non-negligible periodic image effects. These latter are expected to be more significant when the box length is small. Such an occurrence is clearly highlighted by results proposed in Fig. 2.6, where significant differences in the material mechanical response occur within the full plastic regime (namely, in the zone z3 introduced in Fig. 2.5). In detail, and as a result of periodic image effects, small values of L/B induce marked sequences of rises and falls, characterised by average stress levels which are higher than those obtained for large L/B. Nevertheless, periodic image effects are proven to negligibly affect the adopted strength measure, irrespective of the considered triaxiality levels. In detail, Fig. 2.7a confirms that

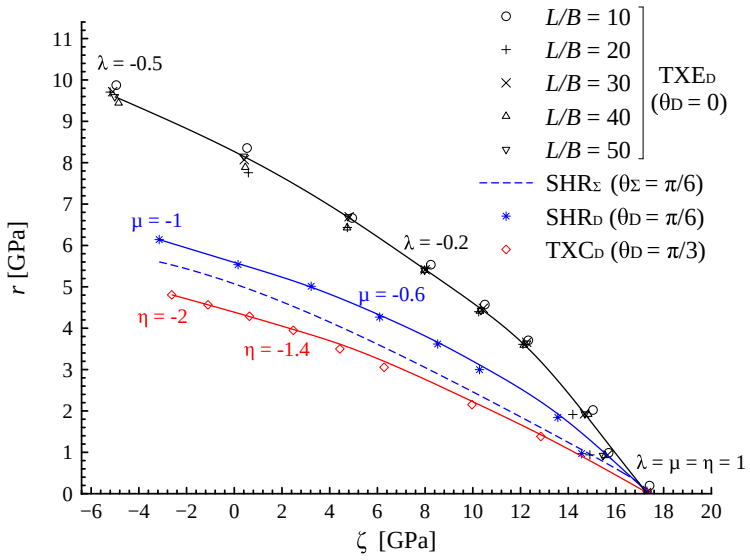

(a)

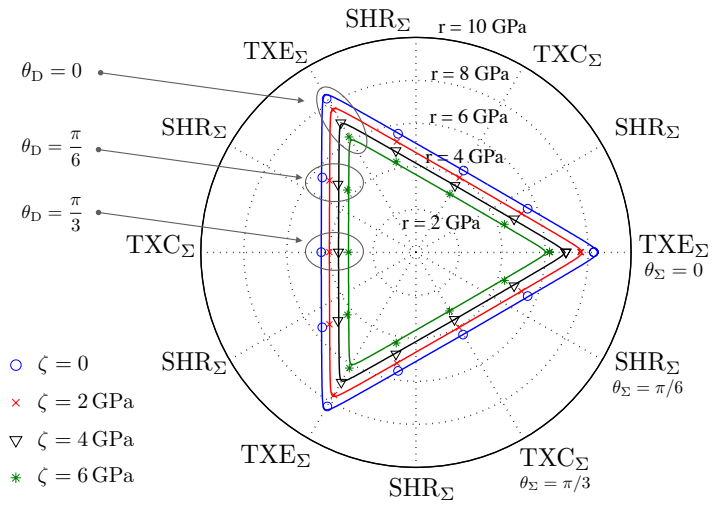

(b)

Figure 2.7 – Bulk sample. Strength states computed under TXE_D, TXC_D and SHR_D deformation paths. (a) Meridian strength profiles. (b) Deviatoric strength profiles. Symbols denote computed strength states, curves indicate estimated strength profiles.

in the case TXE_D, computed strength states are almost coincident when the box length is varied, resulting in negligible discrepancies. Thereby, in the following the average results obtained for different L/B will be considered as representative of strength states for the bulk sample. Similar observations can be provided for TXC_D and SHR_D deformation paths, whose results are herein not reported for the sake of compactness.

Figure 2.7b depicts strength results in the deviatoric plane (π-plane), highlighting that cross sections of the strength domain at different ζ coordinates are characterised by a triangular shape.

Accordingly, proposed results clearly show the significant influence of all the three stress invariants I_1^Σ, J_2^Σ and J_3^Σ. Furthermore, the analysis of Fig. 2.7a indicates that strength states computed under pure strain-based deviatoric conditions ($\lambda = -0.5$, $\eta = -2$, $\mu = -1$, see Table 2.1) exhibit non-negligible hydrostatic stress components.

Table 2.2 summarizes computed values of the stress Lode angle θ_Σ for different deformation paths and for several values of ζ. As also shown in Fig. 2.7b, the axisymmetric strain conditions TXE_D ($\theta_D = 0$) and TXC_D ($\theta_D = \pi/3$) generate stress states which are in turn almost axisymmetric and characterised by $\theta_\Sigma \approx \theta_D$. Thereby, triaxial strain expansion TXE_D (respectively, compression TXC_D) practically corresponds to triaxial stress expansion TXE_Σ (respectively, compression TXC_Σ), irrespective of the value assumed for ζ. In contrast, in the case of SHR_D ($\theta_D = \pi/6$), the computed values of θ_Σ are significantly different from θ_D. As a result, SHR_D strain condition does not induce a pure shear stress state SHR_Σ (namely, corresponding to $\theta_\Sigma = \pi/6$). This occurrence has been also observed by Lemarchand et al. (2015), as associated to the dependency of strength properties on all the three stress invariants.

Accordingly, addressing Fig. 2.7a, estimated curves for strength states relevant to the TXE_D and TXC_D cases straight correspond to the intersections of the strength domain with meridian planes $\theta_\Sigma = 0$ and $\theta_\Sigma = \pi/3$, respectively. On the contrary, an estimate of the strength profile in the meridian plane $\theta_\Sigma = \pi/6$ (dashed curves) is obtained by interpolating numerical results computed by varying θ_D.

2.4.2 Nanovoided sample

Figures 2.8 to 2.12 summarize numerical results relevant to strength analyses on nanovoided samples, for a fixed value of porosity ($p = 1\%$) and for different values of the ratio L/B (this corresponds to proportionally vary the void radius). The case of the bulk sample is also reported for comparison, when necessary.

As in the case of the bulk sample, MD-based analyses have revealed that axisymmetric deformation paths practically result in axisymmetric stress states, leading to $\theta_\Sigma \approx \theta_D$, (see for instance Figs. 2.9 and 2.10). On the other hand, a significant discrepancy between stress- and strain-based Lode angles is observed for the deformation path SHR_D, as depending on: the Haigh-Westergaard coordinate ζ (that is, on the hydrostatic stress level), the triaxiality parameter ζ/r, and the ratio L/B (Fig. 2.8). Such an evidence on a nanovoided sample is in agreement with theoretical findings proposed by Lemarchand et al. (2015), obtained for a solid phase that obeys to a strength criterion depending on all

Table 2.2 – Bulk sample. Values of the stress Lode angle θ_Σ (normalised with respect to the corresponding values of θ_D for deformation paths SHR_D and TXC_D) for different hydrostatic stress levels.

	TXE_D	SHR_D	TXC_D
ζ [GPa]	θ_Σ [rad]	θ_Σ/θ_D	θ_Σ/θ_D
0	0.0018	0.7122	0.9969
1	0.0014	0.6961	0.9966
2	0.0012	0.6746	0.9963
3	0.0011	0.6512	0.9961
4	0.0011	0.6290	0.9961
5	0.0014	0.6087	0.9963
6	0.0019	0.5898	0.9967
7	0.0024	0.5722	0.9972
8	0.0028	0.5586	0.9979
9	0.0027	0.5531	0.9984
10	0.0025	0.5584	0.9987

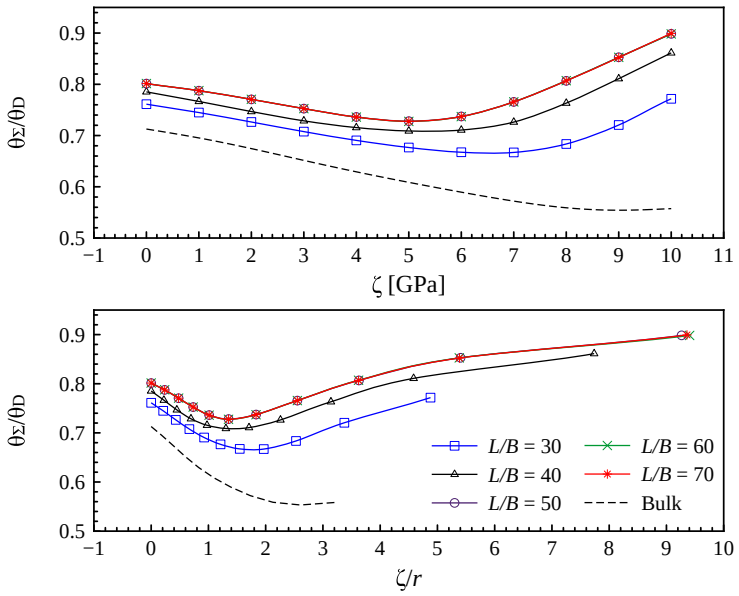

Figure 2.8 – Values of the stress Lode angle θ_Σ (normalised with respect to the corresponding value of θ_D) versus ζ (top) and ζ/r (bottom), computed for a nanovoided sample ($p = 1\%$) undergoing the SHR_D deformation path, and for different ratios L/B. The case of the bulk specimen is also reported.

the three stress invariants.

Referring to Fig. 2.8, two main effects can be highlighted. Firstly, the presence of a nanovoid tends to reduce the difference between θ_Σ and θ_D with respect to the bulk case, mainly for high values of hydrostatic stress and triaxiality levels. Secondly, for a fixed value of ζ, a reduction in the void size induces an increment of the discrepancy between θ_Σ and θ_D, especially for high hydrostatic stress amounts. Such an influence of the void

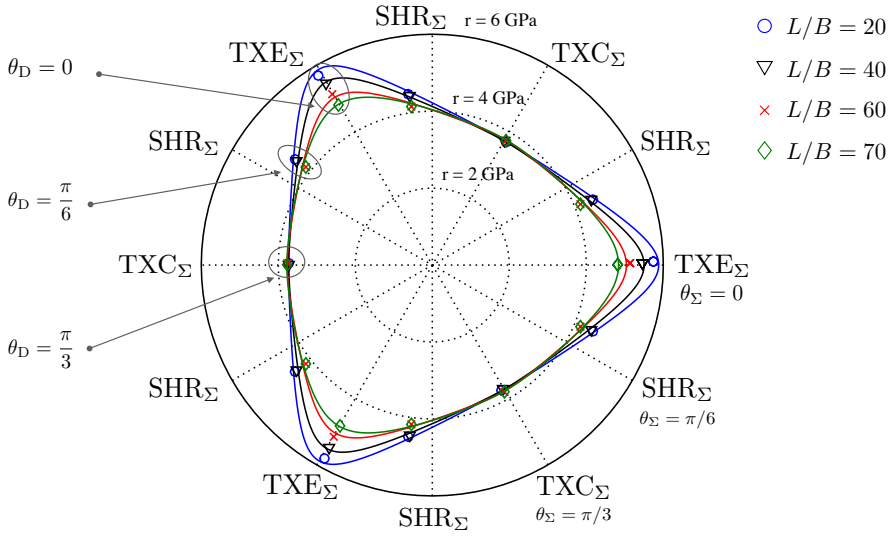

(a)

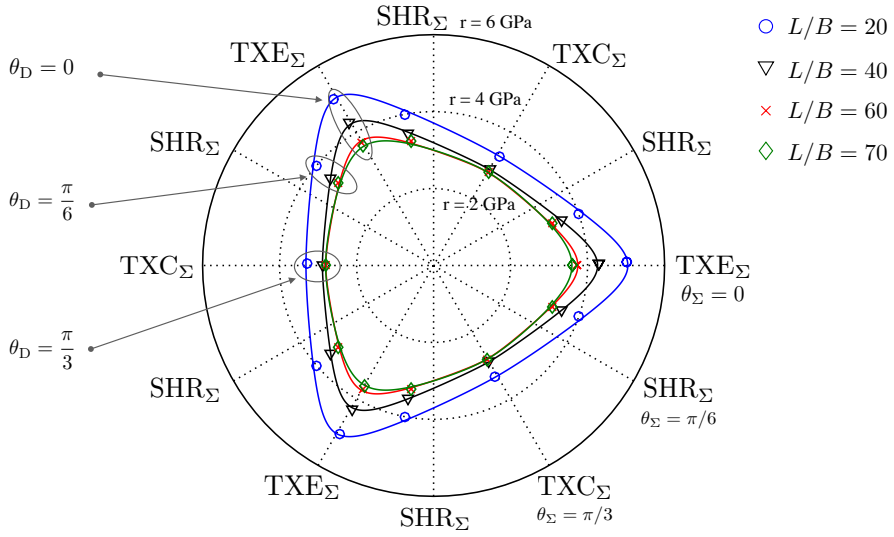

(b)

Figure 2.9 – Nanovoided sample ($p = 1\%$). Numerical results (symbols) and estimated strength profiles in the π-plane. (a) $\zeta = 2\,\mathrm{GPa}$. (b) $\zeta = 6\,\mathrm{GPa}$.

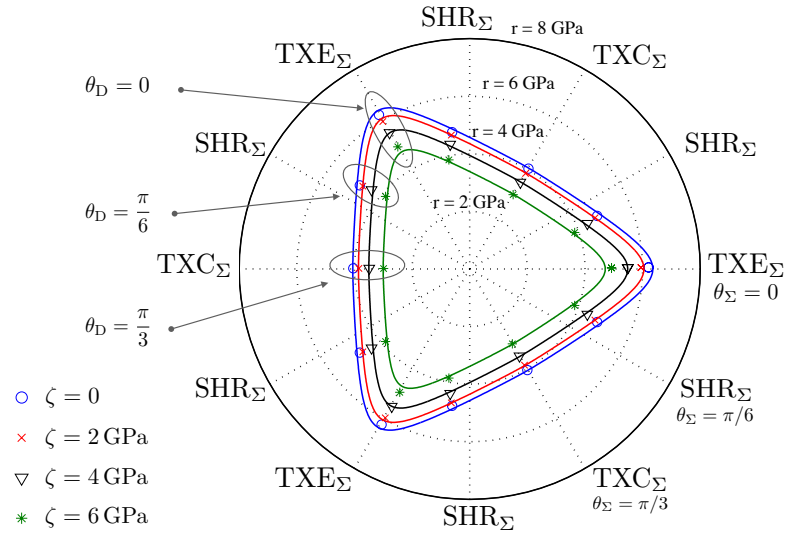

(a)

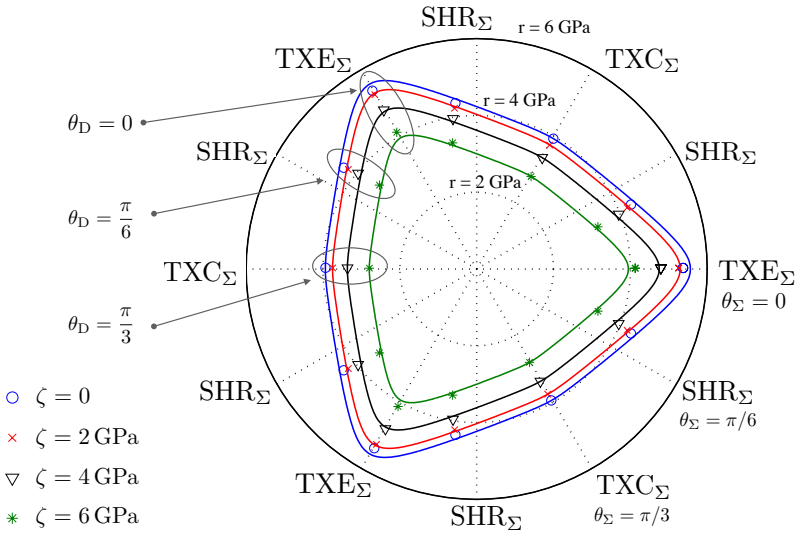

(b)

Figure 2.10 – Nanovoided sample ($p = 1\%$). Numerical results (symbols) and estimated deviatoric strength profiles for different hydrostatic stress levels. (a) $L/B = 30$ ($R = 0.812\,\mathrm{nm}$). (b) $L/B = 50$ ($R = 1.353\,\mathrm{nm}$).

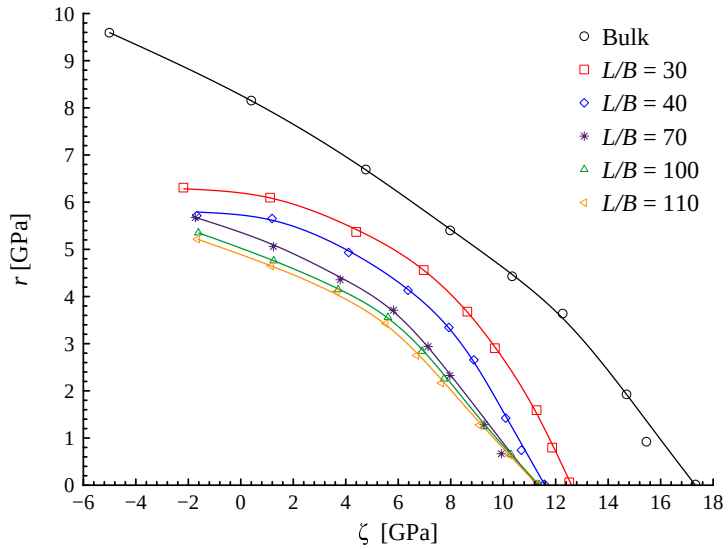

Figure 2.11 – Nanovoided sample ($p = 1\%$). Numerical results (symbols) and estimated meridian strength profiles for different values of L/B and for a TXE_Σ state ($\theta_\Sigma = 0$). The bulk case is also reported.

radius tends to disappear for values of L/B greater than 50 (that is, for $R > 1.353\,\mathrm{nm}$).

As a general remark, the measured stress state does not systematically correspond to the applied strain one. Such an occurrence is also evident in meridian planes (Figs. 2.11 and 2.12), where non-negligible hydrostatic stress components can be observed when pure strain-based deviatoric conditions are considered.

The analysis of Figs.2.9 to 2.12 suggests a clear dependence of the numerically-estimated strength properties on all the three stress invariants previously introduced. As a matter of fact, the influence on I_1^Σ and J_2^Σ can be mainly observed by referring to meridian representations in Figs. 2.11 and 2.12, as well as the dependency on J_3^Σ is highlighted by addressing the non circular profiles in π-planes of Figs. 2.9 and 2.10.

With respect to the actual state-of-the-art, this evidence confirms that a proper characterization of strength properties for nanoporous materials can be still considered as an open and challenging issue. In fact, the influence of the stress invariants is not accurately taken into account in current available theoretical models (e.g., Dormieux and Kondo, 2010, 2013; Goudarzi et al., 2010; Zhang and Wang, 2007; Zhang et al., 2010), resulting in an unsatisfactory description of the material strength domain. For instance, non-linear homogenization-based criteria by Zhang and Wang (2007) and Zhang et al. (2010) describe the meridian strength profile as elliptic, and any dependency on the third stress invariant is not accounted for (thereby resulting in a circular deviatoric strength profile). This is clearly in contrast with obtained results, confirming that MD simulations open towards novel insights for developing and validating more effective theoretical approaches.

Proposed meridian and deviatoric strength profiles are shown to be significantly affected by void-size effects, mainly resulting in the improvement of the strength properties

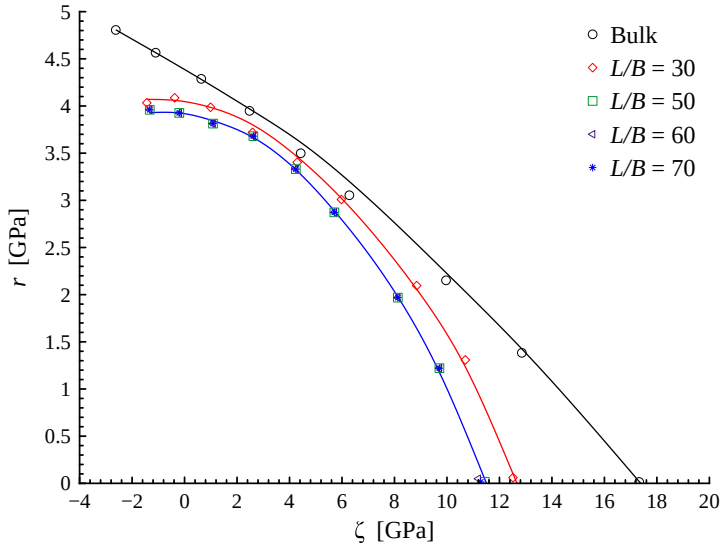

(a)

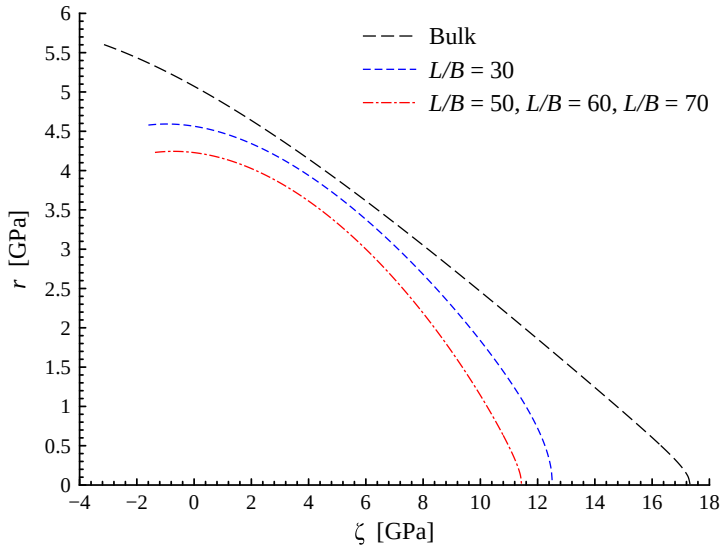

(b)

Figure 2.12 – Nanovoided sample ($p = 1\%$). Numerical results (symbols) and estimated meridian strength profiles for different values of L/B. (a) TXC_Σ ($\theta_\Sigma = \pi/3$). (b) SHR_Σ ($\theta_\Sigma = \pi/6$). The bulk case is also reported. As for the bulk sample, curves for SHR_Σ case are obtained by interpolating numerical results computed by varying θ_D.

when the void radius reduces. Occurrence and amount of such a strengthening effect strongly depend on the value assumed by the stress Lode angle, as it clearly appears in Figs.2.9, 2.11 and 2.12. In detail, referring to Fig. 2.9 and for a fixed hydrostatic stress level ζ, the highest influence is observed in the case of a triaxial expansion. Moreover, a shape transition is observed in the deviatoric profiles, these latter passing from a multi-sided polygonal shape to a triangular-like one when the void size reduces. Equivalently, an increase of the ratio L/B tends to mitigate the influence of the third stress invariant. This shape-transition is observed for any hydrostatic coordinate ζ, and it is associated to void-size effects only. In fact, when the void radius is fixed, the shape of π-plane strength profiles is proven to be constant with respect to ζ (Fig. 2.10).

Referring to meridian strength profiles depicted in Fig. 2.11, it is also observed that, in the TXE_Σ case, the lower the ratio L/B the higher the values of the profiles mean curvature are. Such a shape-transition effect practically does not occur in TXC_Σ and SHR_Σ meridian planes.

As a quantitative indication, when the void radius is reduced from 2.977 nm ($L/B = 110$) to 0.812 nm ($L/B = 30$), the strength measure Σ_{eq} at $\zeta = 4$ GPa (resp., $\zeta = 8$ GPa) increases of about: 40 % (resp., 105 %) for TXE_Σ (see Fig. 2.11); 5 % (resp., 20 %) for TXC_Σ (see Fig. 2.12a); 11 % (resp., 18 %) for SHR_Σ (see Fig. 2.12b). Nevertheless, computed results for $p = 1$ % prove that strength properties turn out to be almost independent from the void radius for values greater than 2.7 nm (i.e., for L/B greater than about 100) in the case TXE_Σ, and for values greater than 1.35 nm (i.e., L/B greater than about 50, Fig.2.12) in the cases SHR_Σ and TXC_Σ.

The influence of the porosity p on meridian and deviatoric strength profiles is shown in Figs. 2.13 to 2.15, relevant to further two porosity values $p = 0.1\%$ and $p = 0.5\%$. As expected, when p is reduced strength properties tend to increase towards the bulk ones. As in the case of $p = 1\%$, Figs. 2.13 and 2.14 reveal that axisymmetric strain-rate conditions TXE_D and TXC_D practically correspond to triaxial expansion and compression stress states, respectively, leading to $\theta_\mathrm{D} \approx \theta_\Sigma$. In contrast, in the case of SHR_D, the computed values of θ_Σ are significantly different from θ_D. Comparisons among results obtained for different porosity levels suggest that discrepancies between θ_Σ and θ_D tend to reduce when porosity increases. Moreover, the occurrence of a strengthening void-size effect, previously-described for $p = 1\%$, is confirmed by results in Figs. 2.13 ($p = 0.5$ %) and 2.14 ($p = 0.1$ %), where material strength properties are proven to increase when the void radius is reduced. As already observed in Figs. 2.9 and 2.10, the increase of the void radius (i.e., of L/B) leads to a shape transition of deviatoric strength profiles, almost irrespective of porosity level. Since the highest amount of the strengthening void-size effect occurs for TXE_Σ stress states, only the corresponding meridian planes are reported in Fig. 2.15, for the sake of compactness. As a quantitative indication and referring to the TXE_Σ case, for $p = 0.5\%$ (resp., $p = 0.1\%$) a reduction in the void radius from 1.49 nm (resp., 0.87 nm, $L/B = 70$) to 0.64 nm (resp., 0.37 nm, $L/B = 30$) induces an increase in the strength measure Σ_{eq} of about 16 % (resp., 13 %) for $\zeta = 4$ GPa and of about 43 % (resp., 39 %) for $\zeta = 8$ GPa.

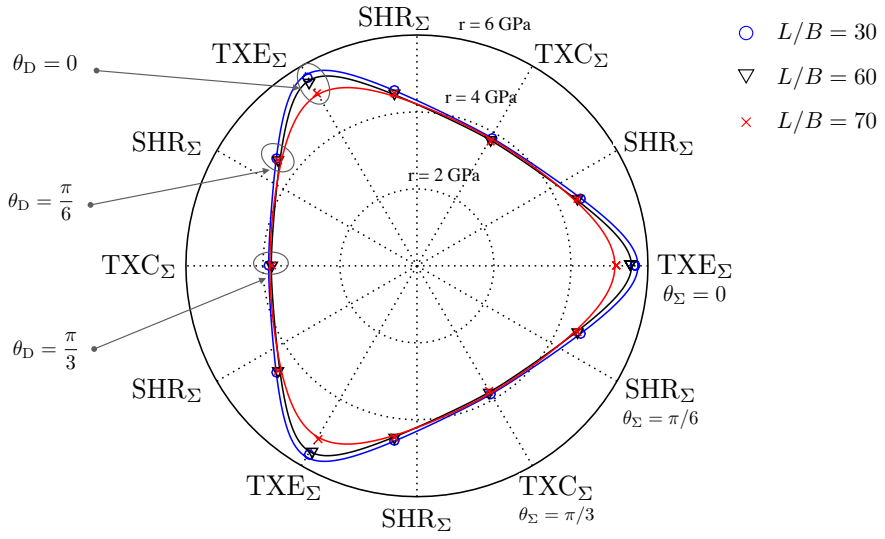

(a)

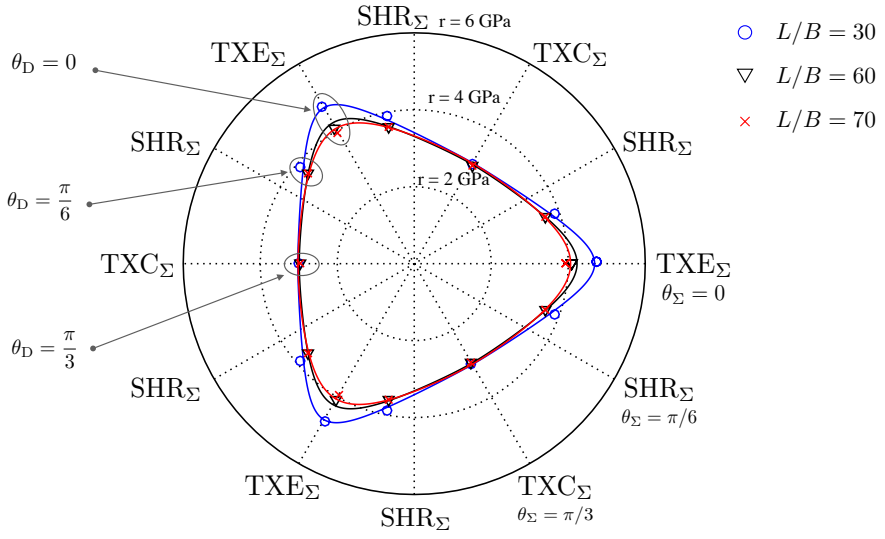

(b)

Figure 2.13 – Nanovoided sample ($p = 0.5\%$). Numerical results (symbols) and estimated deviatoric strength profiles in the π-planes for different values of L/B. (a) $\zeta = 2\,\mathrm{GPa}$. (b) $\zeta = 6\,\mathrm{GPa}$.

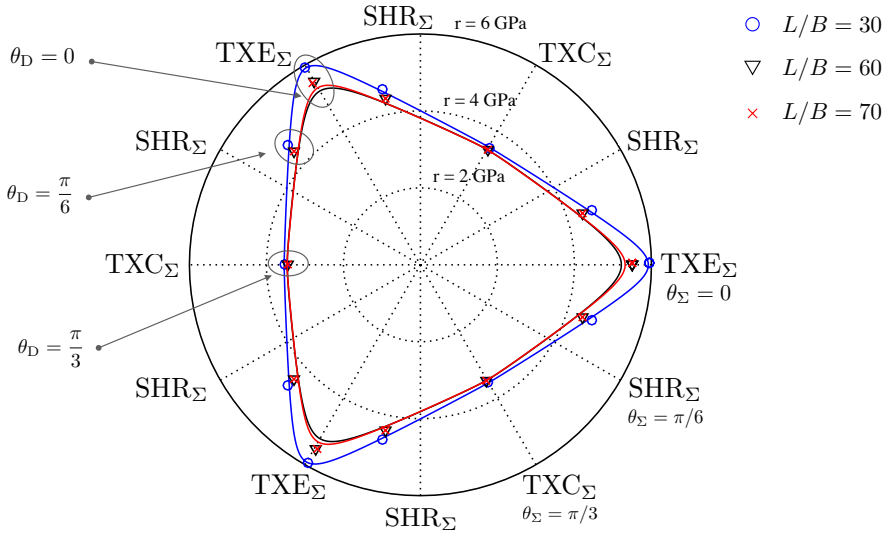

(a)

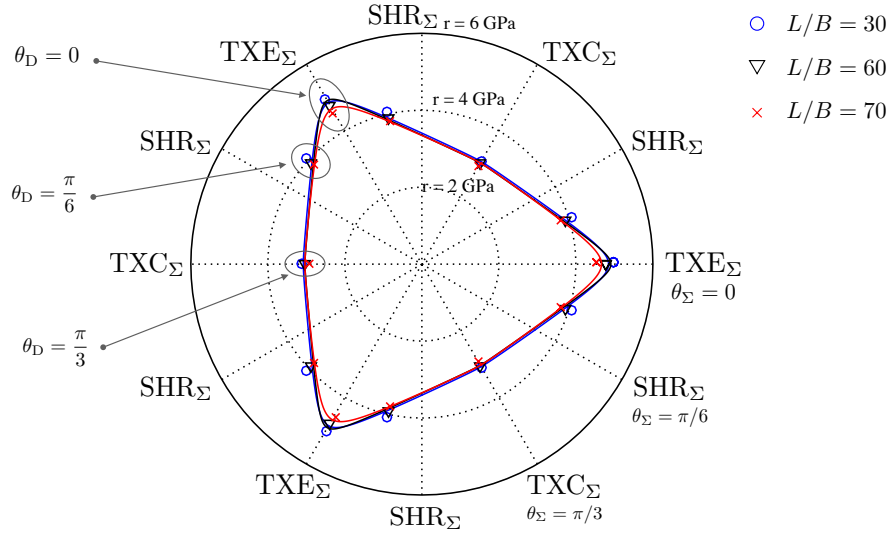

(b)

Figure 2.14 – Nanovoided sample ($p = 0.1\%$). Numerical results (symbols) and estimated deviatoric strength profiles in the π-planes for different values of L/B. (a) $\zeta = 2\,\mathrm{GPa}$. (b) $\zeta = 6\,\mathrm{GPa}$.

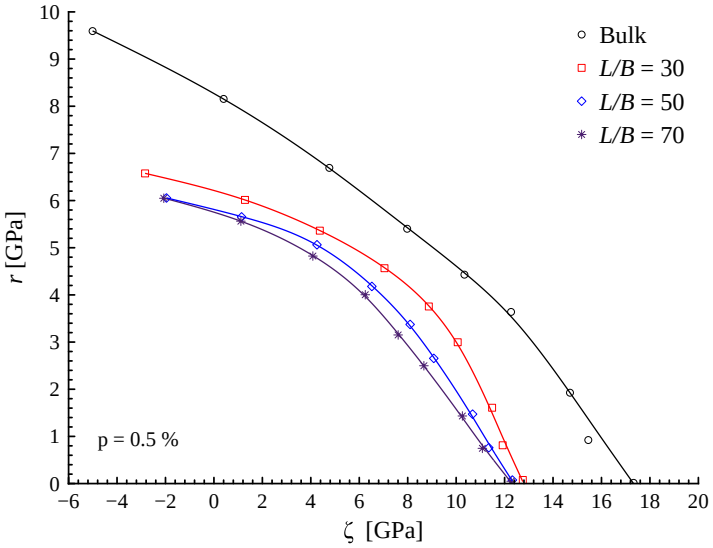

(a)

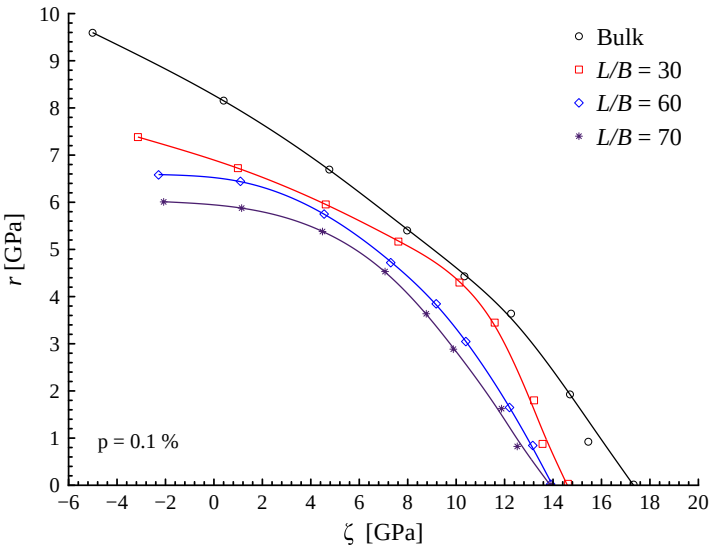

(b)

Figure 2.15 – Nanovoided sample. Numerical results (symbols) and estimated meridian strength profiles for different values of L/B and for a TXE_Σ state ($\theta_\Sigma = 0$). (a) $p = 0.5\%$. (b) $p = 0.1\%$.

2.5 Conclusions

In this Chapter, the influence of void-size effects on strength properties of nanoporous materials are focused by numerically-experiencing, via a Molecular Dynamics approach, the mechanical response of a spherically-nanovoided aluminium single crystal. The case of a bulk sample (namely, with a null porosity) is also preliminarily investigated aiming to furnish a comparative benchmark.

Although many MD-based analyses on nanoporous in-silico samples have been recently established, they are usually limited to the study of specific loading cases (uniaxial, volumetric or simple shear tests), mainly focusing on the identification of void-growth mechanisms and dislocation interactions, without providing an effective quantification of void-size effects. In detail, available results are sufficient neither to furnish a three-dimensional description of the corresponding strength domains (since they identify only particular stress limit conditions), nor to establish the influence of void size as depending on the loading state, thereby not allowing for a straight correlation towards the definition of engineering strength measures for nanoporous materials.

Similarly, current experimental evidence, mainly related to simple testing scenarios, does not provide suitable indications on failure mechanisms under multiaxial loading conditions. Therefore, available findings can not be considered useful tools for properly assessing the effectiveness of theoretical descriptions of strength features for nanoporous materials.

With the aim to give novel contributions in this context, more complex scenarios have been herein addressed, involving triaxial strain-based expansion and compression, as well as shear strain conditions. For each case, different triaxiality levels have been considered, describing deformation paths ranging from pure deviatoric states to pure hydrostatic ones. For different porosity levels, strength properties of nanoporous samples have been investigated as a function of the void radius, in order to explore the influence of the void size.

Although available experimental data are not sufficient to provide an effective comparative benchmark, present numerical results have been proven to be fully consistent with findings obtained via other MD-based approaches (Bringa et al., 2010; Marian et al., 2004, 2005; Mi et al., 2011; Ruestes et al., 2013; Tang et al., 2010; Traiviratana et al., 2008; Zhao et al., 2009), in terms of stress-strain relationships, as well as of dominant atomistic mechanisms and irreversible heating occurring in the plastic regime.

For the cases under investigation, estimates of strength domains have been proposed. The classical Haigh-Westergaard representation, expressed by the three isotropic stress invariants, has been employed.

As main aspects, the analysis of meridian and deviatoric strength profiles computed for different porosity values has shown:

- a clear influence of all the three stress invariants;
- a complex relationship between the applied strain states and the obtained strength ones;

- significant void-size effects.

In detail, numerical results have proven that an axisymmetric stress state is obtained when axisymmetric strain conditions are applied to the sample, corresponding to practically-coinciding stress- and strain-based Lode angles. This is not the case when shear numerical tests are performed, resulting in significant differences between applied-strain and computed-stress Lode angles. Such a constitutive response at limit states is in agreement with recent theoretical findings (Lemarchand et al., 2015).

Similar effects have been also observed for the strength profiles in the meridian planes, where non-negligible hydrostatic stress components are obtained when pure deviatoric deformation paths are considered.

Furthermore, numerical results confirmed that a reduction in the void size induces an enhancement of the strength properties. This is qualitatively in agreement with available experimental (Biener et al., 2005, 2006; Hakamada and Mabuchi, 2007) and numerical (e.g., Mi et al., 2011; Traiviratana et al., 2008; Zhao et al., 2009) evidence, although these latter have been obtained by considering different testing conditions, geometries and materials.

Both occurrence and amount of void-size effects have been proven as strongly dependent on the Lode angle, resulting in the highest strengthening for a triaxial expansion, and leading to a shape-transition of deviatoric strength profiles when the void radius is varied.

It is worth pointing out that, in the framework of an ideal periodic nanostructure, the single-crystal and single-voided reference domain herein adopted could be considered as not properly representative of realistic experimental samples. Nevertheless, within the limitations of the present approach, the herein-adopted computational domain enables to limit as much as possible any coupling effect (such as effects associated to: shape of voids, porosity level, polycrystalline domains), allowing to focus on dominant influence of void-size effects only.

As a matter of fact, in a number of nanoporous strength models (e.g., Dormieux and Kondo, 2010, 2013; Goudarzi et al., 2010; Monchiet and Kondo, 2012; Zhang et al., 2010), the influence of the third stress invariant is not accounted for, and solid phase is generally assumed to obey to a von Mises strength criterion (namely, independent also from the first stress invariant). Moreover, as regards the analytical description of void-size effects, it usually requires some model parameters that have to be properly calibrated and physically interpreted. In this context, proposed numerical results, both for bulk and nanoporous cases, clearly indicate a significant dependence of strength states from all the three stress invariants, suggesting the need of improving previously-cited theoretical descriptions. Furthermore, quantitative indications provided by the present approach allow to highlight some mechanical meanings of theoretical model parameters, enabling also to establish their physically-consistent ranges of variation.

Accordingly, present numerical study can be considered as an useful and novel contribution to provide comparative benchmarks for validating and calibrating available theoretical formulations, as well as for drawing novel analytical models towards a compre-

hensive and consistent description of nanoporous materials strength properties. As an example, in order to pave the way to more effective theoretical modelling strategies, able to reproduce available evidence, a richer description of the bulk strength behaviour with respect to the von Mises one (namely, accounting for the influence of all the stress invariants) should be addressed. In this way, an effective description of the influence of the third stress invariant combined with void-size effects would be accounted for in the context of a general plastic behaviour.

2.A Crystallographic background

Notation based on Miller indexes (Hull and Bacon, 2001) is used. As indicated by Marian et al. (2005) and Traiviratana et al. (2008), in the case of a spherical voided FCC-based sample the maximum of the resolved shear stress is reached in planes $\{111\}$ embedding the void and angled by $\pm 45°$ with respect to the sample local axes. Besides, since the energy stored in a dislocation is proportional to the modulus of its Burgers vector, the glide of perfect dislocations characterized by $\mathbf{b} = B < 110 >$ is energetically disfavoured (Hull and Bacon, 2001).

Referring for instance to closed packed planes (111) and $(11\overline{1})$ in Fig.2.16a, let two perfect dislocations $\mathbf{b}_1 = B[101]$ and $\mathbf{b}'_1 = B[01\overline{1}]$ be considered, belonging to the Thompson tetrahedrons HKJY and H'K'JY, respectively. In agreement with energetic arguments discussed by Hull and Bacon (2001), atom in Y, instead of moving directly in K through $\mathbf{b}_1$, moves firstly in the nearby site γ (via $\mathbf{b}_2$) and next in K (via $\mathbf{b}_3$), γ being such that $\overline{Y\gamma} = \overline{\gamma K}$. As a result, the perfect dislocation $\mathbf{b}_1 = B[101]$ dissociates into two Shockley partials in the plane $(11\overline{1})$, according to the following decomposition:

$$\mathbf{b}_1 = \frac{B}{3}[112] + \frac{B}{3}[2\overline{1}1] = \mathbf{b}_2 + \mathbf{b}_3 \tag{2.7}$$

Likewise, the perfect dislocation $\mathbf{b}'_1 = B[01\overline{1}]$ dissociates into Shockley partials $\mathbf{b}'_2$ and $\mathbf{b}'_3$, both belonging to the plane (111):

$$\mathbf{b}'_1 = \frac{B}{3}[11\overline{2}] + \frac{B}{3}[\overline{1}2\overline{1}] = \mathbf{b}'_2 + \mathbf{b}'_3 \tag{2.8}$$

Furthermore, leading partials $\mathbf{b}_3$ and $\mathbf{b}'_3$ modify the local stacking sequence of closed packed planes $\{111\}$ from FCC to HCP. On the contrary, trailing partials $\mathbf{b}_2$ and $\mathbf{b}'_2$ remove the fault, restoring the original FCC lattice. Thereby, Shockley partial dislocations as in Eqs. (2.7) and (2.8) always enclose a stacking fault region, characterized by the presence of HCP sub-arrangements (Hull and Bacon, 2001) (see Fig. 2.16b). Accordingly, the initiation of the plastic deformation can be associated to the HCP occurrence.

As regards the evolution of plastic deformation, it is strictly related to Shockley partials interactions. As a matter of fact, leading partials $\mathbf{b}_3$ and $\mathbf{b}'_3$ interact each other at the intersection of slip planes $(11\overline{1})$ and (111), yielding to a Lomer-Cottrell (LC) dislocation

$$\frac{B}{3}[110] = \frac{B}{3}[2\overline{1}1] + \frac{B}{3}[\overline{1}2\overline{1}] \tag{2.9}$$

that does not belong to a slip plane. As a result, such a LC dislocation is sessile and it acts as a barrier (the so-called Lomer-Cottrell lock (Hull and Bacon, 2001)) for any additional slipping process in planes $(11\overline{1})$ and (111), repulsing the remaining two trailing Shockley partials $\mathbf{b}_2$ and $\mathbf{b}'_2$. Accordingly, material behaviour in plastic regime strictly depends on the evolution of such a locking mechanism.

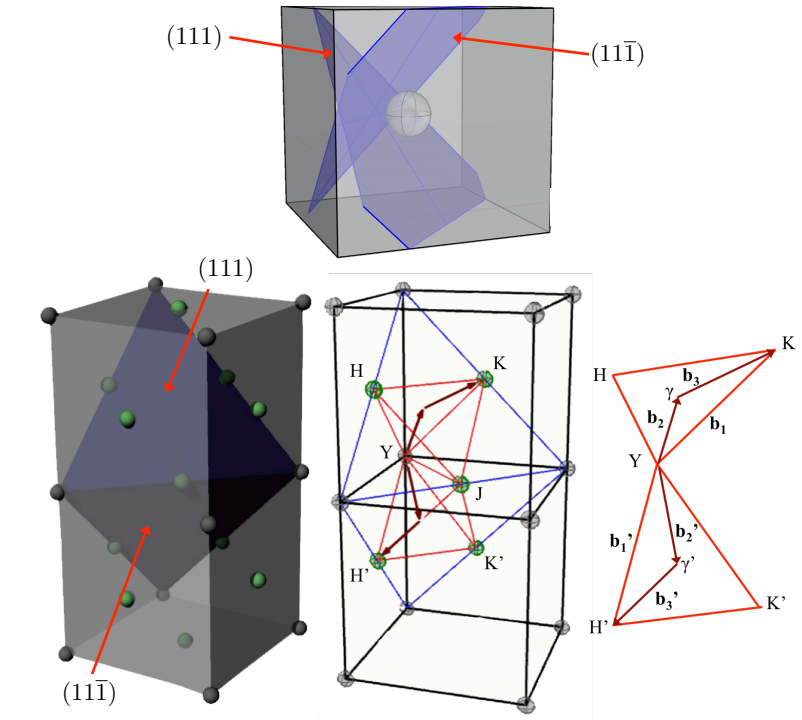

(a)

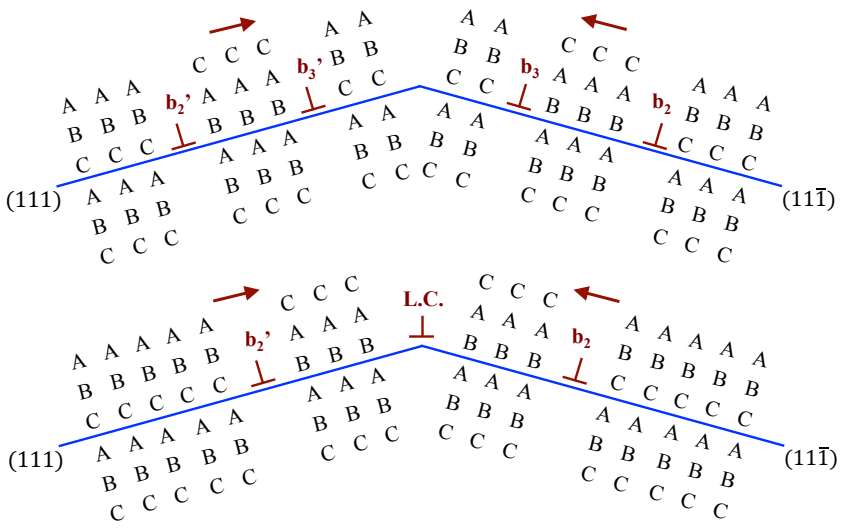

(b)

Figure 2.16 – (a) An example of Shockley-partials nucleation. Perfect dislocations $\mathbf{b}_1$ and $\mathbf{b}_1'$ dissociate into partials, namely leading partials $\mathbf{b}_3$ and $\mathbf{b}_3'$, and trailing partials $\mathbf{b}_2$ and $\mathbf{b}_2'$. (b) Leading partials $\mathbf{b}_3$ and $\mathbf{b}_3'$ modify the local stacking sequence of closed packed planes {111} from FCC (sequence ABC-ABC) into HCP (sequence AB-AB). On the contrary, trailing partials $\mathbf{b}_2$ and $\mathbf{b}_2'$ remove the fault, restoring the original FCC lattice. L.C.: Lomer-Cottrell lock.

References

Allen, M.P., & Tildesley, D.J. (1991). *Computer Simulation of Liquids*. Clarendon Press Oxford.

Amelang, J.S., & Kochmann, D.M. (2015). Surface effects in nanoscale structures investigated by a fully-nonlocal energy-based quasicontinuum method. *Mechanics of Materials*, 90, 166-184.

Arico, A.S., Bruce, P., Scrosati, B., Tarascon, J.M., & Van Schalkwijk, W. (2005). Nanostructured materials for advanced energy conversion and storage devices. *Nature materials*, 4(5), 366-377.

Biener, J., Hodge, A.M., Hamza, A.V., Hsiung, L.M., & Satcher, J.H. (2005). Nanoporous Au: A high yield strength material. *Journal of Applied Physics*, 97, 024301.

Biener, J., Hodge, A.M., Hayes, J.R., Volkert, C.A., Zepeda-Ruiz, L.A., Hamza, A.V., & Abraham, F.F. (2006). Size Effects on the Mechanical Behavior of Nanoporous Au. *Nano Letters*, 6, 2379-2382.

Borg, U., Niordson, C.F., & Kysar, J.W. (2008). Size effects on void growth in single crystals with distributed voids. *International Journal of Plasticity*, 24, 688-701.

Brach, S., Dormieux, L., Kondo, D., & Vairo, G. (2016). A computational insight into void-size effects on strength properties of nanoporous materials. *Mechanics of Materials*, 101, 102-117.

Bringa, E.M., Traiviratana, S., & Meyers, M.A. (2010). Void initiation in fcc metals: Effects of loading orientation and nanocrystalline effects. *Acta Materialia*, 58, 4458-4477.

Daw, M.S., & Baskes, M.I. (1984). Embedded-atom method: derivation and application to impurities, surfaces and other defects in metals. *Physical Review B*, 29, 6443-6453.

Dormieux, L., & Kondo, D. (2010). An extension of Gurson model incorporating interface stress effects. *International Journal of Engineering Science*, 48, 575-581.

Dormieux, L., & Kondo, D. (2013). Non linear homogenization approach of strength of nanoporous materials with interface effects. *International Journal of Engineering Science*, 71, 102-110.

Duan, H.L., Wang, J., Huang, Z.P., & Karihaloo B.L. (2005). Size-dependent effective elastic constants of solids containing nano-inhomogeneities with interface stress. *Journal of the Mechanics and Physics of Solids*, 53, 1574-1596.

Duan, H.L., Wang, J., Huang, Z.P., & Karihaloo, B.L. (2005). Eshelby formalism for nano-inhomogeneities. *Proceedings of the Royal Society A*, 461, 3335-3353.

Farrissey, L., Ludwig, M., McHugh, P.E., & Schmauder, S. (2000). An atomistic study of void growth in single crystalline copper. *Computational Materials Science*, 18, 102-117.

Gologanu, M., Leblond, J.-B., & Devaux, J. (1993). Approximate models for ductile metals containing non-spherical voids in the case of axisymmetric prolate ellipsoidal cavities. *Journal of the Mechanics Physics and Solids*, 41, 1723-1754.

Gologanu, M., Leblond, J.-B., Perrin, G., & Devaux, J. (1994). Approximate models for ductile metals containing non-spherical voids - case of axisymmetric oblate ellipsoidal cavities. *Journal of Engineering Materials and Technology*, 116, 290-297.

Goudarzi, T., Avazmohammadi, R., & Naghdabadi, R. (2010). Surface energy effects on the yield strength of nanoporous materials containing nanoscale cylindrical voids. *Mechanics of Materials*, 42, 852-862.

Gurson, A.L. (1977). Continuum theory of ductile rupture by void nucleation and growth: Part I. - Yield criterion and flow rules for porous ductile media. *Journal of Engineering Materials and Technology*, 99, 2-15.

Gurtin, M.E., & Murdoch, A.I. (1975). Continuum theory of elastic material surfaces. *Archive for Rational Mechanics and Analysis*, 57, 291-323.

Hakamada, M., & Mabuchi, M. (2007). Mechanical strength of nanoporous gold fabricated by dealloying. *Scripta Materalia*, 56, 1003-1006.

Hashin, Z. (1962). The elastic moduli of heterogeneous materials. *Journal of Applied Mechanics*, 29, 143-150.

Higginbotham, A., Bringa, E.M., Marian, J., Park, N., Suggit, M., & Wark, J.S. (2011). Simulations of copper single crystals subjected to rapid shear. *Journal of Applied Physics*, 109, 063530.

Hill, R. (1948). A theory of the yielding and plastic flow of anisotropic metals. *In Proceedings of the Royal Society of London A: Mathematical, Physical and Engineering Sciences*, 193, 281-297.

Honeycutt, J.D., & Andemen, H.C. (1987). Molecular Dynamics Study of Melting and Freezing of Small Lennard-Jones Clusters. *The Journal of Physical Chemistry*, 91, 4950-4963.

Horstemeyer, M.F., Baskes, M.I., & Plimpton, S.J. (2001). Length scale and time scale effects on the plastic flow of FCC metals. *Acta Materalia*, 49, 4363-4374.

Huang, M., Li, Z., & Wang, C. (2005). Coupling effects of void size and void shape on the growth of prolate ellipsoidal microvoid. *Acta Mechanica Sinica*, 21, 272-277.

Hull, D., & Bacon, D.J. (2001). *Introduction to Dislocations*. Butterworth-Heinemann.

Jenkins, S.B. (2010). *Nanoporous Materials: Types, Properties, and Uses*. Nova Science Publishers.

Kelchner, C.L., Plimpton, S.J., & Hamilton, J.C. (1998). Dislocation nucleation and defect structure during surface indentation. *Physical Review B*, 58, 11085.

Khan, A.S., & Huang, S., (1995). *Continuum Theory of Plasticity*. John Wiley & Sons, New York.

Li, Z., & Huang, M. (2005). Combined effects of void shape and void size-oblate spheroidal microvoid embedded in infinite non-linear solid. *International Journal of Plasticity*, 21, 625-650.

Leblond, J.-B., Perrin, G., & Suquet, P. (1994). Exact results and approximate models for porous viscoplastic solids. *International Journal of Plasticity*, 10, 213-235.

Lemarchand, E., Dormieux, L., & Kondo, D. (2015). Lode's angle effect on the definition of the strength criterion of porous media. *International Journal for Numerical and Analytical Methods in Geomechanics*, 39(14), 1506-1526.

Levenberg, K. (1944). A Method for the Solution of Certain Problems in Least-Squares. *Quarterly of Applied Mathematics*, 2, 164-168.

Lu, G.Q., Zhao, X.S., & Wei, T.K. (2004). *Nanoporous materials: science and engineering*. Imperial College Press.

Lubarda, V.A. (2011). Emission of dislocations from nanovoids under combined loading. *International Journal of Plasticity*, 27, 181-200.

Lubarda, V.A., Schneider, M.S., Kalantar, D.H., Remington, B.A., & Meyers, M.A. (2004). Void growth by dislocation emission. *Acta Materialia*, 52, 1397-1408.

Lubliner, J. (2008). *Plasticity Theory*. Dover Publications Inc., Mineola, New York.

Marian, J., Knap, J., & Ortiz, M. (2004). Nanovoid Cavitation by Dislocation Emission in Aluminum. *Physical Review*, 93.

Marian, J., Knap, J., & Ortiz, M. (2005). Nanovoid deformation in aluminum under simple shear. *Acta Materialia*, 53, 2893-2900.

Marquardt, D. (1963). An Algorithm for Least-Squares Estimation of Nonlinear Parameters. *SIAM Journal on Applied Mathematics*, 11, 431-441.

Menetrey, P.H., & Willam, K.J. (1995). Triaxial Failure Criterion for Concrete and Its Generalization. *ACI Structural Journal*, 92, 311-318.

Mi, C., Buttry, D.A., Sharma, P., & Kouris, D.A. (2011). Atomistic insights into dislocation-based mechanisms of void growth and coalescence. *Journal of the Mechanics and Physics of Solids*, 59, 1858-1871.

Michel, J.C., & Suquet, P. (1992). The constitutive law of nonlinear viscous and porous materials. *Journal of the Mechanics and Physics of Solids*, 40(4), 783-812.

Mishin, Y., Farkas, D., Mehl, M.J., & Papaconstantopoulos D.A. (1999). Interatomic potentials for monoatomic metals from experimental data and ab initio calculations. *Physical Review B*, 59, 3393.

Monchiet, V., Cazacu, O., Charkaluk, E., & Kondo, D. (2008). Macroscopic yield criteria for plastic anisotropic materials containing spheroidal voids. *International Journal of Plasticity*, 24, 1158-1189.

Monchiet, V., & Kondo, D. (2012). Exact solution of a plastic hollow sphere with a Mises–Schleicher matrix. *International Journal of Engineering Science*, 51, 168-178.

Monchiet, V., & Kondo, D. (2013). Combined voids size and shape effects on the macroscopic criterion of ductile nanoporous materials. *International Journal of Plasticity*, 43, 20-41.

Moshtaghin, A.F., Naghdabadi, R., & Asghari, M. (2012). Effects of surface residual stress and surface elasticity on the overall yield surfaces of nanoporous materials with cylindrical nanovoids. *Mechanics of Materials*, 51, 74-87.

Needs, R.J., Godfrey, M.J., & Mansfield, M. (1991). Theory of surface stress and surface reconstruction. *Surface Science*, 242, 215-221.

Oliveira, B.F., da Cunda, L.A., Öchsner, A., & Creus, G.J. (2010). Computational Analysis of Loading–Unloading and Non-homogeneity Effects in Metallic Hollow Sphere Structures. *In Materials with Complex Behaviour*, 83-97.

Plimpton, S.J. (1995). Fast parallel algorithms for short-range molecular dynamics. *Journal of Computational Physics*, 117, 1-19.

Pogorelko, V.V., & Mayer, A.E. (2016). Influence of titanium and magnesium nanoinclusions on the strength of aluminum at high-rate tension: Molecular dynamics simulations. *Materials Science and Engineering: A*, 662, 227-240.

Ponte Castaneda, P. (1991). The effective mechanical properties of nonlinear isotropic composites. *Journal of the Mechanics and Physics of Solids*, 39, 45-71.

Rittel, D., Ravichandran, G., & Venkert, A. (2006). The mechanical response of pure iron at high strain rates under dominant shear. *Materials Science and Engineering: A*, 432, 191-201.

Ruestes, C.J., Bringa, E.M., Stukowski, A., Rodriguez Nieva, J.F., Bertolino, G., Tang, Y., & Meyers, M.A. (2013). Atomistic simulation of the mechanical response of a nanoporous body-centered cubic metal. *Scripta Materialia*, 68, 817-820.

Seppala, E.T., Belak, J., & Rudd, R.E. (2004). Effect of stress triaxiality on void growth in dynamic fracture of metals: A molecular dynamics study. *Physical Review B*, 69, 134101.

Shabib, I., & Miller, R.E. (2009). Deformation characteristics and stress-strain response of nanotwinned copper via molecular dynamics simulation. *Acta Materialia*, 57, 4364-4373.

Stukowski, A. (2010). Visualization and analysis of atomistic simulation data with OVITO-the Open Visualization Tool. *Modelling and Simulation in Materials Science and Engineering*, 18, 015012.

Stukowski, A. (2012). Structure identification methods for atomistic simulations of crystalline materials. *Modelling and Simulation in Materials Science and Engineering*, 20, 4.

Subramaniyan, A.K., & Sun, C. (2008). Continuum interpretation of virial stress in molecular simulations. *International Journal of Solids and Structures*, 45, 4340-4346.

Tang, T., Kim S., & Horstemeyer, M.F. (2010). Molecular dynamics simulations of void growth and coalescence in single crystal magnesium. *Acta Materalia*, 58, 4742-4759.

Traiviratana, S., Bringa, E.M., Benson, D.J., & Meyers, M.A. (2008). Void growth in metals: Atomistic calculations. *Acta Materalia*, 56, 3874-3886.

Tvergaard, V., & Needleman, A. (1984). Analysis of the cup-cone fracture in a round tensile bar. *Acta metallurgica*, 32, 157-169.

Verlet, L. (1967). Computer "Experiments" on Classical Fluids. I. Thermodynamical Properties of Lennard-Jones Molecules. *Physical Review*, 159, 98.

Zhao, K.J., Chen, C.Q., Shen, Y.P., & Lu, T.J. (2009). Molecular dynamics study on the nano-void growth in face-centered cubic single crystal copper. *Computational Materials Science*, 46, 749-754.

Zhang, W., & Wang, T.J. (2007). Effect of surface energy on the yield strength of nanoporous materials. *Applied Physics Letters*, 90, 063104.

Zhang, W., Wang, T.J., & Chen, X. (2010). Effect of surface/interface stress on the plastic deformation of nanoporous materials and nanocomposites. *International Journal of Plasticity*, 26, 957-975.

CHAPTER 3

Nanoporous materials with a general isotropic plastic matrix: Exact limit state under isotropic loadings

Abstract

In this Chapter, hydrostatic strength properties of nanoporous materials are investigated by addressing the limit state of a hollow sphere undergoing isotropic loading conditions. Void-size effects are modelled by treating the cavity boundary as a coherent-imperfect homogeneous interface. The hollow sphere is assumed to be comprised of a rigid-ideal-plastic material obeying to a general isotropic yield criterion. The latter is defined by considering a simplified form of the yield function proposed by Bigoni and Piccolroaz in [Int J Solids Struct; 41: 2855–2878], resulting able to account for a broad class of pressure-sensitive materials whose plastic response is also affected by the stress Lode angle. The corresponding support function is consistently derived and discussed. The exact solution of the limit-state problem is fully determined, providing a closed-form description of stress, strain-rate and velocity fields, as well as the macroscopic hydrostatic strength of nanoporous media. Proposed approach allows to consistently generalise available analytical solutions for porous and nanoporous materials, by accounting for a general plastic response of the solid matrix and for void-size effects. Finally, present exact solution, as well as the identification of the support function for the adopted general strength criterion, open towards novel kinematic limit-analysis approaches for describing macroscale strength properties of nanoporous materials under arbitrary triaxial loadings.

Present Chapter corresponds to the published research paper (Brach et al., 2016c) [Int J Plasticity; DOI: 10.1016/j.ijplas.2016.10.007 (2016)].
A self-consistent notation is adopted.

Keywords: Nanoporous materials, strength properties, hollow-sphere model, general isotropic plastic matrix, support function, void-size effects.

3.1 Introduction

In the last two decades nanoporous materials have been characterised by a fast-growing development, attracting a world-wide interest in both industrial and academic domains (e.g., Arico et al., 2005; Jenkins, 2010; Lu et al., 2004). As a matter of fact, owing to their good properties in terms of stiffness and strength, combined with particular and special electrochemical features, nanoporous materials open towards groundbreaking applications in several technical fields, involving ultra-high performance devices and challenging multifunctional uses. In order to fulfil these promising applications, one of the most fundamental aspects consists in describing, into an effective engineering design framework, strength properties of these materials as dependent on the size of voids.

Recent nano-mechanical experiments (e.g., Biener et al., 2005, 2006; Hakamada and Mabuchi, 2007) have shown that, for a fixed porosity value, a reduction in the length-scale of nanovoids induces an increase in the material yield strength. Similarly, Molecular-Dynamics simulations carried out on in-silico nanoporous samples (Brach et al., 2016a; Mi et al., 2011; Traiviratana et al., 2008; Zhao et al., 2009) have proven that the predicted strength decreases towards asymptotic values when the size of voids increases. The physical origin of such a phenomenon has been related by Needs et al. (1991) to the presence of self-equilibrated surface stresses at the cavity boundaries, induced by a local perturbation in the material atomic arrangement close to the nanovoids and usually negligible for porous materials. Accordingly, in the framework of a continuum approach, void-size effects have been generally addressed by introducing coherent-imperfect interface laws at the cavity boundaries (e.g., Duan et al., 2005a,b; Gurtin and Murdoch, 1975, 1978; Povstenko and Yu, 1993; Wang et al., 2011), that is accounting for surface stresses by prescribing the discontinuity of the stress vector across the interface.

Although the effective elastic properties of nanoporous/nanocomposite materials have been extensively investigated in literature (e.g., Duan et al., 2005a,b; Le Quang and He, 2007), few attention has been paid so far to the influence of void-size effects on the material response in the ductile regime. As a matter of fact, available strength models for porous materials (e.g., Gurson, 1977; Ponte Castañeda, 1991) are able to account for porosity effects only (although recent advanced formulations and applications include also effects related to matrix anisotropy, void shape, voids distribution and interaction (e.g., Fritzen et al., 2012; Shen et al., 2012; Zhai et al., 2016)), thereby resulting in void-size independent plastic behaviours.

Taking advantage of a plastic generalization of interface stress models (Monchiet and Bonnet, 2010), and as a result of a limit-analysis approach (Salençon, 1983) on a rigid-ideal-plastic hollow sphere with a nanosized void, Dormieux and Kondo (2010) extended to nanoporous materials the well-established criterion proposed by Gurson (1977). Furthermore, void-size dependent yield criteria have been recently proposed by Goudarzi et al. (2010), Moshtaghin et al. (2012), Zhang and Wang (2007), Zhang et al. (2008) and Zhang et al. (2010), in the framework of non-linear homogenization methods including also interface effects.

As regards limit-analysis approaches, the capability of furnishing an effective estimate

of the macroscopic yield domain for porous and nanoporous materials requires a suitable choice of static or kinematic trial fields. As a matter of fact, following the technique adopted by Gurson (1977), and referring to a rigid-ideal-plastic matrix, strength estimates have been obtained in the framework of a kinematic approach (e.g., Anoukou et al., 2016; Cazacu et al., 2014; Dormieux and Kondo, 2010) by building up the trial field via the superposition of suitable terms to the exact velocity field associated to the limit problem of a hollow sphere under a radial constant velocity at the external boundary (i.e., under isotropic boundary conditions, corresponding to a macroscopic hydrostatic state). Accordingly, the identification of the exact local fields at the limit state (namely, velocity, strain-rate and stress fields) for a hollow sphere undergoing isotropic loadings is recognized to be of the utmost importance for establishing effective strength estimates for porous and nanoporous materials under general triaxial states.

It is worth observing that most of the afore-mentioned strength models have been derived by assuming that the solid matrix obeys to a von Mises yield criterion, thereby not accounting either for hydrostatic-stress dependence or for stress-Lode-angle effects (the latter being related to the third deviatoric stress invariant). Nevertheless, the solid matrix of engineering-relevant nanoporous materials may exhibit a more complex plastic behaviour. For instance, the ductile regime of bulk metals (namely, without nanovoids) may be characterised (as for geomaterials or cohesive-frictional media) by a pressure-sensitive plastic response, also significantly affected by the second and the third deviatoric stress invariants. This evidence has been confirmed by recent Molecular-Dynamics simulations (Brach et al., 2016a), which also showed that the dependence of the bulk-material strength domain on all the three isotropic stress invariants can not be generally accounted for by simply calibrating available classical yield criteria (e.g., Mohr-Coulomb), and that, in turn, this induces a complex plastic response of nanovoided samples.

An attempt to include the influence of all the three isotropic stress invariants for describing strength properties of porous media (i.e., without interface effects) has been recently provided by Anoukou et al. (2016), in the special case of a Mohr-Coulomb plastic matrix.

To this end, Anoukou et al. (2016) have adopted a limit-analysis procedure by considering a trial velocity field defined on the basis of the exact solution proposed by Thoré et al. (2009) for a Mohr-Coulomb hollow-sphere model without interface effects and undergoing isotropic loading conditions. Nevertheless, aiming to reproduce available evidence, a richer description of the local yield behaviour that accounts for the influence of all the stress invariants has to be addressed. In this light, the general and flexible yield criterion proposed by Bigoni and Piccolroaz (2004) can be considered as a promising candidate to comply with benchmarking indications on local strength properties, allowing to effectively describe the limit behaviour of a broad class of pressure-sensitive, frictional, ductile and cohesive bulk materials.

Therefore, in order to pave the way to more comprehensive limit-analysis modelling strategies for nanoporous materials, the starting point is represented by the identification of the exact local fields under a macroscopic hydrostatic state, accounting for void-size

effects and in the case of a general local plastic behaviour. The latter, in the framework of kinematic approaches, has to be formulated via the local support function, that is via the maximum material plastic dissipation.

This Chapter aims to contribute to these aspects by proposing the exact solution of the mechanical local fields at the limit state for a hollow sphere with a nanosized void, treated via a coherent-imperfect interface, and in the case of isotropic boundary loading conditions. Accordingly, a closed-form description of the macroscopic hydrostatic limit stress for nanoporous materials is also provided. The solid matrix is assumed to be comprised of a rigid-ideal-plastic material, obeying to a simplified form of the criterion proposed by Bigoni and Piccolroaz (2004), expressed in terms of the three isotropic stress invariants. In detail, the adopted yield function is described as linear in meridian planes, and as proposed by Bigoni and Piccolroaz (2004) in the deviatoric ones.

The Chapter is organised as follows. In Section 3.2, the problem under stake is formulated by accounting for interface effects. Section 3.3 is devoted to the introduction of the Bigoni-like yield function, carefully focusing on the possible occurrence of sharp vertices in the deviatoric plane. In order to allow for kinematic limit analyses based on such a general criterion, the corresponding support function is consistently derived in Section 3.4. The limit state of a hollow sphere with or without interface effects and undergoing isotropic boundary conditions is exactly determined in Section 3.5. By choosing suitable values of criterion parameters, exact analytical descriptions are also obtained in the particular case of local plastic behaviours described via classical yield functions (von Mises, Tresca, Drucker-Prager, Mohr-Coulomb). The usefulness of obtained results to build up trial fields for novel limit analysis approaches, addressing both porous and nanoporous materials, is highlighted in Section 3.6. Finally, some conclusions are traced in Section 3.7.

3.2 Problem statement

Let the hollow sphere in Fig. 3.1 be considered, whose internal and external radii are denoted as R_i and R_e, respectively. Moreover, let $\partial\Omega_\mathrm{i}$ and $\partial\Omega_\mathrm{e}$ be the corresponding internal and external surfaces, the total boundary of the system resulting in $\partial\Omega = \partial\Omega_\mathrm{i} \cup \partial\Omega_\mathrm{e}$. Denoting as $|\Omega_\mathrm{s}|$ and $|\Omega_\mathrm{v}|$ the volume measures of the solid region (namely, Ω_s) and of the spherical void (Ω_v), respectively, the total volume of the system (namely, $\Omega = \Omega_\mathrm{s} \cup \Omega_\mathrm{v}$) is $|\Omega| = |\Omega_\mathrm{s}| + |\Omega_\mathrm{v}|$, and the porosity f is equal to $f = |\Omega_\mathrm{v}|/|\Omega|$. The solid matrix Ω_s is assumed to be homogeneous and comprised of a rigid-ideal-plastic isotropic material. Therefore, material strength properties can be straight identified by referring to the yield limit state.

In agreement with continuum-based descriptions (Duan et al., 2005a; Gurtin and Murdoch, 1975, 1978; Wang et al., 2011) and available strength models for nanoporous materials (e.g., Dormieux and Kondo, 2010), the influence of non-negligible surface stresses induced by the possibly-nanosized void is herein addressed by introducing a coherent and imperfect homogeneous interface $\mathcal{I}$ at the void boundary $\partial\Omega_\mathrm{i}$ (Fig. 3.1). In particular, the velocity field (resp., the stress vector) is prescribed to be continuous (resp., discontinuous)

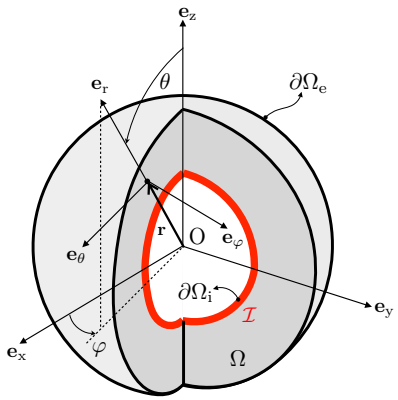

Figure 3.1 – Problem statement. Notation.

through $\partial\Omega_\mathrm{i}$. In the framework of a plastic generalization (Monchiet and Bonnet, 2010) of the stress-interface model by Gurtin and Murdoch (1975), the material comprising the interface is assumed to be isotropic and rigid-ideal-plastic.

Let the Cartesian reference system $(\mathbf{e}_\mathrm{x}, \mathbf{e}_\mathrm{y}, \mathbf{e}_\mathrm{z})$ be introduced, with the origin O at the sphere center. For what follows, and referring to the notation in Fig. 3.1, it is useful to consider the spherical coordinate system (θ, φ, r), and the corresponding local orthonormal basis $(\mathbf{e}_\theta, \mathbf{e}_\varphi, \mathbf{e}_\mathrm{r})$, r being the radial coordinate, $\theta \in [0, \pi]$ and $\varphi \in [0, 2\pi]$ the zenith and the azimuth angular coordinates, respectively. Accordingly, the position with respect to O of a point in Ω (resp., at the interface $\mathcal{I}$) is identified by $\mathbf{r} = r\,\mathbf{e}_\mathrm{r}(\theta, \varphi)$ (resp., by $\mathbf{r}_\mathrm{i} = R_\mathrm{i}\,\mathbf{e}_\mathrm{r}(\theta, \varphi)$).

As a notation rule, vectors and second-order tensors are denoted by bold letters; symbols $\cdot$, $:$, and $\otimes$ indicate inner, double-dot, and tensor product operators, respectively; ∇ (resp., $\nabla^{\mathcal{I}}$) is the nabla operator in Ω_s (resp., along the interface), $\widetilde{\nabla}$ identifying the symmetric part of the corresponding gradient operator.

Let the fourth-order projector tensor $\mathbb{T} = \mathbf{P}\underline{\otimes}\mathbf{P}$ be introduced, where $\mathbf{P} = (\mathbf{1} - \mathbf{e}_\mathrm{r} \otimes \mathbf{e}_\mathrm{r})$ with $\mathbf{1}$ the second-order identity tensor, and where the operator $\underline{\otimes}$ is component-wise defined by $\mathbb{T}_{ijkl} = (P_{ik}P_{jl} + P_{il}P_{jk})/2$. Accordingly, $\mathbf{A}_\mathbb{T} = \mathbb{T} : \mathbf{A}$ is the projection on planes orthogonal to $\mathbf{e}_\mathrm{r}$ of the second-order tensor $\mathbf{A}$. In the following, $\mathbf{A}$ is referred to as a planar tensor if $\mathbf{A} = \mathbf{A}_\mathbb{T}$.

The hollow sphere is assumed to undergo isotropic loading conditions at the exterior boundary, corresponding to a macroscopic hydrostatic stress state. Therefore, the set

$$\mathcal{BC}_\sigma = \left\{\boldsymbol{\sigma}(\mathbf{r}) \quad \text{s.t.} \quad \boldsymbol{\sigma}^- \cdot \mathbf{e}_\mathrm{r} = \mathbf{0} \quad \text{on } \partial\Omega_\mathrm{i} \quad \text{and} \quad \boldsymbol{\sigma} \cdot \mathbf{e}_\mathrm{r} = \Sigma_\mathrm{m}^\mathrm{c}\mathbf{e}_\mathrm{r} \quad \text{on } \partial\Omega_\mathrm{e}\right\} \tag{3.1}$$

is introduced, where $\Sigma_\mathrm{m}^\mathrm{c}$ is the unknown macroscopic hydrostatic strength, $\boldsymbol{\sigma}^-$ (resp., $\boldsymbol{\sigma}^+$) is the second-order stress tensor $\boldsymbol{\sigma}$ for $r \to R_\mathrm{i}^-$ (resp., $r \to R_\mathrm{i}^+$), so that $(\boldsymbol{\sigma}^+ - \boldsymbol{\sigma}^-)$ allows to describe the stress jump across the interface.

The sets of statically-admissible ($\mathcal{S}_\sigma$) and plastically-admissible ($\mathcal{P}_\sigma$) stress fields are

respectively introduced as

$$\mathcal{S}_\sigma = \left\{ (\boldsymbol{\sigma},\boldsymbol{\tau}) \quad \text{s.t.} \quad \begin{array}{l} \nabla\cdot\boldsymbol{\sigma} = \mathbf{0} \text{ in } \Omega_\mathrm{s}\,, \\ (\boldsymbol{\sigma}^+ - \boldsymbol{\sigma}^-)\cdot\mathbf{e}_\mathrm{r} + (\boldsymbol{\tau} : \mathbf{K})\mathbf{e}_\mathrm{r} = \nabla^{\mathcal{I}}\cdot\boldsymbol{\tau} \quad \text{on } \partial\Omega_\mathrm{i}\,, \\ \text{with} \quad \boldsymbol{\sigma} \in \mathcal{BC}_\sigma \end{array} \right\} \tag{3.2a}$$

$$\mathcal{P}_\sigma = \left\{ (\boldsymbol{\sigma},\boldsymbol{\tau}) \quad \text{s.t.} \quad \mathcal{G}^\mathrm{s}(\boldsymbol{\sigma}) = 0 \text{ in } \Omega_\mathrm{s}\,, \qquad \mathcal{G}^{\mathcal{I}}(\boldsymbol{\tau}) = 0 \text{ on } \partial\Omega_\mathrm{i} \right\} \tag{3.2b}$$

where $\boldsymbol{\tau}$ is the surface stress tensor at $\mathcal{I}$, $\mathbf{K}$ is the interface curvature tensor, $\mathcal{G}^\mathrm{s}$ (resp., $\mathcal{G}^{\mathcal{I}}$) indicates the yield function of the solid matrix (resp., of the interface). It is worth pointing out that the set $\mathcal{S}_\sigma$ is defined in the absence of body forces and that the equilibrium at $\mathcal{I}$ (see Eq. (3.2a)) is expressed by a generalized form of the Young-Laplace equation (Gurtin and Murdoch, 1975; Duan et al., 2005b). Moreover, prescribing that $(\boldsymbol{\sigma},\boldsymbol{\tau}) \in \mathcal{P}_\sigma$ is equivalent to prescribe that the material is everywhere yielding in Ω.

The sets of kinematically-admissible ($\mathcal{K}_d$) and plastically-admissible ($\mathcal{P}_d$) strain-rate fields are introduced as:

$$\mathcal{K}_d = \left\{ (\mathbf{d},\mathbf{d}^{\mathcal{I}}) \quad \text{s.t.} \quad \mathbf{d} = \widetilde{\nabla}\mathbf{v} \text{ in } \Omega_\mathrm{s}\,, \quad \mathbf{d}^{\mathcal{I}} = \mathbf{d}\big|_{\mathbf{r}=\mathbf{r}_\mathrm{i}} \text{ on } \partial\Omega_\mathrm{i} \right\} \tag{3.3a}$$

$$\mathcal{P}_d = \left\{ (\mathbf{d},\mathbf{d}^{\mathcal{I}}) \quad \text{s.t.} \quad \mathbf{d} = \lambda^\mathrm{s}\,\frac{\partial\mathcal{G}^\mathrm{s}(\boldsymbol{\sigma})}{\partial\boldsymbol{\sigma}} \text{ in } \Omega_\mathrm{s}\,, \quad \mathbf{d}^{\mathcal{I}} = \lambda^{\mathcal{I}}\,\frac{\partial\mathcal{G}^{\mathcal{I}}(\boldsymbol{\tau})}{\partial\boldsymbol{\tau}} \text{ on } \partial\Omega_\mathrm{i} \right\} \tag{3.3b}$$

with $\mathbf{d}$ (resp., $\mathbf{d}^{\mathcal{I}}$) denoting the microscopic second-order strain-rate tensor in Ω_s (resp., on $\partial\Omega_\mathrm{i}$), and where λ^s and $\lambda^{\mathcal{I}}$ are the positive plastic multipliers. It is worth observing that prescribing $(\mathbf{d},\mathbf{d}^{\mathcal{I}}) \in \mathcal{P}_\mathrm{d}$ is equivalent to prescribe that the associated normality rule is everywhere satisfied in Ω.

Owing to the spherical symmetry of both boundary conditions and geometry, the mechanical behaviour governed by Eqs. (3.2) and (3.3) does not depend on the angular coordinates θ and φ. Thereby, the local velocity reads as $\mathbf{v}(r) = v_\mathrm{r}(r)\mathbf{e}_\mathrm{r}$, and the local stress $(\boldsymbol{\sigma}(r),\boldsymbol{\tau})$ and strain-rate $(\mathbf{d}(r),\mathbf{d}^{\mathcal{I}})$ fields have to belong to $(\mathcal{Q},\mathcal{Q})$, where $\mathcal{Q}$ is the space of axisymmetric second-order tensors defined as

$$\mathcal{Q} = \{\, \mathbf{Q} \quad \text{s.t.} \quad \mathbf{Q} = Q_\mathrm{r}\mathbf{e}_\mathrm{r}\otimes\mathbf{e}_\mathrm{r} + Q_\theta(\mathbf{e}_\theta\otimes\mathbf{e}_\theta + \mathbf{e}_\varphi\otimes\mathbf{e}_\varphi)\,\} \tag{3.4}$$

Accordingly, the exact solution of the limit-state problem for the hollow sphere with interface is completely identified by statically-admissible stress $(\boldsymbol{\sigma},\boldsymbol{\tau}) \in (\mathcal{S}_\sigma \cap (\mathcal{Q},\mathcal{Q}))$ and kinematically-admissible strain-rate $(\mathbf{d},\mathbf{d}^{\mathcal{I}}) \in (\mathcal{K}_\mathrm{d} \cap (\mathcal{Q},\mathcal{Q}))$ fields that simultaneously verify plastic admissibility conditions introduced in sets $\mathcal{P}_\sigma$ and $\mathcal{P}_\mathrm{d}$, respectively.

3.3 Local yield function

Since the isotropy assumption on strength properties, the yield surface $\partial\mathcal{Y}^\mathrm{s} = \{\boldsymbol{\sigma} \text{ s.t. } \mathcal{G}^\mathrm{s}(\boldsymbol{\sigma}) = 0\}$ of the material comprising the hollow sphere can be completely described by referring to the Lode coordinate system (p, q, θ_σ). As a matter of fact, denoting with $\theta_\sigma \in [0, \pi/3]$ the stress Lode angle, a local limit stress state $\boldsymbol{\sigma} \in \partial\mathcal{Y}^\mathrm{s}$ is uniquely determined by the

following isotropic stress invariants

$$p = \frac{I_1^\sigma}{3}, \qquad q = \sqrt{3J_2^\sigma}, \qquad \cos 3\theta_\sigma = \frac{3\sqrt{3}}{2}\frac{J_3^\sigma}{J_2^{\sigma\,3/2}} \tag{3.5}$$

where $I_1^\sigma = \operatorname{tr}\boldsymbol{\sigma}$, $J_2^\sigma = \operatorname{tr}\boldsymbol{\sigma}_\mathrm{d}^2/2$ and $J_3^\sigma = \operatorname{tr}\boldsymbol{\sigma}_\mathrm{d}^3/3$ are the hydrostatic, the second-order deviatoric and the third-order deviatoric stress invariants, respectively, with $\boldsymbol{\sigma}_\mathrm{d} = \boldsymbol{\sigma} - p\mathbf{1}$ being the deviatoric stress tensor. The Lode coordinate system (p, q, θ_σ) represents a cylindrical system in the space of the principal stresses $(\sigma_1, \sigma_2, \sigma_3)$, p and q being respectively proportional to the magnitudes of the orthogonal projections of the stress tensor $\boldsymbol{\sigma}$ on the hydrostatic axis $q = 0$ (namely, $I_1^\sigma/\sqrt{3}$) and on the deviatoric plane (or π-plane) $p = \text{const}$ (namely, $\sqrt{2J_2^\sigma}$). Therefore, the three-dimensional shape of the yield surface $\mathcal{G}^\mathrm{s} = 0$ can be represented by means of its cross sections (that is, the intersections between $\partial\mathcal{Y}^\mathrm{s}$ and the deviatoric planes) and its meridian profiles (that is, the intersections between $\partial\mathcal{Y}^\mathrm{s}$ and planes at $\theta_\sigma = \text{const}$ containing the hydrostatic axis, namely the meridian planes).

In the present Chapter, the yield function $\mathcal{G}^\mathrm{s}$ is assumed of the form

$$\mathcal{G}^\mathrm{s}(\boldsymbol{\sigma}) = m(p) + \frac{q}{g(\theta_\sigma)} \tag{3.6}$$

where m and g define the shape of the limit surface in meridian and deviatoric planes, respectively. With the aim to allow for an extremely flexible description of strength properties in π-planes, the deviatoric dimensionless function g is chosen as proposed by Bigoni and Piccolroaz (2004), that is:

$$g(\theta_\sigma) = \frac{1}{\cos\left[\beta\frac{\pi}{6} - \frac{1}{3}\arccos(\gamma\cos 3\theta_\sigma)\right]} \tag{3.7}$$

where β and γ are dimensionless parameters that, in order to assure convexity of deviatoric profiles, have to satisfy the consistency requirements $0 \leq \beta \leq 2$ and $0 \leq \gamma \leq 1$. As specified by Bigoni (2012), the deviatoric function $g(\theta_\sigma)$ in Eq. (3.7) was firstly introduced by Podgórski (1985a,b) and, since $\theta_\sigma \in [0, \pi/3]$ and $0 \leq \gamma \leq 1$, it is strictly positive.

As already shown by Bigoni and Piccolroaz (2004), the trascendental function $g(\theta_\sigma)$ allows for an extreme shape distortion of deviatoric sections, simultaneously guaranteeing both the possibility to account for stress-Lode-angle effects and a great flexibility for reproducing several strength-domain shapes. This occurrence is highlighted in Fig. 3.2, where $g(\theta_\sigma)$ is represented for different values of model parameters β and γ. In detail, parameter γ induces a smoothing effect on corners, resulting in a shape transition of deviatoric profiles, that pass from a multi-sided polygonal shape to a circular one when γ is varied from 1 to 0. Moreover, Fig. 3.2 clearly shows that sharp vertices appear in the deviatoric planes for $\gamma = 1$, corresponding to tangency discontinuities for $\theta_\sigma = 0$ and/or $\theta_\sigma = \pi/3$, depending on the value of β. In particular, for $0 < \beta < 2$, the shape of $g(\theta_\sigma)$ is characterised by six corners (at $\theta_\sigma = 0$ and $\theta_\sigma = \pi/3$), whereas for $\beta = 0$ and $\beta = 2$, three corners appear (at $\theta_\sigma = \pi/3$ or $\theta_\sigma = 0$, respectively).

As a matter of fact, the parameter β allows to range from the lower (for $\beta = 0$ and $\gamma = 1$) to the upper (for $\beta = 2$ and $\gamma = 1$) convexity bounds addressed by Haythornthwaite (1985). In particular, for non-zero values of γ, Fig. 3.2 highlights that a distortion of the deviatoric profiles occurs, the highest strength resulting for: triaxial compression (TXC, $\theta_\sigma = \pi/3$) when $0 \leq \beta < 1$; both triaxial expansion (TXE, $\theta_\sigma = 0$) and compression (TXC) when $\beta = 1$; triaxial expansion (TXE) when $1 < \beta \leq 2$.

In agreement with isotropic strength criteria generally adopted in engineering practice (such as, for instance, Drucker-Prager and Mohr-Coulomb), the material pressure-sensitivity is assumed to be represented by a linear meridian profile. Accordingly, and as a special case of the meridian function introduced by Bigoni and Piccolroaz (2004), m in Eq. (3.6) is chosen of the form

$$m(p) = -3\left(h - \frac{p}{\xi}\right) \tag{3.8}$$

where ξ and h are shape parameters which do not have to comply with any specific convexity requirement. Nevertheless, since limit stress state for $p = 0$ corresponds to $q = 3hg$, the consistency condition $h \geq 0$ has to be verified, h being a strength parameter that has the dimension of a stress. Furthermore, ξ is assumed to be a strictly-positive dimensionless quantity, thereby resulting in a finite tensile strength at $q = 0$ when $\xi < +\infty$. The case $\xi \to +\infty$ allows to describe a pressure-independent limit behaviour (such as in von Mises or Tresca criteria).

As summarized in Table 3.1, the Bigoni-like strength model defined by Eqs. (3.6) to (3.8) allows to recover classical yield functions by a proper choice of values for model parameters. For instance, by suitably calibrating β, ξ and h, von Mises (vM) and Drucker-Prager (DP) criteria can be recovered for $\gamma = 0$, as well as Tresca (Tr) and Mohr-Coulomb (MC) yield functions straight result for $\gamma = 1$.

The yield function $\mathcal{G}^{\mathcal{I}}(\boldsymbol{\tau})$ for the interface $\mathcal{I}$ is assumed of the same form as in Eqs. (3.6) to (3.8), and it is expressed in terms of the planar surface stress tensor $\boldsymbol{\tau}$ and of model parameters $\{\xi, h^{\mathcal{I}}, \beta, \gamma\}$, where $h^{\mathcal{I}}$ has the dimension of a membrane stress (namely, a force per unit length).

In the following, aiming to properly implement plastic admissibility conditions introduced in Eq. (3.3b), the cases of local yield functions $\mathcal{G}^{\mathrm{s}}$ and $\mathcal{G}^{\mathcal{I}}$ presenting smooth or sharp vertices in deviatoric planes are separately addressed. Accordingly, and as a specific notation, symbols $\overline{\mathcal{G}}^{\mathrm{s}}$ and $\widehat{\mathcal{G}}^{\mathrm{s}}$ (resp., $\overline{\mathcal{G}}^{\mathcal{I}}$ and $\widehat{\mathcal{G}}^{\mathcal{I}}$) are adopted to refer to the Bigoni-like yield functions for the solid matrix (resp., for the interface) with smooth (namely, for $0 \leq \gamma < 1$) and sharp (for $\gamma = 1$) deviatoric profiles, respectively. The corresponding yield surfaces are denoted as $\partial\overline{\mathcal{Y}}^{\mathrm{s}}$ and $\partial\widehat{\mathcal{Y}}^{\mathrm{s}}$ (resp., as $\partial\overline{\mathcal{Y}}^{\mathcal{I}}$ and $\partial\widehat{\mathcal{Y}}^{\mathcal{I}}$ for $\mathcal{I}$).

It is worth observing that, by considering $\gamma = 1$, the Bigoni-like yield function reduces to the following sharp form

$$\widehat{\mathcal{G}}^{\mathrm{s}}(\boldsymbol{\sigma}) = \left[\left(c_\beta \cos\theta_\sigma + s_\beta \sin\theta_\sigma\right) q - 3h\right]\xi + 3p \tag{3.9}$$

where $c_\beta = \cos(\beta\pi/6)$ and $s_\beta = \sin(\beta\pi/6)$, characterised by discontinuous first- and

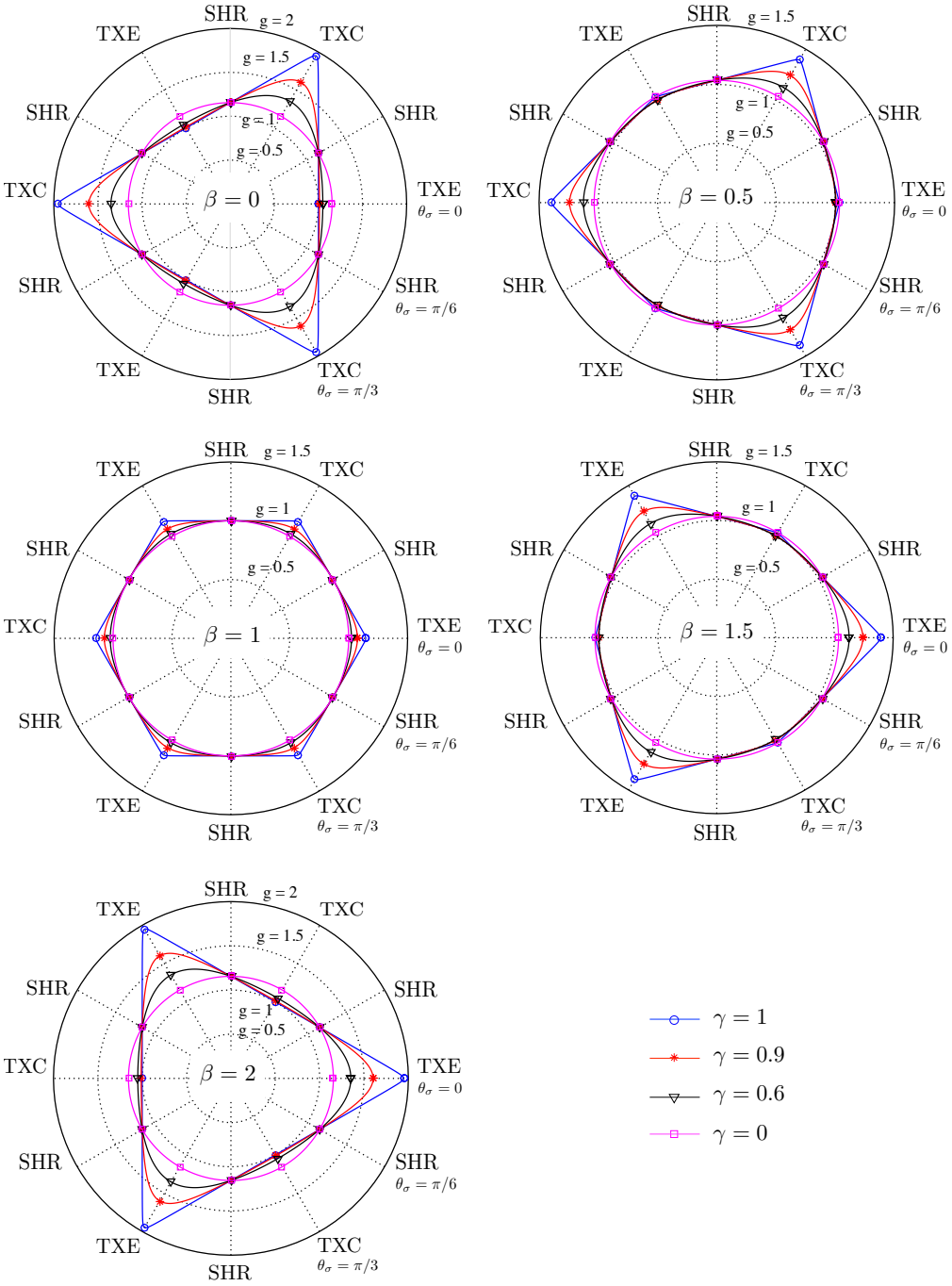

Figure 3.2 – Function $g(\theta_\sigma)$ in Eq. (3.7) for different values of model parameters β and γ. TXE: triaxial expansion. TXC: triaxial compression. SHR: shear.

Table 3.1 – Values of model parameters for the adopted Bigoni-like strength criterion, allowing to recover yield (i.e., $\mathcal{G}^{\mathrm{s}}(\boldsymbol{\sigma})$) and support (i.e., $\pi^{\mathrm{s}}(\mathbf{d})$) functions for: von Mises (vM), Tresca (Tr), Drucker-Prager (DP), and Mohr-Coulomb (MC) criteria. Notation: σ_0 is the deviatoric strength; c is the cohesion; ϕ is the friction angle; I_1^{d} and J_2^{d} indicate the first ($I_1^{\mathrm{d}} = \operatorname{tr}\mathbf{d}$) and the second-order deviatoric ($J_2^{\mathrm{d}} = \operatorname{tr}\mathbf{d}_{\mathrm{d}}^2/2$) strain-rate invariants, respectively; d_i and σ_i (with $i \in \{1,2,3\}$) denote principal strain-rate and principal stress components, respectively.

vM	$\mathcal{G}^{\mathrm{s}}(\boldsymbol{\sigma}) = \overline{\mathcal{G}}^{\mathrm{s}}(\boldsymbol{\sigma}) = q - \sigma_0 = 0$ $\pi^{\mathrm{s}}(\mathbf{d}) = \overline{\pi}^{\mathrm{s}}(\mathbf{d}) = \begin{cases} \dfrac{2\sqrt{3}}{3}\sigma_0\sqrt{J_2^{\mathrm{d}}} & \text{if} \quad I_1^{\mathrm{d}} = 0 \\ +\infty & \text{if} \quad I_1^{\mathrm{d}} \neq 0 \end{cases}$ $h = \dfrac{\sigma_0}{3}, \quad \xi \to +\infty, \quad \gamma = 0, \quad \beta = 1$
Tr	$\mathcal{G}^{\mathrm{s}}(\boldsymbol{\sigma}) = \widehat{\mathcal{G}}^{\mathrm{s}}(\boldsymbol{\sigma}) = \max_{i \neq j} \{\, \lvert\sigma_i - \sigma_j\rvert \,\} - \sigma_0 = q \sin\left(\theta_\sigma + \dfrac{\pi}{3}\right) - \dfrac{\sigma_0\sqrt{3}}{2} = 0$ $\pi^{\mathrm{s}}(\mathbf{d}) = \widehat{\pi}^{\mathrm{s}}(\mathbf{d}) = \begin{cases} \dfrac{\sigma_0}{2}(\lvert d_1\rvert + \lvert d_2\rvert + \lvert d_3\rvert) & \text{if} \quad I_1^{\mathrm{d}} = 0 \\ +\infty & \text{if} \quad I_1^{\mathrm{d}} \neq 0 \end{cases}$ $h = \dfrac{\sigma_0\sqrt{3}}{6}, \quad \xi \to +\infty, \quad \gamma = 1, \quad \beta = 1$
DP	$\mathcal{G}^{\mathrm{s}}(\boldsymbol{\sigma}) = \overline{\mathcal{G}}^{\mathrm{s}}(\boldsymbol{\sigma}) = p - c\cot\phi + q\dfrac{\sqrt{3+\sin^2\phi}}{3\sin\phi} = 0$ $\pi^{\mathrm{s}}(\mathbf{d}) = \overline{\pi}^{\mathrm{s}}(\mathbf{d}) = \begin{cases} c\cot\phi\, I_1^{\mathrm{d}} & \text{if} \quad \dfrac{I_1^{\mathrm{d}}}{\sqrt{J_2^{\mathrm{d}}}} \geq \dfrac{2\sqrt{3}\sin\phi}{\sqrt{3+\sin^2\phi}} \\ +\infty & \text{if} \quad \dfrac{I_1^{\mathrm{d}}}{\sqrt{J_2^{\mathrm{d}}}} < \dfrac{2\sqrt{3}\sin\phi}{\sqrt{3+\sin^2\phi}} \end{cases}$ $h = \dfrac{c\cot\phi}{3}, \quad \xi = 3, \quad \gamma = 0, \quad \beta = -2 + \dfrac{6}{\pi}\arcsin\left(\dfrac{\sqrt{3+\sin^2\phi}}{3\sin\phi}\right)$
MC	$\mathcal{G}^{\mathrm{s}}(\boldsymbol{\sigma}) = \widehat{\mathcal{G}}^{\mathrm{s}}(\boldsymbol{\sigma}) = \max_{i \neq j} \{\, \lvert\sigma_i - \sigma_j\rvert + (\sigma_i + \sigma_j)\sin\phi \,\} - 2c\cos\phi =$ $= p - c\cot\phi + q\left[\dfrac{1}{\sqrt{3}\sin\phi}\sin\left(\theta_\sigma + \dfrac{\pi}{3}\right) + \dfrac{1}{3}\cos\left(\theta_\sigma + \dfrac{\pi}{3}\right)\right] = 0$ $\pi^{\mathrm{s}}(\mathbf{d}) = \widehat{\pi}^{\mathrm{s}}(\mathbf{d}) = \begin{cases} c\cot\phi\, I_1^{\mathrm{d}} & \text{if} \quad I_1^{\mathrm{d}} \geq (\lvert d_1\rvert + \lvert d_2\rvert + \lvert d_3\rvert)\sin\phi \\ +\infty & \text{if} \quad I_1^{\mathrm{d}} < (\lvert d_1\rvert + \lvert d_2\rvert + \lvert d_3\rvert)\sin\phi \end{cases}$ $h = \dfrac{c\,\cos\phi}{\sqrt{3+\sin^2\phi}}, \quad \xi = \dfrac{\sqrt{3+\sin^2\phi}}{\sin\phi}$ $\gamma = 1, \quad \beta = \dfrac{6}{\pi}\arctan\left(\dfrac{\sqrt{3}(1-\sin\phi)}{3+\sin\phi}\right)$

second-order derivatives with respect to $\boldsymbol{\sigma}$ at sharp vertices.

In agreement with approaches proposed for classical criteria presenting singularities (as Tresca or Mohr-Coulomb, see Salençon (1983)), it is convenient to express Eq. (3.9) in terms of principal stresses. These latter are denoted as σ_i, σ_j, and σ_k, where different indexes i, j, k belong to $\{1,2,3\}$, leading to six different index permutations that result in six different ordered sequences of principal stresses. For each index permutation, let $\sigma_{\max} = \max\{\sigma_i, \sigma_j, \sigma_k\}$, $\sigma_{\min} = \min\{\sigma_i, \sigma_j, \sigma_k\}$ and $\sigma_{\text{mid}} = I_1^\sigma - (\sigma_{\max} + \sigma_{\min})$ be introduced. By combining the following relationships

$$\begin{aligned} \sigma_{\max} &= p + \frac{2}{3} q \cos\theta_\sigma \\ \sigma_{\text{mid}} &= p - \frac{2}{3} q \cos\left(\theta_\sigma + \frac{\pi}{3}\right) \\ \sigma_{\min} &= p - \frac{2}{3} q \cos\left(\theta_\sigma - \frac{\pi}{3}\right) \end{aligned} \tag{3.10}$$

transcendental functions in Eq. (3.9) can be expressed as

$$\begin{aligned} \cos\theta_\sigma &= \frac{3}{2}\left(\frac{\sigma_{\max} - p}{q}\right) \\ \sin\theta_\sigma &= \frac{\sqrt{3}}{2}\left(\frac{\sigma_{\text{mid}} - \sigma_{\min}}{q}\right) \end{aligned} \tag{3.11}$$

allowing to recast $\widehat{\mathcal{G}}^{\text{s}}$ in the form of a piece-wise linear yield function, consisting in six different yield planes $\widehat{\mathcal{G}}^{\text{s}}_\ell = 0$ (where $\ell \in \{1, \ldots, 6\}$), one for each possible ordered sequence of principal stresses, and defined by

$$\begin{aligned} \widehat{\mathcal{G}}^{\text{s}}_\ell(\boldsymbol{\sigma}) = &\left[\left(\sigma_{\max} - \frac{\sigma_{\text{mid}} + \sigma_{\min}}{2}\right) c_\beta + (\sigma_{\text{mid}} - \sigma_{\min}) \frac{\sqrt{3}}{2} s_\beta - 3h\right] \xi + \\ &+ \sigma_{\max} + \sigma_{\text{mid}} + \sigma_{\min} \end{aligned} \tag{3.12}$$

The case of a pressure-independent sharp yield function is obtained by enforcing $\gamma = 1$ and $\xi \to +\infty$ in Eqs. (3.6) to (3.8) (or equivalently in Eqs.(3.9) and (3.12)), resulting in

$$\widehat{\mathcal{G}}^{\text{s}}(\boldsymbol{\sigma}) = (c_\beta \cos\theta_\sigma + s_\beta \sin\theta_\sigma)\, q - 3h \tag{3.13}$$

$$\widehat{\mathcal{G}}^{\text{s}}_\ell(\boldsymbol{\sigma}) = \left(\sigma_{\max} - \frac{\sigma_{\text{mid}} + \sigma_{\min}}{2}\right) c_\beta + (\sigma_{\text{mid}} - \sigma_{\min}) \frac{\sqrt{3}}{2} s_\beta - 3h \tag{3.14}$$

The same considerations straight apply to the sharp form of the yield function at the interface, namely for $\widehat{\mathcal{G}}^{\mathcal{I}}(\boldsymbol{\tau})$.

3.4 Support function

As previously observed, kinematic limit-analysis approaches require as a starting point the definition of material strength properties via the local support function. By distinguishing between solid matrix and interface, the corresponding support functions are respectively defined as (e.g., Salençon, 1983)

$$\pi^{\mathrm{s}}(\mathbf{d}) = \sup_{\boldsymbol{\sigma}\in\mathcal{Y}^{\mathrm{s}}} (\boldsymbol{\sigma} : \mathbf{d}), \qquad \text{with} \qquad \mathcal{Y}^{\mathrm{s}} = \{\boldsymbol{\sigma} \quad \text{s.t.} \quad \mathcal{G}^{\mathrm{s}}(\boldsymbol{\sigma}) \leq 0\} \tag{3.15}$$

$$\pi^{\mathcal{I}}(\mathbf{d}^{\mathcal{I}}) = \sup_{\boldsymbol{\tau}\in\mathcal{Y}^{\mathcal{I}}} (\boldsymbol{\tau} : \mathbf{d}^{\mathcal{I}}_{\mathbb{T}}), \qquad \text{with} \qquad \mathcal{Y}^{\mathcal{I}} = \left\{\boldsymbol{\tau} \quad \text{s.t.} \quad \mathcal{G}^{\mathcal{I}}(\boldsymbol{\tau}) \leq 0\right\} \tag{3.16}$$

with $\mathbf{d}^{\mathcal{I}}_{\mathbb{T}} = \mathbb{T} : \mathbf{d}^{\mathcal{I}}$ and where π^{s} (resp., $\pi^{\mathcal{I}}$) has the meaning of the maximum volume (resp., surface) plastic dissipation that can be locally achieved by the material in Ω_{s} (resp., on $\partial\Omega_{\mathrm{i}}$), when the kinematically-admissible local strain-rate field $\mathbf{d}$ (resp., $\mathbf{d}^{\mathcal{I}}$) is considered. In order to ensure the boundedness of the maximum plastic dissipation in Eqs. (3.15) and (3.16), the strain-rate state $(\mathbf{d}, \mathbf{d}^{\mathcal{I}})$ has to belong to $\mathcal{P}_{\mathrm{d}}$ (see Eq. (3.3b)), resulting in plastic admissibility conditions on $(\mathbf{d}, \mathbf{d}^{\mathcal{I}})$.

Although explicit expressions for support functions associated to classical criteria are already available in literature, at the best of the authors' knowledge, the case of a general isotropic yield function has not been exhaustively addressed yet.

In agreement with the previously-introduced notation, in the following $\overline{\pi}^{\mathrm{s}}$ and $\widehat{\pi}^{\mathrm{s}}$ (resp., $\overline{\pi}^{\mathcal{I}}$ and $\widehat{\pi}^{\mathcal{I}}$) indicate support functions associated to yield surfaces with smooth or sharp deviatoric profiles, respectively.

3.4.1 Support functions for smooth yield surfaces

Aiming to determine $\overline{\pi}^{\mathrm{s}}$ and $\overline{\pi}^{\mathcal{I}}$, as well as the corresponding admissibility conditions, reference is made to the theoretical framework established by Lemarchand et al. (2015), which is straight applicable to the case of unbounded yield functions with smooth deviatoric profiles. Such an approach is herein employed by addressing Bigoni-like yield functions $\overline{\mathcal{G}}^{\mathrm{s}}$ and $\overline{\mathcal{G}}^{\mathcal{I}}$, defined by Eqs. (3.6) to (3.8) for $0 \leq \gamma < 1$. For the sake of compactness, analytical details, support functions and specific comments related to the identification of admissibility requirements, are summarised in 3.A.

As shown in Table 3.1, obtained support functions (see Eqs. (3.99) and (3.102)) fully recover, by a suitable choice of values for model parameters, the corresponding available expressions for von Mises and Drucker-Prager criteria (e.g., Salençon, 1983).

3.4.2 Support functions for sharp yield surfaces

Due to the presence of sharp vertices in the deviatoric plane for $\gamma = 1$, support functions $\widehat{\pi}^{\mathrm{s}}$ and $\widehat{\pi}^{\mathcal{I}}$ differ from those deduced in 3.A for: plastic admissibility conditions when a pressure-dependent yield function is addressed (namely, for $\xi < +\infty$); maximum plastic dissipation when pressure-independence is enforced (namely, for $\xi \to +\infty$).

For the sake of compactness, in the following reference is explicitly made to the case

of the solid matrix only, the interface case requiring analogous analytical details starting from Eq. (3.16).

Aiming to determine the support function in Eq. (3.15), the supremum of the local plastic dissipation $\boldsymbol{\sigma} : \mathbf{d}$ has to be computed over all local stress states complying with the strength criterion $\widehat{\mathcal{G}}^{\mathrm{s}}(\boldsymbol{\sigma}) \leq 0$. By referring to the notation introduced in Section 3.3 and since Eq. (3.12), the following inequality holds

$$\begin{aligned}\boldsymbol{\sigma} : \mathbf{d} \leq & \left[d_1 - \frac{I_1^{\mathrm{d}}}{3}\left(1 + c_\beta \xi\right)\right]\sigma_{\max} + \left[d_2 - \frac{I_1^{\mathrm{d}}}{3}\left(1 + \frac{1}{2}\left(-c_\beta + \sqrt{3}s_\beta\right)\xi\right)\right]\sigma_{\mathrm{mid}} \\ & + \left[d_3 - \frac{I_1^{\mathrm{d}}}{3}\left(1 - \frac{1}{2}\left(c_\beta + \sqrt{3}s_\beta\right)\xi\right)\right]\sigma_{\min} + h\xi I_1^{\mathrm{d}}\end{aligned} \tag{3.17}$$

Therefore, following analogous arguments as in 3.A (see Eq. (3.98)), the finite value of the maximum plastic dissipation results in $h\xi I_1^{\mathrm{d}}$.

Admissibility conditions can be explicitly obtained by prescribing that strain-rate field belongs to $\mathcal{P}_{\mathrm{d}}$, thereby enforcing the normality law in Eq. (3.3b) for the yield function $\mathcal{G}^{\mathrm{s}}$ described via the piece-wise form in Eq. (3.12) (for $\xi < +\infty$) or in Eq. (3.14) (for $\xi \to +\infty$).

With reference to the case $\xi < +\infty$ and depending on the values assumed by the principal stresses in Eq. (3.12), the following three plastic regimes can be attained at the limit state, that is for $\boldsymbol{\sigma} \in \partial\widehat{\mathcal{Y}}^{\mathrm{s}}$.

- **Face regime**. It corresponds to the case $\sigma_i \neq \sigma_j \neq \sigma_k$. Thereby, for a any possible choice of i, j and k, only one of the six yield functions in Eq. (3.12) is equal to zero, and the plastically-admissible strain-rate states are identified by

$$\mathbf{d} = \lambda_\ell^{\mathrm{s}} \frac{\partial \widehat{\mathcal{G}}_\ell^{\mathrm{s}}(\boldsymbol{\sigma})}{\partial \boldsymbol{\sigma}} \tag{3.18}$$

  where $\lambda_\ell^{\mathrm{s}}$ is the strictly-positive plastic multiplier associated to the yield plane $\widehat{\mathcal{G}}_\ell^{\mathrm{s}} = 0$. Therefore, depending on the values of β (via c_β and s_β) and ξ, and identifying principal strain-rate components d_1, d_2 and d_3 via Eq. (3.18), the following relationships hold for any possible choice of different indexes $i\,, j\,, k \in \{1, 2, 3\}$ (namely, for any yield plane $\widehat{\mathcal{G}}_\ell^{\mathrm{s}} = 0$):

  $\diamondsuit$ case $0 \leq \beta < 1$

$$|d_1| + |d_2| + |d_3| = \begin{cases} I_1^{\mathrm{d}} & \text{if} \quad \xi \leq \xi^* \\ \dfrac{I_1^{\mathrm{d}}}{3}\left[1 + \left(c_\beta + \sqrt{3}\, s_\beta\right)\xi\right] & \text{if} \quad \xi^* \leq \xi \leq \xi^{**} \\ \dfrac{I_1^{\mathrm{d}}}{3}\left(2c_\beta \xi - 1\right) & \text{if} \quad \xi \geq \xi^{**} \end{cases} \tag{3.19}$$

$\diamondsuit$ case $1 \leq \beta \leq 2$

$$|d_1| + |d_2| + |d_3| = \begin{cases} I_1^{\mathrm{d}} & \text{if} \quad \xi \leq \xi^* \\ \dfrac{I_1^{\mathrm{d}}}{3}\left[1 + \left(c_\beta + \sqrt{3}\, s_\beta\right)\xi\right] & \text{if} \quad \xi \geq \xi^* \end{cases} \tag{3.20}$$

with $I_1^{\mathrm{d}} = \operatorname{tr} \mathbf{d}$, and where

$$\xi^* = \frac{2}{c_\beta + \sqrt{3} s_\beta}\,, \qquad \xi^{**} = \frac{2}{c_\beta - \sqrt{3} s_\beta} \tag{3.21}$$

- **Edge regime**. It corresponds to the case $\sigma_i = \sigma_j \neq \sigma_k$. Thereby, two of the six yield functions in Eq. (3.12), say $\widehat{\mathcal{G}}^{\mathrm{s}}_{\ell^+}$ and $\widehat{\mathcal{G}}^{\mathrm{s}}_{\ell^-}$ (with ℓ^+, $\ell^- \in \{1, \ldots, 6\}$ and such that $\ell^+ \neq \ell^-$), are simultaneously equal to zero, and the plastically-admissible strain-rate states are identified by the convex cone

$$\mathbf{d} = \lambda^{\mathrm{s}}_{\ell^+} \frac{\partial \widehat{\mathcal{G}}^{\mathrm{s}}_{\ell^+}(\boldsymbol{\sigma})}{\partial \boldsymbol{\sigma}} + \lambda^{\mathrm{s}}_{\ell^-} \frac{\partial \widehat{\mathcal{G}}^{\mathrm{s}}_{\ell^-}(\boldsymbol{\sigma})}{\partial \boldsymbol{\sigma}} \tag{3.22}$$

Therefore, due to the triangle inequality, the following relationships hold for any possible choice of different indexes $i\,, j\,, k \in \{1, 2, 3\}$ (namely, for each edge of the sharp yield surface $\partial \widehat{\mathcal{Y}}^{\mathrm{s}}$):

$\diamondsuit$ case $0 \leq \beta < 1$

$$|d_1| + |d_2| + |d_3| \leq \begin{cases} I_1^{\mathrm{d}} & \text{if} \quad \xi \leq \xi^* \\ \dfrac{I_1^{\mathrm{d}}}{3}\left[1 + \left(c_\beta + \sqrt{3}\, s_\beta\right)\xi\right] & \text{if} \quad \xi^* \leq \xi \leq \xi^{**} \\ \dfrac{I_1^{\mathrm{d}}}{3}\left(2 c_\beta \xi - 1\right) & \text{if} \quad \xi \geq \xi^{**} \end{cases} \tag{3.23}$$

$\diamondsuit$ case $1 \leq \beta \leq 2$

$$|d_1| + |d_2| + |d_3| \leq \begin{cases} I_1^{\mathrm{d}} & \text{if} \quad \xi \leq \xi^* \\ \dfrac{I_1^{\mathrm{d}}}{3}\left[1 + \left(c_\beta + \sqrt{3}\, s_\beta\right)\xi\right] & \text{if} \quad \xi \geq \xi^* \end{cases} \tag{3.24}$$

- **Apex regime**. It corresponds to the case $\sigma_i = \sigma_j = \sigma_k$. Thereby, all yield functions in Eq. (3.12) are simultaneously equal to zero, and the normality law reads as

$$\mathbf{d} = \sum_{\ell=1}^{6} \lambda^{\mathrm{s}}_{\ell} \frac{\partial \widehat{\mathcal{G}}^{\mathrm{s}}_{\ell}(\boldsymbol{\sigma})}{\partial \boldsymbol{\sigma}} \tag{3.25}$$

straight resulting in inequalities (3.23) and (3.24).

Thereby, plastically-admissible strain-rate fields have to simultaneously satisfy Eqs. (3.19) and (3.23) when $0 \leq \beta < 1$, and Eqs. (3.20) and (3.24) when $1 \leq \beta \leq 2$. Accordingly, depending on values of β, admissiblity requirements are expressed by Eqs. (3.23) and (3.24),

and -due to Eq. (3.17)- the support function $\widehat{\pi}^{\mathrm{s}}$ for the solid matrix Ω_{s} reads as:

$\diamondsuit$ case $0 \leq \beta < 1$

$$\widehat{\pi}^{\mathrm{s}}(\mathbf{d}) = \begin{cases} h\xi I_1^{\mathrm{d}} & \text{if} \quad I_1^{\mathrm{d}} \geq \begin{cases} |d_1| + |d_2| + |d_3| & \text{if} \quad \xi \leq \xi^* \\ \dfrac{3\left(|d_1| + |d_2| + |d_3|\right)}{1 + \left(c_\beta + \sqrt{3}\, s_\beta\right)\xi} & \text{if} \quad \xi^* \leq \xi \leq \xi^{**} \\ \dfrac{3\left(|d_1| + |d_2| + |d_3|\right)}{2c_\beta \xi - 1} & \text{if} \quad \xi \geq \xi^{**} \end{cases} \\ +\infty & \text{otherwise} \end{cases} \tag{3.26}$$

$\diamondsuit$ case $1 \leq \beta \leq 2$

$$\widehat{\pi}^{\mathrm{s}}(\mathbf{d}) = \begin{cases} h\xi I_1^{\mathrm{d}} & \text{if} \quad I_1^{\mathrm{d}} \geq \begin{cases} |d_1| + |d_2| + |d_3| & \text{if} \quad \xi \leq \xi^* \\ \dfrac{3\left(|d_1| + |d_2| + |d_3|\right)}{1 + \left(c_\beta + \sqrt{3}\, s_\beta\right)\xi} & \text{if} \quad \xi \geq \xi^* \end{cases} \\ +\infty & \text{otherwise} \end{cases} \tag{3.27}$$

It is noted that the support function for a pressure-independent sharp criterion (that is, for $\xi \to +\infty$) can be obtained as a particular case of Eqs. (3.26) and (3.27). As a matter of fact, for $\xi \to +\infty$ (thereby for $\xi > \xi^{**}$ when $0 \leq \beta < 1$, and for $\xi > \xi^*$ when $1 \leq \beta \leq 2$) admissibility conditions in Eqs. (3.23) and (3.24) are non trivial only if $I_1^{\mathrm{d}} = 0$. These latter, in the limit of $\xi \to +\infty$ and $I_1^{\mathrm{d}} \to 0^+$, lead to

$$I_1^{\mathrm{d}} = \begin{cases} \dfrac{3\left(|d_1| + |d_2| + |d_3|\right)}{2c_\beta \xi - 1} & \text{if} \quad 0 \leq \beta < 1 \\ \dfrac{3\left(|d_1| + |d_2| + |d_3|\right)}{1 + \left(c_\beta + \sqrt{3}\, s_\beta\right)\xi} & \text{if} \quad 1 \leq \beta \leq 2 \end{cases} \tag{3.28}$$

Accordingly, by adopting Eq. (3.28) to recast the finite branch of $\widehat{\pi}^{\mathrm{s}}$ in Eqs. (3.26) and (3.27), the support function for $\xi \to +\infty$ results in

$\diamondsuit$ case $0 \leq \beta < 1$

$$\widehat{\pi}^{\mathrm{s}}(\mathbf{d}) = \begin{cases} \dfrac{3h}{2c_\beta}\left(|d_1| + |d_2| + |d_3|\right) & \text{if} \quad I_1^{\mathrm{d}} = 0 \\ +\infty & \text{otherwise} \end{cases} \tag{3.29}$$

$\diamondsuit$ case $1 \leq \beta \leq 2$

$$\widehat{\pi}^{\mathrm{s}}(\mathbf{d}) = \begin{cases} \dfrac{3h}{c_\beta + \sqrt{3} s_\beta}\left(|d_1| + |d_2| + |d_3|\right) & \text{if} \quad I_1^{\mathrm{d}} = 0 \\ +\infty & \text{otherwise} \end{cases} \tag{3.30}$$

As shown in Table 3.1, support functions and plastic admissibility conditions for Mohr-Coulomb and Tresca criteria can be readily recovered via Eqs. (3.26) and (3.30), respectively, by a proper choice of values for model parameters.

Similarly, the interface local support function $\widehat{\pi}^{\mathcal{I}}$ in Eq. (3.16), as well as the cor-

responding admissibility conditions, formally read as in Eqs. (3.26) and (3.27) (or in Eqs. (3.29) and (3.30) for $\xi \to +\infty$) and are expressed in terms of the local strain-rate tensor $\mathbf{d}^{\mathcal{I}}$.

3.4.3 Consistency assessment

Support functions in Eqs. (3.26) to (3.30) and associated to a sharp yield surfaces, as well as relationships (3.99) and (3.102) provided in 3.A for the smooth case, comply with the following consistency properties (Salençon, 1983).

- Property $\mathcal{P}1$: $\pi^{\mathrm{s}}(\mathbf{d})$ is *non negative* and $\pi^{\mathrm{s}}(\mathbf{0}) = 0$.
  As regards pressure-dependent yield function $\widehat{\mathcal{G}}^{\mathrm{s}}$ in Eq. (3.12) (resp., $\overline{\mathcal{G}}^{\mathrm{s}}$ defined by Eqs. (3.6) to (3.8) for $0 \leq \gamma < 1$), since $h > 0$ and $\xi > 0$, support function $\widehat{\pi}^{\mathrm{s}}$ (resp., $\overline{\pi}^{\mathrm{s}}$) is positive when the local strain-rate field $\mathbf{d}$ satisfies admissibility requirements in Eqs. (3.26) and (3.27) (resp., in Eq. (3.99)), these latter providing $I_1^{\mathrm{d}} \geq 0$. This occurrence straight results from conditions $c_\beta > 0$ and $s_\beta \geq 0$ (for $\widehat{\pi}^{\mathrm{s}}$), and from the strict positiveness of function g (for $\overline{\pi}^{\mathrm{s}}$).

  Analogously, addressing a pressure-independent yield function, the same arguments allow to prove that support function $\widehat{\pi}^{\mathrm{s}}$ in Eqs. (3.29) and (3.30) (resp., $\overline{\pi}^{\mathrm{s}}$ in Eq. (3.102)) is positive.

  Finally, it is immediate to verify that both $\widehat{\pi}^{\mathrm{s}}$ and $\overline{\pi}^{\mathrm{s}}$ are equal to zero for vanishing strain-rate states.

- Property $\mathcal{P}2$: π^{s} is *positively homogeneous of degree* 1.
  In the case of both sharp and smooth yield criteria, it is simple to prove that, for any plastically-admissible strain-rate $\mathbf{d}$, the corresponding support functions comply with condition
  $$\pi^{\mathrm{s}}(\alpha\,\mathbf{d}) = \alpha\,\pi^{\mathrm{s}}(\mathbf{d})\,, \qquad \forall\,\alpha \geq 0 \tag{3.31}$$
  Accordingly, owing to property $\mathcal{P}1$, relationship (3.31) proves that support function π^{s} is positively homogeneous of degree 1.

- Property $\mathcal{P}3$: π^{s} is *convex*.
  Both support functions $\widehat{\pi}^{\mathrm{s}}$ and $\overline{\pi}^{\mathrm{s}}$ are expressed as linear combinations of strain-rate components, thereby providing the convexity requirement to be straight satisfied.

3.5 Exact limit state under isotropic loadings

In what follows, the local fields (stress, strain-rate and velocity) satisfying the hollow-sphere limit problem introduced in Section 3.2, as well as the corresponding macroscopic limit stress state, are exactly determined.

It is worth observing that, the identification of statically- and plastically-admissible stresses via Eqs. (3.2a) and (3.2b) is not affected by the possible occurrence of sharp vertices in π-planes for both $\mathcal{G}^{\mathrm{s}}$ and $\mathcal{G}^{\mathcal{I}}$. Accordingly, Eqs. (3.2a) and (3.2b) are faced by considering the general form of yield functions for solid matrix and interface, defined

by Eqs. (3.6) to (3.8). On the contrary, due to the normality law in Eq. (3.3b), the identification of plastically-admissible strain-rate and velocity fields requires to distinguish between plastic matrices obeying to yield criteria with smooth or sharp deviatoric profiles.

3.5.1 Local stress field and macroscopic limit stress

By considering $(\boldsymbol{\sigma}, \boldsymbol{\tau}) \in (\mathcal{Q}, \mathcal{Q})$ (see Eq. (3.4)), where the surface-stress tensor $\boldsymbol{\tau}$ is planar and it has the form $\boldsymbol{\tau} = \tau_\theta(\mathbf{e}_\theta \otimes \mathbf{e}_\theta + \mathbf{e}_\varphi \otimes \mathbf{e}_\varphi)$, the Lode coordinates introduced in Eqs. (3.5) can be expressed as

$$p = \frac{2\sigma_\theta + \sigma_\mathrm{r}}{3}, \qquad q = \iota(\sigma_\mathrm{r} - \sigma_\theta), \qquad \theta_\sigma = \frac{1}{3}\arccos(\iota)\,, \qquad \text{in } \Omega_\mathrm{s} \tag{3.32}$$

$$p = \frac{2\tau_\theta}{3}, \qquad q = -\iota^{\mathcal{I}}\tau_\theta, \qquad \theta_\sigma = \frac{1}{3}\arccos(\iota^{\mathcal{I}})\,, \qquad \text{on } \partial\Omega_\mathrm{i} \tag{3.33}$$

where

- $\iota = \mathrm{sgn}(\sigma_\mathrm{r} - \sigma_\theta)$, that is $\iota = +1$ (resp., $\iota = -1$) for a local triaxial-expansion ($\theta_\sigma = 0$) stress state (resp., triaxial-compression, $\theta_\sigma = \pi/3$) in Ω_s;
- $\iota^{\mathcal{I}} = -\,\mathrm{sgn}(\tau_\theta)$, corresponding to a surface-stress state on $\partial\Omega_\mathrm{i}$, characterised by $\theta_\sigma = 0$ and $\theta_\sigma = \pi/3$, when $\iota^{\mathcal{I}} = +1$ and $\iota^{\mathcal{I}} = -1$, respectively.

Therefore, yield functions for solid matrix and interface are respectively expressed by (see Eqs. (3.6) to (3.8))

$$\mathcal{G}^\mathrm{s}(\boldsymbol{\sigma}) = -3h + \frac{1}{\xi}(2\sigma_\theta + \sigma_\mathrm{r}) + (\sigma_\mathrm{r} - \sigma_\theta)\Lambda \tag{3.34}$$

$$\mathcal{G}^{\mathcal{I}}(\boldsymbol{\tau}) = -3h^{\mathcal{I}} + \frac{2\tau_\theta}{\xi} - \Lambda^{\mathcal{I}}\tau_\theta \tag{3.35}$$

where functions

$$\Lambda(\iota) = \iota\cos\left(\beta\frac{\pi}{6} - \frac{1}{3}\arccos\left(\gamma\iota\right)\right) \tag{3.36}$$

$$\Lambda^{\mathcal{I}}\left(\iota^{\mathcal{I}}\right) = \iota^{\mathcal{I}}\cos\left(\beta\frac{\pi}{6} - \frac{1}{3}\arccos\left(\gamma\iota^{\mathcal{I}}\right)\right) \tag{3.37}$$

account for the influence of the local stress Lode angle ($\theta_\sigma = 0$ or $\theta_\sigma = \pi/3$), and they are such that $\mathrm{sgn}(\Lambda) = \iota$ and $\mathrm{sgn}(\Lambda^{\mathcal{I}}) = \iota^{\mathcal{I}}$.

Plastically-admissible stresses $(\boldsymbol{\sigma}, \boldsymbol{\tau}) \in \mathcal{P}_\sigma \cap (\mathcal{Q}, \mathcal{Q})$ have to comply with the yielding conditions $\mathcal{G}^\mathrm{s}(\boldsymbol{\sigma}) = 0$ and $\mathcal{G}^{\mathcal{I}}(\boldsymbol{\tau}) = 0$ (see Eq. (3.2b)), resulting in

$$\sigma_\theta = \frac{3h\xi - \sigma_\mathrm{r}\,(1 + \Lambda\xi)}{2 - \Lambda\xi} \tag{3.38}$$

$$\tau_\theta = \frac{3\xi}{2 - \Lambda^{\mathcal{I}}\xi}h^{\mathcal{I}} \tag{3.39}$$

Furthermore, statically-admissible stresses $(\boldsymbol{\sigma}, \boldsymbol{\tau}) \in \mathcal{S}_\sigma \cap (\mathcal{Q}, \mathcal{Q})$ have to satisfy the

following equilibrium equations

$$\frac{d\sigma_{\rm r}}{dr}+2\frac{\sigma_{\rm r}-\sigma_\theta}{r}=0 \qquad \text{for } r\in(R_{\rm i},R_{\rm e}] \tag{3.40a}$$

$$\sigma_{\rm r}=\frac{2\tau_\theta}{R_{\rm i}} \qquad \text{at } r\to R_{\rm i}^{+} \tag{3.40b}$$

$$\sigma_{\rm r}=\Sigma_{\rm m}^{\rm c} \qquad \text{at } r=R_{\rm e} \tag{3.40c}$$

where $\Sigma_{\rm m}^{\rm c}$ is the unknown macroscopic hydrostatic stress and Eq. (3.40b) results from the Young-Laplace equilibrium condition at the interface $\mathcal{I}$ (see Eq. (3.2a)).

The first-order differential equation that results by combining Eqs. (3.38) and (3.40a) is integrated by enforcing the boundary condition (3.40b), expressed in terms of plastically-admissible surface stresses in Eq. (3.39). The following fully-admissible stress components are obtained

$$\tau_\theta=\frac{3\xi h}{2-\Lambda^{\mathcal{I}}\xi}R_{\rm i}\kappa\,, \qquad r=R_{\rm i} \tag{3.41a}$$

$$\sigma_{\rm r}(r)=h\xi\left[1-\left(\frac{R_{\rm e}f^{\frac{1}{3}}}{r}\right)^{\frac{6}{2-\Lambda\xi}}\left(1-\frac{6\kappa}{2-\Lambda^{\mathcal{I}}\xi}\right)\right], \qquad r\in(R_{\rm i},R_{\rm e}] \tag{3.41b}$$

$$\sigma_\theta(r)=h\xi\left[1+\frac{1+\Lambda\xi}{2-\Lambda\xi}\left(\frac{R_{\rm e}f^{\frac{1}{3}}}{r}\right)^{\frac{6}{2-\Lambda\xi}}\left(1-\frac{6\kappa}{2-\Lambda^{\mathcal{I}}\xi}\right)\right], \; r\in(R_{\rm i},R_{\rm e}] \tag{3.41c}$$

where the dimensionless parameter

$$\kappa=\frac{h^{\mathcal{I}}}{R_{\rm i}h} \tag{3.42}$$

accounts for the influence of void-size effects.

It is worth observing that Eqs. (3.41) allow to prove that ι is independent from r, as well as that $\iota=\iota^{\mathcal{I}}$, and thereby that

$$\Lambda^{\mathcal{I}}(\iota^{\mathcal{I}})=\Lambda(\iota) \tag{3.43}$$

Denoting with $\langle\mathbf{a}\rangle$ the Ω-based average of a certain space-dependent field $\mathbf{a}(\mathbf{r})$ (namely, $\langle\mathbf{a}\rangle=|\Omega|^{-1}\int_\Omega\mathbf{a}\,d\Omega$), the macroscopic stress tensor $\boldsymbol{\Sigma}^{\rm c}$ associated to the fully-admissible stress fields described by Eqs. (3.41), is then obtained as

$$\boldsymbol{\Sigma}^{\rm c}=\langle\boldsymbol{\sigma}\rangle=\frac{R_{\rm e}}{|\Omega|}\int_{\partial\Omega_{\rm e}}(\boldsymbol{\sigma}\cdot\mathbf{e}_{\rm r})\otimes\mathbf{e}_{\rm r}\,dA=3\sigma_{\rm r}\big|_{r=R_{\rm e}}(\mathbf{e}_{\rm r}\otimes\mathbf{e}_{\rm r}) \tag{3.44}$$

that results, since the equilibrium at the exterior boundary (see Eq. (3.40c)), in the following closed-form relationship for the macroscopic hydrostatic strength

$$\Sigma_{\rm m}^{\rm c}=\frac{\operatorname{tr}\boldsymbol{\Sigma}^{\rm c}}{3}=h\xi\left[1-f^{\frac{2}{2-\Lambda\xi}}\left(1-\kappa\,\frac{6}{2-\Lambda\xi}\right)\right] \tag{3.45}$$

corresponding to the macroscopic stress Lode angle $\theta_\Sigma=\arccos(\operatorname{sgn}(\Sigma_{\rm m}^{\rm c}))/3$ (that is,

$\theta_\Sigma = 0$ or $\theta_\Sigma = \pi/3$). It is noticed that, by combining Eqs. (3.41) and (3.45), it is possible to prove that $\iota = -\operatorname{sgn}(\Sigma_{\rm m}^{\rm c})$. Accordingly, the value $\Sigma_{\rm m}^{\rm c}$ computed for $\Lambda|_{\iota=+1}$ (resp., $\Lambda|_{\iota=-1}$) is associated to a macroscopic hydrostatic compression (resp., expansion).

In the particular case of a pressure-independent plastic behaviour of the solid matrix (that is, for $\xi \to +\infty$), previous solution reduces to

$$\sigma_{\rm r}(r) = \frac{6h}{\Lambda}\left[\ln\left(\frac{R_{\rm e}}{r}f^{1/3}\right) - \kappa\right] \tag{3.46a}$$

$$\sigma_\theta(r) = \frac{3h}{\Lambda}\left\{2\left[\ln\left(\frac{R_{\rm e}}{r}f^{1/3}\right) - \kappa\right] - 1\right\} \tag{3.46b}$$

$$\tau_\theta = -3\frac{R_{\rm i}h}{\Lambda}\kappa \tag{3.46c}$$

$$\Sigma_{\rm m}^{\rm c} = \frac{6h}{\Lambda}\left[\ln(f^{1/3}) - \kappa\right] \tag{3.46d}$$

Remark 1 *For a matrix plastic behaviour complying with the condition $\xi > 2/|\Lambda|$, Eqs.* (3.41) *allows to prove that limit states corresponding to finite values of the macroscopic strength may be attained for both local triaxial expansion ($\iota = +1$) and triaxial compression ($\iota = -1$). On the other hand, when $\xi < 2/|\Lambda|$, the limit state can correspond to a local triaxial compression stress state ($\iota = -1$), only. Finally, for $\xi = 2/|\Lambda|$, the limit state can not be attained, resulting in unbounded fully-admissible stresses in Eqs.* (3.41).

Remark 2 *The case of negligible surface stresses τ_θ (that is, the case of porous materials) can be straight obtained by setting $\kappa \to 0^+$ in Eqs.* (3.41), (3.45) *and* (3.46). *This occurrence corresponds to the limit problem defined in Section 3.2 when interface $\mathcal{I}$ is not accounted for.*

3.5.2 Local velocity and strain-rate fields

Kinematically-admissible strain-rate fields $(\mathbf{d}, \mathbf{d}^{\mathcal{I}}) \in \mathcal{K}_{\rm d} \cap (\mathcal{Q}, \mathcal{Q})$ (see Eq. (3.3a)) have to comply with the strain-rate compatibility conditions

$$d_{\rm r}(r) = \frac{dv_{\rm r}}{dr}\,, \qquad d_\theta(r) = \frac{v_{\rm r}(r)}{r} \tag{3.47}$$

$$d_{\rm r}^{\mathcal{I}} = d_{\rm r}|_{r=R_{\rm i}}\,, \qquad d_\theta^{\mathcal{I}} = d_\theta|_{r=R_{\rm i}} \tag{3.48}$$

The case of smooth yield surfaces

Let the yield function in Eqs. (3.6) to (3.8) with $0 \leq \gamma < 1$ be expressed for the solid matrix (resp., for the interface) in terms of principal stress components $\sigma_{\rm r}$, σ_θ and σ_φ (resp., $\tau_{\rm r}$, τ_θ and τ_φ). The normality law in Eq. (3.3b) computed for $\sigma_\theta = \sigma_\varphi$ (resp., for $\tau_{\rm r} = 0$ and $\tau_\theta = \tau_\varphi$) allows to determine plastically-admissible strain-rate fields $(\mathbf{d}, \mathbf{d}^{\mathcal{I}}) \in \mathcal{P}_{\rm d} \cap (\mathcal{Q}, \mathcal{Q})$,

whose components are

$$d_{\mathrm{r}}(r) = \frac{\lambda^{\mathrm{s}}(r)}{\xi}\left(1+\overline{\Lambda}\xi\right), \qquad d_\theta(r) = d_\varphi(r) = \frac{\lambda^{\mathrm{s}}(r)}{2\xi}\left(2-\overline{\Lambda}\xi\right) \tag{3.49}$$

$$d^{\mathcal{I}}_{\mathrm{r}} = \frac{\lambda^{\mathcal{I}}}{\xi}\left(1+\overline{\Lambda}^{\mathcal{I}}\xi\right), \qquad d^{\mathcal{I}}_\theta = d^{\mathcal{I}}_\varphi = \frac{\lambda^{\mathcal{I}}}{2\xi}\left(2-\overline{\Lambda}^{\mathcal{I}}\xi\right) \tag{3.50}$$

where $\overline{\Lambda}$ and $\overline{\Lambda}^{\mathcal{I}}$ indicate functions Λ and $\Lambda^{\mathcal{I}}$ defined in Eqs. (3.36) and (3.37) for $0 \le \gamma < 1$, and they depend on the local plastically-admissible stress state $(\boldsymbol{\sigma}, \boldsymbol{\tau}) \in \mathcal{P}_\sigma \cap (\mathcal{Q}, \mathcal{Q})$.

Statically- and plastically-admissible stress fields in Eqs. (3.41) are enforced, leading $\overline{\Lambda}$ independent from r and $\overline{\Lambda}^{\mathcal{I}} = \overline{\Lambda}$.

Accordingly, by combining Eqs. (3.47) to (3.50), plastic multipliers result in

$$\lambda^{\mathrm{s}}(r) = \overline{\mathcal{C}}\, r^{\frac{3\overline{\Lambda}\xi}{2-\overline{\Lambda}\xi}} \tag{3.51}$$

$$\lambda^{\mathcal{I}} = \lambda^{\mathrm{s}}|_{r=R_{\mathrm{i}}} = \overline{\mathcal{C}}\, R_{\mathrm{i}}^{\frac{3\overline{\Lambda}\xi}{2-\overline{\Lambda}\xi}} \tag{3.52}$$

leading to the following fully-admissible kinematics, expressed in terms of fully-admissible stress fields

$$d_{\mathrm{r}}(r) = \frac{\left(1+\overline{\Lambda}\xi\right)}{\xi}\overline{\mathcal{C}}\, r^{\frac{3\overline{\Lambda}\xi}{2-\overline{\Lambda}\xi}}, \qquad d_\theta(r) = \frac{\left(2-\overline{\Lambda}\xi\right)}{2\xi}\overline{\mathcal{C}}\, r^{\frac{3\overline{\Lambda}\xi}{2-\overline{\Lambda}\xi}} \tag{3.53}$$

$$v_{\mathrm{r}}(r) = \overline{\mathcal{C}}\,\frac{2-\overline{\Lambda}\xi}{2\xi}\, r^{\frac{2\left(1+\overline{\Lambda}\xi\right)}{2-\overline{\Lambda}\xi}} \tag{3.54}$$

$\overline{\mathcal{C}}$ being an arbitrary positive constant, in order to ensure the positiveness of λ^{s} as a consistency condition on plastic multiplier.

In the case of a pressure-independent local plastic behaviour (namely, for $\xi \to +\infty$), previous solution reduces to

$$d_{\mathrm{r}}(r) = \overline{\mathcal{C}}\,\frac{\overline{\Lambda}}{r^3}, \qquad d_\theta(r) = -\overline{\mathcal{C}}\,\frac{\overline{\Lambda}}{2r^3} \tag{3.55}$$

$$v_{\mathrm{r}}(r) = -\overline{\mathcal{C}}\,\frac{\overline{\Lambda}}{2r^2} \tag{3.56}$$

The corresponding interface strain-rate state $\mathbf{d}^{\mathcal{I}}$ straight results from kinematic admissibility conditions in Eqs. (3.48).

The case of sharp yield surfaces

Since the spherical symmetry of the problem under stake, $\boldsymbol{\sigma} \in \mathcal{Q}$ (see Eq. (3.4)) and principal stresses result in $\sigma_\theta = \sigma_\varphi \neq \sigma_r$. Therefore, owing to Eqs. (3.12) and (3.14), the corresponding limit stress state in the space of Lode coordinates (p, q, θ_σ) always belongs to an edge of the polyhedral yield surface $\partial\widehat{\mathcal{Y}}^{\mathrm{s}}$, locally achieving a triaxial expansion ($\sigma_r > \sigma_\theta = \sigma_\varphi$, that is $\iota = 1$ and $\theta_\sigma = 0$) or a triaxial compression ($\sigma_\theta = \sigma_\varphi > \sigma_r$, that is $\iota = -1$ and $\theta_\sigma = \pi/3$). Contiguous planar yield surfaces identifying an edge at $\theta_\sigma = 0$

(resp., at $\theta_\sigma = \pi/3$) are denoted as $\widehat{\mathcal{G}}^{\mathrm{s}}_{E^-} = 0$ and $\widehat{\mathcal{G}}^{\mathrm{s}}_{E^+} = 0$ (resp., $\widehat{\mathcal{G}}^{\mathrm{s}}_{C^-} = 0$ and $\widehat{\mathcal{G}}^{\mathrm{s}}_{C^+} = 0$), with

$$\widehat{\mathcal{G}}^{\mathrm{s}}_{E^-} = \left[\left(\sigma_{\mathrm{r}} - \frac{\sigma_\theta + \sigma_\varphi}{2}\right) c_\beta + (\sigma_\theta - \sigma_\varphi)\,\frac{\sqrt{3}}{2} s_\beta - 3h\right] \xi + \sigma_{\mathrm{r}} + \sigma_\theta + \sigma_\varphi \tag{3.57}$$

$$\widehat{\mathcal{G}}^{\mathrm{s}}_{E^+} = \left[\left(\sigma_{\mathrm{r}} - \frac{\sigma_\theta + \sigma_\varphi}{2}\right) c_\beta + (\sigma_\varphi - \sigma_\theta)\,\frac{\sqrt{3}}{2} s_\beta - 3h\right] \xi + \sigma_{\mathrm{r}} + \sigma_\theta + \sigma_\varphi \tag{3.58}$$

$$\widehat{\mathcal{G}}^{\mathrm{s}}_{C^-} = \left[\left(\sigma_\theta - \frac{\sigma_{\mathrm{r}} + \sigma_\varphi}{2}\right) c_\beta + (\sigma_\varphi - \sigma_{\mathrm{r}})\,\frac{\sqrt{3}}{2} s_\beta - 3h\right] \xi + \sigma_{\mathrm{r}} + \sigma_\theta + \sigma_\varphi \tag{3.59}$$

$$\widehat{\mathcal{G}}^{\mathrm{s}}_{C^+} = \left[\left(\sigma_\varphi - \frac{\sigma_{\mathrm{r}} + \sigma_\theta}{2}\right) c_\beta + (\sigma_\theta - \sigma_{\mathrm{r}})\,\frac{\sqrt{3}}{2} s_\beta - 3h\right] \xi + \sigma_{\mathrm{r}} + \sigma_\theta + \sigma_\varphi \tag{3.60}$$

where reference is made to the case of a pressure-dependent plastic behaviour ($\xi < +\infty$).

Accordingly, the edge normality law in Eq. (3.22) allows to determine the corresponding plastically-admissible strain-rate fields as

$$\mathbf{d}^{\mathrm{E}} = \lambda^{\mathrm{s}}_{\mathrm{E}^-} \frac{\partial \widehat{\mathcal{G}}^{\mathrm{s}}_{E^-}}{\partial \boldsymbol{\sigma}} + \lambda^{\mathrm{s}}_{\mathrm{E}^+} \frac{\partial \widehat{\mathcal{G}}^{\mathrm{s}}_{E^+}}{\partial \boldsymbol{\sigma}} \tag{3.61}$$

$$\mathbf{d}^{\mathrm{C}} = \lambda^{\mathrm{s}}_{\mathrm{C}^-} \frac{\partial \widehat{\mathcal{G}}^{\mathrm{s}}_{C^-}}{\partial \boldsymbol{\sigma}} + \lambda^{\mathrm{s}}_{\mathrm{C}^+} \frac{\partial \widehat{\mathcal{G}}^{\mathrm{s}}_{C^+}}{\partial \boldsymbol{\sigma}} \tag{3.62}$$

$\lambda^{\mathrm{s}}_{\mathrm{E}^\pm}$ and $\lambda^{\mathrm{s}}_{\mathrm{C}^\pm}$ being positive plastic multipliers. In particular, the following plastically-admissible strain-rate components result

$$d^{\mathrm{E}}_{\mathrm{r}} = (c_\beta \xi + 1)(\lambda^{\mathrm{s}}_{\mathrm{E}^-} + \lambda^{\mathrm{s}}_{\mathrm{E}^+}) \tag{3.63}$$

$$d^{\mathrm{E}}_\theta = \lambda^{\mathrm{s}}_{\mathrm{E}^-} \left[-\left(c_\beta - \sqrt{3} s_\beta\right) \frac{\xi}{2} + 1\right] + \lambda^{\mathrm{s}}_{\mathrm{E}^+} \left[-\left(c_\beta + \sqrt{3} s_\beta\right) \frac{\xi}{2} + 1\right] \tag{3.64}$$

$$d^{\mathrm{E}}_\varphi = \lambda^{\mathrm{s}}_{\mathrm{E}^-} \left[-\left(c_\beta + \sqrt{3} s_\beta\right) \frac{\xi}{2} + 1\right] + \lambda^{\mathrm{s}}_{\mathrm{E}^+} \left[-\left(c_\beta - \sqrt{3} s_\beta\right) \frac{\xi}{2} + 1\right] \tag{3.65}$$

$$d^{\mathrm{C}}_{\mathrm{r}} = \left[-\left(c_\beta + \sqrt{3} s_\beta\right) \frac{\xi}{2} + 1\right] \left(\lambda^{\mathrm{s}}_{\mathrm{C}^-} + \lambda^{\mathrm{s}}_{\mathrm{C}^+}\right) \tag{3.66}$$

$$d^{\mathrm{C}}_\theta = \lambda^{\mathrm{s}}_{\mathrm{C}^-} (c_\beta \xi + 1) + \lambda^{\mathrm{s}}_{\mathrm{C}^+} \left[-\left(c_\beta - \sqrt{3} s_\beta\right) \frac{\xi}{2} + 1\right] \tag{3.67}$$

$$d^{\mathrm{C}}_\varphi = \lambda^{\mathrm{s}}_{\mathrm{C}^+} (c_\beta \xi + 1) + \lambda^{\mathrm{s}}_{\mathrm{C}^-} \left[-\left(c_\beta - \sqrt{3} s_\beta\right) \frac{\xi}{2} + 1\right] \tag{3.68}$$

Owing to spherical symmetry, it must be verified that $d^{\mathrm{E}}_\theta = d^{\mathrm{E}}_\varphi$ and $d^{\mathrm{C}}_\theta = d^{\mathrm{C}}_\varphi$, leading to $\lambda^{\mathrm{s}}_{\mathrm{E}^-} = \lambda^{\mathrm{s}}_{\mathrm{E}^+} \equiv \lambda^{\mathrm{s}}_{\mathrm{E}}$ and $\lambda^{\mathrm{s}}_{\mathrm{C}^-} = \lambda^{\mathrm{s}}_{\mathrm{C}^+} \equiv \lambda^{\mathrm{s}}_{\mathrm{C}}$, respectively. Therefore, Eqs. (3.63) to (3.68) reduce to

$$d^{\mathrm{E}}_{\mathrm{r}} = 2\lambda^{\mathrm{s}}_{\mathrm{E}}(c_\beta \xi + 1)\,, \qquad d^{\mathrm{E}}_\theta = -\lambda^{\mathrm{s}}_{\mathrm{E}}(c_\beta \xi - 2) \tag{3.69}$$

$$d^{\mathrm{C}}_{\mathrm{r}} = -\lambda^{\mathrm{s}}_{\mathrm{C}} \left[\left(c_\beta + \sqrt{3} s_\beta\right) \xi - 2\right]\,, \qquad d^{\mathrm{C}}_\theta = \frac{\lambda^{\mathrm{s}}_{\mathrm{C}}}{2} \left[\left(c_\beta + \sqrt{3} s_\beta\right) \xi + 4\right] \tag{3.70}$$

Statically- and plastically-admissible stress fields in Eqs. (3.41) are enforced, leading

$\iota = \mathrm{sgn}(\sigma_\mathrm{r}(r) - \sigma_\theta(r))$ independent from r. Accordingly, for $\iota = +1$ (resp., $\iota = -1$), it results $\mathbf{d} = \mathbf{d}^\mathrm{E}$ (resp., $\mathbf{d} = \mathbf{d}^\mathrm{C}$) for any $r \in [R_\mathrm{i}, R_\mathrm{e}]$.

By combining Eqs. (3.69) and (3.70) with Eq. (3.47), plastic multipliers are obtained in the form

$$\lambda^\mathrm{s}_\mathrm{E}(r) = \widehat{\mathcal{C}}\, r^{-\frac{3c_\beta\xi}{c_\beta\xi-2}}\,, \qquad \lambda^\mathrm{s}_\mathrm{C}(r) = \widehat{\mathcal{C}}\, r^{-\frac{3(c_\beta+\sqrt{3}s_\beta)\xi}{(c_\beta+\sqrt{3}s_\beta)\xi+4}} \tag{3.71}$$

where $\widehat{\mathcal{C}}$ is an arbitrary positive constant, in order to ensure the positiveness of plastic multipliers.

Therefore, the local fully-admissible strain-rate kinematics, expressed in terms of fully-admissible stress fields in Eqs. (3.41), results in

$$d_\mathrm{r}(r) = 2\left(1+\widehat{\Lambda}\xi\right)\widehat{\mathcal{C}}\, r^{\frac{3\widehat{\Lambda}\xi}{2-\widehat{\Lambda}\xi}}\,, \qquad d_\theta(r) = \left(2-\widehat{\Lambda}\xi\right)\widehat{\mathcal{C}}\, r^{\frac{3\widehat{\Lambda}\xi}{2-\widehat{\Lambda}\xi}} \tag{3.72}$$

$$v_\mathrm{r}(r) = \left(2-\widehat{\Lambda}\xi\right)\widehat{\mathcal{C}}\, r^{\frac{2\left(1+\widehat{\Lambda}\xi\right)}{2-\widehat{\Lambda}\xi}} \tag{3.73}$$

where $\widehat{\Lambda} = \Lambda|_{\gamma=1}$ (see Eq. (3.36)).

When the pressure-independent plastic yield function in Eq. (3.14) is addressed (i.e., for $\xi \to +\infty$), similar analytical arguments allow to obtain

$$d_\mathrm{r}(r) = \widehat{\mathcal{C}}\,\frac{2\widehat{\Lambda}}{r^3}\,, \qquad d_\theta(r) = -\widehat{\mathcal{C}}\,\frac{\widehat{\Lambda}}{r^3} \tag{3.74}$$

$$v_\mathrm{r}(r) = -\widehat{\mathcal{C}}\,\frac{\widehat{\Lambda}}{r^2} \tag{3.75}$$

The corresponding interface strain-rate state $\mathbf{d}^\mathcal{I}$ straight results from kinematic admissibility conditions in Eqs. (3.48).

It is worth pointing out that, with respect to the local strain-rate and velocity fields in Eqs. (3.50) to (3.56) for a smooth yield surface, relationships (3.72) to (3.75) differ only for a constant term, the dependence on r being exactly the same. Nevertheless, as it will be shown in Section 3.6, the two kinematics completely coincide when arbitrary constants $\overline{\mathcal{C}}$ and $\widehat{\mathcal{C}}$ are computed via strain-rate based boundary conditions.

Remark 3 *Fully-admissible stresses (that is, equilibrated stresses at the limit state) and fully-admissible kinematics (that is, verifying both kinematic compatibility conditions and normality law) have been related each other via Eqs.* (3.49) *and* (3.50) *(for a smooth yield surface), or via Eqs.* (3.61) *and* (3.62) *(for a sharp yield surface), these latter thereby taking on the meaning of plastic constitutive laws.*

Accordingly, stress and strain-rate states provided in Sections 3.5.1 and 3.5.2, respectively, are simultaneously fully-admissible, and thereby they express the exact limit state for the hollow-sphere model with interface and undergoing isotropic boundary loadings.

Remark 4 *Since $\iota = \mathrm{sgn}(\sigma_r(r) - \sigma_\theta(r))$ is constant with respect to r, stress components in Eqs.* (3.41) *and velocity fields for both smooth (Eq.* (3.54)*) and sharp (Eq.* (3.73)*) yield*

surfaces comply with the following condition

$$r^2 v_r(r)\left[\sigma_\theta(r)-\sigma_r(r)\right] = const = \begin{cases} \dfrac{3}{2}\,\overline{\mathcal{C}}\,h\left(1-\dfrac{6\kappa}{2-\overline{\Lambda}\xi}\right)\ (R_e f^{1/3})^{\frac{6}{2-\overline{\Lambda}\xi}} \\ 3\,\widehat{\mathcal{C}}\,\xi h\left(1-\dfrac{6\kappa}{2-\widehat{\Lambda}\xi}\right)\ (R_e f^{1/3})^{\frac{6}{2-\widehat{\Lambda}\xi}} \end{cases} \tag{3.76}$$

which generalises, to the case of a general isotropic plastic matrix with interface effects, the result obtained by Perrin (1992) for even local yield functions (i.e., quadratic in stress components), as well as the observations provided by Monchiet and Kondo (2012) for a von Mises-Schleicher criterion.

In the case of a pressure-independent yield function, by referring to velocity fields in Eqs. (3.56) *and* (3.75)*, the following condition is obtained*

$$r^2 v_r(r)\left[\sigma_\theta(r)-\sigma_r(r)\right] = const = \begin{cases} \dfrac{3}{2}\,\overline{\mathcal{C}}\,h \\ 3\,\widehat{\mathcal{C}}\,h \end{cases} \tag{3.77}$$

the dependence on κ *disappearing.*

3.5.3 Illustrative computations

As a consistency assessment and with the aim to generalise available exact results, previously-provided general solution is firstly applied to the particular case of classical plastic behaviours summarised in Table 3.1.

In detail, as shown in Table 3.2, present results exactly recover for $\kappa \to 0^+$ available relationships provided in the case of porous materials (namely, without interface effects) by Thoré et al. (2009) for Drucker-Prager and Mohr-Coulomb criteria, and by Gurson (1977) and Cazacu et al. (2014) for von Mises and Tresca local plastic behaviours, respectively. Moreover, when interface effects are taken into account (namely, for $\kappa > 0$), available relationships for local stresses and macroscopic limit strength are generalised to the case of nanoporous media, thereby accounting for void-size effects, and also recovering the void-size-dependent solution proposed by Dormieux and Kondo (2010) for a von Mises plastic matrix.

By referring to criteria in Table 3.1, the influence of porosity f and of void-size effects on the macroscopic strength is depicted in Figs. 3.3a, 3.4a and 3.5a, wherein the dimensionless quantity $\Sigma_{\rm m}^{\rm c}/h$ is represented versus f and for different values of the dimensionless parameter κ introduced in Eq. (3.42). As expected, the magnitude of $|\Sigma_{\rm m}^{\rm c}|$ decreases with f. Moreover, when κ increases a significant improvement of the macroscopic strength features with respect to the case of porous materials (that is, for $\kappa \to 0^+$) is observed, for both triaxial expansion and triaxial compression, fully in agreement with available experimental and numerical evidence on void-size effects. As a matter of fact, an increase in κ corresponds, for a fixed value of the matrix strength parameter h, to an increase in the ratio $h^{\mathcal{I}}/R_{\rm i}$, and it results from a reduction in the void size. This effect is also highlighted in Fig. 3.6, wherein, for a fixed porosity value, it is shown that decreasing

Table 3.2 – Hollow sphere with interface effects (i.e., nanoporous materials with non vanishing values of $\kappa = h^{\mathcal{I}}/(R_{\rm i}h)$) under isotropic loadings. Exact local solution (stress, strain-rate and velocity fields) and exact macroscopic hydrostatic limit stress for strength criteria in Table 3.1. The case of negligible interface effects (i.e., porous materials) straight results for $\kappa \to 0^+$. Notation: $\overline{\mathcal{C}}$ (for a smooth yield surface) and $\widehat{\mathcal{C}}$ (for a sharp yield surface) are arbitrary constants; $\iota = +1$ (resp., $\iota = -1$) corresponds to a macroscopic triaxial compression (resp., expansion).

Criterion	Statics	Kinematics
vM, **Tr**	$\sigma_{\rm r} = 2\sigma_0\iota\left[\ln\left(\dfrac{R_{\rm e}f^{1/3}}{r}\right) - \kappa\right]$ $\sigma_\theta = 2\sigma_0\iota\left[-\dfrac{1}{2} + \ln\left(\dfrac{R_{\rm e}f^{1/3}}{r}\right) - \kappa\right]$ $\Sigma_{\rm m}^{\rm c} = 2\sigma_0\iota\left(\ln f^{1/3} - \kappa\right)$	$d_{\rm r}^{\rm vM} = \iota\dfrac{\overline{\mathcal{C}}}{r^3}$, $\quad d_{\rm r}^{\rm Tr} = \iota\dfrac{\sqrt{3}\,\widehat{\mathcal{C}}}{r^3}$ $d_\theta^{\rm vM} = -\dfrac{\iota}{2}\dfrac{\overline{\mathcal{C}}}{r^3}$, $\quad d_\theta^{\rm Tr} = -\dfrac{\iota}{2}\dfrac{\sqrt{3}\,\widehat{\mathcal{C}}}{r^3}$ $v_{\rm r}^{\rm vM} = -\dfrac{\iota}{2}\dfrac{\overline{\mathcal{C}}}{r^2}$, $\quad v_{\rm r}^{\rm Tr} = -\dfrac{\iota}{2}\dfrac{\sqrt{3}\,\widehat{\mathcal{C}}}{r^2}$
DP	$\sigma_{\rm r} = c\cot\phi\left[1 - (1-a\kappa)\left(\dfrac{R_{\rm e}f^{1/3}}{r}\right)^a\right]$ $\sigma_\theta = c\cot\phi\left[1 + \dfrac{\sin\phi + \iota\sqrt{3+\sin^2\phi}}{2\sin\phi - \iota\sqrt{3+\sin^2\phi}}(1-a\kappa)\left(\dfrac{R_{\rm e}f^{1/3}}{r}\right)^a\right]$ $\Sigma_{\rm m}^{\rm c} = c\cot\phi\left[1 - (1-a\kappa)\,f^{\frac{a}{3}}\right]$ with $\quad a = \dfrac{6\sin\phi}{2\sin\phi - \iota\sqrt{3+\sin^2\phi}}$	$d_{\rm r} = \dfrac{\sin\phi + \iota\sqrt{3+\sin^2\phi}}{3\sin\phi}\overline{\mathcal{C}}r^b$ $d_\theta = \dfrac{2\sin\phi - \iota\sqrt{3+\sin^2\phi}}{6\sin\phi}\overline{\mathcal{C}}r^b$ $v_{\rm r} = \dfrac{2\sin\phi - \iota\sqrt{3+\sin^2\phi}}{6\sin\phi}\overline{\mathcal{C}}r^{1+b}$ with $\quad b = \dfrac{3\iota\sqrt{3+\sin^2\phi}}{2\sin\phi - \iota\sqrt{3+\sin^2\phi}}$
MC	$\sigma_{\rm r} = c\cot\phi\left[1 - (1-a\kappa)\left(\dfrac{R_{\rm e}f^{1/3}}{r}\right)^a\right]$ $\sigma_\theta = c\cot\phi\left[1 + \dfrac{\sin\phi + \iota}{\sin\phi - \iota}(1-a\kappa)\left(\dfrac{R_{\rm e}f^{1/3}}{r}\right)^a\right]$ $\Sigma_{\rm m}^{\rm c} = c\cot\phi\left[1 - (1-a\kappa)\,f^{\frac{a}{3}}\right]$ with $\quad a = \dfrac{4\sin\phi}{\sin\phi - \iota}$	$d_{\rm r} = 3\dfrac{\sin\phi + \iota}{\sin\phi}\widehat{\mathcal{C}}r^b$ $d_\theta = \dfrac{3}{2}\dfrac{\sin\phi - \iota}{\sin\phi}\widehat{\mathcal{C}}r^b$ $v_{\rm r} = \dfrac{3}{2}\dfrac{\sin\phi - \iota}{\sin\phi}\widehat{\mathcal{C}}r^{1+b}$ with $\quad b = \dfrac{\sin\phi + 3\iota}{\sin\phi - \iota}$

κ (namely, increasing the void-size) leads to an asymptotic behaviour of the hydrostatic strength towards the porous case.

Furthermore, for von Mises and Tresca local plastic responses, a symmetric hydrostatic strength appears, the absolute value of the limit stress $\Sigma_{\mathrm{m}}^{\mathrm{c}}$ being the same under both macroscopic triaxial expansion ($\iota = -1$) and compression ($\iota = 1$), for any choice of f and κ. On the other hand, for a fixed value of f and in the case of Drucker-Prager and Mohr-Coulomb local yield functions, the compressive macroscopic limit stress ($\iota = 1$) is higher than the tensile one ($\iota = -1$), such a difference being reduced when the friction angle ϕ reduces. Moreover, proposed results highlight that an increase in ϕ tends to amplify the influence of the interface parameter κ (namely, of void-size effects).

For the sake of completeness, the velocity field at the limit state is addressed in Figs. 3.3b, 3.4b and 3.5b. In detail, the dimensionless velocity $v_{\mathrm{r}}^{*} = v_{\mathrm{r}}/(\mathcal{C}R_{\mathrm{e}}^{w})$ is represented versus the normalized radial coordinate $r^{*} = r/R_{\mathrm{e}}$ (for $r^{*} \geq f^{1/3}$), where $\mathcal{C}$ is equal to $\overline{\mathcal{C}}$ or $\widehat{\mathcal{C}}$, depending on the smoothness level of the local criterion, and where $w = -2$ (resp., $w = 1 + b$, parameter b being introduced in Table 3.2) for von Mises and Tresca criteria (resp., for Drucker-Prager and Mohr-Coulomb). Illustrative computations show that the local velocity decreases when the distance from the void increases, with a decay rate strongly dependent on the matrix plastic response. As for $\Sigma_{\mathrm{m}}^{\mathrm{c}}$, the velocity field experiences a symmetric behaviour in expansion and compression for von Mises and Tresca criteria, whereas dimensionless velocity values are higher in compression than in expansion for Drucker-Prager and Mohr-Coulomb plastic matrices, the reduction of the friction angle tending to reduce such an asymmetry.

Since the high flexibility of the adopted Bigoni-like yield function, proposed results allow to provide the exact local limit state under isotropic boundary loadings, as well as the corresponding macroscopic hydrostatic strength, also for a broad class of plastic behaviours of the solid matrix, not properly described via classical yield criteria. In this case, model parameters should be preliminarily calibrated on the basis of available evidence. Just as an illustrative example, Fig. 3.7 shows the results of a model-calibration procedure based on a constrained optimization fitting with respect to the numerical indications provided by Brach et al. (2016a) for a nanoscaled aluminium bulk sample. In detail, a sound description of the influence of the three isotropic stress invariants on local strength properties is provided, for a certain choice of model parameters complying with consistency requirements introduced in Section 3.3.

Finally, the influence of local criterion parameters on the proposed closed-form results is addressed in Figs. 3.8 and 3.9, wherein the normalized macroscopic hydrostatic strength $\Sigma_{\mathrm{m}}^{\mathrm{c}}/h$ is represented for different values of β, γ, and ξ, for both triaxial expansion ($\iota = -1$) and compression ($\iota = 1$), and addressing the cases of both negligible (Fig. 3.8) and non-negligible (Fig. 3.9) interface effects. Proposed results confirm that present solution allows to consistently account for void-size effects. Moreover, the variability of the macroscopic strength with β is shown to improve when γ increases and, for $\iota = -1$ (resp., $\iota = +1$), when ξ increases (resp., decreases), the case of a local pressure-independent plastic matrix (i.e., $\xi \to \infty$) resulting in upper (resp., lower) bounds for $\Sigma_{\mathrm{m}}^{\mathrm{c}}/h$.

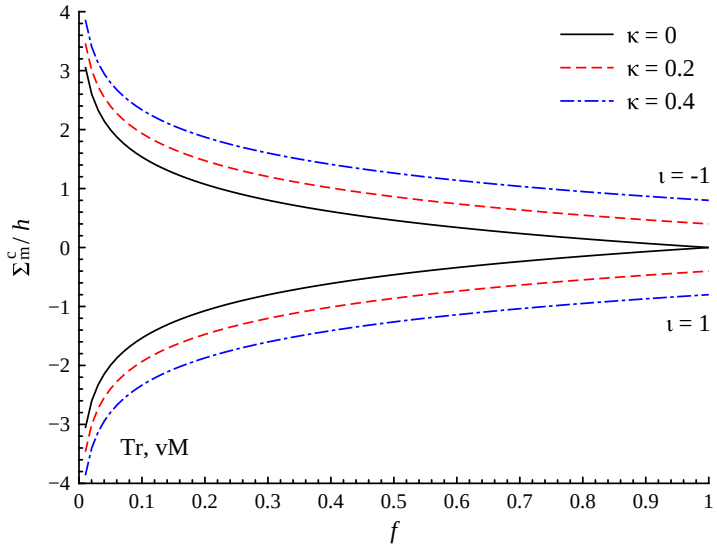

(a)

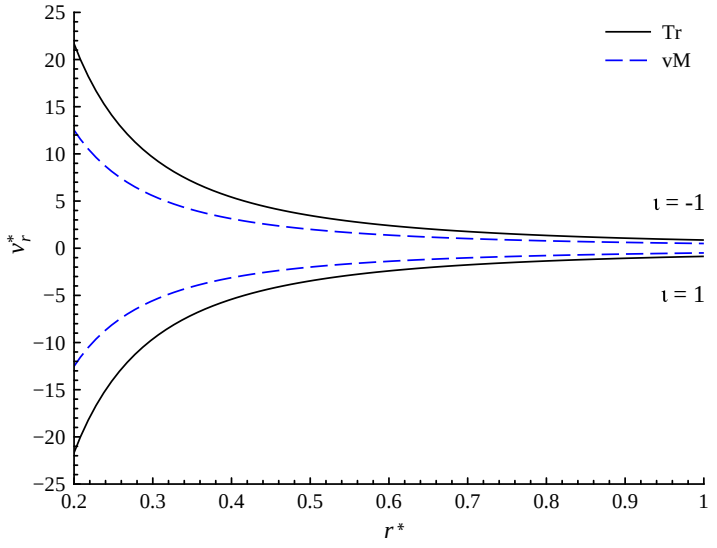

(b)

Figure 3.3 – Hollow sphere with (i.e., nanoporous materials, $\kappa \neq 0$) and without (i.e., porous materials, $\kappa \to 0^+$) interface effects: the case of von Mises (vM) and Tresca (Tr) local yield functions. (a) Normalized macroscopic hydrostatic limit stress Σ^c_m/h vs. porosity f. (b) Normalized velocity field $v^*_r = (v_r\, R_e^2)/\mathcal{C}$ vs. the normalized radius $r^* = r/R_e$ (where $\mathcal{C} = \overline{\mathcal{C}}$ for vM and $\mathcal{C} = \widehat{\mathcal{C}}$ for Tr), curves being defined for $r^* \geq f^{1/3}$.

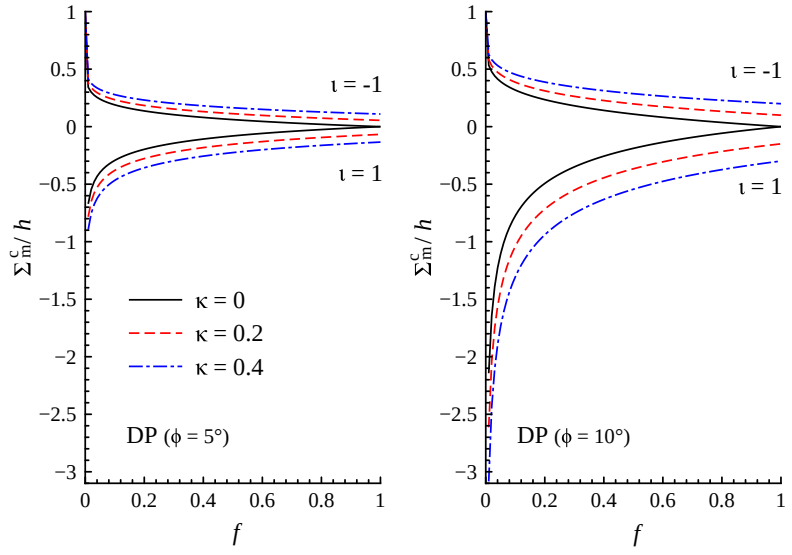

(a)

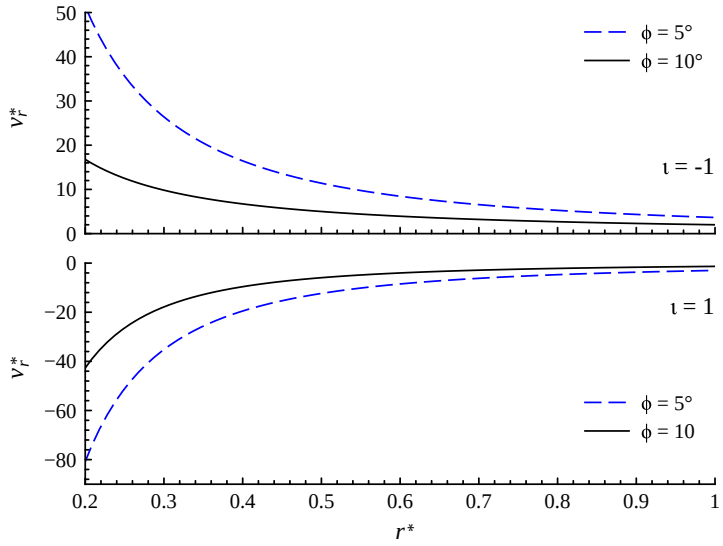

(b)

Figure 3.4 – Hollow sphere with (i.e., nanoporous materials, $\kappa \neq 0$) and without (i.e., porous materials, $\kappa \to 0^+$) interface effects: the case of Drucker-Prager (DP) local yield function for different values of the friction angle ϕ. (a) Normalized macroscopic hydrostatic limit stress Σ^c_m/h vs. porosity f. (b) Normalized velocity field $v^*_r = v_r/(\overline{\mathcal{C}} R_e^{1+b})$ vs. the normalized radius $r^* = r/R_e$ (parameter b is introduced in Table 3.2), curves being defined for $r^* \geq f^{1/3}$.

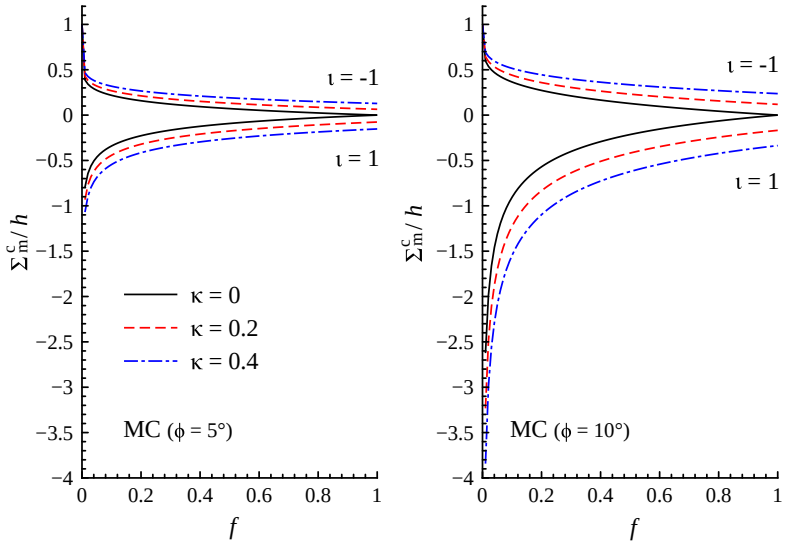

(a)

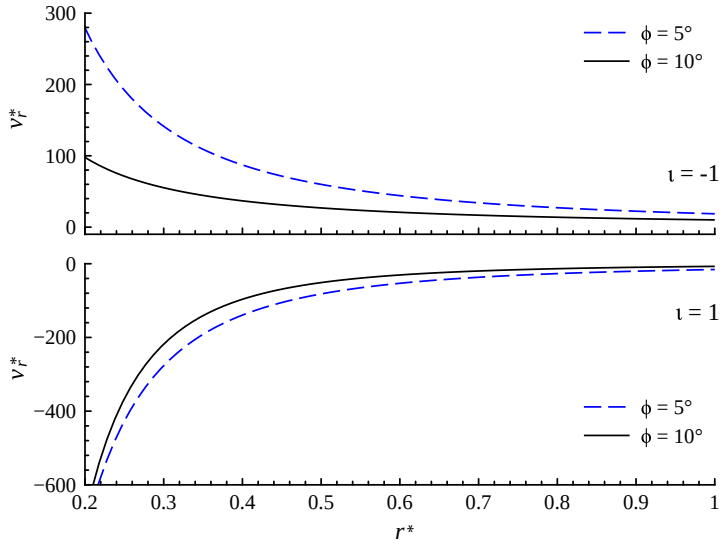

(b)

Figure 3.5 – Hollow sphere with (i.e., nanoporous materials, $\kappa \neq 0$) and without (i.e., porous materials, $\kappa \to 0^+$) interface effects: the case of Mohr-Coulomb (MC) local yield function for different values of the friction angle ϕ. (a) Normalized macroscopic hydrostatic limit stress $\Sigma_{\mathrm{m}}^{\mathrm{c}}/h$ vs. porosity f. (b) Normalized velocity field $v_{\mathrm{r}}^* = v_{\mathrm{r}}/(\widehat{\mathcal{C}} R_{\mathrm{e}}^{1+b})$ vs. the normalized radius $r^* = r/R_{\mathrm{e}}$ (parameter b is introduced in Table 3.2), curves being defined for $r^* \geq f^{1/3}$.

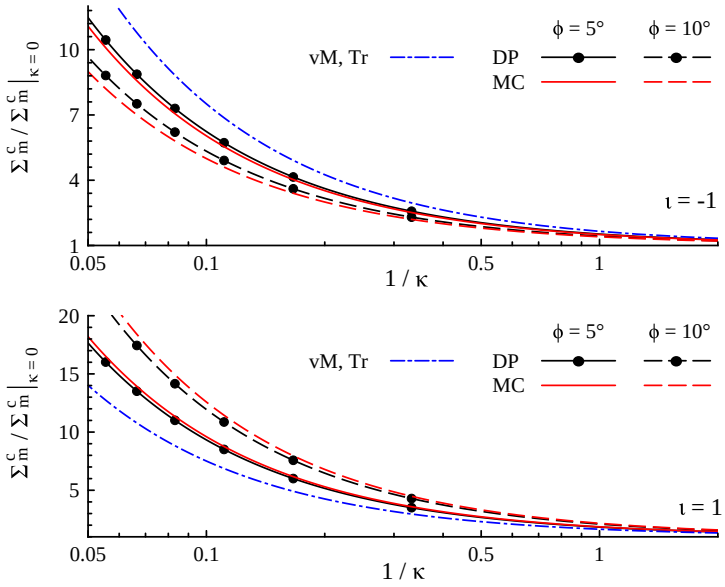

Figure 3.6 – Macroscopic hydrostatic limit stress normalized with respect to the corresponding value for $\kappa = 0$ ($\Sigma_{\rm m}^{\rm c}/\Sigma_{\rm m}^{\rm c}|_{\kappa=0}$) vs. $1/\kappa$ (the latter quantity being proportional to the void size $R_{\rm i}$) and for $f = 1\%$. Model parameters are set referring to local yield criteria in Table 3.1.

3.6 Towards novel limit analysis approaches for nanoporous materials

As highlighted in Section 3.1, the modelling strategy introduced by Gurson (1977) in the framework of a kinematic limit analysis approach (recently adopted for pressure-dependent -or independent- plastic matrices accounting -or not- for stress Lode angle effects) is recognized to be consistent and effective in order to establish accurate strength estimates for porous and nanoporous materials under arbitrary loadings. To this aim, the starting point is represented by the definition of a suitable trial kinematics based on the exact velocity field at the limit state for an isotropically-loaded hollow sphere without or with interface effects.

Aiming to formulate the corresponding limit-analysis problem, let the hollow sphere in Fig. 3.1 be subjected, at the external boundary, to the velocity field $\mathbf{v}_{\rm e}(\theta,\varphi)$, and let the set

$$\mathcal{BC}_{\rm v} = \{\mathbf{v}(\mathbf{r}) \quad \text{s.t.} \quad \mathbf{v} = \mathbf{v}_{\rm e} \quad \text{on } \partial\Omega_{\rm e}\} \tag{3.78}$$

be introduced. Moreover, let statically-admissible stress fields in $\mathcal{S}_\sigma$ (see Eq. (3.2a)) be defined not accounting for stress-based boundary conditions $\mathcal{BC}_\sigma$.

By considering statically-admissible stress (i.e., $(\boldsymbol{\sigma},\boldsymbol{\tau}) \in \mathcal{S}_\sigma$) and kinematically-admissible strain-rate (i.e., $(\mathbf{d},\mathbf{d}^{\mathcal{I}}) \in \mathcal{K}_{\rm d}$ with $\mathbf{v} \in \mathcal{BC}_{\rm v}$) local fields, the Hill's lemma holds

$$|\Omega|\,\boldsymbol{\Sigma} : \mathbf{D} = \int_{\Omega^{\rm s}} \boldsymbol{\sigma} : \mathbf{d}\, d\Omega + \int_{\partial\Omega_{\rm i}} \boldsymbol{\tau} : \mathbf{d}_{\mathbb{T}}^{\mathcal{I}}\, dA \tag{3.79}$$

$\boldsymbol{\Sigma}$ and $\mathbf{D}$ being the macroscopic stress and strain-rate tensors, respectively. Nevertheless,

the exterior power has to be lower or at the most equal to the maximum plastic dissipation $\mathcal{W}$ that can be afforded in Ω

$$|\Omega|\,\boldsymbol{\Sigma} : \mathbf{D} \leq \mathcal{W}\,, \quad \text{with} \quad \mathcal{W}(\mathbf{d}) = \int_{\Omega^{\mathrm{s}}} \pi^{\mathrm{s}}(\mathbf{d})\, d\Omega + \int_{\partial\Omega_{\mathrm{i}}} \pi^{\mathcal{I}}(\mathbf{d}^{\mathcal{I}})\, dA \tag{3.80}$$

where the equality sign in Eq. (3.80) holds at the limit state, that is by simultaneously considering statically and plastically-admissible stress, and kinematically and plastically-admissible strain-rate fields.

Accordingly, the macroscopic limit stress tensor $\boldsymbol{\Sigma}^{\mathrm{c}}$ results from

$$\boldsymbol{\Sigma}^{\mathrm{c}} = \frac{\partial \Pi(\mathbf{D})}{\partial \mathbf{D}} \tag{3.81}$$

where Π is the macroscopic support function, defined in the case of nanoporous materials as (see Dormieux and Kondo, 2010):

$$\Pi(\mathbf{D}) = \inf_{\substack{(\mathbf{d},\mathbf{d}^{\mathcal{I}})\,\in\,\mathcal{K}_{\mathrm{d}} \\ \mathbf{v}\,\in\,\mathcal{BC}_{\mathrm{v}}}} \left(\langle \pi^{\mathrm{s}}(\mathbf{d}) \rangle + \frac{1}{|\Omega|} \int_{\partial\Omega_{\mathrm{i}}} \pi^{\mathcal{I}}(\mathbf{d}^{\mathcal{I}})\, dA \right) \tag{3.82}$$

Aiming to furnish an estimate Π_{est} of the macroscopic support function and an upper bound of the macroscopic limit stress, instead of seeking the infimum in Eq. (3.82) over all the kinematically-admissible strain-rate states $(\mathbf{d}, \mathbf{d}^{\mathcal{I}})$, a particular microscopic trial velocity field $\mathbf{v}_{\mathrm{trial}} \in \mathcal{BC}_{\mathrm{v}}$ yielding to the local trial strain-rate fields $(\mathbf{d}_{\mathrm{trial}}, \mathbf{d}^{\mathcal{I}}_{\mathrm{trial}}) \in \mathcal{K}_{\mathrm{d}}$ may be chosen. It is worth noticing that an estimate for Π is significant only if the trial strain-rate state $(\mathbf{d}_{\mathrm{trial}}, \mathbf{d}^{\mathcal{I}}_{\mathrm{trial}})$ complies also with admissibility conditions in Eq. (3.99) or in Eqs. (3.26) and (3.27), that is if it is plastically-admissible.

In the particular case of isotropic boundary conditions, the set in Eq. (3.78) is defined by considering the uniform radial velocity $\mathbf{v}_{\mathrm{e}} = D_{\mathrm{m}} R_{\mathrm{e}} \mathbf{e}_{\mathrm{r}}$, where D_{m} is a constant strain-rate parameter. Accordingly, kinematically-admissible strain-rate fields and local velocity have to satisfy $(\mathbf{d}, \mathbf{d}^{\mathcal{I}}) \in (\mathcal{Q}, \mathcal{Q})$ and $\mathbf{v} = v_{\mathrm{r}}(r)\mathbf{e}_{\mathrm{r}}$, respectively.

In this light, and depending on the local yield function, the strain-rate field expressed by Eqs. (3.53) and (3.54), or by Eqs.(3.72) and (3.73), may be considered as a trial kinematics, provided that its plastic admissibility is verified and that the arbitrary constants $\overline{\mathcal{C}}$ and $\widehat{\mathcal{C}}$ are equal to

$$\overline{\mathcal{C}} = \frac{2\xi D_{\mathrm{m}} R_{\mathrm{e}}^{\,-\frac{3\overline{\Lambda}\xi}{2-\overline{\Lambda}\xi}}}{2-\overline{\Lambda}\xi}\,, \qquad \widehat{\mathcal{C}} = \frac{D_{\mathrm{m}} R_{\mathrm{e}}^{\,-\frac{3\widehat{\Lambda}\xi}{2-\widehat{\Lambda}\xi}}}{2-\widehat{\Lambda}\xi} \tag{3.83}$$

in order to comply with the boundary condition at $r = R_{\mathrm{e}}$, that is to comply with kinematic admissibility. Since this strain-rate state has been proven to be plastically-admissible for the hollow-sphere model under isotropic loadings, plastic admissibility requirement is surely satisfied. Therefore, in the case of a kinematic isotropic boundary condition, a possible trial kinematics for the smooth or sharp yield function, is respec-

tively expressed by

$$\overline{v}_{\mathrm{r,\,trial}}(r) = D_{\mathrm{m}} \left(\frac{R_{\mathrm{e}}}{r}\right)^{\frac{3\overline{\Lambda}\xi}{\overline{\Lambda}\xi-2}} , \qquad \widehat{v}_{\mathrm{r,\,trial}}(r) = D_{\mathrm{m}} \left(\frac{R_{\mathrm{e}}}{r}\right)^{\frac{3\widehat{\Lambda}\xi}{\widehat{\Lambda}\xi-2}} \tag{3.84}$$

As a result, an estimate for the macroscopic support function in Eq. (3.82) reads as

$$\begin{aligned} \overline{\Pi}_{\mathrm{est}} &= \frac{1}{|\Omega|}\left[\int_{\Omega_{\mathrm{s}}} \overline{\pi}^{\mathrm{s}}(\mathbf{d}_{\mathrm{trial}})\, d\Omega + \int_{\partial\Omega_{\mathrm{i}}} \overline{\pi}^{\mathcal{I}}(\mathbf{d}^{\mathcal{I}}_{\mathrm{trial}})\, dA\right] \\ &= 3D_{\mathrm{m}}\, h\xi \left[1 - f^{\,\frac{2}{2-\overline{\Lambda}\xi}} \left(1 - \kappa\, \frac{6}{2-\overline{\Lambda}\xi}\right)\right] \end{aligned} \tag{3.85}$$

$$\widehat{\Pi}_{\mathrm{est}} = 3D_{\mathrm{m}}\, h\xi \left[1 - f^{\,\frac{2}{2-\widehat{\Lambda}\xi}} \left(1 - \kappa\, \frac{6}{2-\widehat{\Lambda}\xi}\right)\right] \tag{3.86}$$

where the yield function with smooth (i.e., $\overline{\pi}^{\mathrm{s}}$ and $\overline{\pi}^{\mathcal{I}}$) or sharp (i.e., $\widehat{\pi}^{\mathrm{s}}$ and $\widehat{\pi}^{\mathcal{I}}$) deviatoric profiles is respectively considered.

By using Eq. (3.81), the following estimates for the macroscopic hydrostatic strength are obtained

$$\overline{\Sigma}^{\mathrm{c}}_{\mathrm{m,\,est}} = \frac{1}{3}\frac{\partial \overline{\Pi}_{\mathrm{est}}}{\partial D_{\mathrm{m}}} = h\xi \left[1 - f^{\,\frac{2}{2-\overline{\Lambda}\xi}} \left(1 - \kappa\, \frac{6}{2-\overline{\Lambda}\xi}\right)\right] \tag{3.87}$$

$$\widehat{\Sigma}^{\mathrm{c}}_{\mathrm{m,\,est}} = \frac{1}{3}\frac{\partial \widehat{\Pi}_{\mathrm{est}}}{\partial D_{\mathrm{m}}} = h\xi \left[1 - f^{\,\frac{2}{2-\widehat{\Lambda}\xi}} \left(1 - \kappa\, \frac{6}{2-\widehat{\Lambda}\xi}\right)\right] \tag{3.88}$$

resulting equal to the exact solution expressed in Eq. (3.45), and recovering the case corresponding to a yield function with smooth and sharp deviatoric profiles for $\Lambda = \overline{\Lambda}$ and $\Lambda = \widehat{\Lambda}$, respectively. Therefore, Eq. (3.84) provides the exact kinematics and Eqs. (3.85) and (3.86) provide the exact macroscopic support function under isotropic loads, that is $\Pi = \overline{\Pi}_{\mathrm{est}}$ (for $0 \leq \gamma < 1$) and $\Pi = \widehat{\Pi}_{\mathrm{est}}$ (for $\gamma = 1$).

Remark 5 *Owing to Eqs.* (3.81) *and* (3.85) *(or* (3.86)*),* $\mathrm{sgn}(D_m) = \mathrm{sgn}(\Sigma^c_m) = -\iota$*, resulting in a macroscopic triaxial expansion (resp., compression) for* $D_m > 0$ *(resp.,* $D_m < 0$*). Moreover, since the positiveness of* $\overline{\mathcal{C}}$ *and* $\widehat{\mathcal{C}}$ *in Eq.* (3.83) *resulting from the positiveness of plastic multiplier in the normality law (see Eqs.* (3.51) *and* (3.71)*), plastically-admissible strain-rate states can be attained only if the macroscopic strain-rate parameter* D_m *satisfies the following conditions*

$$\mathrm{sgn}(D_m) = \mathrm{sgn}\left(\frac{\xi}{2-\overline{\Lambda}\xi}\right) , \qquad \mathrm{sgn}(D_m) = \mathrm{sgn}\left(\frac{1}{2-\widehat{\Lambda}\xi}\right) \tag{3.89}$$

where local yield functions $\overline{\mathcal{G}}^s$ *and* $\widehat{\mathcal{G}}^s$ *are respectively addressed.*

Fully in agreement with Remark 1, for a matrix behaviour complying with $\xi > 2/|\Lambda|$*, consistency conditions in Eqs.* (3.83) *and* (3.89) *are verified for any choice of* D_m*, the hollow sphere thereby achieving the limit state in both macroscopic expansion and compression states. This is the case of classical strength criteria in Table 3.1, as shown in Figs. 3.3a, 3.4a and 3.5a. On the other hand, when* $\xi < 2/|\Lambda|$*, only a macroscopic*

triaxial-expansion limit state ($\iota = -1$) can be reached, whereas for $\xi = 2/|\Lambda|$ the hollow sphere does not experience any limit state under isotropic loadings, thereby resulting in a pressure-independent macroscopic plastic response.

As a matter of fact, in the general case of triaxial loadings and following the modelling strategy proposed by Gurson (1977), effective macroscopic strength estimates for porous and nanoporous materials can be derived via Eqs. (3.81) and (3.82) by considering a trial velocity field defined as

$$\mathbf{v}_{\text{trial}}(\mathbf{r}) = \mathbf{E} \cdot \mathbf{r} + \frac{v_{\text{r}}(r)}{r}\mathbf{r} \tag{3.90}$$

where $\mathbf{E}$ is a homogeneous strain-rate tensor and where v_{r} is a local heterogeneous part corresponding to the exact velocity field at the limit state under isotropic loadings, such that the kinematic admissibility condition $\mathbf{v}_{\text{trial}} \in \mathcal{BC}_{\text{v}}$ is satisfied (see Eq. (3.84)). Such a modelling technique has been already adopted by Anoukou et al. (2016) and by Dormieux and Kondo (2010) in the case of Mohr-Coulomb and von Mises matrix plastic behaviours, respectively.

In this framework and since all previous considerations, it clearly appears that the use of the exact solution proposed in Eq. (3.54) or (3.73), or equivalently in Eqs. (3.84), for representing the local heterogeneous part $v_{\text{r}}(r)$ of a general trial kinematics as in Eq. (3.90) paves the way towards novel and accurate macroscopic strength criteria for porous and nanoporous materials, locally not obeying to classical strength criteria and accounting for general triaxiality levels.

3.7 Concluding remarks

In this Chapter, the microscopic limit state of a hollow sphere, representative of a particular microstructure for porous and nanoporous materials, is exactly determined in the case of isotropic loading conditions. Void-size effects associated to the possible nanosize of voids (Biener et al., 2005, 2006; Hakamada and Mabuchi, 2007) have been accounted for via a coherent and imperfect homogeneous interface at the cavity boundary. The hollow sphere has been assumed to be comprised of a rigid-ideal-plastic material, obeying to a general isotropic strength criterion. Aiming to take into account a broad class of pressure-sensitive limit responses (typical of many ductile, frictional and cohesive media), as well as to allow for a certain flexibility in reproducing evidence-based data, the local plastic behaviour has been represented via a general isotropic yield function. In detail, the latter has been defined by considering linear meridian strength profiles and the deviatoric function proposed by Bigoni and Piccolroaz (2004). The case of yield surfaces presenting sharp vertices in the deviatoric planes has been carefully addressed. As a first step towards more comprehensive studies based on kinematic limit-analysis approaches, the corresponding support function and its admissibility conditions have been explicitly determined, distinguishing between cases of smooth and sharp deviatoric profiles.

The microscopic limit state and the macroscopic limit stress have been derived in the case of both negligible (i.e., for materials with large values of the void radius, namely for

porous materials) and significant void-size effects (i.e., for nanoporous materials). As a result, closed-form relationships for local strain-rate, velocity and stress fields have been obtained, identifying the exact limit state for the hollow-sphere model under isotopic boundary loadings.

As a consistency assessment, established results fully recover available analytical expressions (Cazacu et al., 2014; Gurson, 1977; Thoré et al., 2009) deduced in the case of negligible void-size effects, and associated to classical local plastic behaviours. Furthermore, the relationship between stress and velocity components provided by Perrin (1992) for even isotropic strength criteria, and generalised to the case of a von Mises-Schleicher plastic matrix by Monchiet and Kondo (2012), has been proven to hold also in the case of a general non-even isotropic local plastic behaviour, presenting -or not- sharp vertices in the deviatoric plane and accounting -or not- for interface effects. The proposed general expression of the macroscopic hydrostatic strength has been also proven to straight recover, in the case of a von Mises plastic matrix, the results proposed by Gurson (1977) for porous materials and by Dormieux and Kondo (2010) for nanoporous ones.

On the other hand, since the high flexibility of the adopted local strength criterion, proposed results allow to provide the exact local limit state under isotropic boundary loadings, as well as the corresponding macroscopic hydrostatic strength, also for a wide range of local plastic behaviours, possibly-affected by all the three isotropic stress invariants and that may not be properly described via classical yield models.

Proposed illustrative computations confirm that an effective description of void-size effects can be provided, resulting in an increase of the predicted macroscopic hydrostatic strength as the void radius decreases.

Finally, in the framework of a limit analysis approach, proposed general exact solutions could be used for building up effective trial fields useful to provide accurate strength estimates for porous and nanoporous materials, addressing arbitrary loading states and accounting for general local plastic behaviours. Accordingly, simply by setting bulk-material strength properties in agreement with experimental and/or numerical benchmarking evidence, proposed results open towards the consistent deduction of novel macroscopic strength criteria for porous and nanoporous materials, locally not obeying to classical strength criteria.

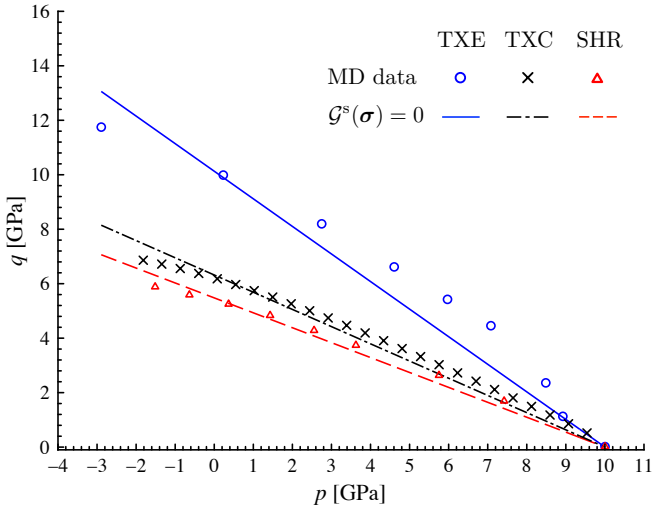

(a)

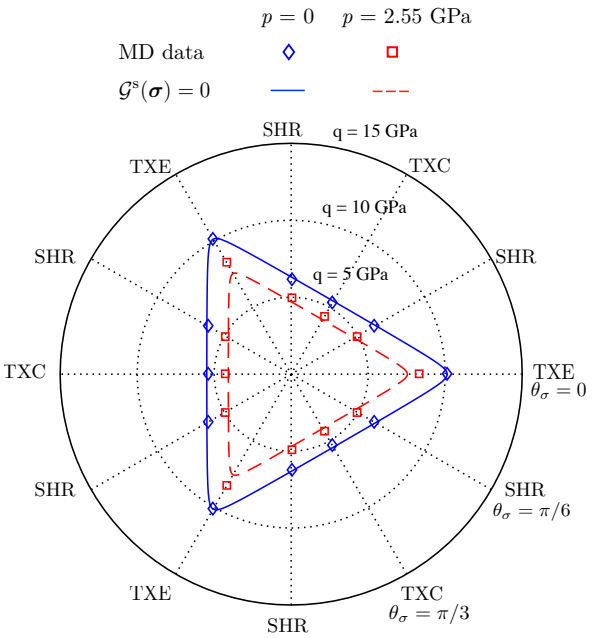

(b)

Figure 3.7 – Calibration of the adopted yield function $\mathcal{G}^s(\boldsymbol{\sigma})$ with respect to Molecular Dynamics-based data (denoted as MD) proposed by Brach et al. (2016a). (a) Meridian strength profiles for $\theta_\sigma = 0$ (TXE), $\theta_\sigma = \pi/6$ (SHR) and $\theta_\sigma = \pi/3$ (TXC). (b) Deviatoric strength profiles for different values of p. Values of model parameters resulting from a constrained optimization fitting: $\gamma = 0.99$, $\xi = 5.48$, $h = 1.82$ GPa and $\beta = 2$.

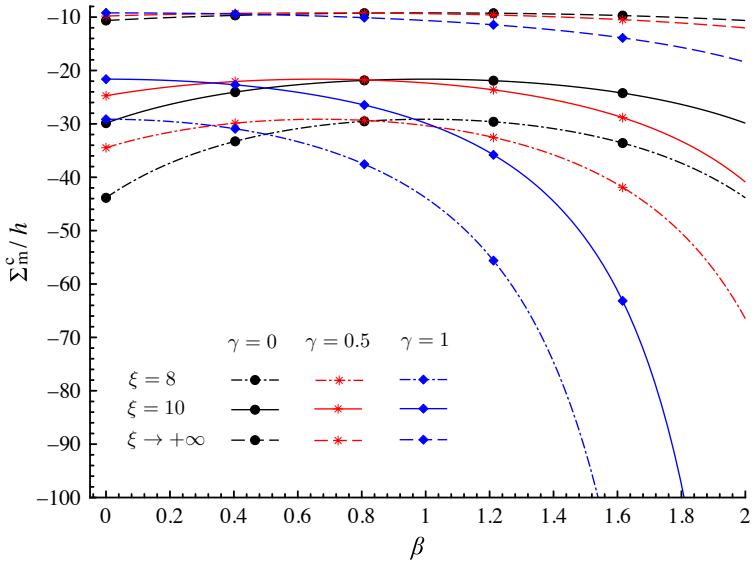

(a)

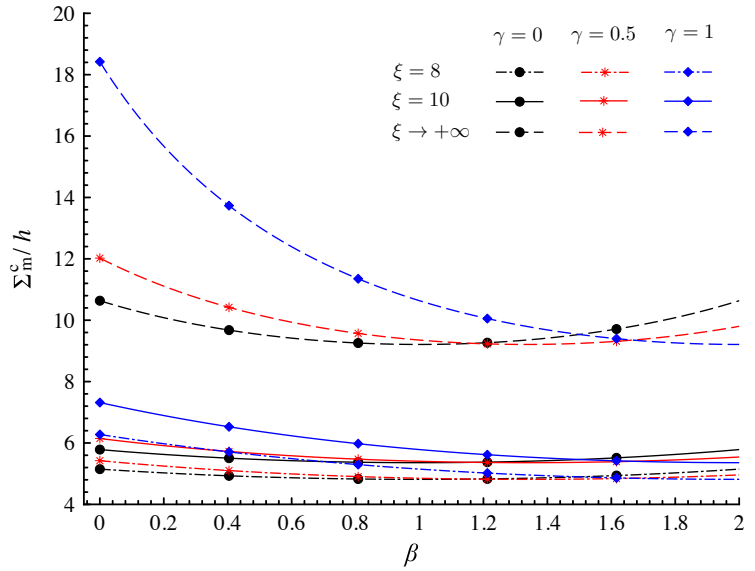

(b)

Figure 3.8 – Hollow sphere without interface effects (i.e., porous materials, $\kappa \to 0^+$) and in the case $f = 1\%$. Normalized macroscopic hydrostatic limit stress Σ_m^c/h for different values of model parameters β, ξ and γ. (a) Macroscopic triaxial compression ($\iota = +1$). (b) Macroscopic triaxial expansion ($\iota = -1$).

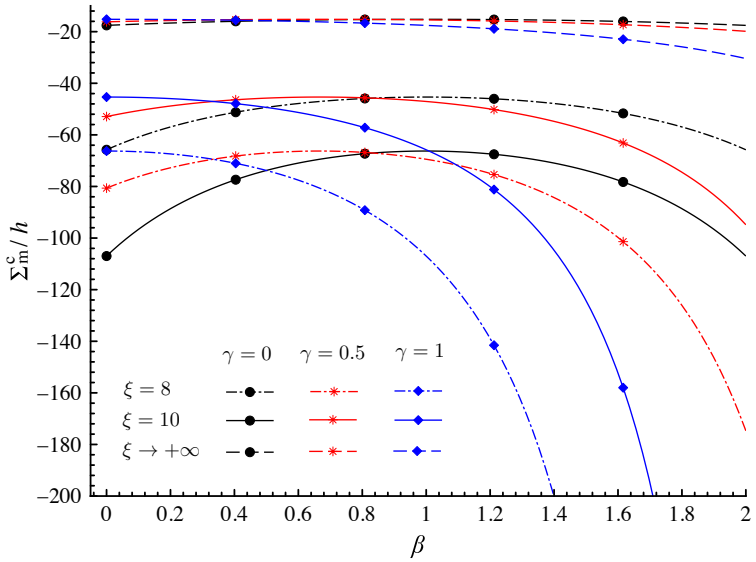

(a)

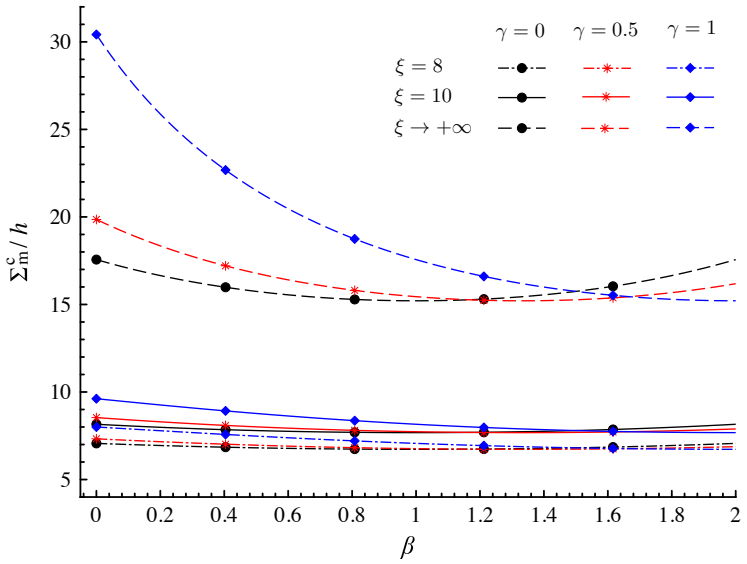

(b)

Figure 3.9 – Hollow sphere with interface effects (i.e., nanoporous materials, for $\kappa = 1$) and in the case $f = 1\%$. Normalized macroscopic hydrostatic limit stress Σ_m^c/h for different values of model parameters β, ξ and γ. (a) Macroscopic triaxial compression ($\iota = +1$). (b) Macroscopic triaxial expansion ($\iota = -1$).

3.A Support function for smooth yield surfaces

Reference is made to the theoretical framework established by Lemarchand et al. (2015). Accordingly, the yield function $\overline{\mathcal{G}}^{\mathrm{s}}$, defined via Eqs. (3.6) to (3.8) for $0 \leq \gamma < 1$, can be expressed as

$$\overline{\mathcal{G}}^{\mathrm{s}}(\boldsymbol{\sigma}) = \sqrt{J_2^\sigma} - \mathcal{F}(I_1^\sigma, \theta_\sigma), \qquad \text{with} \qquad \mathcal{F}(I_1^\sigma, \theta_\sigma) = \sqrt{3} g \left(h - \frac{p}{\xi} \right) \tag{3.91}$$

Therefore, by applying the normality law in Eq. (3.3b), the hydrostatic strain-rate ($d_{\mathrm{m}} = \operatorname{tr} \mathbf{d}/3$) and the deviatoric part ($\mathbf{d}_{\mathrm{d}} = \mathbf{d} - d_{\mathrm{m}}\mathbf{1}$) of the strain-rate tensor $\mathbf{d}$ result, respectively, in

$$d_{\mathrm{m}} = -\lambda^{\mathrm{s}} \frac{\partial \mathcal{F}}{\partial I_1^\sigma}, \qquad \mathbf{d}_{\mathrm{d}} = \lambda^{\mathrm{s}} \left(\frac{\boldsymbol{\sigma}_{\mathrm{d}}}{2\sqrt{J_2^\sigma}} - \frac{\partial \mathcal{F}}{\partial \theta_\sigma} \frac{\partial \theta_\sigma}{\partial \boldsymbol{\sigma}} \right) \tag{3.92}$$

where

$$\frac{\partial \theta_\sigma}{\partial \boldsymbol{\sigma}} = \frac{\sqrt{3}}{2\sqrt{J_2^\sigma} \sin(3\theta_\sigma)} \left[\frac{2}{3}\mathbf{1} + \frac{3}{2} \frac{J_3^\sigma}{(J_2^\sigma)^2} \boldsymbol{\sigma}_{\mathrm{d}} - \frac{(\boldsymbol{\sigma}_{\mathrm{d}})^2}{J_2^\sigma} \right] . \tag{3.93}$$

Since the following equalities hold

$$\mathbf{1} : \frac{\partial \theta_\sigma}{\partial \boldsymbol{\sigma}} = 0, \qquad \boldsymbol{\sigma}_{\mathrm{d}} : \frac{\partial \theta_\sigma}{\partial \boldsymbol{\sigma}} = 0, \qquad (\boldsymbol{\sigma}_{\mathrm{d}})^2 : \frac{\partial \theta_\sigma}{\partial \boldsymbol{\sigma}} = -\sqrt{\frac{J_2^\sigma}{3}} \sin(3\theta_\sigma) \tag{3.94}$$

the first ($I_1^{\mathrm{d}} = \operatorname{tr} \mathbf{d}$) and the second-order deviatoric ($J_2^{\mathrm{d}} = \operatorname{tr} \mathbf{d}_{\mathrm{d}}^2/2$) strain-rate invariants can be expressed as

$$I_1^{\mathrm{d}} = -3\lambda^{\mathrm{s}} \frac{\partial \mathcal{F}}{\partial I_1^\sigma} \tag{3.95a}$$

$$J_2^{\mathrm{d}} = \frac{(\lambda^{\mathrm{s}})^2}{4} \left(1 + F^2 \right), \quad \text{with} \quad F(\theta_\sigma) = \frac{1}{\mathcal{F}} \frac{\partial \mathcal{F}}{\partial \theta_\sigma} = \frac{1}{g} \frac{dg}{d\theta_\sigma} \tag{3.95b}$$

Accordingly, by using Eqs. (3.94), and by solving the plastic multiplier λ^{s} from Eq. (3.95b), the local plastic dissipation results in

$$\boldsymbol{\sigma} : \mathbf{d} = I_1^\sigma d_{\mathrm{m}} + \frac{2}{\sqrt{1+F^2}} \sqrt{J_2^\sigma J_2^{\mathrm{d}}} \tag{3.96}$$

In agreement with Eq. (3.15), the supremum of Eq. (3.96) has to be computed over all the local stress states complying with the strength criterion $\mathcal{G}^{\mathrm{s}}(\boldsymbol{\sigma}) \leq 0$. The latter, due to Eqs. (3.5) and (3.91), can be recast as

$$I_1^\sigma \leq 3h\xi - \frac{\xi}{g} \sqrt{3 J_2^\sigma} \tag{3.97}$$

which, combined with Eq. (3.96), yields to

$$\boldsymbol{\sigma} : \mathbf{d} \leq \underbrace{\left(-\frac{\sqrt{3}}{3} \frac{\xi}{g} I_1^{\mathrm{d}} + \frac{2}{\sqrt{1+F^2}} \sqrt{J_2^{\mathrm{d}}} \right)}_{\mathcal{A}} \sqrt{J_2^\sigma} + h\xi I_1^{\mathrm{d}} \tag{3.98}$$

Since there not exists a positive real number $\mathcal{M}$ such that $\sqrt{J_2^\sigma} \leq \mathcal{M}$ for every stress tensor $\boldsymbol{\sigma}$, the supremum of the plastic dissipation $(\boldsymbol{\sigma} : \mathbf{d})$ is infinity if $\mathcal{A} > 0$. Accordingly, the local support function $\overline{\pi}^{\mathrm{s}}$ results in

$$\overline{\pi}^{\mathrm{s}}(\mathbf{d}) = \begin{cases} h\xi I_1^{\mathrm{d}} & \text{if} \quad \dfrac{I_1^{\mathrm{d}}}{\sqrt{J_2^{\mathrm{d}}}} \geq \dfrac{1}{\xi}\,\Gamma(\theta_\sigma) \qquad \text{(i.e., if } \mathcal{A} \leq 0) \\ +\infty & \text{otherwise} \end{cases} \tag{3.99}$$

where the admissibility condition on the strain-rate triaxiality ratio $I_1^{\mathrm{d}}/\sqrt{J_2^{\mathrm{d}}}$ is expressed in terms of the strictly-positive function (due to the strict positiveness of $g(\theta_\sigma)$)

$$\Gamma(\theta_\sigma) = 2\sqrt{3}\frac{g(\theta_\sigma)}{\sqrt{1+F^2(\theta_\sigma)}} \tag{3.100}$$

depicted in Fig. 3.10 with respect to the stress Lode angle θ_σ and for different values of model parameters. In detail, results in Fig. 3.10 show that for $\gamma = 0$ function $\Gamma(\theta_\sigma)$ is constant, whereas for $0 < \gamma < 1$ the highest value of $\Gamma(\theta_\sigma)$ occurs for: triaxial compression (TXC) when $0 \leq \beta < 1$; both triaxial expansion (TXE) and compression (TXC) when $\beta = 1$; triaxial expansion (TXE) when $1 < \beta \leq 2$. It must be noticed that the requirement $0 \leq \gamma < 1$ allows to guarantee the continuity of $\Gamma(\theta_\sigma)$ for any values of θ_σ and β. On the other hand, when $\gamma = 1$ the function $\Gamma(\theta_\sigma)$ is not defined at sharp vertices of deviatoric yield profiles (i.e., for $\theta_\sigma = 0$ and/or for $\theta_\sigma = \pi/3$).

The dependence of Γ on the stress Lode angle θ_σ implicitly contains the dependence on the strain-rate Lode angle θ_{d} defined by $\cos 3\theta_{\mathrm{d}} = 3\sqrt{3}J_3^{\mathrm{d}}/(2{J_2^{\mathrm{d}}}^{3/2})$, where $J_3^{\mathrm{d}} = \operatorname{tr}\mathbf{d}_{\mathrm{d}}^3/3$ is the third deviatoric strain-rate invariant. In detail, the following relationship was provided by Lemarchand et al. (2015)

$$\cos(3\theta_{\mathrm{d}}) = \frac{\cos(3\theta_\sigma)(1-3F^2) + \sin(3\theta_\sigma)F(3-F^2)}{(1+F^2)^{3/2}} \tag{3.101}$$

It is worth observing that Eq. (3.99) allows to recover also the case of pressure-independent yield response for $\xi \to +\infty$. In this case, the admissibility condition reduces to $\mathcal{A} = 0$, since the case $\mathcal{A} < 0$ leads the quantity $h\xi I_1^{\mathrm{d}}$ to be infinite. Accordingly, for $\xi \to +\infty$, the support function $\overline{\pi}^{\mathrm{s}}$ in Eq. (3.99) becomes

$$\overline{\pi}^{\mathrm{s}}(\mathbf{d}) = \begin{cases} h\sqrt{J_2^{\mathrm{d}}}\,\Gamma(\theta_\sigma(\theta_{\mathrm{d}})) & \text{if} \quad I_1^{\mathrm{d}} = 0 \\ +\infty & \text{if} \quad I_1^{\mathrm{d}} \neq 0 \end{cases} \tag{3.102}$$

As shown in Table 3.1, relationships (3.99) and (3.102) recover, by a suitable choice of model parameters, the corresponding available expressions for von Mises and Drucker-Prager strength criteria (Salençon, 1983).

Similarly, interface strength properties can be described by introducing the local support function $\overline{\pi}^{\mathcal{I}}$ (see Eq. (3.16)). The latter, and the corresponding admissibility conditions, formally read as in Eqs. (3.99) and (3.102), and they are expressed in terms of the

local strain-rate tensor $\mathbf{d}^{\mathcal{I}}$ as:

$$\overline{\pi}^{\mathcal{I}}(\mathbf{d}^{\mathcal{I}}) = \begin{cases} h^{\mathcal{I}} \xi I_1^{\mathrm{d}}\big|_{\mathbf{r}=\mathbf{r}_{\mathrm{i}}} & \text{if} \quad \dfrac{I_1^{\mathrm{d}}}{\sqrt{J_2^{\mathrm{d}}}} \geq \dfrac{1}{\xi}\,\Gamma(\theta_\sigma(\theta_{\mathrm{d}})) \text{ on } \partial\Omega_{\mathrm{i}} \\ +\infty & \text{if} \quad \dfrac{I_1^{\mathrm{d}}}{\sqrt{J_2^{\mathrm{d}}}} < \dfrac{1}{\xi}\,\Gamma(\theta_\sigma(\theta_{\mathrm{d}})) \text{ on } \partial\Omega_{\mathrm{i}} \end{cases} \tag{3.103}$$

References

Anoukou, K., Pastor, F., Dufrenoy, P., & Kondo, D. (2016). Limit analysis and homogenization of porous materials with Mohr–Coulomb matrix. Part I: Theoretical formulation. *Journal of the Mechanics and Physics of Solids*, 91, 145-171.

Arico, A.S., Bruce, P., Scrosati, B., Tarascon, J.M., & Van Schalkwijk, W. (2005). Nanostructured materials for advanced energy conversion and storage devices. *Nature materials*, 4, 366-377.

Biener, J., Hodge, A.M., Hamza, A.V., Hsiung, L.M., & Satcher, J.H. (2005). Nanoporous Au: A high yield strength material. *Journal of Applied Physics*, 97, 024301.

Biener, J., Hodge, A.M., Hayes, J.R., Volkert, C.A., Zepeda-Ruiz, L.A., Hamza, A.V., & Abraham, F.F. (2006). Size Effects on the Mechanical Behaviour of Nanoporous Au. *Nano Letters*, 6, 2379-2382.

Bigoni, D. (2012). Nonlinear solid mechanics: bifurcation theory and material instability. Cambridge University Press.

Bigoni, D., & Piccolroaz, A., (2004). Yield criteria for quasibrittle and frictional materials. *International Journal of Solids and Structures*, 41, 2855-2878.

Brach, S., Dormieux, L., Kondo, D., & Vairo, G. (2016). A computational insight into void-size effects on strength properties of nanoporous materials. *Mechanics of Materials*, 101, 102-117.

Brach, S., Dormieux, L., Kondo, D., & Vairo, G. (2016). Nanoporous materials with a general isotropic plastic matrix: exact limit state under isotropic loadings. *International Journal of Plasticity*, DOI: 10.1016/j.ijplas.2016.10.007.

Cazacu, O., Revil-Baudard, B., Chandola, N., & Kondo, D. (2014). New analytical criterion for porous solids with Tresca matrix under axisymmetric loadings. *International Journal of Solids and Structures*, 51, 861-874.

Dormieux, L., & Kondo, D. (2010). An extension of Gurson model incorporating interface stress effects. *International Journal of Engineering Science*, 48, 575-581.

Drucker, D.C., Prager, W., & Greenberg, H.J., (1952). Extended limit design theorems for continuous media. *The Quarterly of Applied Mathematics*, 9, 381-389.

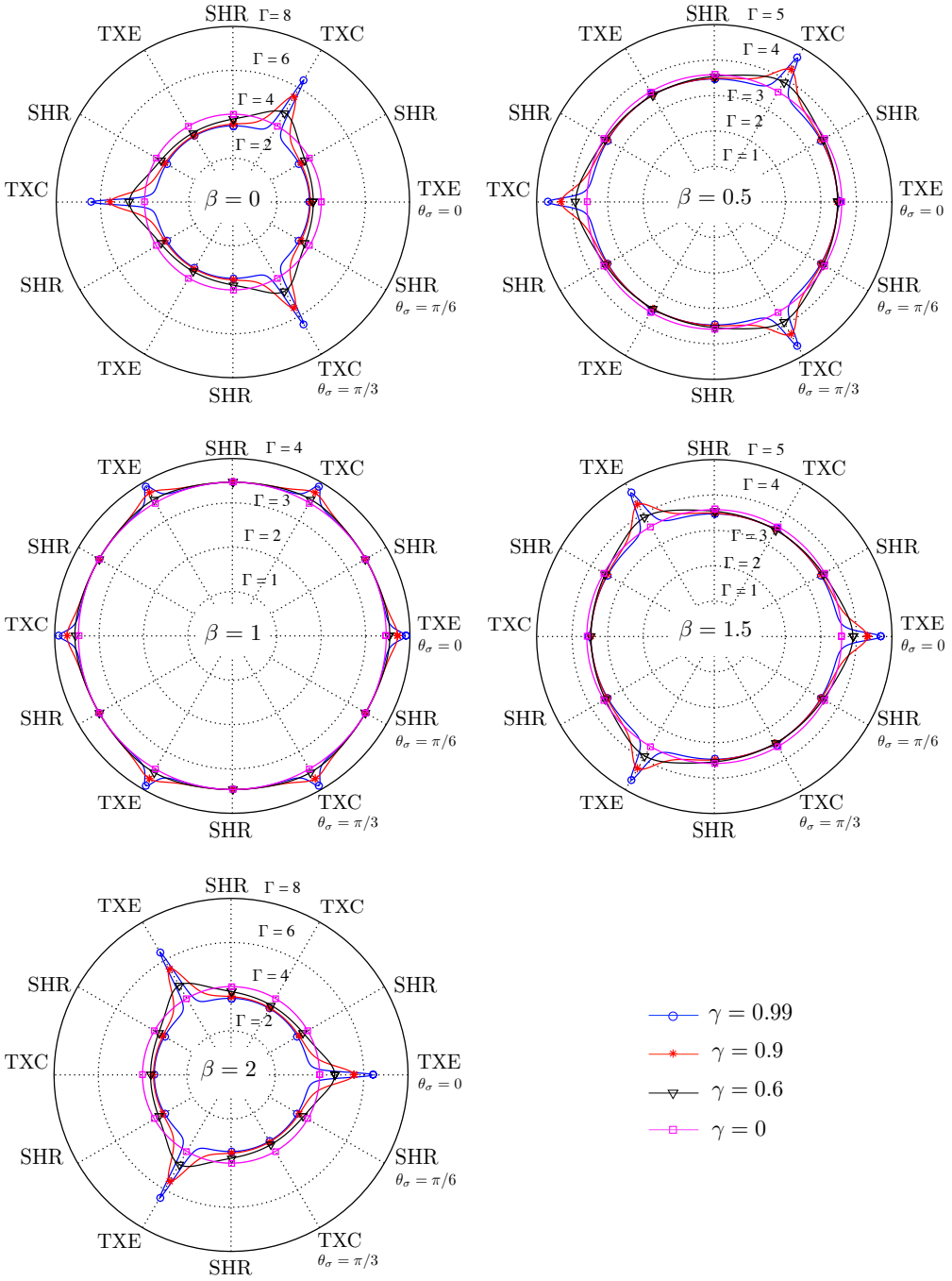

Figure 3.10 – Function $\Gamma(\theta_\sigma)$ introduced in Eq. (3.100) for different values of model parameters β and γ. TXE: triaxial expansion. TXC: triaxial compression. SHR: shear.

Duan, H.L., Wang, J., Huang, Z.P., & Luo, Z.Y. (2005). Stress concentration tensors of inhomogeneities with interface effects. *Mechanics of Materials*, 37, 723-736.

Duan, H.L., Wang, J., Huang, Z.P., & Karihaloo, B.L. (2005). Size-dependent effective elastic constants of solids containing nano-inhomogeneities with interface stress. *Journal of the Mechanics and Physics of Solids*, 53, 1574-1596.

Fritzen, F., Forest, S., Böhlke, T., Kondo, D., & Kanit, T. (2012). Computational homogenization of elasto-plastic porous metals. *International Journal of Plasticity*, 29, 102-119.

Goudarzi, T., Avazmohammadi, R., & Naghdabadi, R. (2010). Surface energy effects on the yield strength of nanoporous materials containing nanoscale cylindrical voids. *Mechanics of Materials*, 42, 852-862.

Guo, T., Faleskog, J., & Shih, C., (2008). Continuum modelling of a porous solid with pressure-sensitive dilatant matrix. *Journal of Mechanics and Physics of Solids*, 56, 2188-2212.

Gurson, A.L. (1977). Continuum theory of ductile rupture by void nucleation and growth: Part I. - Yield criterion and flow rules for porous ductile media. *Journal of Engineering Materials and Technology*, 99, 2-15.

Gurtin, M.E., & Murdoch, A.I. (1975). A continuum theory of elastic material surfaces. *Archive for Rational Mechanics and Analysis*, 57, 291-323.

Gurtin, M.E., & Murdoch, A.I. (1978). Surface stress in solids. *International Journal of Solids and Structures*, 14, 431-440.

Hakamada, M., & Mabuchi, M. (2007). Mechanical strength of nanoporous gold fabricated by dealloying. *Scripta Materialia*, 56, 1003-1006.

Haythornthwaite, R.M. (1985). A family of smooth yield surfaces. *Mechanics research communications*, 12(2), 87-91.

Jenkins, S.B. (2010). Nanoporous Materials: Types, Properties, and Uses. *Nova Science Publishers*.

Lemarchand, E., Dormieux, L., & Kondo, D. (2015). Lode's angle effect on the definition of the strength criterion of porous media. International *Journal for Numerical and Analytical Methods in Geomechanics*, 39(14), 1506-1526.

Le Quang, H., & He, Q.-C. (2007). Size-dependent effective thermoelastic properties of nanocomposites with spherically anisotropic phases. *Journal of the Mechanics and Physics of Solids*, 55, 1899-1931.

Lu, G.Q., Zhao, X.S., & Wei, T.K. (2004). Nanoporous materials: science and engineering. *Imperial College Press*.

Mi, C., Buttry, D.A., Sharma, P., & Kouris, D.A. (2011). Atomistic insights into dislocation-based mechanisms of void growth and coalescence. *Journal of the Mechanics and Physics of Solids*, 59, 1858-1871.

Monchiet, V., & Bonnet, G. (2010). Interfacial models in viscoplastic composites materials. *International Journal of Engineering Science*, 48, 1762-1768.

Monchiet, V., & Kondo, D. (2012). Exact solution of a plastic hollow sphere with a Mises-Schleicher matrix. *International Journal of Engineering Science*, 51 168-178.

Moshtaghin, A.F., Naghdabadi, R., & Asghari, M. (2008). Effects of surface residual stress and surface elasticity on the overall yield surfaces of nanoporous materials with cylindrical nanovoids. *Mechanics of Materials*, 51, 74-87.

Needs, R.J., Godfrey, M.J., & Mansfield, M. (1991). Theory of surface stress and surface reconstruction. *Surface Science*, 242, 215-221.

Perrin, G. (1992). Contribution à l'étude théorique et numérique de la rupture ductile des métaux. Thèse de doctorat, Ecole Polytechnique.

Podgórski, J. (1985). Limit state condition and the dissipation function for isotropic materials. *Archives of Mechanics*, 36, 322-342.

Podgórski, J. (1985). General failure criterion for isotropic media. *Journal of Engineering Mechanics*, 111, 188-201.

Ponte Castañeda, P. (1991). The effective mechanical properties of nonlinear isotropic composites. *Journal of the Mechanics and Physics of Solids*, 39, 45-71.

Povstenko, Yu. Z. (1993). Theoretical investigation of phenomena caused by heterogeneous surface tension in solids. *Journal of the Mechanics and Physics of Solids*, 41, 1499-1514.

Salençon, J., (1983). Calcul à la rupture et analyse limite. *Presses de l'ENPC*.

Shen, W. Q., Shao, J. F., Kondo, D., & Gatmiri, B. (2012). A micro–macro model for clayey rocks with a plastic compressible porous matrix. *International Journal of Plasticity*, 36, 64-85.

Thoré, P., Pastor, F., Pastor, J., & Kondo, D. (2009). Closed-form solutions for the hollow sphere model with Coulomb and Drucker–Prager materials under isotropic loadings. *Comptes Rendus Mécanique*, 337(5), 260-267.

Traiviratana, S., Bringa, E.M., Benson, D.J., & Meyers, M.A. (2008). Void growth in metals: Atomistic calculations. *Acta Materialia*, 56, 3874-3886.

Wang, J., Huang, Z., Duan, H., Yu, S., Feng, X., Wang, G., Zhang, W., & Wang, T. (2011). Surface stress effect in mechanics of nanostructured materials. *Acta Mechanica Solida Sinica*, 52-82.

Zhai, J., Luo, T., Gao, X., Graham, S. M., Baral, M., Korkolis, Y. P., & Knudsen, E. (2016). Modeling the ductile damage process in commercially pure titanium. *International Journal of Solids and Structures*, 91, 26-45.

Zhang, W., & Wang, T.J. (2007). Effect of surface energy on the yield strength of nanoporous materials. *Applied Physics Letters*, 90, 063104.

Zhang, W., Wang, T.J., & Chen, X. (2008). Effect of surface stress on the asymmetric yield strength of nanowires. *Journal of Applied Physics*, 103, 123527.

Zhang, W., Wang, T.J., & Chen, X. (2010). Effect of surface/interface stress on the plastic deformation of nanoporous materials and nanocomposites. *International Journal of Plasticity*, 26, 957-975.

Zhao, K.J., Chen, C.Q., Shen, Y.P., & Lu, T.J. (2009). Molecular dynamics study on the nano-void growth in face-centered cubic single crystal copper. *Computational Materials Science*, 46, 749-754.

CHAPTER 4

Nanoporous materials with a general isotropic plastic matrix: Limit analysis and homogenization under axisymmetric loadings

Abstract

In this Chapter, a macroscopic general strength criterion for nanoporous materials accounting for void-size effects is analytically established. A homogenization procedure based on a kinematic limit-analysis is performed addressing a hollow-sphere model comprising a rigid-ideal-plastic solid matrix and undergoing axisymmetric strain-rate boundary conditions. Void-size effects are accounted for by introducing an imperfect-coherent interface at the cavity boundary. Both the interface and the solid matrix are assumed to obey to a simplified form of the general yield function proposed by Bigoni and Piccolroaz [Int J Solids Struct; 41: 2855-2878], thereby allowing for an extreme flexibility in describing triaxiality and Lode-angle effects. A parametric closed-form relationship for the macroscopic strength criterion is obtained as the unique physically-consistent solution of an inequality-constrained minimization problem, the latter being faced via the Lagrangian method combined with Karush-Kuhn-Tucker conditions. Any possible choice of local-yield-function parameters is carefully addressed, by clearly highlighting the effects of a specific local plastic behaviour on the material macroscopic response. Finally, several comparative illustrations are provided, showing the influence of model parameters on the proposed yield function, as well as the model capability to describe the macroscopic strengthening, typical of nanoporous materials, induced by a void-size reduction for a fixed porosity level.

Present Chapter corresponds to the submitted research paper (Brach et al., 2016d).
A self-consistent notation is adopted.

Keywords: Nanoporous materials, general strength criterion, limit analysis, isotropic plastic matrix, void-size effects.

4.1 Introduction

Nanostructured materials have recently been the object of a ever-growing multidisciplinary research effort, focusing enormous technological developments and attracting a keen interest in both industrial and academic domains (e.g., Jenkins, 2010). An important class of nanostructured materials consists in nanoporous media, presenting long-range ordered or disordered microstructures with voids dimension of a few to tens of nanometers. Due to high specific surface area, possible uniformly-distributed void size and rich surface chemistry, nanoporous materials have allowed for a novel generation of engineering devices with tailorable properties, thereby opening towards challenging multifunctional applications in several technical fields, such as biomechanics, sensoring, energy storage and molecular sieving.

One of the current strategic goal in nanotechnology lies in the design and the manufacturing of nanoporous materials with sizeable interior surfaces and void space, in order to ensure specific mechanical features at the macroscale. In detail, the enhancement of strength properties of light-weight metallic foams for structural applications has been a core focus in the recent nanoscience, resulting in the synthesis of nanoporous specimens with an exceptionally-high yield stress. Thereby, a fundamental research aspect consists in establishing engineering-oriented theoretical models able to predict macroscopic strength properties of nanoporous materials, by properly accounting for dominant nanoscale mechanisms. These latter have been addressed in several recent research works, consisting in both empirical and numerical investigations.

Specifically, experimental tests performed on nanoporous foams (Biener et al., 2005, 2006; Fan and Fang, 2009; Hakamada and Mabuchi, 2007; Hodge et al., 2007) revealed that, for a fixed porosity level, a reduction in the void size induces a significant increase in the yield strength, which results higher than characteristic values observed for conventional porous metals. Analogously, Molecular Dynamics computations carried out on in-silico nanoporous specimens (Brach et al., 2016a; Mi et al., 2011; Traiviratana et al., 2008; Zhao et al., 2009) showed a significant enhancement of the predicted strength measure as the void size reduces.

The physical origin of such a phenomenon may be attributed to the presence of self-equilibrated stresses at the cavity boundary (Fan and Fang, 2009; Needs et al., 1991; Povstenko and Yu, 1993; Weissmüller et al., 2009) caused by the excess of energy characterising surface atoms with respect to the neighbouring ones, usually negligible in conventional porous materials with smaller specific surface area. In this light, continuum theoretical descriptions of size-related effects have been proposed by Duan et al. (2005a), Duan et al. (2005b), Le Quang and He (2007), Le Quang and He (2008), Sharma and Ganti (2004) and Wang et al. (2011), by introducing coherent-imperfect interfaces across which the stress vector (resp., the velocity field) is discontinuous (resp., continuous).

Void-size effects are not accounted for in classical plasticity theories addressing porous materials, constitutive models being generally conceived to predict only the influence of the porosity level. This is the case of the yield criterion proposed by Gurson (1977), based on a kinematic limit-analysis approach. Generalizations of this model have been provided

by Tvergaard (1982) and Tvergaard and Needleman (1984), accounting for certain experimental and numerical evidence on porosity thresholds, and providing an enhanced description of material strength during void growth and coalescence. The identification of parameters of the resulting Gurson-Tvergaard constitutive model has been numerically provided by Corigliano et al. (2000), via finite-element-based calculations. The influence of voids shape on strength properties of porous materials has been also investigated by Mariani and Corigliano (2001), highlighting anisotropy effects associated to aspect ratio and orientation of cavities.

A first attempt to describe strength properties as dependent on the void size has been provided by Dormieux and Kondo (2010), who extended the yield criterion proposed by Gurson (1977) to nanoporous materials. An analogous limit-analysis based strategy has been adopted by Monchiet and Kondo (2013), in order to investigate the combined effects of void size and void shape on macroscopic strength properties. Void-size dependent strength criteria have also been established in the framework of non-linear homogenization approaches (Dormieux and Kondo, 2013; Goudarzi et al., 2010; Moshtaghin et al., 2012; Zhang and Wang, 2007; Zhang et al., 2008, 2010), based on the so-called modified secant method (Suquet, 1995).

All the afore-mentioned strength models have been formulated by considering a von Mises local yield function, thereby not accounting either for hydrostatic-stress dependence nor for stress-Lode-angle effects. However, the solid matrix of many engineering-relevant nanoporous materials may exhibit a more complex local plastic behaviour. As a matter of fact, Molecular Dynamics evidence provided by Brach et al. (2016a) proved that the strength domain of a nanoscaled bulk material may be strongly affected by all the three isotropic stress invariants, and that such an influence can not be effectively described by simply calibrating classical yield criteria (e.g., Mohr-Coulomb), mainly due to the occurrence of significant stress-Lode-angle effects.

Motivated by the above observations, the present Chapter aims to establish a general macroscopic strength criterion for nanoporous materials accounting for void-size effects. A simplified form of the general yield function proposed by Bigoni and Piccolroaz (2004) is considered, allowing for an extreme flexibility in describing the stress-Lode-angle influence on the local plastic behaviour. The parametric form of this criterion permits to properly recover a broad class of pressure-sensitive, frictional and ductile plastic responses, exhibiting a great flexibility to comply with evidence-based benchmarking indications. For instance, a suitable calibration of model parameters allows to consistently describe available Molecular-Dynamics strength estimates for a nanoscaled aluminium bulk sample (Brach et al., 2016a,b). In order to perform a kinematic limit-analysis homogenization, closed-form relationships recently provided by Brach et al. (2016b) for the limit-state problem of a hollow sphere under isotropic loadings are herein considered to build up a suitable trial velocity field.

The Chapter is organized as follows. In Section 4.2, the problem under stake is formulated, and basic elements of the adopted theoretical background are presented. In Section 4.3 the local Bigoni-like yield criterion, as well as the corresponding support function and

plastic admissibility conditions, are introduced. In Section 4.4, the trial velocity field is presented, focusing on kinematic and plastic consistency requirements. By summarizing, for the sake of compactness, some analytical details in 4.A, the macroscopic strength criterion for nanoporous materials under axisymmetric loadings is analytically derived in Section 4.5, hydrostatic and deviatoric strengths being explicitly formulated in Section 4.6. Illustrative comparisons are presented and discussed in Section 4.7, highlighting the effects of both local-yield-function parameters and void size on the macroscopic criterion. Finally, some conclusions are traced in Section 4.8.

4.2 Problem statement and theoretical background

Let a nanoporous material be considered, containing randomly-distributed spherical nanovoids and whose representative cell consists in the hollow-sphere region depicted in Fig. 4.1. This corresponds to a particular but realistic microstructure, namely the Hashin Composite-Sphere-Assemblage (Hashin, 1962), defined as a collection of graduated-in-size hollow spheres embedded into a homogeneous solid matrix (e.g., Leblond et al., 1994; Michel and Suquet, 1992).

Let R_i and R_e respectively be the internal and the external radius of the hollow sphere, and $\partial\Omega_\mathrm{i}$ and $\partial\Omega_\mathrm{e}$ be the corresponding internal and external surfaces, the total boundary of the region resulting in $\partial\Omega = \partial\Omega_\mathrm{i} \cup \partial\Omega_\mathrm{e}$. Moreover, let the porosity f be defined as $f = |\Omega_\mathrm{v}|/|\Omega|$, where $|\Omega| = |\Omega_\mathrm{s}| + |\Omega_\mathrm{v}|$ is the total volume of the hollow-sphere region $\Omega = \Omega_\mathrm{s} \cup \Omega_\mathrm{v}$, with $|\Omega_\mathrm{s}|$ and $|\Omega_\mathrm{v}|$ being the volume measures of the solid region (namely, Ω_s) and of the spherical void (Ω_v), respectively. The solid matrix is assumed to be homogeneous and comprised of a rigid-ideal-plastic isotropic material. Such a modelling assumption, strictly required in limit analysis approaches, allows to straight identify material strength properties by referring to the yield limit state.

In the framework of a plastic generalization (Monchiet and Bonnet, 2010) of the Gurtin-Murdoch stress-interface model (Gurtin and Murdoch, 1975), the influence of non-negligible surface stresses at the void boundary is addressed by introducing a coherent and imperfect homogeneous interface $\mathcal{I}$ at $\partial\Omega_\mathrm{i}$, through which the velocity field (resp., the stress vector) is prescribed to be continuous (resp., discontinuous). The material comprising the interface is itself assumed to be isotropic and rigid-ideal-plastic.

The following notation is adopted throughout the Chapter: boldface letters denote vectors and second-order tensors; blackboard letters indicate fourth-order tensors; symbols $\cdot$, $:$, and $\otimes$ denote dot, double-dot, and tensor product operators, respectively; ∇ (resp., $\nabla^{\mathcal{I}}$) is the nabla operator in Ω_s (resp., along the interface), $\widetilde{\nabla}$ identifying the symmetric part of the corresponding gradient operator. Referring to the notation in Fig. 4.1, the Cartesian reference system $(\mathbf{e}_\mathrm{x}, \mathbf{e}_\mathrm{y}, \mathbf{e}_\mathrm{z})$ is introduced, with the origin O at the sphere center. Furthermore, for following analytical developments, let the cylindrical coordinate system (z, φ, ρ) be defined, as well as the corresponding local orthonormal basis $(\mathbf{e}_\mathrm{z}, \mathbf{e}_\varphi, \mathbf{e}_\rho)$, ρ and z being the longitudinal and altitude coordinates such that $\rho/z = \tan\theta$, and $\varphi \in [0, 2\pi]$ and $\theta \in [0, \pi]$ being the azimuth and zenith angles respectively. Therefore, the position of a point in Ω (resp., at the interface $\mathcal{I}$) with respect to the sphere center

O is identified by $\mathbf{r} = r(\rho, z)\,\mathbf{e}_\mathrm{r}(\varphi)$ (resp., by $\mathbf{r}_\mathrm{i} = R_\mathrm{i}\,\mathbf{e}_\mathrm{r}$), where $r = \sqrt{\rho^2 + z^2} \in [R_\mathrm{i}, R_\mathrm{e}]$ is the radial coordinate and $\mathbf{e}_\mathrm{r}(\varphi) = \mathbf{e}_\rho(\varphi) + \mathbf{e}_\mathrm{z}$ is the radial direction. Symbols $\langle\mathbf{a}\rangle$ and $\langle\mathbf{a}\rangle_{\mathcal{I}}$ indicate Ω- and $\partial\Omega_\mathrm{i}$-based averages of a certain space-dependent field $\mathbf{a}(\mathbf{r})$, that is $\langle\mathbf{a}\rangle = (1/|\Omega|)\int_\Omega \mathbf{a}\,d\Omega$ and $\langle\mathbf{a}\rangle_{\mathcal{I}} = (1/4\pi R_\mathrm{i}^2)\int_{\partial\Omega_\mathrm{i}} \mathbf{a}(\mathbf{r}_\mathrm{i})\,dA$, respectively. Moreover, let the projector tensor $\mathbb{T}$ be component-wise defined as $\mathbb{T}_{ijkl} = (P_{ik}P_{jl} + P_{il}P_{jk})/2$, where $\mathbf{P} = (\mathbf{1} - \mathbf{e}_\mathrm{r} \otimes \mathbf{e}_\mathrm{r})$ with $\mathbf{1}$ the second-order identity tensor, and such that $\mathbf{A}_\mathbb{T} = \mathbb{T} : \mathbf{A}$ is the projection on planes orthogonal to $\mathbf{e}_\mathrm{r}$ of a given second-order tensor $\mathbf{A}$.

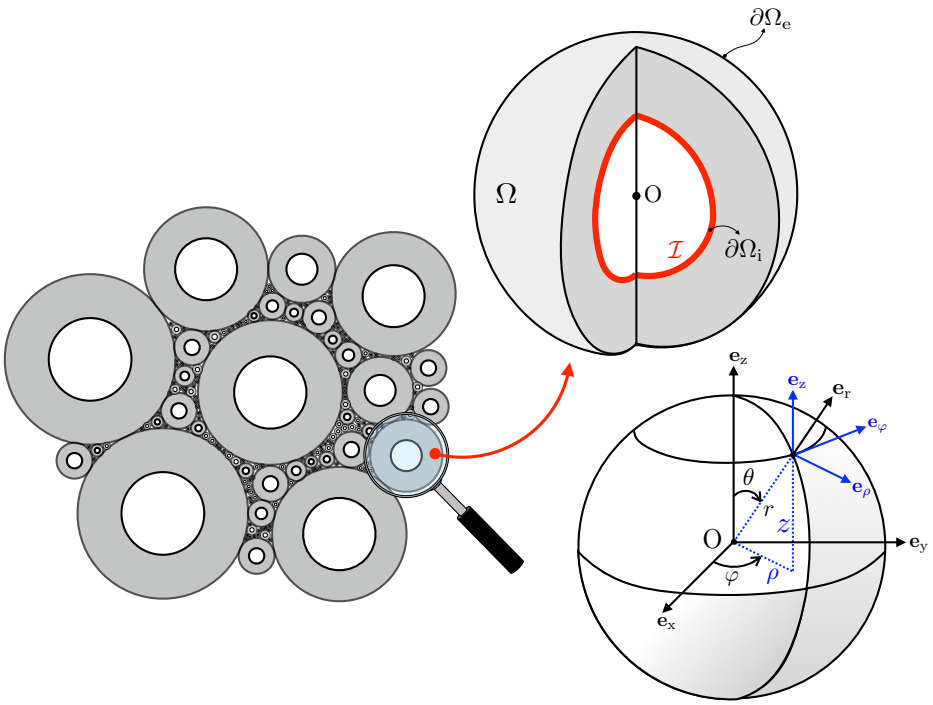

Figure 4.1 – Hashin Composite-Sphere-Assemblage (Hashin, 1962) and the corresponding representative hollow sphere Ω. Notation.

Aiming to determine a closed-form expression of the macroscopic strength criterion via a kinematic limit-analysis approach, the hollow sphere is assumed to undergo axisymmetric strain-rate based boundary conditions at its exterior boundary $\partial\Omega_\mathrm{e}$, expressed in terms of the homogeneous second-order strain-rate tensor $\mathbf{D}$. The latter, in the cylindrical reference system, is chosen as

$$\mathbf{D} = D_\rho(\mathbf{e}_\rho \otimes \mathbf{e}_\rho + \mathbf{e}_\varphi \otimes \mathbf{e}_\varphi) + D_\mathrm{z}\mathbf{e}_\mathrm{z} \otimes \mathbf{e}_\mathrm{z} \tag{4.1}$$

where strain-rate parameters D_ρ and D_z are assumed to be such that $\mathbf{D}$ is non-deviatoric (i.e., $\mathrm{tr}\,\mathbf{D} \neq 0$).

The set of kinematically-admissible velocity fields is introduced as

$$\mathcal{BC}_\mathrm{v} = \{\mathbf{v}(\mathbf{r}) \quad \text{s.t.} \quad \mathbf{v} = \mathbf{D}\cdot\mathbf{r} \quad \text{on } \partial\Omega_\mathrm{e}\} \tag{4.2}$$

allowing to define kinematically-admissible strain-rate fields as belonging to the set

$$\mathcal{K}_{\mathrm{d}} = \left\{ (\mathbf{d}, \mathbf{d}^{\mathcal{I}}) \quad \text{s.t.} \quad \begin{array}{l} \mathbf{d} = \widetilde{\nabla}\mathbf{v} \quad \text{in } \Omega_{\mathrm{s}}\,, \\ \mathbf{d}^{\mathcal{I}} = \mathbf{d}\big|_{\mathbf{r}=\mathbf{r}_{\mathrm{i}}} \quad \text{on } \partial\Omega_{\mathrm{i}}\,, \\ \text{with } \mathbf{v} \in \mathcal{BC}_{\mathrm{v}} \end{array} \right\} \tag{4.3}$$

$\mathbf{v}$ being the velocity field, and where $\mathbf{d}$ and $\mathbf{d}^{\mathcal{I}}$ denote the microscopic second-order strain-rate tensors in Ω_{s} and on $\partial\Omega_{\mathrm{i}}$, respectively.

Moreover, by denoting with $\boldsymbol{\sigma}$ (resp., with $\boldsymbol{\tau}$) the Cauchy second-order local stress tensor (resp., surface tensor) in Ω_{s} (resp., at $\mathcal{I}$), the set of statically-admissible stress fields is introduced as

$$\mathcal{S}_{\sigma} = \left\{ (\boldsymbol{\sigma}, \boldsymbol{\tau}) \quad \text{s.t.} \quad \begin{array}{l} \nabla \cdot \boldsymbol{\sigma} = \mathbf{0} \quad \text{in } \Omega_{\mathrm{s}}\,, \\ (\boldsymbol{\sigma}^{+} - \boldsymbol{\sigma}^{-}) \cdot \mathbf{e}_{\mathrm{r}} + (\boldsymbol{\tau} : \mathbf{K})\mathbf{e}_{\mathrm{r}} = \nabla^{\mathcal{I}} \cdot \boldsymbol{\tau} \quad \text{on } \partial\Omega_{\mathrm{i}} \end{array} \right\} \tag{4.4}$$

where the equilibrium at $\mathcal{I}$ is expressed by the generalized Young-Laplace equation (Gurtin and Murdoch, 1975; Duan et al., 2005b), with $\boldsymbol{\sigma}^{\pm} = \lim_{r \to R_{\mathrm{i}}^{\pm}} \boldsymbol{\sigma}(\mathbf{r})$ and $\mathbf{K}$ the interface curvature tensor.

When statically-admissible stress (i.e., $(\boldsymbol{\sigma}, \boldsymbol{\tau}) \in \mathcal{S}_{\sigma}$) and kinematically-admissible strain-rate (i.e., $(\mathbf{d}, \mathbf{d}^{\mathcal{I}}) \in \mathcal{K}_{\mathrm{d}}$) local fields are considered, the Hill's lemma holds

$$|\Omega|\, \boldsymbol{\Sigma} : \mathbf{D} = \int_{\Omega_{\mathrm{s}}} \boldsymbol{\sigma} : \mathbf{d}\, d\Omega + \int_{\partial\Omega_{\mathrm{i}}} \boldsymbol{\tau} : \mathbf{d}^{\mathcal{I}}_{\mathbb{T}}\, dA \tag{4.5}$$

with $\mathbf{d}^{\mathcal{I}}_{\mathbb{T}} = \mathbb{T} : \mathbf{d}^{\mathcal{I}}$, and where $\boldsymbol{\Sigma} = \langle \boldsymbol{\sigma} \rangle$ is the macroscopic second-order stress tensor. Since the exterior power has to be lower or at the most equal to the maximum plastic dissipation Π that can be overall afforded in Ω, Eq. (4.5) can be recast as (e.g., Salençon, 1983)

$$\boldsymbol{\Sigma} : \mathbf{D} \leq \Pi(\mathbf{D}) \tag{4.6}$$

with

$$\Pi(\mathbf{D}) = \inf_{(\mathbf{d}, \mathbf{d}^{\mathcal{I}}) \in \mathcal{K}_{\mathrm{d}}} \left(\langle \pi^{\mathrm{s}}(\mathbf{d}) \rangle + \frac{1}{|\Omega|} \int_{\partial\Omega_{\mathrm{i}}} \pi^{\mathcal{I}}(\mathbf{d}^{\mathcal{I}})\, dA \right) \tag{4.7}$$

where π^{s} and $\pi^{\mathcal{I}}$ are the maximum plastic dissipations that can be locally achieved in the solid matrix and on the interface, respectively

$$\pi^{\mathrm{s}}(\mathbf{d}) = \sup_{\boldsymbol{\sigma} \in \mathcal{Y}^{\mathrm{s}}} (\boldsymbol{\sigma} : \mathbf{d}), \qquad \text{with} \qquad \mathcal{Y}^{\mathrm{s}} = \{\boldsymbol{\sigma} \quad \text{s.t.} \quad \mathcal{G}^{\mathrm{s}}(\boldsymbol{\sigma}) \leq 0\} \tag{4.8}$$

$$\pi^{\mathcal{I}}(\mathbf{d}^{\mathcal{I}}) = \sup_{\boldsymbol{\tau} \in \mathcal{Y}^{\mathcal{I}}} (\boldsymbol{\tau} : \mathbf{d}^{\mathcal{I}}_{\mathbb{T}}), \qquad \text{with} \qquad \mathcal{Y}^{\mathcal{I}} = \left\{\boldsymbol{\tau} \quad \text{s.t.} \quad \mathcal{G}^{\mathcal{I}}(\boldsymbol{\tau}) \leq 0\right\} \tag{4.9}$$

$\mathcal{G}^{\mathrm{s}}$ (resp., $\mathcal{G}^{\mathcal{I}}$) indicating the yield function of the solid matrix (resp., of the interface). Relationship in Eq. (4.8) (resp., in Eq. (4.9)) also identifies the support function for the solid matrix (resp., for the interface), that is the hyperplane tangent to the yield surface $\partial\mathcal{Y}^{\mathrm{s}} = \{\boldsymbol{\sigma} \text{ s.t. } \mathcal{G}^{\mathrm{s}}(\boldsymbol{\sigma}) = 0\}$ (resp., $\partial\mathcal{Y}^{\mathcal{I}} = \{\boldsymbol{\tau} \text{ s.t. } \mathcal{G}^{\mathcal{I}}(\boldsymbol{\tau}) = 0\}$) in the space of volume (resp., surface) stresses. Similarly, Eq. (4.7) defines the support function associated to

the macroscopic yield function $\mathcal{G}$.

Instead of seeking the infimum in Eq. (4.7) over all the kinematically-admissible velocity fields $\mathbf{v} \in \mathcal{BC}_{\mathrm{v}}$ that lead to strain-rate states $(\mathbf{d}, \mathbf{d}^{\mathcal{I}}) \in \mathcal{K}_{\mathrm{d}}$, an upper-bound $\widehat{\Pi}$ of the macroscopic support function can be determined as

$$\boldsymbol{\Sigma} : \mathbf{D} \leq \Pi(\mathbf{D}) \leq \widehat{\Pi}(\mathbf{D}) = \left\langle \pi^{\mathrm{s}}(\widehat{\mathbf{d}}) \right\rangle + \frac{1}{|\Omega|} \int_{\partial\Omega_{\mathrm{i}}} \pi^{\mathcal{I}}(\widehat{\mathbf{d}}^{\mathcal{I}})\, dA \tag{4.10}$$

where $(\widehat{\mathbf{d}}, \widehat{\mathbf{d}}^{\mathcal{I}})$ is a strain-rate state obtained from a particular trial velocity field $\widehat{\mathbf{v}} \in \mathcal{BC}_{\mathrm{v}}$. Accordingly, owing to Eqs. (4.6) and (4.10), an estimate $\widehat{\boldsymbol{\Sigma}}^{\mathrm{c}}$ of the macroscopic strength $\boldsymbol{\Sigma}^{\mathrm{c}}$ can be computed as

$$\widehat{\boldsymbol{\Sigma}}^{\mathrm{c}} = \frac{\partial \widehat{\Pi}(\mathbf{D})}{\partial \mathbf{D}} \tag{4.11}$$

thereby identifying, in the space of macroscopic stresses, the surface $\partial\widehat{\mathcal{Y}} = \{\widehat{\boldsymbol{\Sigma}}^{\mathrm{c}} \text{ s.t. } \widehat{\mathcal{G}}(\widehat{\boldsymbol{\Sigma}}^{\mathrm{c}}) = 0\}$. It is worth observing that $\widehat{\Pi}(\mathbf{D})$ can be regarded as the hyperplane tangent to the surface $\partial\widehat{\mathcal{Y}}$, in the stress point $\widehat{\boldsymbol{\Sigma}}^{\mathrm{c}}$ where $\mathbf{D}$ is orthogonal to $\partial\widehat{\mathcal{Y}}$.

Finally, it is noted that trial velocity fields generally considered to compute the upper bound in Eq. (4.10) are uniquely determined by imposing the kinematic admissibility requirement $\widehat{\mathbf{v}} \in \mathcal{BC}_{\mathrm{v}}$ (see for instance Gurson, 1977). On the contrary, an enhanced estimate of the macroscopic maximum plastic dissipation may be obtained by considering a *class* of kinematically-admissible trial velocity fields, that is by defining $\widehat{\mathbf{v}}$ as a function of a suitable number of parameters non-uniquely identified by the requirement $\widehat{\mathbf{v}} \in \mathcal{BC}_{\mathrm{v}}$, namely by referring to $\widehat{\mathbf{v}} \in \mathcal{V} \subseteq \mathcal{BC}_{\mathrm{v}}$. Specifically, the lowest upper bound $\widetilde{\Pi}$ for Π when $\widehat{\mathbf{v}} \in \mathcal{V}$ results from the following minimization problem

$$\min_{\widehat{\mathbf{v}} \in \mathcal{V}} \left[\widehat{\Pi}(\mathbf{D}) - \boldsymbol{\Sigma} : \mathbf{D} \right] = \min_{\widehat{\mathbf{v}} \in \mathcal{V}} \left[\widehat{\Pi}(\mathbf{D}) - \widetilde{\boldsymbol{\Sigma}}^{\mathrm{c}} : \mathbf{D} \right] \tag{4.12}$$

where estimates $\widetilde{\boldsymbol{\Sigma}}^{\mathrm{c}} = \partial\widetilde{\Pi}/\partial\mathbf{D}$ allow to identify the estimate $\widetilde{\mathcal{G}}$ of the macroscopic yield function $\mathcal{G}$.

4.3 Local yield criterion

Since the material comprising the hollow sphere is assumed to be isotropic, a limit stress state belonging to the yield surface $\partial\mathcal{Y}^{\mathrm{s}}$ can be uniquely identified, within the space of principal stress components $(\sigma_1, \sigma_2, \sigma_3)$, by referring to the cylindrical system of Lode coordinates (p, q, θ_σ) with

$$p = \frac{I_1^\sigma}{3}, \qquad q = \sqrt{3J_2^\sigma}, \qquad \cos 3\theta_\sigma = \frac{3\sqrt{3}}{2} \frac{J_3^\sigma}{{J_2^\sigma}^{3/2}} \tag{4.13}$$

$\theta_\sigma \in [0, \pi/3]$ being the stress Lode angle, and where $I_1^\sigma = \operatorname{tr} \boldsymbol{\sigma}$, $J_2^\sigma = \operatorname{tr} \boldsymbol{\sigma}_{\mathrm{d}}^2/2$ and $J_3^\sigma = \operatorname{tr} \boldsymbol{\sigma}_{\mathrm{d}}^3/3$ are the hydrostatic, the second-order deviatoric and the third-order deviatoric stress invariants, respectively, with $\boldsymbol{\sigma}_{\mathrm{d}} = \boldsymbol{\sigma} - p\mathbf{1}$ the deviatoric part of the stress tensor. Therefore, the yield surface $\partial\mathcal{Y}^{\mathrm{s}}$ results completely defined in terms of its meridian profiles

(i.e., the intersections between $\partial\mathcal{Y}^{\mathrm{s}}$ and the meridian planes, these latter being at $\theta_\sigma = \text{const}$ and containing the hydrostatic axis $\sigma_1 = \sigma_2 = \sigma_3$) and of its deviatoric sections (i.e., the intersections between $\partial\mathcal{Y}^{\mathrm{s}}$ and the deviatoric planes, or π-planes, at $p = \text{const}$).

The yield function of the solid matrix $\mathcal{G}^{\mathrm{s}}$ is assumed equal to

$$\mathcal{G}^{\mathrm{s}}(\boldsymbol{\sigma}) = m(p) + \frac{q}{g(\theta_\sigma)}\,, \tag{4.14}$$

where, in agreement with the theoretical framework proposed by Brach et al. (2016b) and as a simplified form of the strength criterion proposed by Bigoni and Piccolroaz (2004); Bigoni (2012), functions m and g are defined as

$$m(p) = -3\left(h - \frac{p}{\xi}\right) \tag{4.15}$$

$$g(\theta_\sigma) = \frac{1}{\cos\frac{\beta\pi}{6}\cos\theta_\sigma + \sin\frac{\beta\pi}{6}\sin\theta_\sigma} \tag{4.16}$$

ξ and β being dimensionless parameters which comply with the physical consistency conditions $\xi > 0$ (the case $\xi \to +\infty$ allowing to describe a pressure-independent yield function) and with the convexity requirement $0 \le \beta \le 2$, whereas $h \ge 0$ is a strength coefficient having the dimension of a stress.

Relationships (4.14) to (4.16) describe a polyhedral yield surface $\partial\mathcal{Y}_{\mathrm{s}}$ in the space of the Lode coordinates, with linear and multi-sided yield profiles in meridian and in deviatoric planes, respectively. In detail, as shown in Fig. 4.2, function $g(\theta)$ in Eq. (4.16) allows for an extreme shape distortion of deviatoric yield profiles when β is varied, resulting in the occurrence of sharp vertices in the π-plane at triaxial-compression (TXC_σ, $\theta_\sigma = \pi/3$), at triaxial-expansion (TXE_σ, $\theta_\sigma = 0$), and at both TXC_σ and TXE_σ stress states, for $\beta = 0$, $\beta = 2$, and $0 < \beta < 2$, respectively.

Moreover, introducing the notation

$$\xi^* = \frac{2}{c_\beta + \sqrt{3}s_\beta}\,, \qquad\qquad \xi^{**} = \frac{2}{c_\beta - \sqrt{3}s_\beta} \tag{4.17}$$

with $c_\beta = \cos(\beta\pi/6)$ and $s_\beta = \sin(\beta\pi/6)$, and depending on the value assumed by model parameters β and ξ, the support function π^{s} of a pressure-dependent solid matrix and the corresponding plastic admissibility condition result in (Brach et al., 2016b)

$\circ$ case $0 \le \beta < 1$

$$\pi^{\mathrm{s}}(\mathbf{d}) = \begin{cases} h\xi I_1^{\mathrm{d}} & \text{if} \quad d_{\mathrm{m}} \ge \begin{cases} \dfrac{|d_1| + |d_2| + |d_3|}{3} & \text{if} \quad \xi \le \xi^* \\ \dfrac{|d_1| + |d_2| + |d_3|}{1 + \left(c_\beta + \sqrt{3}\,s_\beta\right)\xi} & \text{if} \quad \xi^* \le \xi \le \xi^{**} \\ \dfrac{|d_1| + |d_2| + |d_3|}{2c_\beta\xi - 1} & \text{if} \quad \xi \ge \xi^{**} \end{cases} \\ +\infty & \text{otherwise} \end{cases} \tag{4.18}$$

∘ case $1 \leq \beta \leq 2$

$$\pi^{\mathrm{s}}(\mathbf{d}) = \begin{cases} h\xi I_1^{\mathrm{d}} & \text{if} \quad d_{\mathrm{m}} \geq \begin{cases} \dfrac{|d_1|+|d_2|+|d_3|}{3} & \text{if} \quad \xi \leq \xi^* \\ \dfrac{|d_1|+|d_2|+|d_3|}{1+\left(c_\beta+\sqrt{3}\,s_\beta\right)\xi} & \text{if} \quad \xi \geq \xi^* \end{cases} \\ +\infty & \text{otherwise} \end{cases} \tag{4.19}$$

where d_i (with $i \in \{1,2,3\}$) denotes a principal strain-rate component, $I_1^{\mathrm{d}} = \operatorname{tr}\mathbf{d}$, and $d_{\mathrm{m}} = I_1^{\mathrm{d}}/3$ is the hydrostatic strain rate. On the other hand, when the case of a pressure-independent local plastic behaviour is addressed (that is, for $\xi \to +\infty$), Eqs. (4.18) and (4.19) reduce to (see Brach et al., 2016b)

∘ case $0 \leq \beta < 1$

$$\pi^{\mathrm{s}}(\mathbf{d}) = \begin{cases} \dfrac{3h}{2c_\beta}(|d_1|+|d_2|+|d_3|) & \text{if} \quad I_1^{\mathrm{d}} = 0 \\ +\infty & \text{otherwise} \end{cases} \tag{4.20}$$

∘ case $1 \leq \beta \leq 2$

$$\pi^{\mathrm{s}}(\mathbf{d}) = \begin{cases} \dfrac{3h}{c_\beta+\sqrt{3}s_\beta}(|d_1|+|d_2|+|d_3|) & \text{if} \quad I_1^{\mathrm{d}} = 0 \\ +\infty & \text{otherwise} \end{cases} \tag{4.21}$$

It is worth observing that the general isotropic strength criterion defined by Eqs. (4.14) to (4.16) and the support function in Eqs. (4.18) to (4.21) allow to describe the plastic behaviour of a broad class of pressure-dependent or independent materials, accounting for the influence of stress-Lode-angle effects. As special cases, classical yield functions with sharp deviatoric profiles, as well as the corresponding expressions for support functions and admissibility conditions, can be straight recovered via a proper choice of values for model parameters β, ξ and h, as it is summarized in Table 4.1 for Tresca (Tr) and Mohr-Coulomb (MC) criteria.

The yield function $\mathcal{G}^{\mathcal{I}}(\boldsymbol{\tau})$ for the interface $\mathcal{I}$ is assumed of the same form as in Eqs. (4.14) to (4.16), and it is expressed in terms of model parameters $\{\xi, h^{\mathcal{I}}, \beta\}$, where $h^{\mathcal{I}}$ has the dimension of a membrane stress (namely, a force per unit length). Similarly, the interface support function $\pi^{\mathcal{I}}$ and its admissibility condition formally read as in Eqs. (4.18) to (4.21), these latter being expressed in terms of the strain rate $\mathbf{d}^{\mathcal{I}}$ and the interface strength $h^{\mathcal{I}}$.

Remark 6 *Since the strength parameter $h^{\mathcal{I}}$ affects only the value of the maximum plastic dissipation at the interface, plastic admissibility conditions in Eqs. (4.18) to (4.21) for π^s exactly recover plastic admissibility for the support function $\pi^{\mathcal{I}}$ at the interface when $\mathbf{d}$ is replaced by $\mathbf{d} = \mathbf{d}_{\mathbf{r}=\mathbf{r}_i}$.*

Table 4.1 – Values of model parameters for the adopted Bigoni-like strength criterion, allowing to recover yield (i.e., $\mathcal{G}^{\mathrm{s}}(\boldsymbol{\sigma})$) and support (i.e., $\pi^{\mathrm{s}}(\mathbf{d})$) functions for Tresca (Tr) and Mohr-Coulomb (MC) criteria. σ_0: deviatoric strength; c: cohesion; ϕ: friction angle. Symbols σ_i and d_i with $i \in \{1,2,3\}$ denote principal stress and strain-rate components, respectively.

Tr	$\mathcal{G}^{\mathrm{s}}(\boldsymbol{\sigma}) = q\sin\left(\theta_\sigma + \dfrac{\pi}{3}\right) - \dfrac{\sigma_0\sqrt{3}}{2} = \max_{i\neq j}\left(\,|\sigma_i - \sigma_j|\,\right) - \sigma_0 = 0$
	$\pi^{\mathrm{s}}(\mathbf{d}) = \begin{cases} \dfrac{\sigma_0}{2}(\lvert d_1\rvert + \lvert d_2\rvert + \lvert d_3\rvert) & \text{if} \quad I_1^{\mathrm{d}} = 0 \\ +\infty & \text{if} \quad I_1^{\mathrm{d}} \neq 0 \end{cases}$
	$h = \dfrac{\sigma_0\sqrt{3}}{6}, \quad \xi \to +\infty, \quad \gamma = 1, \quad \beta = 1$
MC	$\mathcal{G}^{\mathrm{s}}(\boldsymbol{\sigma}) = p - c\cot\phi + q\left[\dfrac{1}{\sqrt{3}\sin\phi}\sin\left(\theta_\sigma + \dfrac{\pi}{3}\right) + \dfrac{1}{3}\cos\left(\theta_\sigma + \dfrac{\pi}{3}\right)\right] =$
	$= \max_{i\neq j}\left[\,|\sigma_i - \sigma_j| + (\sigma_i + \sigma_j)\sin\phi\,\right] - 2c\cos\phi = 0$
	$\pi^{\mathrm{s}}(\mathbf{d}) = \begin{cases} c\cot\phi\, I_1^{\mathrm{d}} & \text{if} \quad I_1^{\mathrm{d}} \geq (\lvert d_1\rvert + \lvert d_2\rvert + \lvert d_3\rvert)\sin\phi \\ +\infty & \text{if} \quad I_1^{\mathrm{d}} < (\lvert d_1\rvert + \lvert d_2\rvert + \lvert d_3\rvert)\sin\phi \end{cases}$
	$h = \dfrac{c\,\cos\phi}{\sqrt{3+\sin^2\phi}}, \quad \xi = \dfrac{\sqrt{3+\sin^2\phi}}{\sin\phi}$
	$\gamma = 1, \quad \beta = \dfrac{6}{\pi}\arctan\left(\dfrac{\sqrt{3}(1-\sin\phi)}{3+\sin\phi}\right)$

4.4 Local kinematics

In the framework of the kinematic limit-analysis approach introduced in Section 4.2, and with the aim to determine an effective estimate for the macroscopic support function as in Eq. (4.10), strain-rate states $(\widehat{\mathbf{d}}, \widehat{\mathbf{d}}^{\mathcal{I}}) \in \mathcal{K}_{\mathrm{v}}$ have to be introduced by considering suitable kinematically-admissible trial velocity fields $\widehat{\mathbf{v}} \in \mathcal{BC}_{\mathrm{v}}$. Furthermore, plastic admissibility conditions in Eqs. (4.18) to (4.21) have to be correspondingly formulated. Since the support function of a pressure-independent yield criterion can be straight obtained as a particular case of Eqs. (4.18) and (4.19), in the following reference is made to pressure-dependent local plastic behaviours only.

4.4.1 Trial velocity field

Following the approach proposed by Gurson (1977) and recently adopted in several limit-analysis models (e.g., Anoukou et al., 2016; Dormieux and Kondo, 2010; Guo et al., 2008), the trial velocity field $\widehat{\mathbf{v}}$ is herein chosen of the form

$$\widehat{\mathbf{v}} = \mathbf{v}^{\mathrm{hom}} + \mathbf{v}^{\mathrm{het}}\,, \qquad \text{with} \quad \mathbf{v}^{\mathrm{hom}} = \mathbf{C}\cdot\mathbf{r} \tag{4.22}$$

where $\mathbf{C}$ is a homogeneous second-order symmetric strain-rate tensor, and where $\mathbf{v}^{\mathrm{het}} = w(r)\mathbf{r}$ a heterogeneous velocity term. This latter corresponds to the exact solution of the limit-state problem for the hollow sphere in Fig. 4.1, when isotropic strain-rate loading

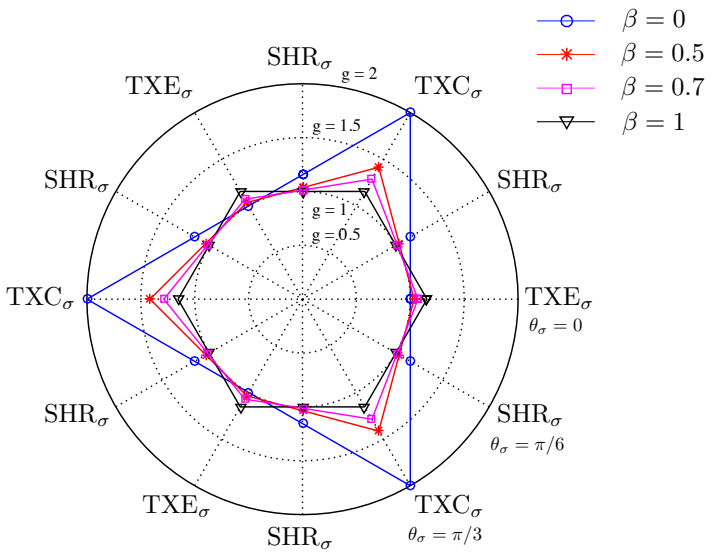

(a)

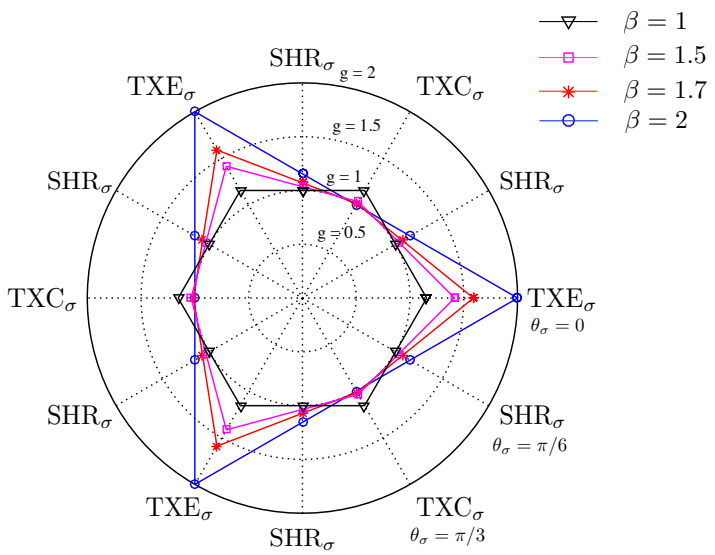

(b)

Figure 4.2 – Local yield criterion. Function $g(\theta_\sigma)$ in Eq. (4.16) for different values of model parameter β. TXE$_\sigma$: local triaxial expansion. TXC$_\sigma$: local triaxial compression. SHR$_\sigma$: local shear state.

conditions are considered. In detail, for the Bigoni-like yield function defined in Eqs. (4.14) to (4.16), the heterogeneous part of the trial velocity field is defined, in agreement with results recently provided by Brach et al. (2016b), as

$$w(r) = C_0 \left(\frac{R_\mathrm{e}}{r}\right)^{3\alpha}, \qquad \text{with} \quad \alpha = \frac{\xi}{\xi - \Xi} \tag{4.23}$$

where C_0 is an arbitrary constant, and function Ξ is equal to

$$\Xi(\epsilon) = -\frac{2\epsilon}{\cos\left(\frac{\pi}{6}(2-\beta) - \frac{1}{3}\arccos(\epsilon)\right)}, \qquad \text{with} \quad \epsilon = \operatorname{sgn} C_0 \tag{4.24}$$

In the following, reference is made to local strength criteria complying with condition $\xi > |\Xi|$ (also verified by classical yield functions in Table 4.1). As a consequence, the exponent α of the heterogeneous velocity field (4.23) is strictly positive. Specifically, $0 < \alpha \leq 1$ (resp., $\alpha \geq 1$) when $\epsilon = 1$ (resp., $\epsilon = -1$), the case $\alpha = 1$ being related to a pressure-independent local plastic behaviour (i.e., for $\xi \to +\infty$). In agreement with results proposed by Brach et al. (2016b), the condition $\xi > |\Xi|$ yields to finite values of both tensile and compressive macroscopic hydrostatic strengths.

The homogeneous strain-rate tensor $\mathbf{C}$ in Eq. (4.22) is usually chosen for allowing to satisfy plastic admissibility condition on support function. In particular, in the case of pressure-independent local yield functions (as for the Tresca strength criterion), $\mathbf{C}$ is generally defined as a deviatoric strain-rate tensor (e.g., Gurson, 1977), thereby resulting in a trial strain-rate field $\widehat{\mathbf{d}}$ which automatically complies with the plastic admissibility condition $I_1^\mathrm{d} = 0$ in Eqs. (4.20) and (4.21). On the other hand, when the case of a pressure-dependent plastic behaviour is addressed, a different form for $\mathbf{C}$ has to be introduced, for allowing to verify the plastic dilatancy requirement expressed in Eqs. (4.18) and (4.19).

Due to the considered strain-rate boundary conditions (see Eqs. (4.1) and (4.2)), and in agreement with the modelling strategy adopted by Guo et al. (2008) and Anoukou et al. (2016) for Drucker-Prager and Mohr-Coulomb plastic matrices, tensor $\mathbf{C}$ is herein assumed characterised by an axisymmetric form $\mathbf{C} = C_1(\mathbf{e}_\rho \otimes \mathbf{e}_\rho + \mathbf{e}_\varphi \otimes \mathbf{e}_\varphi) + C_2 \mathbf{e}_\mathrm{z} \otimes \mathbf{e}_\mathrm{z}$, C_1 and C_2 being constant parameters. Thereby, Eqs. (4.22) and (4.23) yield

$$\widehat{\mathbf{v}} = v_\rho \mathbf{e}_\rho + v_\mathrm{z} \mathbf{e}_\mathrm{z} = C_0 \left(\frac{R_\mathrm{e}}{r}\right)^{3\alpha} (\rho\, \mathbf{e}_\rho + z\, \mathbf{e}_\mathrm{z}) + C_1\, \rho\, \mathbf{e}_\rho + C_2\, z\, \mathbf{e}_\mathrm{z} \tag{4.25}$$

with $r = \sqrt{\rho^2 + z^2}$.

4.4.2 Local strain-rate field

Owing to kinematic admissibility conditions detailed in Eq. (4.3), the trial velocity field in Eq. (4.25) allows to compute the following expressions for non-null strain-rate components

of $\widehat{\mathbf{d}}$

$$\widehat{\mathbf{d}} : (\mathbf{e}_\rho \otimes \mathbf{e}_\rho) = C_0(1 - 3\alpha \sin^2\theta)\left(\frac{R_\mathrm{e}}{r}\right)^{3\alpha} + C_1 \tag{4.26a}$$

$$\widehat{\mathbf{d}} : (\mathbf{e}_\varphi \otimes \mathbf{e}_\varphi) = C_0\left(\frac{R_\mathrm{e}}{r}\right)^{3\alpha} + C_1 \tag{4.26b}$$

$$\widehat{\mathbf{d}} : (\mathbf{e}_\mathrm{z} \otimes \mathbf{e}_\mathrm{z}) = C_0(1 - 3\alpha \cos^2\theta)\left(\frac{R_\mathrm{e}}{r}\right)^{3\alpha} + C_2 \tag{4.26c}$$

$$\widehat{\mathbf{d}} : (\mathbf{e}_\rho \otimes \mathbf{e}_\mathrm{z}) = -3\alpha C_0\left(\frac{R_\mathrm{e}}{r}\right)^{3\alpha} \sin\theta\cos\theta \tag{4.26d}$$

where, since $\widehat{\mathbf{v}} \in \mathcal{BC}_\mathrm{v}$, constants C_0, C_1 and C_2 have to comply with (see Eq. (4.1))

$$C_0 + C_1 = D_\rho\,, \qquad C_0 + C_2 = D_\mathrm{z} \tag{4.27}$$

Accordingly, by introducing the hydrostatic $I_1^\mathrm{D} = \operatorname{tr}\mathbf{D}$, the second-order deviatoric $J_2^\mathrm{D} = \operatorname{tr}\mathbf{D}_\mathrm{d}^2/2$ and the third-order deviatoric $J_3^\mathrm{D} = \operatorname{tr}\mathbf{D}_\mathrm{d}^3/3$ macroscopic strain-rate invariants (with $\mathbf{D}_\mathrm{d} = \mathbf{D} - I_1^\mathrm{D}\mathbf{1}/3$), the following relationships are obtained by combining Eqs. (4.1) and (4.27)

$$D_\mathrm{m} = C_0 + D_\mathrm{m}^\mathrm{hom} \qquad \text{with} \quad D_\mathrm{m}^\mathrm{hom} = \frac{2C_1 + C_2}{3} \tag{4.28a}$$

$$D_\mathrm{eq} = \frac{2}{3}(C_2 - C_1)\delta \qquad \text{with} \quad \delta = \operatorname{sgn}(C_2 - C_1) = \operatorname{sgn} J_3^\mathrm{D} \tag{4.28b}$$

$$\theta_\mathrm{D} = \frac{1}{3}\arccos(\delta) \tag{4.28c}$$

where $D_\mathrm{m} = I_1^\mathrm{D}/3$, $D_\mathrm{eq} = 2\sqrt{J_2^\mathrm{D}/3}$ and $\cos 3\theta_\mathrm{D} = 3\sqrt{3}J_3^\mathrm{D}/[2(J_2^\mathrm{D})^{3/2}]$, with $\theta_\mathrm{D} \in [0, \pi/3]$ being the macroscopic strain-rate Lode angle. Therefore, the mean deformation rate D_m is equal to the sum of two contributions, $D_\mathrm{m}^\mathrm{hom}$ and C_0, respectively associated to the homogeneous ($\mathbf{v}^\mathrm{hom}$) and the heterogeneous ($\mathbf{v}^\mathrm{het}$) part of the local velocity field in Eq. (4.22). Furthermore, owing to Eq. (4.28c), $\delta = 1$ and $\delta = -1$ correspond to macroscopic triaxial-expansion (that is, $\mathrm{TXE_D}$ with $\theta_\mathrm{D} = 0$) and triaxial-compression (that is, $\mathrm{TXC_D}$ with $\theta_\mathrm{D} = \pi/3$) strain-rate states, respectively.

In the following, with a little abuse of notation and unless otherwise specified, local strain-rate components and invariants will be denoted without the hat superscript, although they refers to the trial strain-rate field $(\widehat{\mathbf{d}}, \widehat{\mathbf{d}}^\mathcal{I})$.

Strain-rate components in Eqs. (4.26) and (4.27) result in the local mean deformation rate

$$d_\mathrm{m} = \frac{\operatorname{tr}\widehat{\mathbf{d}}}{3} = D_\mathrm{m}^\mathrm{hom} - C_0\left(\frac{R_\mathrm{e}}{r}\right)^{3\alpha}(\alpha - 1) \tag{4.29}$$

which can be recast in terms of macroscopic strain-rate parameters ϵ and δ as

$$d_\mathrm{m} = \frac{D_\mathrm{eq}}{2}\left(\frac{1-\alpha}{\alpha}\epsilon\,\mathtt{x} + \tilde{\omega}\right) \tag{4.30}$$

notation

$$\mathtt{x} = \omega \left(\frac{R_{\mathrm{e}}}{r} \right)^{3\alpha} \quad , \quad \text{with} \quad \omega = 2\alpha \frac{|C_0|}{D_{\mathrm{eq}}} \quad \text{and} \quad \tilde{\omega} = \frac{2D_{\mathrm{m}}^{\mathrm{hom}}}{D_{\mathrm{eq}}} \tag{4.31}$$

being introduced, where $\omega \geq 0$ is a measure of the macroscopic strain-rate triaxiality ratio, and $\mathtt{x} \geq 0$. Moreover, principal strain-rate components of tensor $\widehat{\mathbf{d}}$ are equal to

$$\begin{aligned} d_1 &= d_{\mathrm{m}} + \frac{D_{\mathrm{eq}}}{2} \left(\epsilon \, \mathtt{x} - \delta \right) \\ d_2 &= d_{\mathrm{m}} - \frac{1}{2} \left(d_{\mathrm{d}1} + \sqrt{\Delta} \right) \\ d_3 &= d_{\mathrm{m}} - \frac{1}{2} \left(d_{\mathrm{d}1} - \sqrt{\Delta} \right) \end{aligned} \tag{4.32}$$

with

$$\Delta = \frac{9}{4} D_{\mathrm{eq}}^2 \left(1 + \mathtt{x}^2 - 2\delta\epsilon\mathtt{x} \cos 2\theta \right) \tag{4.33}$$

and where symbols $d_{\mathrm{d}1}$, $d_{\mathrm{d}2}$ and $d_{\mathrm{d}3}$ denote principal deviatoric strain-rates components (that is, $d_{\mathrm{d}i} = d_i - d_{\mathrm{m}}$ with $i \in \{1, 2, 3\}$).

In order to ensure positive finite values of the local maximum plastic dissipation π^{s}, the kinematically-admissible strain-rate field $\widehat{\mathbf{d}}$ defined by Eqs. (4.26) and (4.27) has to comply with plastic admissibility conditions introduced in Eqs. (4.18) and (4.19). Owing to Remark 6, this also ensures boundedness and positiveness of the interface support function $\pi^{\mathcal{I}}$, computed via the local trial strain-rate field $\widehat{\mathbf{d}}^{\mathcal{I}} = \widehat{\mathbf{d}}|_{\mathbf{r}=\mathbf{r}_{\mathrm{i}}}$. Since requirements in Eqs. (4.18) and (4.19) are expressed in terms of the absolute values of principal strain-rates components in Eqs. (4.32), the sign of d_i (with $i \in \{1, 2, 3\}$) has to be discussed. To this aim, reference is made to results provided by Anoukou et al. (2016) and, in particular, to the following relationship

$$|d_1| + |d_2| + |d_3| = |d_{\mathrm{m}} + d_{\mathrm{d}1}| + \sqrt{\Delta} \tag{4.34}$$

where the local mean deformation rate d_{m} has to be strictly positive, due to admissibility requirements in Eqs. (4.18) and (4.19). Therefore, depending on the value assumed by macroscopic strain-rate coefficients ϵ and δ in Eqs. (4.32) (namely, on the strain-rate boundary conditions), as well as on parameters ξ and β (namely, on the local strength criterion), the following cases have to be addressed in order to explicitly formulate plastic admissibility conditions in Eqs. (4.18) and (4.19).

Case A $\mathrm{TXC_D}$ with $C_0 > 0$ (that is, $\epsilon = +1$ and $\delta = -1$).
Owing to Eqs. (4.32), the principal deviatoric strain-rate component $d_{\mathrm{d}1} = d_1 - d_{\mathrm{m}}$ is strictly positive and equal to

$$d_{\mathrm{d}1} = \frac{D_{\mathrm{eq}}}{2} (1 + \mathtt{x}) \tag{4.35}$$

resulting in strictly positive values of quantity $(d_{\mathrm{m}} + d_{\mathrm{d}1})$ in Eq. (4.34).

Thereby, by replacing Eqs. (4.30) and (4.35) into Eq. (4.34), plastic admissibility con-

ditions in Eqs. (4.18) and (4.19) read as

$$d_{\mathrm{m}} \geq \eta_1 \left(d_{\mathrm{d1}} + \sqrt{\Delta}\right) \tag{4.36}$$

with

$$\Delta = \frac{9}{4} D_{\mathrm{eq}}^2 \left(1 + \mathtt{x}^2 + 2\mathtt{x}\cos 2\theta\right) \tag{4.37}$$

and

$$\eta_1(\xi,\beta) = \begin{cases} \dfrac{1}{(c_\beta + \sqrt{3}s_\beta)\xi} & \text{if} \quad (\xi,\beta) \in (\mathcal{M} \oplus \mathcal{O}) \\ \dfrac{1}{2(c_\beta \xi - 1)} & \text{if} \quad (\xi,\beta) \in \mathcal{N} \end{cases} \tag{4.38}$$

sets $\mathcal{M}$, $\mathcal{N}$ and $\mathcal{O}$ being introduced as

$$\mathcal{M} = \{(\xi,\beta) \quad \text{s.t.} \quad (\xi^* \leq \xi \leq \xi^{**},\, 0 \leq \beta < 1)\} \tag{4.39a}$$

$$\mathcal{N} = \{(\xi,\beta) \quad \text{s.t.} \quad (\xi \geq \xi^{**},\, 0 \leq \beta < 1)\} \tag{4.39b}$$

$$\mathcal{O} = \{(\xi,\beta) \quad \text{s.t.} \quad (\xi \geq \xi^{*},\, 1 \leq \beta \leq 2)\} \tag{4.39c}$$

Case B $\mathrm{TXE_D}$ with $C_0 > 0$ (that is, $\epsilon = +1$ and $\delta = +1$).
The principal deviatoric strain-rate component d_{d1} is equal to

$$d_{\mathrm{d1}} = \frac{D_{\mathrm{eq}}}{2}(\mathtt{x} - 1) \tag{4.40}$$

and quantity $(d_{\mathrm{m}} + d_{\mathrm{d1}})$ in Eq. (4.34) may assume positive or negative values:

$$\begin{cases} d_{\mathrm{m}} + d_{\mathrm{d1}} > 0 & \text{if} \quad \alpha(1-\tilde{\omega}) < \mathtt{x} < 1 \quad \text{or} \quad \mathtt{x} > 1 \\ d_{\mathrm{m}} + d_{\mathrm{d1}} < 0 & \text{if} \quad 0 < \mathtt{x} < \alpha(1-\tilde{\omega}) \end{cases} \tag{4.41}$$

It is worth observing that it is difficult to provide a precise delimitation on the variable $\mathtt{x}$ satisfying relationships (4.41), since quantity $\tilde{\omega}$ depends on strain-rate boundary conditions as well as on local-strength-criterion parameters. Nevertheless, due to the positiveness of $\mathtt{x}$, quantity $\tilde{\omega}$ has to be lower than 1, resulting in $\alpha(1-\tilde{\omega}) < \alpha$. By adopting the same approximation introduced by Anoukou et al. (2016), proven to be effective in the case of porous materials with a Mohr-Coulomb local plastic behaviour, inequalities $\alpha(1-\tilde{\omega}) < \mathtt{x} < 1$ and $\mathtt{x} < \alpha(1-\tilde{\omega})$ are respectively replaced by $\alpha < \mathtt{x} < 1$ and $\mathtt{x} < \alpha$. Accordingly, plastic admissibility conditions in Eqs. (4.18) and (4.19) reduce to

$$d_{\mathrm{m}} \geq \begin{cases} \eta_2 \left(-d_{\mathrm{d1}} + \sqrt{\Delta}\right) & \text{if} \quad 0 < \mathtt{x} < \alpha \\ \eta_1 \left(d_{\mathrm{d1}} + \sqrt{\Delta}\right) & \text{if} \quad \alpha < \mathtt{x} < 1 \\ \eta_1 \left(d_{\mathrm{d1}} + \sqrt{\Delta}\right) & \text{if} \quad \mathtt{x} > 1 \end{cases} \tag{4.42}$$

with

$$\Delta = \frac{9}{4} D_{\mathrm{eq}}^2 \left(1 + \mathtt{x}^2 - 2\mathtt{x}\cos 2\theta\right) \tag{4.43}$$

and where η_1 reads as in Eq. (4.38), and η_2 is equal to

$$\eta_2 = \begin{cases} \dfrac{1}{2+(c_\beta+\sqrt{3}s_\beta)\xi} & \text{if} \quad (\xi,\beta)\in(\mathcal{M}\oplus\mathcal{O}) \\ \dfrac{1}{2c_\beta\xi} & \text{if} \quad (\xi,\beta)\in\mathcal{N} \end{cases} \tag{4.44}$$

Case C $\mathrm{TXE_D}$ with $C_0<0$ (that is, $\epsilon=-1$ and $\delta=+1$).
The principal deviatoric strain-rate component $d_{\mathrm{d}1}$ is strictly negative and it is equal to

$$d_{\mathrm{d}1} = -\frac{D_{\mathrm{eq}}}{2}(1+\mathtt{x}) \tag{4.45}$$

Accordingly, using the same approximation strategy involving parameter $\tilde{\omega}$ and enforced in Case B, quantity $(d_{\mathrm{m}}+d_{\mathrm{d}1})$ assumes negative values everywhere in the hollow sphere, thereby resulting in the following plastic admissibility condition

$$d_{\mathrm{m}} \geq \eta_2\,(-d_{\mathrm{d}1}+\sqrt{\Delta}) \tag{4.46}$$

with

$$\Delta = \frac{9}{4}D_{\mathrm{eq}}^2\left(1+\mathtt{x}^2+2\mathtt{x}\cos 2\theta\right) \tag{4.47}$$

and where η_2 reads as in Eq. (4.44).

Case D $\mathrm{TXC_D}$ with $C_0<0$ (that is, $\epsilon=-1$ and $\delta=-1$).
The principal deviatoric strain-rate component $d_{\mathrm{d}1}$ is equal to

$$d_{\mathrm{d}1} = \frac{D_{\mathrm{eq}}}{2}(1-\mathtt{x}) \tag{4.48}$$

and quantity $(d_{\mathrm{m}}+d_{\mathrm{d}1})$ in Eq. (4.34) may assume positive or negative values, as in the Case B. However, by adopting the same approximation strategy involving $\tilde{\omega}$, Eqs. (4.18) and (4.19) lead to

$$d_{\mathrm{m}} \geq \begin{cases} \eta_1\,(d_{\mathrm{d}1}+\sqrt{\Delta}) & \text{if} \quad 0<\mathtt{x}<1 \\ \eta_1\,(d_{\mathrm{d}1}+\sqrt{\Delta}) & \text{if} \quad 1<\mathtt{x}<\alpha \\ \eta_2\,(-d_{\mathrm{d}1}+\sqrt{\Delta}) & \text{if} \quad \mathtt{x}>\alpha \end{cases} \tag{4.49}$$

with

$$\Delta = \frac{9}{4}D_{\mathrm{eq}}^2\left(1+\mathtt{x}^2-2\mathtt{x}\cos 2\theta\right) \tag{4.50}$$

η_1 and η_2 being expressed as in Eqs. (4.38) and (4.44), respectively.

Remark 7 *Conditions $\mathtt{x}=\alpha$ and $\mathtt{x}=1$ have not been addressed in previous Cases B and D. They will be detailed in Section 4.5.1 and in 4.A.*

4.5 Macroscopic yield criterion

The trial velocity field in Eq. (4.25) and the corresponding strain-rate state $(\widehat{\mathbf{d}},\widehat{\mathbf{d}}^{\mathcal{I}})\in\mathcal{K}_{\mathrm{d}}$ are expressed in terms of constant parameters C_0, C_1, and C_2, which have to comply

with kinematic admissibility requirements in Eqs. (4.27). By combining these latter with macroscopic strain-rate invariants in Eqs. (4.28a) and (4.28b), constants C_1 and C_2 are recast as

$$C_1 = D_\mathrm{m} - C_0 - \frac{D_\mathrm{eq}}{2\delta}\,, \qquad C_2 = D_\mathrm{m} - C_0 + \frac{D_\mathrm{eq}}{\delta} \tag{4.51}$$

Consequently, the estimate $\widehat{\Pi}$ in Eq. (4.10) of the macroscopic support function, computed via $(\widehat{\mathbf{d}}, \widehat{\mathbf{d}}^{\mathcal{I}}) \in \mathcal{K}_\mathrm{d}$ and under plastic admissibility conditions in Eqs. (4.36), (4.42), (4.46) and (4.49), depends on C_0. Since this latter has not to comply with any specific requirement, it can be considered as a free parameter, thereby allowing for a certain optimization in the determination of the macroscopic strength criterion. As a consequence, due to Eqs. (4.25) and (4.51), a class $\mathcal{V} \subseteq \mathcal{BC}_\mathrm{v}$ of kinematically-admissible velocity fields is defined as

$$\mathcal{V} = \mathrm{span}\,\{\widehat{\mathbf{v}}_0\} + \{\widehat{\mathbf{v}}_1\} \tag{4.52}$$

where

$$\begin{aligned} \widehat{\mathbf{v}}_0 &= \left[\left(\frac{R_\mathrm{e}}{r}\right)^{3\alpha} - 1\right](\rho\mathbf{e}_\rho + z\mathbf{e}_\mathrm{z}) \\ \widehat{\mathbf{v}}_1 &= \left(D_\mathrm{m} - \frac{D_\mathrm{eq}}{2\delta}\right)\rho\mathbf{e}_\rho + \left(D_\mathrm{m} + \frac{D_\mathrm{eq}}{\delta}\right) z\mathbf{e}_\mathrm{z} \end{aligned} \tag{4.53}$$

Accordingly and since Remark 6, denoting as $\widetilde{\boldsymbol{\Sigma}}^\mathrm{c}$ the sought macroscopic strength estimate related to the estimate $\widetilde{\Pi}$ in Eq. (4.12), the following inequality-constrained minimization problem $\mathcal{P}$ is introduced

$$\mathcal{P}: \quad \begin{cases} \min\limits_{\widehat{\mathbf{v}}\in\mathcal{V}} \left[\widehat{\Pi} - (3\widetilde{\Sigma}^\mathrm{c}_\mathrm{m} D_\mathrm{m} + \widetilde{\Sigma}^\mathrm{c}_\mathrm{eq} D_\mathrm{eq})\right] & \text{in} \quad \Omega_\mathrm{s} \cup \partial\Omega_\mathrm{i} \\ d_\mathrm{m} \geq \eta_\pm \left(\pm\, d_\mathrm{d1} + \sqrt{\Delta}\right) & \text{in} \quad \Omega_\mathrm{s} \cup \partial\Omega_\mathrm{i} \end{cases} \tag{4.54}$$

with $\widetilde{\Sigma}^\mathrm{c}_\mathrm{m} = \mathrm{tr}\,\widetilde{\boldsymbol{\Sigma}}^\mathrm{c}/3$ and $\widetilde{\Sigma}_\mathrm{eq} = \sqrt{3\widetilde{J}^\Sigma_2}$ ($\widetilde{J}^\Sigma_2 = \mathrm{tr}\,\widetilde{\boldsymbol{\Sigma}}^2_\mathrm{d}/2$ being the macroscopic second-order deviatoric stress invariant, with $\widetilde{\boldsymbol{\Sigma}}_\mathrm{d} = \widetilde{\boldsymbol{\Sigma}} - \widetilde{\Sigma}^\mathrm{c}_\mathrm{m}\mathbf{1}$) and where the sign plus (with $\eta_+ = \eta_1$) or minus (with $\eta_- = \eta_2$) applies depending on the value assumed by strain-rate parameters δ and ϵ, that is depending on cases A, B, C and D introduced in Section 4.4.2.

Rigorously, the plastic admissibility condition in Eq. (4.54) should be point-wise verified by strain-rate states $(\widehat{\mathbf{d}}, \widehat{\mathbf{d}}^{\mathcal{I}}) \in \mathcal{K}_\mathrm{d}$ computed via $\widehat{\mathbf{v}} \in \mathcal{V}$, in order to ensure the boundedness of local maximum plastic dissipations at each material point. However, the spatial dependence of plastic requirements in Eqs. (4.36), (4.42), (4.46) and (4.49) introduces a major difficulty in the resolution of problem $\mathcal{P}$, preventing the explicit determination of closed-form relationships for strength estimates $\widetilde{\Sigma}^\mathrm{c}_\mathrm{m}$ and $\widetilde{\Sigma}^\mathrm{c}_\mathrm{eq}$. Therefore, in agreement with modelling approaches proposed by Guo et al. (2008) and Anoukou et al. (2016) for porous materials with Drucker-Prager and Mohr-Coulomb plastic matrices, local plastic admissibility conditions are herein reformulated in an average sense, resulting

in the following auxiliary problem

$$\mathcal{P}^* : \quad \begin{cases} \min\limits_{\widehat{\boldsymbol{v}} \in \mathcal{V}} \left[\widehat{\Pi} - (3\widetilde{\Sigma}^{\mathrm{c}}_{\mathrm{m}} D_{\mathrm{m}} + \widetilde{\Sigma}^{\mathrm{c}}_{\mathrm{eq}} D_{\mathrm{eq}}) \right] & \text{in} \quad \Omega_{\mathrm{s}} \cup \partial\Omega_{\mathrm{i}} \\ \langle d_{\mathrm{m}} \rangle \geq \mathcal{H} & \text{in} \quad \Omega_{\mathrm{s}} \cup \partial\Omega_{\mathrm{i}} \end{cases} \tag{4.55}$$

with

$$\mathcal{H} = \eta_{\pm} \left\langle \pm\, d_{\mathrm{d1}} + \sqrt{\Delta} \right\rangle \tag{4.56}$$

The latter can be solved via the Lagrangian method for inequality-constrained optimizations, that is via Karush-Kuhn-Tucker (KKT) conditions. Since Eq. (4.28a), the Lagrangian function $\mathcal{L}$ associated to problem $\mathcal{P}^*$ can be introduced as

$$\mathcal{L} = -\widehat{\Pi} + 3\widetilde{\Sigma}^{\mathrm{c}}_{\mathrm{m}} (C_0 + D^{\mathrm{hom}}_{\mathrm{m}}) + \widetilde{\Sigma}^{\mathrm{c}}_{\mathrm{eq}} D_{\mathrm{eq}} + \lambda \left(\langle d_{\mathrm{m}} \rangle - \mathcal{H} \right) \tag{4.57}$$

where λ is the Lagrange-KKT multiplier associated to the average plastic admissibility condition $\langle d_{\mathrm{m}} \rangle \geq \mathcal{H}$, and where, owing to Eqs. (4.10), (4.18) and (4.19), the estimate $\widehat{\Pi}$ is equal to

$$\widehat{\Pi} = 3h\xi \left[\langle d_{\mathrm{m}} \rangle + 3f\kappa \left\langle d^{\mathcal{I}}_{\mathrm{m}} \right\rangle_{\mathcal{I}} \right] \tag{4.58}$$

the dimensionless parameter κ being defined as

$$\kappa = \frac{h^{\mathcal{I}}}{R_{\mathrm{i}} h} \tag{4.59}$$

accounting for the influence of void-size effects (Dormieux and Kondo, 2010; Brach et al., 2016b). As a matter of fact, an increase in κ corresponds, for a fixed value of the matrix strength parameter h, to an increase in the ratio $h^{\mathcal{I}}/R_{\mathrm{i}}$, that is to a reduction in the void size R_{i}. Moreover, the case of negligible interface effects (namely, for porous materials characterized by large values of R_{i}) can be addressed by considering $\kappa \to 0^+$.

The following problem is thereby introduced.

Problem 6 *Find* $\{C_0, D^{hom}_m, D_{eq}, \lambda\}$ *such that*

- *Stationarity conditions:* $$\frac{\partial \mathcal{L}}{\partial C_0} = 0\,, \quad \frac{\partial \mathcal{L}}{\partial D^{hom}_m} = 0\,, \quad \frac{\partial \mathcal{L}}{\partial D_{eq}} = 0 \tag{4.60a}$$
- *Primal feasibility:* $$\frac{\partial \mathcal{L}}{\partial \lambda} \geq 0 \quad \Leftrightarrow \quad \langle d_m \rangle \geq \mathcal{H} \tag{4.60b}$$
- *Dual feasibility:* $$\lambda \geq 0 \tag{4.60c}$$
- *Complementary slackness:* $$\lambda \left(\langle d_m \rangle - \mathcal{H} \right) = 0 \tag{4.60d}$$

Nevertheless, aiming to determine the macroscopic yield function $\widetilde{\mathcal{G}}\,(\widetilde{\boldsymbol{\Sigma}}^{\mathrm{c}})$, the full resolution of Problem 6 in terms of the macroscopic strain-rate parameters C_0, $D^{\mathrm{hom}}_{\mathrm{m}}$ and D_{eq}, and of the Lagrange-KKT multiplier λ is not mandatory. As a matter of fact, KKT conditions in Eqs. (4.60) can be directly used to compute $(\widetilde{\Sigma}^{\mathrm{c}}_{\mathrm{m}}, \widetilde{\Sigma}^{\mathrm{c}}_{\mathrm{eq}}, \lambda)$, by enforcing function $\widetilde{\mathcal{G}}\,(\widetilde{\boldsymbol{\Sigma}}^{\mathrm{c}})$ to describe physically-consistent macroscopic strength states.

In detail, owing to dual feasibility, two study cases have to be addressed:

1) $\lambda = 0 \Rightarrow \langle d_{\mathrm{m}} \rangle \geq \mathcal{H}$;

2) $\lambda > 0 \Rightarrow \langle d_{\mathrm{m}} \rangle = \mathcal{H}$;

where primal feasibility condition results from the complementary slackness one. As regards the first case (that is, $\lambda = 0$), by combining Eqs. (4.57) and (4.58), the following expression is obtained for the Lagrangian function

$$\mathcal{L} = -3h\xi \left[\langle d_{\mathrm{m}} \rangle + 3f\kappa \left\langle d_{\mathrm{m}}^{\mathcal{I}} \right\rangle_{\mathcal{I}} \right] + 3\widetilde{\Sigma}_{\mathrm{m}}^{\mathrm{c}} (C_0 + D_{\mathrm{m}}^{\mathrm{hom}}) + \widetilde{\Sigma}_{\mathrm{eq}}^{\mathrm{c}} D_{\mathrm{eq}} \tag{4.61}$$

where, due to Eq. (4.29), averages of d_{m} and $d_{\mathrm{m}}^{\mathcal{I}}$ are equal to

$$\langle d_{\mathrm{m}} \rangle = (1-f) \left[D_{\mathrm{m}}^{\mathrm{hom}} + C_0 \frac{1 - f^{1-\alpha}}{1-f} \right] \tag{4.62}$$

$$\left\langle d_{\mathrm{m}}^{\mathcal{I}} \right\rangle_{\mathcal{I}} = D_{\mathrm{m}}^{\mathrm{hom}} + C_0 \frac{1-\alpha}{f^{\alpha}} \tag{4.63}$$

By computing derivatives of the Lagrangian function (4.61) with respect to macroscopic strain-rate parameters, stationarity conditions (4.60a) lead to $\widetilde{\Sigma}_{\mathrm{eq}}^{\mathrm{c}} = 0$ and to two different values for $\widetilde{\Sigma}_{\mathrm{m}}^{\mathrm{c}}$ for any strain-rate boundary condition $\mathbf{D}$, thereby identifying a physically-inconsistent macroscopic stress state.

Accordingly, the case $\lambda = 0$ not allowing for any acceptable solution, the Lagrange-KKT multiplier λ has to assume strictly positive values in order to comply with the dual feasibility condition. Therefore, by recasting primal feasibility and complementary slackness in the form $\langle d_{\mathrm{m}} \rangle = \mathcal{H}$, the KKT Problem 6 is reformulated as

Problem 7 *Find* $\left\{ \widetilde{\Sigma}_m^c, \widetilde{\Sigma}_{eq}^c, \lambda \right\}$ *such that*

$$\frac{\partial \mathcal{L}}{\partial C_0} = 0\,, \quad \frac{\partial \mathcal{L}}{\partial D_m^{hom}} = 0\,, \quad \frac{\partial \mathcal{L}}{\partial D_{eq}} = 0 \tag{4.64a}$$

$$\lambda > 0 \tag{4.64b}$$

$$\langle d_m \rangle = \mathcal{H} \tag{4.64c}$$

where the Lagrangian function is equal to

$$\mathcal{L} = -3h\xi \left[\langle d_m \rangle + 3f\kappa \mathcal{H}^{\mathcal{I}} \right] + 3\widetilde{\Sigma}_m^c (C_0 + D_m^{hom}) + \widetilde{\Sigma}_{eq}^c D_{eq} + \lambda \left(\langle d_m \rangle - \mathcal{H} \right) \tag{4.65}$$

and where

$$\mathcal{H}^{\mathcal{I}} = \eta_{\pm} \left\langle \pm d_{d1}^{\mathcal{I}} + \sqrt{\Delta|_{\boldsymbol{x}=\boldsymbol{x}^{\mathcal{I}}}} \right\rangle_{\mathcal{I}} \qquad \textit{with} \qquad \boldsymbol{x}^{\mathcal{I}} = \boldsymbol{x}|_{r=R_i} \tag{4.66}$$

the average plastic admissibility condition on the interface being straight satisfied in its equality form $\left\langle d_m^{\mathcal{I}} \right\rangle_{\mathcal{I}} = \mathcal{H}^{\mathcal{I}}$*, since* $\lambda > 0$.

By replacing Eq. (4.62) into the Lagrangian function in Eq. (4.65), the following expres-

sions for stationarity conditions in Eq. (4.64a) are obtained

$$\frac{\partial \mathcal{L}}{\partial C_0} = 3\widetilde{\Sigma}^{\mathrm{c}}_{\mathrm{m}} + (\lambda - 3h\xi)\left(1 - f^{1-\alpha}\right) - 9h\xi f\kappa\epsilon\,\Psi^{\mathcal{I}}_{\mathrm{m}} - \lambda\epsilon\,\Psi_{\mathrm{m}} = 0 \tag{4.67}$$

$$\frac{\partial \mathcal{L}}{\partial D^{\mathrm{hom}}_{\mathrm{m}}} = 3\widetilde{\Sigma}^{\mathrm{c}}_{\mathrm{m}} + (\lambda - 3h\xi)\,(1 - f) = 0 \tag{4.68}$$

$$\frac{\partial \mathcal{L}}{\partial D_{\mathrm{eq}}} = \widetilde{\Sigma}^{\mathrm{c}}_{\mathrm{eq}} - 9h\xi f\kappa\,\Psi^{\mathcal{I}}_{\mathrm{eq}} - \lambda\,\Psi_{\mathrm{eq}} = 0 \tag{4.69}$$

where solid matrix (Ψ_{m} and Ψ_{eq}), and interface ($\Psi^{\mathcal{I}}_{\mathrm{m}}$ and $\Psi^{\mathcal{I}}_{\mathrm{eq}}$) model functions are defined as

$$\Psi_{\mathrm{m}} = \epsilon\frac{\partial \mathcal{H}}{\partial C_0}\,, \qquad \Psi^{\mathcal{I}}_{\mathrm{m}} = \epsilon\frac{\partial \mathcal{H}^{\mathcal{I}}}{\partial C_0} \tag{4.70}$$

$$\Psi_{\mathrm{eq}} = \frac{\partial \mathcal{H}}{\partial D_{\mathrm{eq}}}\,, \qquad \Psi^{\mathcal{I}}_{\mathrm{eq}} = \frac{\partial \mathcal{H}^{\mathcal{I}}}{\partial D_{\mathrm{eq}}} \tag{4.71}$$

$\mathcal{H}$ and $\mathcal{H}^{\mathcal{I}}$ in Eqs. (4.56) and (4.66) depending on C_0 and D_{eq} only (see Eqs. (4.32)).

The Lagrange-KKT multiplier λ is determined by subtracting Eqs. (4.68) to (4.67), resulting in

$$\lambda = 3h\xi\,\frac{f^{1-\alpha} - f - 3f\kappa\epsilon\Psi^{\mathcal{I}}_{\mathrm{m}}}{f^{1-\alpha} - f + \epsilon\Psi_{\mathrm{m}}} \tag{4.72}$$

Moreover, by replacing Eq. (4.72) into stationarity conditions (4.68) and (4.69), the estimate for the macroscopic yield function is obtained as

$$\widetilde{\mathcal{G}}\,(\widetilde{\boldsymbol{\Sigma}}^{\mathrm{c}}):\quad \begin{cases} \dfrac{\widetilde{\Sigma}^{\mathrm{c}}_{\mathrm{m}}}{h} = \xi\epsilon(1-f)\,\dfrac{\Psi_{\mathrm{m}} + 3f\kappa\Psi^{\mathcal{I}}_{\mathrm{m}}}{f^{1-\alpha} - f + \epsilon\Psi_{\mathrm{m}}} \\ \dfrac{\widetilde{\Sigma}^{\mathrm{c}}_{\mathrm{eq}}}{h} = \xi\left[3f\kappa\Psi^{\mathcal{I}}_{\mathrm{eq}} + \dfrac{f^{1-\alpha} - f - 3f\kappa\epsilon\Psi^{\mathcal{I}}_{\mathrm{m}}}{f^{1-\alpha} - f + \epsilon\Psi_{\mathrm{m}}}\,\Psi_{\mathrm{eq}}\right] \end{cases} \tag{4.73}$$

Accordingly, Eqs. (4.72) and (4.73) identify the unique physically-consistent solution of the KKT problem in Eqs. (4.64), provided that the dual feasibility condition $\lambda > 0$ is verified or, equivalently, the local strain-rate field complies with primal feasibility and slackness condition $\langle d_{\mathrm{m}}\rangle = \mathcal{H}$.

Remark 8 *Denoting as* $\widetilde{\Pi} = \widetilde{\boldsymbol{\Sigma}}^{c} : \mathbf{D}$ *the macroscopic support function of* $\widetilde{\mathcal{G}}$ *in Eq.* (4.73)*, primal feasibility relationship* $\langle d_m\rangle = \mathcal{H}$ *corresponds to the macroscopic plastic admissibility condition on* $\widetilde{\Pi}$*, that is it represents the requirement to be verified for ensuring finite positive values of macroscopic maximum plastic dissipation.*

Remark 9 *The strictly-positive Lagrange-KKT multiplier in Eq.* (4.72)*, introduced in problem* (4.55) *in order to enforce the average plastic admissibility condition* (4.64c)*, assumes the physical meaning of strictly-positive plastic multiplier in the macroscopic normality law*

$$\mathbf{D} = \lambda\,\frac{\partial\widetilde{\mathcal{G}}\,(\widetilde{\boldsymbol{\Sigma}}^{c})}{\partial\widetilde{\boldsymbol{\Sigma}}^{c}} \tag{4.74}$$

In agreement with results provided by Rice (1971), the normality law governing the local

plastic behaviour is proven to upscale at the macroscopic level.

It is worth noticing that, owing to Eqs. (4.32), solid matrix ($\Psi_{\rm m}$ and $\Psi_{\rm eq}$) and interface ($\Psi^{\mathcal{I}}_{\rm m}$ and $\Psi^{\mathcal{I}}_{\rm eq}$) model functions introduced in Eqs. (4.70) and (4.71) depend on macroscopic strain-rate parameters ϵ, ω, and δ. The macroscopic yield function in Eq. (4.73) thereby results in parametric expressions for $\widetilde{\Sigma}^{\rm c}_{\rm m}$ and $\widetilde{\Sigma}^{\rm c}_{\rm eq}$, which implicitly account for the dependency on the macroscopic stress Lode angle $\widetilde{\theta}_\Sigma$ (see Benallal et al., 2014), the latter defined as $\cos 3\widetilde{\theta}_\Sigma = 3\sqrt{3}\widetilde{J}^\Sigma_2/[2(\widetilde{J}^\Sigma_2)^{3/2}]$ with $\widetilde{J}^\Sigma_3 = \operatorname{tr}\widetilde{\boldsymbol{\Sigma}}^3_{\rm d}/3$ the third-order deviatoric stress invariant.

4.5.1 Solid matrix and interface model functions

In order to compute the plastic multiplier and the macroscopic yield criterion in Eqs. (4.72) and (4.73), solid matrix ($\Psi_{\rm m}$ and $\Psi_{\rm eq}$) and interface ($\Psi^{\mathcal{I}}_{\rm m}$ and $\Psi^{\mathcal{I}}_{\rm eq}$) model functions have to be explicitly determined. Owing to Eqs. (4.70) and (4.71), this corresponds to compute derivatives of functions $\mathcal{H}$ and $\mathcal{H}^{\mathcal{I}}$ with respect to macroscopic strain-rate parameters C_0 and $D_{\rm eq}$.

The change of variable $r = R_{\rm e}\,\omega \mathbf{x}^{-3\alpha}$ (see Eq. (4.31)) is adopted to recast Ω- and $\partial\Omega_{\rm i}$-based averages in Eqs. (4.56) and (4.66) in terms of the macroscopic strain-rate triaxiality measure ω, the latter depending on parameters C_0 and $D_{\rm eq}$. Functions $\mathcal{H}$ and $\mathcal{H}^{\mathcal{I}}$ thereby result in

$$\mathcal{H} = \frac{D_{\rm eq}}{4\alpha}\omega^{1/\alpha}\mathcal{J}(\omega)\,, \qquad \mathcal{H}^{\mathcal{I}} = \frac{D_{\rm eq}}{4}\mathcal{J}^{\mathcal{I}}(\omega) \tag{4.75}$$

where the closed-form expression for $\mathcal{J}(\omega)$ coincides with the piece-wise relationship analytically provided by Anoukou et al. (2016) (see 4.A), and where function $\mathcal{J}^{\mathcal{I}}(\omega)$ is equal to

$$\mathcal{J}^{\mathcal{I}}(\omega) = \eta_\pm\ \Upsilon(\omega)|_{\mathbf{x}=\mathbf{x}^{\mathcal{I}}} \tag{4.76}$$

$\Upsilon(\omega)$ being defined as

$$\Upsilon(\omega) = \int_0^\pi \iota(\theta)\sin\theta\, d\theta\,, \qquad \text{with} \qquad \iota = \frac{2}{D_{\rm eq}}\left(\pm\, d_{\rm d1} + \sqrt{\Delta}\right) \tag{4.77}$$

Therefore, by denoting as $\mathcal{J}'$ (resp., $\mathcal{J}^{\mathcal{I}\prime}$) the first-order derivative of function $\mathcal{J}$ (resp., $\mathcal{J}^{\mathcal{I}}$) with respect to ω, solid matrix and interface model functions can be obtained, via Eqs. (4.70) and (4.71), from the following relationships

$$\frac{\partial\mathcal{H}}{\partial C_0} = \frac{\omega^{1/\alpha-1}}{2\epsilon}\left[\frac{1}{\alpha}(\mathcal{J}+\ell_{\rm m}) + \omega\mathcal{J}'\right] \tag{4.78a}$$

$$\frac{\partial\mathcal{H}}{\partial D_{\rm eq}} = \frac{\omega^{1/\alpha}}{4\alpha}\left[\frac{\alpha-1}{\alpha}(\mathcal{J}+\ell_{\rm eq}) - \omega\mathcal{J}'\right] \tag{4.78b}$$

$$\frac{\partial\mathcal{H}^{\mathcal{I}}}{\partial C_0} = \frac{\alpha}{2\epsilon}\mathcal{J}^{\mathcal{I}\prime} + \ell^{\mathcal{I}}_{\rm m} \tag{4.78c}$$

$$\frac{\partial\mathcal{H}^{\mathcal{I}}}{\partial D_{\rm eq}} = \frac{1}{4}\left(\mathcal{J}^{\mathcal{I}} - \omega\mathcal{J}^{\mathcal{I}\prime}\right) + \ell^{\mathcal{I}}_{\rm eq} \tag{4.78d}$$

where constant parameters $\ell_{\rm m}$, $\ell_{\rm eq}$, $\ell^{\mathcal{I}}_{\rm m}$ and $\ell^{\mathcal{I}}_{\rm eq}$ have been introduced (as detailed in

4.A) in order to ensure the continuity of the macroscopic yield function in Eq. (4.73) for any value of the strain-rate triaxiality measure ω. It is worth pointing out that, since admissibility conditions are piece-wise defined with respect to $\mathbf{x}$ (namely, with respect to ω), the continuity of the macroscopic yield function $\widetilde{\mathcal{G}}$ could be not straight satisfied.

With the aim to furnish explicit relationships for functions $\mathcal{J}$ and $\mathcal{J}^{\mathcal{I}}$ in derivatives (4.78), study cases introduced in Section 4.4.2 have to be separately addressed, depending on the sign of the principal deviatoric strain-rate component $d_{\mathrm{d}1}$ (that is, on the value assumed for strain-rate parameters ϵ and δ). For the sake of compactness, corresponding analytical details and resulting expressions for $\mathcal{J}$ and $\mathcal{J}^{\mathcal{I}}$ are reported in 4.A.

4.5.2 Relationships among macroscopic strain-rate and stress invariants

Closed-form relationships provided for $\mathcal{J}(\omega)$ and $\mathcal{J}^{\mathcal{I}}(\omega)$ allow to compute in a piece-wise fashion derivatives of functions $\mathcal{H}$ and $\mathcal{H}^{\mathcal{I}}$ in Eqs. (4.78), by separately addressing strain-rate loading conditions described via parameters $\epsilon = \operatorname{sgn} C_0$ and $\delta = \operatorname{sgn} J_3^{\mathrm{D}}$. Therefore, owing to Eqs. (4.70) and (4.71), piece-wise defined model functions $\Psi_{\mathrm{m}}(\omega)$, $\Psi_{\mathrm{eq}}(\omega)$, $\Psi_{\mathrm{m}}^{\mathcal{I}}(\omega)$ and $\Psi_{\mathrm{eq}}^{\mathcal{I}}(\omega)$ straight deliver parametric expressions for $\widetilde{\Sigma}_{\mathrm{m}}^{\mathrm{c}}$ and $\widetilde{\Sigma}_{\mathrm{eq}}^{\mathrm{c}}$ in Eq. (4.73), formulated in terms of the macroscopic strain-rate triaxiality measure ω only. Such an occurrence is due to the introduction of Cases A, B, C and D in Section 4.4.2, allowing to explicitly address the parametric dependence of the predicted strength state $(\widetilde{\Sigma}_{\mathrm{m}}^{\mathrm{c}}, \widetilde{\Sigma}_{\mathrm{eq}}^{\mathrm{c}})$ on both the macroscopic strain-rate Lode angle (i.e., $\theta_{\mathrm{D}} = 0$ or $\theta_{\mathrm{D}} = \pi/3$) and the sign of the heterogeneous mean deformation rate C_0.

Accordingly, in order to clearly formulate relationships between the strain-rate loading condition $(\epsilon, \delta, \omega)$ and the resulting macroscopic strength state $(\widetilde{\Sigma}_{\mathrm{m}}^{\mathrm{c}}, \widetilde{\Sigma}_{\mathrm{eq}}^{\mathrm{c}})$, the parametric form of the proposed macroscopic yield function has to be carefully analysed.

Since the local plastic behaviour is isotropic and due to the spherical symmetry of the reference cell in Fig. 4.1, the estimate $\widetilde{\Pi}$ of the macroscopic support function depends only on isotropic strain-rate invariants D_{m}, D_{eq} and θ_{D} introduced in Eqs. (4.28). Thereby, the estimate $\widetilde{\boldsymbol{\Sigma}}^{\mathrm{c}}$ of the limit stress $\boldsymbol{\Sigma}^{\mathrm{c}}$ reads as

$$\widetilde{\boldsymbol{\Sigma}}^{\mathrm{c}} = \frac{\partial \widetilde{\Pi}}{\partial \mathbf{D}} = \frac{1}{3}\frac{\partial \widetilde{\Pi}}{\partial D_{\mathrm{m}}}\mathbf{1} + \frac{2}{3D_{\mathrm{eq}}}\frac{\partial \widetilde{\Pi}}{\partial D_{\mathrm{eq}}}\mathbf{D}_{\mathrm{d}} + \frac{\partial \widetilde{\Pi}}{\partial \theta_{\mathrm{D}}}\frac{\partial \theta_{\mathrm{D}}}{\partial \mathbf{D}_{\mathrm{d}}} \tag{4.79}$$

where, for symmetry reasons (e.g., Lemarchand et al., 2015), function $\widetilde{\Pi}$ has to comply with $\partial\widetilde{\Pi}/\partial\theta_{\mathrm{D}} = 0$ at $\theta_{\mathrm{D}} = 0$ (i.e., for $\delta = 1$) and at $\theta_{\mathrm{D}} = \pi/3$ (i.e., for $\delta = -1$). Moreover, since the strain-rate boundary conditions expressed in Eq. (4.1), the isotropy of the macroscopic constitutive law in Eq. (4.79) yields

$$\widetilde{\boldsymbol{\Sigma}}^{\mathrm{c}} = \widetilde{\Sigma}_{\rho}(\mathbf{e}_{\rho} \otimes \mathbf{e}_{\rho} + \mathbf{e}_{\varphi} \otimes \mathbf{e}_{\varphi}) + \widetilde{\Sigma}_{\mathrm{z}}\mathbf{e}_{\mathrm{z}} \otimes \mathbf{e}_{\mathrm{z}} \tag{4.80}$$

resulting in

$$\widetilde{\Sigma}_{\mathrm{eq}}^{\mathrm{c}} = \delta_{\widetilde{\Sigma}}\left(\widetilde{\Sigma}_{\mathrm{z}} - \widetilde{\Sigma}_{\rho}\right), \qquad \widetilde{\theta}_{\Sigma} = \frac{1}{3}\arccos\left(\delta_{\widetilde{\Sigma}}\right) \tag{4.81}$$

with $\delta_{\widetilde{\Sigma}} = \operatorname{sgn}(\widetilde{\Sigma}_{\mathrm{z}} - \widetilde{\Sigma}_{\rho})$. Therefore, by introducing the macroscopic generalised plain

strain-rate $D_{\rm gps} = -D_{\rm eq}/\delta$ and plane stress $\widetilde{\Sigma}^{\rm c}_{\rm gps} = -\widetilde{\Sigma}^{\rm c}_{\rm eq}/\delta_{\widetilde{\Sigma}}$ invariants (e.g., Pastor et al., 2004; Thoré et al., 2011), Eq. (4.79) provides the following constitutive relationship

$$\widetilde{\Sigma}^{\rm c}_{\rm gps} = \frac{\partial \widetilde{\Pi}}{\partial D_{\rm eq}} \frac{\partial D_{\rm eq}}{\partial D_{\rm gps}} = -\delta\, \widetilde{\Sigma}^{\rm c}_{\rm eq} \tag{4.82}$$

which straight results in $\delta_{\widetilde{\Sigma}} = \delta$, that is (see also Benallal et al., 2014)

$$\widetilde{\theta}_{\Sigma} = \theta_{\rm D} \tag{4.83}$$

Consequently, macroscopic triaxial-expansion $\mathrm{TXE_D}$ and compression $\mathrm{TXC_D}$ strain-rate loading conditions respectively correspond to macroscopic triaxial-expansion $\mathrm{TXE}_{\widetilde{\Sigma}}$ (i.e., $\widetilde{\theta}_{\Sigma} = 0$) and compression $\mathrm{TXC}_{\widetilde{\Sigma}}$ (i.e., $\widetilde{\theta}_{\Sigma} = \pi/3$) yield stress states.

Furthermore, by computing derivatives in Eqs. (4.78) via relationships provided in 4.A for $\mathcal{J}(\omega)$ and $\mathcal{J}^{\mathcal{I}}(\omega)$, solid matrix and interface model functions in Eqs. (4.70) and (4.71) result to be positive-defined for any value of ω. Accordingly, due to the strictly positiveness of the plastic multiplier in Eq. (4.72), the parametric expression of $\widetilde{\Sigma}^{\rm c}_{\rm m}$ in Eq. (4.73) yields

$$\operatorname{sgn} \widetilde{\Sigma}^{\rm c}_{\rm m} = \epsilon \tag{4.84}$$

Macroscopic strain-rate states in Eq. (4.1) with positive (resp., negative) heterogeneous mean deformation rates $D_{\rm m} - D^{\rm hom}_{\rm m} = C_0$ (see Eq. (4.28a)) thereby correspond to macroscopic yield stress states in Eq. (4.73) with tensile (resp., compressive) hydrostatic parts.

Finally, by replacing Eqs. (4.29) and (4.75) into the macroscopic plastic admissibility condition $\langle d_{\rm m} \rangle = \mathcal{H}$, the following relationship is obtained

$$(1-f) D_{\rm m} + C_0 \left(f - f^{1-\alpha}\right) = \frac{D_{\rm eq}}{4\alpha} \omega^{1/\alpha} \mathcal{J}(\omega) \tag{4.85}$$

that is, owing to Eqs. (4.28) and (4.31),

$$(1-f) D_{\rm m} + \frac{D_{\rm eq}\omega}{4\alpha} \left[\frac{2}{\epsilon} \left(f - f^{1-\alpha}\right) - \omega^{1/\alpha - 1} \mathcal{J}(\omega) \right] = 0 \tag{4.86}$$

which is continuous in ω for any choice of strain-rate parameters ϵ and δ, since function $\mathcal{J}(\omega)$ is continuous. Equation (4.86) proves that the strain-rate triaxiality measure ω allows to range from pure deviatoric (i.e., $\mathbf{D}$ s.t. $D_{\rm m} = 0$) to pure hydrostatic (i.e., $\mathbf{D}$ s.t. $D_{\rm eq} = 0$) macroscopic strain-rate boundary conditions, when ω is varied from zero to infinity.

Accordingly, owing to Eqs. (4.83) and (4.84), model functions obtained in 4.A, by separately addressing $\mathrm{TXE_D}$ and $\mathrm{TXC_D}$ strain rates with $\epsilon = \pm 1$, allow to determine macroscopic triaxial-expansion (Cases B and C) and triaxial-compression (Cases A and D) strength states $(\widetilde{\Sigma}^{\rm c}_{\rm m}, \widetilde{\Sigma}^{\rm c}_{\rm eq})$, with a tensile (Cases A and B) or compressive (Cases C and D) hydrostatic part $\widetilde{\Sigma}^{\rm c}_{\rm m}$.

4.5.3 On the positiveness of the macroscopic plastic multiplier

As previously stated, the plastic multiplier λ and the macroscopic yield function $\widetilde{\mathcal{G}}(\widetilde{\boldsymbol{\Sigma}}^{\mathrm{c}})$ in Eqs. (4.72) and (4.73) identify the unique physically-consistent solution of the constrained minimization problem in Eqs. (4.64), under the requirement $\lambda > 0$.

Since solid matrix and interface model functions Ψ_{m} and $\Psi_{\mathrm{m}}^{\mathcal{I}}$ are continuous and positive-defined for any value of $\omega \in (0, +\infty)$, following study cases have to be addressed depending on the strain-rate parameter ϵ.

Cases A–B $\mathrm{TXC_D}$ and $\mathrm{TXE_D}$ with $C_0 > 0$ (that is, $\epsilon = +1$ and $\delta = \mp 1$).
By computing Eq. (4.72) for $\epsilon = +1$, the macroscopic plastic multiplier reads as

$$\lambda|_{\epsilon=+1} = 3h\xi \, \frac{f^{1-\alpha} - f - 3f\kappa\Psi_{\mathrm{m}}^{\mathcal{I}}|_{\epsilon=+1}}{f^{1-\alpha} - f + \Psi_{\mathrm{m}}|_{\epsilon=+1}} \tag{4.87}$$

where the exponent α of the heterogeneous velocity field is such that $0 < \alpha < 1$, and where $f^{1-\alpha} - f > 0$ for any value of α.

When interface effects are considered as negligible (that is, for $\kappa \to 0^{+}$), the plastic multiplier in Eq. (4.87) results to be strictly positive-defined on the interval $\omega \in (0, +\infty)$, without any further consistency condition being required. This is the case of the Mohr-Coulomb hollow-sphere model proposed by Anoukou et al. (2016) for classical porous materials.

On the other hand, when interface effects are taken into account (that is, for $\kappa > 0$), since the interface model function $\Psi_{\mathrm{m}}^{\mathcal{I}}$ assumes its maximum value for $\omega \to +\infty$ (see 4.A), the consistency requirement $\lambda > 0$ for any value of ω leads to

$$\kappa < \frac{f^{1-\alpha} - f}{3f\Psi_{\mathrm{m}}^{\mathcal{I}}} \leq \frac{f^{1-\alpha} - f}{3f \lim\limits_{\substack{\omega\to+\infty \\ \epsilon=1 \\ \delta=\pm1}} \Psi_{\mathrm{m}}^{\mathcal{I}}} = \frac{f^{1-\alpha} - f}{12\alpha\,\eta_1 f^{1-\alpha}} = \widehat{\kappa} \tag{4.88}$$

thereby straight resulting in an upper limit for the void-size parameter κ, that is $\kappa \in [0, \widehat{\kappa})$. Such a result is analysed in Figs. 4.3a and 4.3b, wherein $\widehat{\kappa}$ is computed as a function of model parameters ξ and β, and for different values of porosity f, when local plastic behaviours with $(\xi, \beta) \in \mathcal{N}$ and $(\xi, \beta) \in \mathcal{O}$ are respectively addressed (see Eqs. (4.39b) and (4.39c)). In detail, for a given choice of parameters ξ and β, the upper-limit value $\widehat{\kappa}$ is shown to increase when porosity f reduces. Moreover, when ξ and f are considered as fixed, an increase in β corresponds to an increase of $\widehat{\kappa}$, such an occurrence being emphasized in the case of a local yield function with $(\xi, \beta) \in \mathcal{N}$. Finally, for given values of β and f, decreasing ξ results in a reduction of the upper-limit value $\widehat{\kappa}$.

Cases C–D $\mathrm{TXE_D}$ and $\mathrm{TXC_D}$ with $C_0 < 0$ (that is, $\epsilon = -1$ and $\delta = \pm 1$).
By computing Eq. (4.72) for $\epsilon = -1$, the macroscopic plastic multiplier reads as

$$\lambda|_{\epsilon=-1} = 3h\xi \, \frac{f^{1-\alpha} - f + 3f\kappa\Psi_{\mathrm{m}}^{\mathcal{I}}|_{\epsilon=-1}}{f^{1-\alpha} - f - \Psi_{\mathrm{m}}|_{\epsilon=-1}} \tag{4.89}$$

where $\alpha > 1$ and $f^{1-\alpha} - f > 0$.

Since the solid matrix model function Ψ_{m} assumes its maximum value for $\omega \to +\infty$, the consistency requirement on the strictly positiveness of the macroscopic plastic multiplier in Eq. (4.89) results in

$$f^{1-\alpha} - f - \lim_{\substack{\omega\to+\infty \\ \epsilon=-1 \\ \delta=\pm1}} \Psi_{\mathrm{m}} > 0\,, \qquad \text{with} \qquad \lim_{\substack{\omega\to+\infty \\ \epsilon=-1 \\ \delta=\pm1}} \Psi_{\mathrm{m}} = \frac{4\alpha\,\eta_2}{1-\alpha}\left(1 - f^{1-\alpha}\right) \tag{4.90}$$

Therefore, by replacing η_2 in Eq. (4.44) into Eq. (4.90), the plastic multiplier in Eq. (4.89) results to be strictly positive

- for any local plastic behaviour such that $(\xi, \beta) \in \mathcal{M}$ (see Eq. (4.39a)), provided that following relationship is verified

$$\frac{2}{\Xi^-} - \frac{f}{\xi^*} - \frac{f^{\frac{\Xi^-}{\Xi^- - \xi}}}{\xi^{**}} + \frac{f^{\frac{\Xi^-}{\Xi^- - \xi}} - f}{\xi} > 0 \tag{4.91}$$

  with $\Xi^- = \Xi|_{\epsilon=-1}$ and $f^{\frac{\Xi^-}{\Xi^- - \xi}} - f > 0$, and where, as shown in Fig. 4.4, parameters Ξ^-, ξ^* and ξ^{**} assume strictly positive values over the interval $\beta \in [0, 1)$;

- for any local plastic behaviour such that $(\xi, \beta) \in \mathcal{N}$ (see Eq. (4.39b)). This is the case of the Mohr-Coulomb hollow-sphere model proposed by Anoukou et al. (2016) for porous materials, which is recovered as a special case of the general yield function in Eqs. (4.14) to (4.16) by setting parameters ξ and β as in Table 4.1;

- for any local plastic behaviour such that $(\xi, \beta) \in \mathcal{O}$ (see Eq. (4.39c)). As a matter of fact, since ξ^{**} assumes negative values for $\beta \in (1, 2]$ and $\xi^{**} \to -\infty$ for $\beta \to 1+$ (Fig. 4.4), relationship (4.91) reads as

$$\frac{2}{\Xi^-} - \frac{f}{\xi^*} + \frac{f^{\frac{\Xi^-}{\Xi^- - \xi}}}{|\xi^{**}|} + \frac{f^{\frac{\Xi^-}{\Xi^- - \xi}} - f}{\xi} > 0 \tag{4.92}$$

  which results to be verified for any value of $(\xi, \beta) \in \mathcal{O}$ and f, since $2/\Xi^- > f/\xi^*$.

Accordingly, within the domain of definition of the void-size parameter $\kappa \in [0, \widehat{\kappa})$ and taking into account the consistency condition in Eq. (4.91) for local yield functions with $(\xi, \beta) \in \mathcal{M}$, the macroscopic plastic multiplier λ in Eq. (4.72) results to be strictly positive. This straight corresponds to verify dual feasibility in Eq. (4.64b), as well as primal feasibility and slackness requirements in Eq. (4.64c). Thereby, the macroscopic plastic admissibility condition $\langle d_{\mathrm{m}} \rangle = \mathcal{H}$ being satisfied (see Remark 8), the macroscopic yield function $\widetilde{\mathcal{G}}(\widetilde{\boldsymbol{\Sigma}}^{\mathrm{c}})$ in Eq. (4.73) identifies the unique acceptable solution of the inequality-constrained minimization problem $\mathcal{P}^*$.

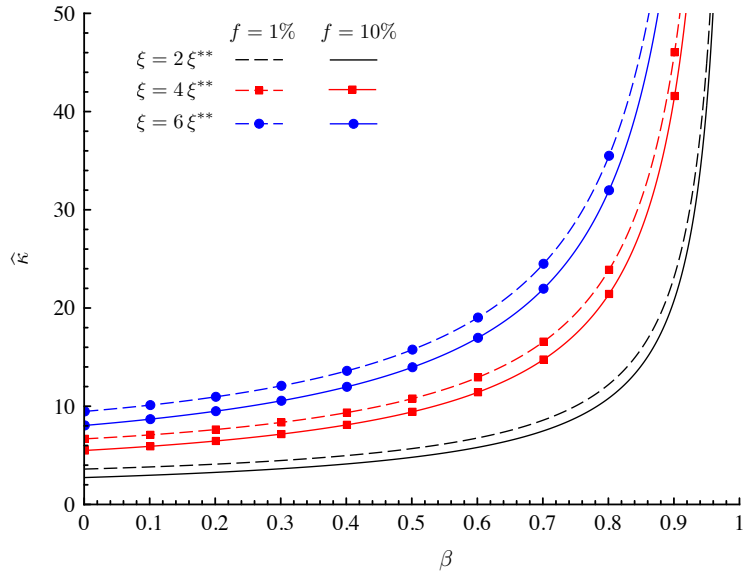

(a)

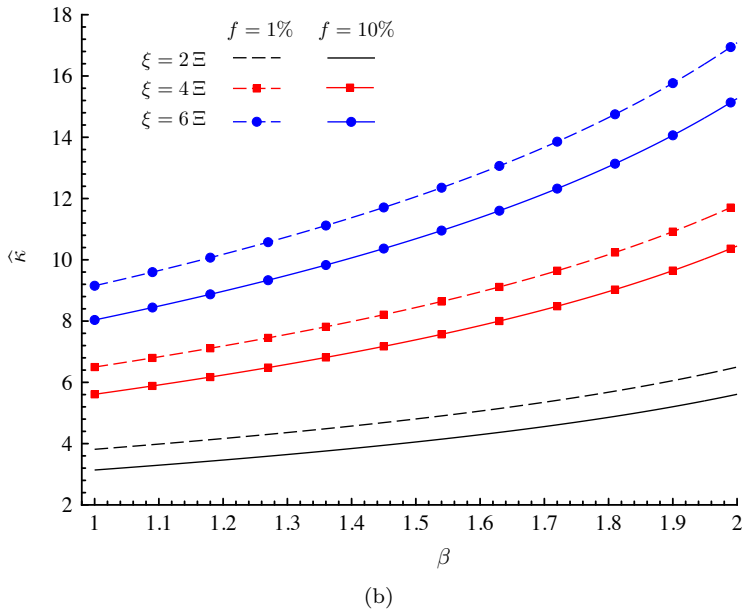

(b)

Figure 4.3 – Hollow sphere with interface effects. Upper-limit void-size parameter $\widehat{\kappa}$ as a function of β, and for different values of ξ and f. (a) $(\xi, \beta) \in \mathcal{N}$ (see Eq. (4.39b)). (b) $(\xi, \beta) \in \mathcal{O}$ (see Eq. (4.39c)).

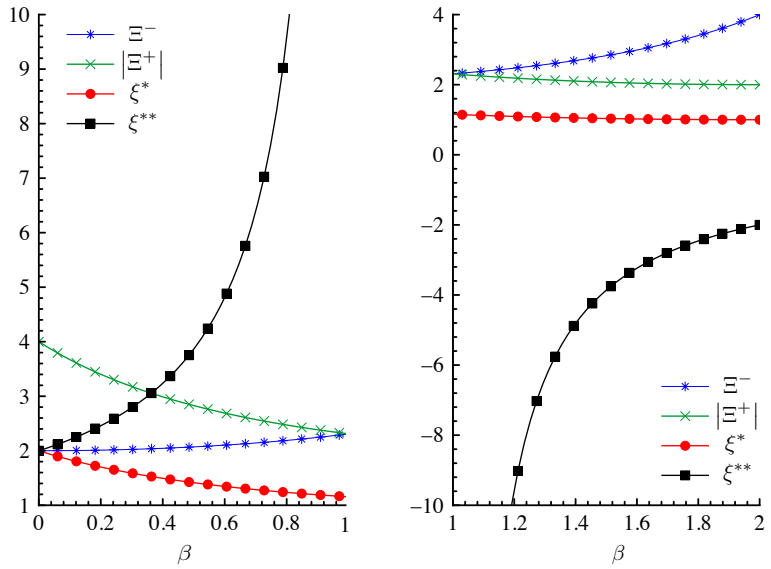

Figure 4.4 – Model parameters $\Xi^- = \Xi|_{\epsilon=-1}$, $\Xi^+ = \Xi|_{\epsilon=+1}$, ξ^* and ξ^{**} defined in Section 4.3 versus β.

4.6 Macroscopic hydrostatic and deviatoric strength stresses

As a particular case of strength estimates provided by the parametric yield function in Eq. (4.73), macroscopic deviatoric (that is, $\widetilde{\boldsymbol{\Sigma}}^{\mathrm{c}}$ s.t. $\widetilde{\Sigma}^{\mathrm{c}}_{\mathrm{m}} = 0$) and hydrostatic (that is, $\widetilde{\boldsymbol{\Sigma}}^{\mathrm{c}}$ s.t. $\widetilde{\Sigma}^{\mathrm{c}}_{\mathrm{eq}} = 0$) stress states are explicitly determined in the following by computing model functions in Eqs. (4.70) and (4.71) in the limits $\omega \to 0^+$ and $\omega \to +\infty$, respectively.

4.6.1 Deviatoric triaxial-espansion or compression strength stress states

The hollow-sphere reference domain is assumed to undergo pure deviatoric $\mathrm{TXE_D}$ (that is, $\delta = +1$, in Cases B and C) or $\mathrm{TXC_D}$ (that is, $\delta = -1$, in Cases A and D) strain-rate boundary conditions.

Owing to relationships provided for $\mathcal{J}(\omega)$ and $\mathcal{J}^{\mathcal{I}}(\omega)$ in 4.A, model functions result at $\omega \to 0^+$ in

$$\lim_{\substack{\omega\to 0^+\\ \epsilon=\pm 1\\ \delta=1}} \Psi_{\mathrm{m}} = \lim_{\substack{\omega\to 0^+\\ \epsilon=\pm 1\\ \delta=1}} \Psi^{\mathcal{I}}_{\mathrm{m}} = 0\,, \qquad \lim_{\substack{\omega\to 0^+\\ \epsilon=\pm 1\\ \delta=-1}} \Psi_{\mathrm{m}} = \lim_{\substack{\omega\to 0^+\\ \epsilon=\pm 1\\ \delta=-1}} \Psi^{\mathcal{I}}_{\mathrm{m}} = 0 \tag{4.93}$$

$$\lim_{\substack{\omega\to 0^+\\ \epsilon=\pm 1\\ \delta=1}} \Psi_{\mathrm{eq}} = 2(1-f)\eta_2\,, \qquad \lim_{\substack{\omega\to 0^+\\ \epsilon=\pm 1\\ \delta=-1}} \Psi_{\mathrm{eq}} = 2(1-f)\eta_1 \tag{4.94}$$

$$\lim_{\substack{\omega\to 0^+\\ \epsilon=\pm 1\\ \delta=1}} \Psi^{\mathcal{I}}_{\mathrm{eq}} = 2\eta_2\,, \qquad \lim_{\substack{\omega\to 0^+\\ \epsilon=\pm 1\\ \delta=-1}} \Psi^{\mathcal{I}}_{\mathrm{eq}} = 2\eta_1 \tag{4.95}$$

where Eqs. (4.93) yield $\widetilde{\Sigma}^{\mathrm{c}}_{\mathrm{m}} = 0$ for $\delta = \pm 1$. Moreover, by replacing η_1 in Eq. (4.38) and η_2 in Eq. (4.44) into Eqs. (4.94) and (4.95), relationships summarised in Table 4.2 are obtained for corresponding values of model functions Ψ_{eq} and $\Psi^{\mathcal{I}}_{\mathrm{eq}}$, as well as for the

Table 4.2 – Hollow-sphere model with interface effects, under pure deviatoric strain-rate boundary conditions ($\omega \to 0^+$) with $\delta = \pm 1$. Corresponding values of solid matrix and interface model functions $\Psi_{\rm m}$, $\Psi_{\rm m}^{\mathcal{I}}$, $\Psi_{\rm eq}$ and $\Psi_{\rm eq}^{\mathcal{I}}$ in Eqs. (4.70) and (4.71), as well as of the macroscopic deviatoric stress $\widetilde{\Sigma}_{\rm eq}^{\rm c}$ in Eq. (4.73), depending on the local plastic behaviour (see Eqs. (4.39)).

	$(\xi,\beta) \in (\mathcal{M} \oplus \mathcal{O})$	$(\xi,\beta) \in \mathcal{N}$
$\delta = 1$ TXE$_{\rm D}$	$\lim\limits_{\substack{\omega\to 0^+\\ \epsilon=\pm 1}} \Psi_{\rm eq} = \dfrac{1-f}{1+\xi\sin\left(\frac{\beta\pi}{6}+\frac{\pi}{6}\right)}$, $\lim\limits_{\substack{\omega\to 0^+\\ \epsilon=\pm 1}} \Psi_{\rm eq}^{\mathcal{I}} = \dfrac{1}{1+\xi\sin\left(\frac{\beta\pi}{6}+\frac{\pi}{6}\right)}$, $\lim\limits_{\substack{\omega\to 0^+\\ \epsilon=\pm 1}} \dfrac{\widetilde{\Sigma}_{\rm eq}^{\rm c}}{h} = \dfrac{3\xi(1-f+3f\kappa)}{1+\xi\sin\left(\frac{\beta\pi}{6}+\frac{\pi}{6}\right)}$	$\lim\limits_{\substack{\omega\to 0^+\\ \epsilon=\pm 1}} \Psi_{\rm eq} = \dfrac{1-f}{\xi\cos\frac{\beta\pi}{6}}$, $\lim\limits_{\substack{\omega\to 0^+\\ \epsilon=\pm 1}} \Psi_{\rm eq}^{\mathcal{I}} = \dfrac{1}{\xi\cos\frac{\beta\pi}{6}}$, $\lim\limits_{\substack{\omega\to 0^+\\ \epsilon=\pm 1}} \dfrac{\widetilde{\Sigma}_{\rm eq}^{\rm c}}{h} = \dfrac{3\,(1-f+3f\kappa)}{\cos\frac{\beta\pi}{6}}$
$\delta = -1$ TXC$_{\rm D}$	$\lim\limits_{\substack{\omega\to 0^+\\ \epsilon=\pm 1}} \Psi_{\rm eq} = \dfrac{1-f}{\xi\sin\left(\frac{\beta\pi}{6}+\frac{\pi}{6}\right)}$, $\lim\limits_{\substack{\omega\to 0^+\\ \epsilon=\pm 1}} \Psi_{\rm eq}^{\mathcal{I}} = \dfrac{1}{\xi\sin\left(\frac{\beta\pi}{6}+\frac{\pi}{6}\right)}$, $\lim\limits_{\substack{\omega\to 0^+\\ \epsilon=\pm 1}} \dfrac{\widetilde{\Sigma}_{\rm eq}^{\rm c}}{h} = \dfrac{3(1-f+3f\kappa)}{\sin\left(\frac{\beta\pi}{6}+\frac{\pi}{6}\right)}$,	$\lim\limits_{\substack{\omega\to 0^+\\ \epsilon=\pm 1}} \Psi_{\rm eq} = \dfrac{1-f}{\xi\cos\frac{\beta\pi}{6}-1}$, $\lim\limits_{\substack{\omega\to 0^+\\ \epsilon=\pm 1}} \Psi_{\rm eq}^{\mathcal{I}} = \dfrac{1}{\xi\cos\frac{\beta\pi}{6}-1}$, $\lim\limits_{\substack{\omega\to 0^+\\ \epsilon=\pm 1}} \dfrac{\widetilde{\Sigma}_{\rm eq}^{\rm c}}{h} = \dfrac{3\xi\,(1-f+3f\kappa)}{\xi\cos\frac{\beta\pi}{6}-1}$

macroscopic deviatoric strength $\widetilde{\Sigma}_{\rm eq}^{\rm c}$.

In detail, it is observed that, for pressure-independent local yield functions (that is, for $\xi \to +\infty$, as in the case of a Tresca criterion), the deviatoric strength $\widetilde{\Sigma}_{\rm eq}^{\rm c}$ does not depend on the stress Lode angle $\widetilde{\theta}_\Sigma = \theta_{\rm D}$, resulting in the same value for TXE$_{\widetilde{\Sigma}}$ and TXC$_{\widetilde{\Sigma}}$ stress states. On the contrary, when pressure-sensitive yield criteria are considered (that is, for $\xi < +\infty$, as in Mohr-Coulomb), different macroscopic strength estimates are obtained for TXE$_{\widetilde{\Sigma}}$ and TXC$_{\widetilde{\Sigma}}$ stress states, as a result of the combined influence of the first I_1^σ and of the third-order deviatoric J_3^σ stress invariants on the local plastic behaviour.

4.6.2 Hydrostatic tensile or compressive strength stress states

Pure hydrostatic strain-rate boundary conditions with $\epsilon = +1$ (that is, Cases A and B) or with $\epsilon = -1$ (that is, Cases C and D) are considered. Owing to results provided in 4.A, model functions in Eqs. (4.70) and (4.71), and computed for $\omega \to +\infty$, read as

$$\lim_{\substack{\omega\to+\infty\\ \epsilon=1\\ \delta=\pm1}} \Psi_{\rm m} = \frac{4\alpha\,\eta_1}{1-\alpha}\left(1-f^{1-\alpha}\right), \qquad \lim_{\substack{\omega\to+\infty\\ \epsilon=-1\\ \delta=\pm1}} = \frac{4\alpha\,\eta_2}{1-\alpha}\left(1-f^{1-\alpha}\right) \tag{4.96}$$

$$\lim_{\substack{\omega\to+\infty\\ \epsilon=1\\ \delta=\pm1}} \Psi_{\rm m}^{\mathcal{I}} = \frac{4\alpha\,\eta_1}{f^\alpha}, \qquad \lim_{\substack{\omega\to+\infty\\ \epsilon=-1\\ \delta=\pm1}} \Psi_{\rm m}^{\mathcal{I}} = \frac{4\alpha\,\eta_2}{f^\alpha} \tag{4.97}$$

$$\lim_{\substack{\omega\to+\infty\\ \epsilon=1\\ \delta=\pm1}} \Psi_{\rm eq} = \lim_{\substack{\omega\to+\infty\\ \epsilon=1\\ \delta=\pm1}} \Psi_{\rm eq}^{\mathcal{I}} = 0, \qquad \lim_{\substack{\omega\to+\infty\\ \epsilon=-1\\ \delta=\pm1}} \Psi_{\rm eq} = \lim_{\substack{\omega\to+\infty\\ \epsilon=-1\\ \delta=\pm1}} \Psi_{\rm eq}^{\mathcal{I}} = 0 \tag{4.98}$$

where, since $0 < \alpha < 1$ (resp., $\alpha > 1$) for $\epsilon = +1$ (resp., $\epsilon = -1$), both Ψ_{m} and $\Psi_{\mathrm{m}}^{\mathcal{I}}$ assume positive values. Relationships in Eq. (4.98) straight provide $\widetilde{\Sigma}_{\mathrm{eq}}^{\mathrm{c}} = 0$. Moreover, by replacing η_1 in Eq. (4.38) and η_2 in Eq. (4.44) into Eqs. (4.96) and (4.97), expressions summarised in Tables 4.3 and 4.4 are obtained for model functions Ψ_{m} and $\Psi_{\mathrm{m}}^{\mathcal{I}}$ at $\omega \to +\infty$, as well as for the macroscopic hydrostatic tensile (for $\epsilon = +1$) and compressive (for $\epsilon = -1$) strength $\widetilde{\Sigma}_{\mathrm{m}}^{\mathrm{c}}$.

As particular cases, proposed results recover the exact macroscopic limit stress provided by Brach et al. (2016b) for nanoporous materials with a Mohr-Coulomb (MC) or a Tresca (Tr) local plastic behaviour. As a matter of fact, simply by setting model parameters ξ and β as shown in Table 4.1, following relationships are obtained for the macroscopic hydrostatic strength

$$\Sigma_{\mathrm{m}}^{\mathrm{c,\,MC}} = c\cot\phi\left[1-\left(1-\frac{4\kappa\sin\phi}{\sin\phi+\epsilon}\right)f^{\frac{4\sin\phi}{3(\sin\phi+\epsilon)}}\right] \tag{4.99}$$

$$\Sigma_{\mathrm{m}}^{\mathrm{c,\,Tr}} = 2\sigma_0\epsilon\left(\kappa-\ln f^{\frac{1}{3}}\right) \tag{4.100}$$

where ϕ, c and σ_0 denote the friction angle, the cohesion parameter and the deviatoric strength, respectively. Moreover, when interface effects are disregarded (that is, for $\kappa \to 0^+$), Eqs. (4.99) and (4.100) recover expressions obtained by Thoré et al. (2009) and Cazacu et al. (2014) for Mohr-Coulomb and Tresca classical porous materials, respectively.

On the other hand, in the case of a general local plastic behaviour (that is, for any choice of ξ and β complying with consistency conditions in Sections 4.3 and 4.5.3), results in Tables 4.3 and 4.4 do not retrieve, for both $\epsilon = -1$ and $\epsilon = +1$, the exact macroscopic hydrostatic yield stress provided by Brach et al. (2016b), that is

$$\frac{\Sigma_{\mathrm{m}}^{\mathrm{c}}}{h} = \xi\left[1-f^{\frac{\Xi}{\Xi-\xi}}\left(1-\frac{3\Xi\kappa}{\Xi-\xi}\right)\right] \tag{4.101}$$

where function Ξ is defined as in Eq. (4.24). In detail, depending on local-yield-function parameters ξ and β, the proposed strength estimate $\widetilde{\Sigma}_{\mathrm{m}}^{\mathrm{c}}$ coincides with the exact value $\Sigma_{\mathrm{m}}^{\mathrm{c}}$ in Eq. (4.101) only when

- $\epsilon = +1$ and $(\xi,\beta) \in (\mathcal{M} \oplus \mathcal{O})$ (see Table 4.3);
- $\epsilon = -1$ and $(\xi,\beta) \in \mathcal{N}$ (see Table 4.4).

Therefore, although the heterogeneous trial velocity in Eq. (4.23) is the exact velocity field at the limit state for the hollow-sphere model under isotropic loadings (see Brach et al., 2016b), the proposed approach allows to recover only one between tensile and compressive hydrostatic stresses in Eq. (4.101), thereby leading only to an estimate for the corresponding exact value of the other one. Such an occurrence has to be related to the adopted macroscopic plastic admissibility condition $\langle d_{\mathrm{m}} \rangle = \mathcal{H}$, resulting from KKT primal feasibility in the inequality-constrained minimization problem $\mathcal{P}^*$ (see Eq. (4.55)).

As a matter of fact, with respect to standard kinematic limit analyses for porous materials with pressure-independent plastic matrices (e.g., Cazacu et al., 2014; Gurson,

Table 4.3 – Hollow-sphere model undergoing pure hydrostatic strain-rate boundary conditions ($\omega \to +\infty$) with $\epsilon = \pm 1$: the case of a local yield function with $(\xi, \beta) \in (\mathcal{M} \oplus \mathcal{O})$. Values of model functions Ψ_{m}, $\Psi_{\mathrm{m}}^{\mathcal{I}}$, Ψ_{eq} and $\Psi_{\mathrm{eq}}^{\mathcal{I}}$ in Eqs. (4.70) and (4.71), and of macroscopic hydrostatic stress $\widetilde{\Sigma}_{\mathrm{m}}^{\mathrm{c}}$ in Eqs. (4.73). Notation $\Sigma_{\mathrm{m}}^{\mathrm{c}}$ indicates the exact strength (Brach et al., 2016b) in Eq. (4.101).

$\epsilon = +1$	$\lim\limits_{\substack{\omega\to+\infty\\ \delta=\pm1}} \Psi_{\mathrm{m}} = \dfrac{2\alpha\left(1-f^{1-\alpha}\right)}{(1-\alpha)\left[\xi\sin\left(\frac{\pi}{6}+\frac{\beta\pi}{6}\right)\right]}$,	$\lim\limits_{\substack{\omega\to+\infty\\ \delta=\pm1}} \Psi_{\mathrm{m}}^{\mathcal{I}} = \dfrac{2\alpha f^{-\alpha}}{\xi\sin\left(\frac{\pi}{6}+\frac{\beta\pi}{6}\right)}$
	$\lim\limits_{\substack{\omega\to+\infty\\ \delta=\pm1}} \dfrac{\widetilde{\Sigma}_{\mathrm{m}}^{\mathrm{c}}}{h} = \xi\left[1-f^{\frac{2}{2+\xi\sin\left(\frac{\pi}{6}+\frac{\beta\pi}{6}\right)}}\left(1-\dfrac{6\kappa}{2+\xi\sin\left(\frac{\pi}{6}+\frac{\beta\pi}{6}\right)}\right)\right] = \dfrac{\Sigma_{\mathrm{m}}^{\mathrm{c}}}{h}$	
	$\lim\limits_{\substack{\omega\to+\infty\\ \delta=\pm1}} \Psi_{\mathrm{eq}} = \lim\limits_{\substack{\omega\to+\infty\\ \delta=\pm1}} \Psi_{\mathrm{eq}}^{\mathcal{I}} = \lim\limits_{\substack{\omega\to+\infty\\ \delta=\pm1}} \dfrac{\widetilde{\Sigma}_{\mathrm{eq}}^{\mathrm{c}}}{h} = 0$	
$\epsilon = -1$	$\lim\limits_{\substack{\omega\to+\infty\\ \delta=\pm1}} \Psi_{\mathrm{m}} = \dfrac{2\alpha\left(1-f^{1-\alpha}\right)}{(1-\alpha)\left[1+\xi\sin\left(\frac{\pi}{6}+\frac{\beta\pi}{6}\right)\right]}$,	$\lim\limits_{\substack{\omega\to+\infty\\ \delta=\pm1}} \Psi_{\mathrm{m}}^{\mathcal{I}} = \dfrac{2\alpha f^{-\alpha}}{1+\xi\sin\left(\frac{\pi}{6}+\frac{\beta\pi}{6}\right)}$
	$\lim\limits_{\substack{\omega\to+\infty\\ \delta=\pm1}} \dfrac{\widetilde{\Sigma}_{\mathrm{m}}^{\mathrm{c}}}{h} = \dfrac{(f-1)\cos\frac{\beta\pi}{6} f^{\frac{2}{\xi\cos\frac{\beta\pi}{6}-2}}}{\sin\left(\frac{\pi}{6}-\frac{\beta\pi}{6}\right)+\sin\left(\frac{\pi}{6}+\frac{\beta\pi}{6}\right) f^{\frac{\xi\cos\frac{\beta\pi}{6}}{\xi\cos\frac{\beta\pi}{6}-2}} - \frac{1}{\xi}\left[1+f^{\frac{2}{\xi\cos\frac{\beta\pi}{6}-2}}\left(f+\xi\cos\frac{\beta\pi}{6}\right)\right]} \dfrac{\Sigma_{\mathrm{m}}^{\mathrm{c}}}{h}$	
	$\lim\limits_{\substack{\omega\to+\infty\\ \delta=\pm1}} \Psi_{\mathrm{eq}} = \lim\limits_{\substack{\omega\to+\infty\\ \delta=\pm1}} \Psi_{\mathrm{eq}}^{\mathcal{I}} = \lim\limits_{\substack{\omega\to+\infty\\ \delta=\pm1}} \dfrac{\widetilde{\Sigma}_{\mathrm{eq}}^{\mathrm{c}}}{h} = 0$	

Table 4.4 – Hollow-sphere model undergoing pure hydrostatic strain-rate boundary conditions ($\omega \to +\infty$) with $\epsilon = \pm 1$: the case of a local yield function with $(\xi, \beta) \in \mathcal{N}$. Values of model functions Ψ_{m}, $\Psi_{\mathrm{m}}^{\mathcal{I}}$, Ψ_{eq} and $\Psi_{\mathrm{eq}}^{\mathcal{I}}$ in Eqs. (4.70) and (4.71), and of macroscopic hydrostatic stress $\widetilde{\Sigma}_{\mathrm{m}}^{\mathrm{c}}$ in Eqs. (4.73). Notation $\Sigma_{\mathrm{m}}^{\mathrm{c}}$ indicates the exact strength (Brach et al., 2016b) in Eq. (4.101).

$\epsilon = +1$	$\lim\limits_{\substack{\omega\to+\infty\\ \delta=\pm1}} \Psi_{\mathrm{m}} = \dfrac{2\alpha\left(1-f^{1-\alpha}\right)}{(1-\alpha)\left(\xi\cos\frac{\beta\pi}{6}-1\right)}$,	$\lim\limits_{\substack{\omega\to+\infty\\ \delta=\pm1}} \Psi_{\mathrm{m}}^{\mathcal{I}} = \dfrac{2\alpha f^{-\alpha}}{\xi\cos\frac{\beta\pi}{6}-1}$
	$\lim\limits_{\substack{\omega\to+\infty\\ \delta=\pm1}} \dfrac{\widetilde{\Sigma}_{\mathrm{m}}^{\mathrm{c}}}{h} = \dfrac{(f-1)\xi\sin\left(\frac{\pi}{6}+\frac{\beta\pi}{6}\right)}{f\left(\xi\cos\frac{\beta\pi}{6}-1\right)-\xi\sin\left(\frac{\pi}{6}+\frac{\beta\pi}{6}\right)+f^{\frac{2}{2+\xi\sin\left(\frac{\pi}{6}+\frac{\beta\pi}{6}\right)}}\left[1-\xi\sin\left(\frac{\pi}{6}-\frac{\beta\pi}{6}\right)\right]}\dfrac{\Sigma_{\mathrm{m}}^{\mathrm{c}}}{h}$	
	$\lim\limits_{\substack{\omega\to+\infty\\ \delta=\pm1}} \Psi_{\mathrm{eq}} = \lim\limits_{\substack{\omega\to+\infty\\ \delta=\pm1}} \Psi_{\mathrm{eq}}^{\mathcal{I}} = \lim\limits_{\substack{\omega\to+\infty\\ \delta=\pm1}} \dfrac{\widetilde{\Sigma}_{\mathrm{eq}}^{\mathrm{c}}}{h} = 0$	
$\epsilon = -1$	$\lim\limits_{\substack{\omega\to+\infty\\ \delta=\pm1}} \Psi_{\mathrm{m}} = \dfrac{2\alpha\left(1-f^{1-\alpha}\right)}{(1-\alpha)\,\xi\cos\frac{\beta\pi}{6}}$,	$\lim\limits_{\substack{\omega\to+\infty\\ \delta=\pm1}} \Psi_{\mathrm{m}}^{\mathcal{I}} = \dfrac{2\alpha f^{-\alpha}}{\xi\cos\frac{\beta\pi}{6}}$
	$\lim\limits_{\substack{\omega\to+\infty\\ \delta=\pm1}} \dfrac{\widetilde{\Sigma}_{\mathrm{m}}^{\mathrm{c}}}{h} = \xi\left[1-f^{\frac{2}{2-\xi\cos\frac{\beta\pi}{6}}}\left(1-\dfrac{6\kappa}{2-\xi\cos\frac{\beta\pi}{6}}\right)\right] = \dfrac{\Sigma_{\mathrm{m}}^{\mathrm{c}}}{h}$	
	$\lim\limits_{\substack{\omega\to+\infty\\ \delta=\pm1}} \Psi_{\mathrm{eq}} = \lim\limits_{\substack{\omega\to+\infty\\ \delta=\pm1}} \Psi_{\mathrm{eq}}^{\mathcal{I}} = \lim\limits_{\substack{\omega\to+\infty\\ \delta=\pm1}} \dfrac{\widetilde{\Sigma}_{\mathrm{eq}}^{\mathrm{c}}}{h} = 0$	

1977), the herein-assumed trial velocity field in Eq. (4.22) does not verify a priori plastic admissibility conditions, which consequently have to be explicitly addressed in the analytical derivation of the macroscopic yield criterion. In agreement with results provided by Guo et al. (2008) and Anoukou et al. (2016) for pressure-dependent yield functions, local admissibility conditions, expressed in terms of *point-wise inequalities* in Eqs. (4.18) to (4.21), have been reformulated in an *average* sense, thereby resulting in the macroscopic plastic requirement $\langle d_{\mathrm{m}} \rangle \geq \mathcal{H}$. Moreover, by enforcing the solution of the KKT problem $\mathcal{P}^*$ to be physically-consistent, the macroscopic plastic admissibility condition $\langle d_{\mathrm{m}} \rangle = \mathcal{H}$ has been obtained. Therefore, by replacing *point-wise inequalities* in Eqs. (4.18) to (4.21) with the *average equality* $\langle d_{\mathrm{m}} \rangle = \mathcal{H}$, a limited selection of plastic admissible strain-rate states has been introduced, excluding some of those obtained from the heterogeneous trial velocity field in Eq. (4.23), and thereby leading to macroscopic hydrostatic strength estimates which may not correspond to the exact value in Eq. (4.101).

Accordingly, in order to elucidate the importance of plastic admissibility in the present approach, as well as its influence on proposed results, local plastic requirements in Eqs. (4.18) to (4.21) are carefully addressed in the following, by highlighting whether they are verified in their equality or inequality form.

To this end, and with reference to the case of isotropic strain-rate boundary loadings, let the strain-rate field $\widehat{\mathbf{d}} = d_{\mathrm{r}} \mathbf{e}_{\mathrm{r}} \otimes \mathbf{e}_{\mathrm{r}} + d_\theta (\mathbf{e}_\theta \otimes \mathbf{e}_\theta + \mathbf{e}_\varphi \otimes \mathbf{e}_\varphi)$, solution of the limit-state problem for a Bigoni-like hollow sphere, be introduced as

$$d_{\mathrm{r}}(r) = 2 \left(1 + \frac{2\xi}{\Xi} \right) C_0 \, r^{\frac{3\xi}{\Xi - \xi}} \tag{4.102}$$

$$d_\theta(r) = 2 \left(1 - \frac{\xi}{\Xi} \right) C_0 \, r^{\frac{3\xi}{\Xi - \xi}} \tag{4.103}$$

which has been established by Brach et al. (2016b) from the heterogeneous velocity field in Eq. (4.23). Depending on the sign assumed by strain-rate components in Eqs. (4.102) and (4.103), following cases have to be addressed in order to determine absolute values in Eqs. (4.18) and (4.19).

Cases A–B $\mathrm{TXC_D}$ and $\mathrm{TXE_D}$ with $C_0 > 0$ (that is, $\epsilon = +1$ and $\delta = \mp 1$)
Owing to the definition of function $\Xi(\epsilon)$ in Eq. (4.24), strain-rate components in Eqs. (4.102) and (4.103) can be expressed as

$$d_{\mathrm{r}}(r) = \left[2 - \left(c_\beta + \sqrt{3} s_\beta \right) \xi \right] C_0 \, r^{-\frac{3(c_\beta + \sqrt{3} s_\beta)\xi}{4 + (c_\beta + \sqrt{3} s_\beta)\xi}} \tag{4.104}$$

$$d_\theta(r) = \frac{1}{2} \left[4 + \left(c_\beta + \sqrt{3} s_\beta \right) \xi \right] C_0 \, r^{-\frac{3(c_\beta + \sqrt{3} s_\beta)\xi}{4 + (c_\beta + \sqrt{3} s_\beta)\xi}} \tag{4.105}$$

resulting in the mean deformation rate

$$d_{\mathrm{m}}(r) = 2 \, C_0 \, r^{-\frac{3(c_\beta + \sqrt{3} s_\beta)\xi}{4 + (c_\beta + \sqrt{3} s_\beta)\xi}} \tag{4.106}$$

Since $c_\beta > 0$ and $s_\beta \geq 0$, the strain-rate component d_θ in Eq. (4.105) is strictly positive. Moreover, under the previously-introduced assumption $\xi > |\Xi^+|$ (see Section 4.4, with $\Xi^+ = \Xi|_{\epsilon=+1}$), it results from Fig. 4.4 that $\xi > \xi^*$ (with ξ^* defined as in Eq. (4.17)), and that the radial strain-rate component in Eq. (4.104) assumes strictly negative values.

The sum of moduli of principal strain-rate components is thereby equal to

$$|d_1| + |d_2| + |d_3| = 2\left[1 + \left(c_\beta + \sqrt{3}s_\beta\right)\xi\right] C_0\, r^{-\frac{3(c_\beta+\sqrt{3}s_\beta)\xi}{4+(c_\beta+\sqrt{3}s_\beta)\xi}} \tag{4.107}$$

Accordingly, depending on the value assumed by local-yield-function parameters ξ and β, different expressions for plastic admissibility conditions have to be considered:

- $0 \leq \beta < 1$
  - if $\xi^* < \xi < \xi^{**}$, plastic admissibility condition in Eq. (4.18) reads as
  $$d_\mathrm{m} \geq \frac{|d_1| + |d_2| + |d_3|}{1 + (c_\beta + \sqrt{3}s_\beta)\xi} \tag{4.108}$$
  which, by combining Eqs. (4.106) and (4.107), results to be verified in its *equality* form.
  - if $\xi \geq \xi^{**}$, plastic admissibility condition in Eq. (4.18) reads as
  $$d_\mathrm{m} \geq \frac{|d_1| + |d_2| + |d_3|}{2c_\beta\xi - 1} \tag{4.109}$$
  yielding, due to Eqs. (4.106) and (4.107),
  $$\xi \geq \xi^{**} \tag{4.110}$$
  which may be verified in both *equality* and *inequality* forms.
- $1 \leq \beta \leq 2$
  plastic admissibility condition in Eq. (4.19) reads as in Eq. (4.108), which results to be satisfied in its *equality* form, by combining Eqs. (4.106) and (4.107).

Cases C–D $\mathrm{TXE_D}$ and $\mathrm{TXC_D}$ with $C_0 < 0$ (that is, $\epsilon = -1$ and $\delta = \pm 1$).
Owing to the definition of function $\Xi(\epsilon)$ in Eq. (4.24), strain-rate components (4.102) and (4.103) read as

$$d_\mathrm{r}(r) = 2\,(1 + c_\beta\xi)\; C_0\, r^{\frac{3c_\beta\xi}{2-c_\beta\xi}} \tag{4.111}$$

$$d_\theta(r) = (2 - c_\beta\xi)\; C_0\, r^{\frac{3c_\beta\xi}{2-c_\beta\xi}} \tag{4.112}$$

resulting in

$$d_\mathrm{m}(r) = 2\, C_0\, r^{\frac{3c_\beta\xi}{2-c_\beta\xi}} \tag{4.113}$$

The radial deformation rate in Eq. (4.111) is strictly positive, since $c_\beta > 0$. Moreover, under the previously-introduced assumption $\xi > |\Xi^-| = \Xi^-$ (see Section 4.4, with $\Xi^- = \Xi|_{\epsilon=-1}$), the strain-rate component d_θ in Eq. (4.112) assumes strictly negative values.

The sum of moduli of principal strain-rate components is thereby equal to

$$|d_1| + |d_2| + |d_3| = (4\, c_\beta \xi - 2)\; C_0\, r^{\frac{3c_\beta\xi}{2-c_\beta\xi}} \tag{4.114}$$

and the following cases have to addressed:

- $0 \leq \beta < 1$
  - if $\xi^* < \xi < \xi^{**}$, plastic admissibility condition in Eq. (4.18) reads as in Eq. (4.108). The latter yields, by combining Eqs. (4.113) and (4.114),

    $$\xi \leq \xi^{**} \tag{4.115}$$

    that is verified in its *strictly inequality* form, since $\Xi^- < \xi < \xi^{**}$.
  - if $\xi \geq \xi^{**}$, plastic admissibility condition in Eq. (4.18) reads as in Eq. (4.109). The latter, by combining Eqs. (4.113) and (4.114), is verified in its *equality* form.
- $1 \leq \beta \leq 2$
  plastic admissibility condition in Eq. (4.19) reads as in Eq. (4.108), resulting in

  $$\xi \geq \xi^{**} \tag{4.116}$$

  which is satisfied in its *strictly inequality* form $\xi > \Xi^-$, since ξ^{**} assumes negatives values over the considered interval of β (see 4.4).

Accordingly, previous considerations prove that the proposed macroscopic yield function (4.73) is able to recover the exact value of tensile and compressive hydrostatic strength in Eq. (4.101) only if the local plastic admissibility condition is verified in its *equality* form, that is when $(\xi, \beta) \in \mathcal{N}$ for $\epsilon = -1$ and when $(\xi, \beta) \in (\mathcal{M} \oplus \mathcal{O})$ for $\epsilon = +1$. Moreover, it is noted that, in the particular case of a Mohr-Coulomb or of a Tresca local strength criterion, model parameters are such that $\xi = \xi^{**}$ and $\beta \in [0, 1)$. This allows to verify local plastic admissibility condition in its equality form for $\epsilon = \pm 1$, thereby resulting in exact values for both tensile and compressive hydrostatic stresses in Eqs. (4.99) and (4.100).

As shown in Figs. 4.5 and 4.6 for local plastic behaviours with $(\xi, \beta) \in \mathcal{N}$ and $(\xi, \beta) \in \mathcal{O}$, respectively, the discrepancy between the exact and the estimated hydrostatic strengths, as well as on the exponent α of the heterogeneous velocity field in Eq. (4.23), strongly depend on yield-function parameters ξ and β.

In detail, with reference to the case $(\xi, \beta) \in \mathcal{N}$ and for $\epsilon = +1$, by assuming ξ as a multiple of $\xi^{**} = \xi^{**}(\beta)$, Fig. 4.5a (resp., Fig. 4.5b) shows that the ratio between the predicted $\widetilde{\Sigma}^{\mathrm{c}}_{\mathrm{m}}$ and the exact $\Sigma^{\mathrm{c}}_{\mathrm{m}}$ tensile strength (resp., the exponent α) decreases when ξ

increases (resp., decreases), for any value of $\beta \in [0,1)$. On the other hand, when a local plastic behaviour $(\xi,\beta) \in \mathcal{O}$ is considered, results in Fig. 4.6 for $\epsilon = -1$ show that, by assuming ξ as a multiple of $\Xi^- = \Xi^-(\beta)$, the ratio between the compressive strengths $\widetilde{\Sigma}^{\mathrm{c}}_{\mathrm{m}}/\Sigma^{\mathrm{c}}_{\mathrm{m}}$ reduces when ξ decreases, for any value of $\beta \in [1,2]$. Therefore, for a given choice of $(\xi,\beta) \in \mathcal{N}$ (resp., $(\xi,\beta) \in \mathcal{O}$), the proposed macroscopic yield function underestimates tensile (resp., compressive) hydrostatic strength, with discrepancy reducing when the exponent α reduces.

4.7 Comparative illustrations

With the aim to highlight the influence of local plastic behaviour, porosity and void-size effects on the estimated strength properties, the macroscopic yield function in Eq. (4.73) is represented in Figs. 4.7 to 4.11, for different values of model parameters ξ, β, f and κ. For illustrative purposes, in the following reference is made to local yield functions with $(\xi,\beta) \in \mathcal{N}$ and $(\xi,\beta) \in \mathcal{O}$, sets $\mathcal{N}$ and $\mathcal{O}$ being defined as in Eqs. (4.39). Moreover, aiming to ensure the strictly positiveness of the macroscopic plastic multiplier in Eq. (4.87), the void-size coefficient κ is varied within the admissible interval $\kappa \in [0,\widehat{\kappa})$.

Model parameter ξ is firstly considered as fixed and equal to $\xi = 2\,\xi^{**}$ (resp., $\xi = 6\,\Xi^-$) for local yield functions complying with $(\xi,\beta) \in \mathcal{N}$ (resp., with $(\xi,\beta) \in \mathcal{O}$). It is worth observing that, in agreement with plastic admissibility conditions in Eqs. (4.18) and (4.19), and since both ξ^{**} and Ξ^- depend on β, such a choice for ξ allows to vary β in the interval $[0,1)$ for $(\xi,\beta) \in \mathcal{N}$ and in $[1,2]$ for $(\xi,\beta) \in \mathcal{O}$ (see Fig. 4.4).

The case of classical porous materials is considered in Fig. 4.7, by evaluating the macroscopic yield function in Eq. (4.73) in the limit $\kappa \to 0^+$, that is by neglecting interface effects. Strength profiles for macroscopic triaxial expansion (i.e., $\mathrm{TXE}_{\widetilde{\Sigma}}$ at $\widetilde{\theta}_\Sigma = 0$) and triaxial compression (i.e., $\mathrm{TXC}_{\widetilde{\Sigma}}$ at $\widetilde{\theta}_\Sigma = \pi/3$) are represented for different values of β and f. As expected, results show that macroscopic strength properties tend to reduce when porosity increases, irrespective of the assumed local plastic behaviour, and for both $\mathrm{TXE}_{\widetilde{\Sigma}}$ and $\mathrm{TXC}_{\widetilde{\Sigma}}$ stress states. Furthermore, as a consequence of combined effects of the first I_1^σ and the third J_3^σ stress invariants on local plastic response, predicted macroscopic strength properties hugely depend on the macroscopic stress Lode angle $\widetilde{\theta}_\Sigma$, resulting higher in $\mathrm{TXC}_{\widetilde{\Sigma}}$ than in $\mathrm{TXE}_{\widetilde{\Sigma}}$, for any choice of β and f (see also Fig. 4.10). Moreover, strength profiles are proven to be strongly asymmetric with respect to the deviatoric axis $\widetilde{\Sigma}_{\mathrm{m}} = 0$, leading to higher values of hydrostatic compressive strength than of hydrostatic tensile ones, such an occurrence being emphasized when porosity f decreases. Results in Fig. 4.7a (resp., Fig. 4.7b) also highlight that, in the case of a local plastic behaviour with $(\xi,\beta) \in \mathcal{N}$ (resp., with $(\xi,\beta) \in \mathcal{O}$), model parameter β has a strengthening (resp., weakening) effect on macroscopic strength properties, resulting in an overall expansion (resp., contraction) of strength profiles when β increases.

Void-size effects on macroscopic strength properties are depicted in Figs. 4.8 and 4.9, by considering the porosity f as fixed and for different values of the dimensionless parameter κ introduced in Eq. (4.59). Proposed results show that, irrespective of the assumed local plastic behaviour, a significant improvement of macroscopic strength properties with

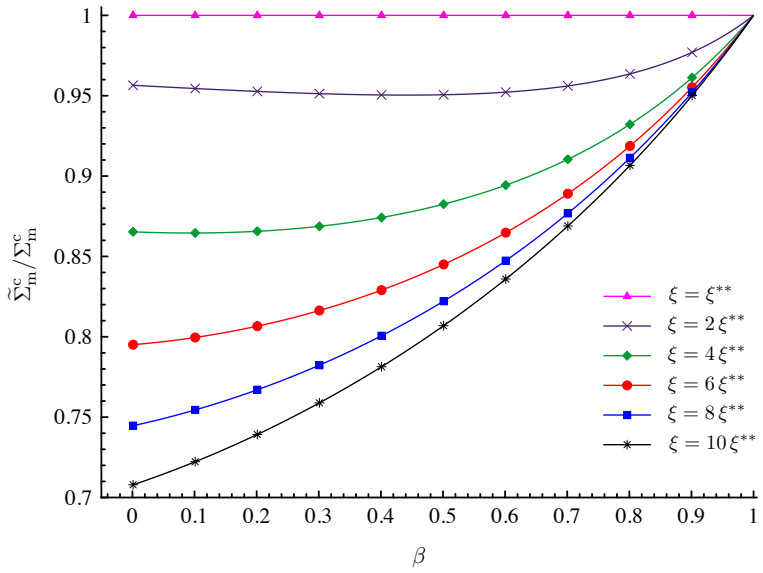

(a)

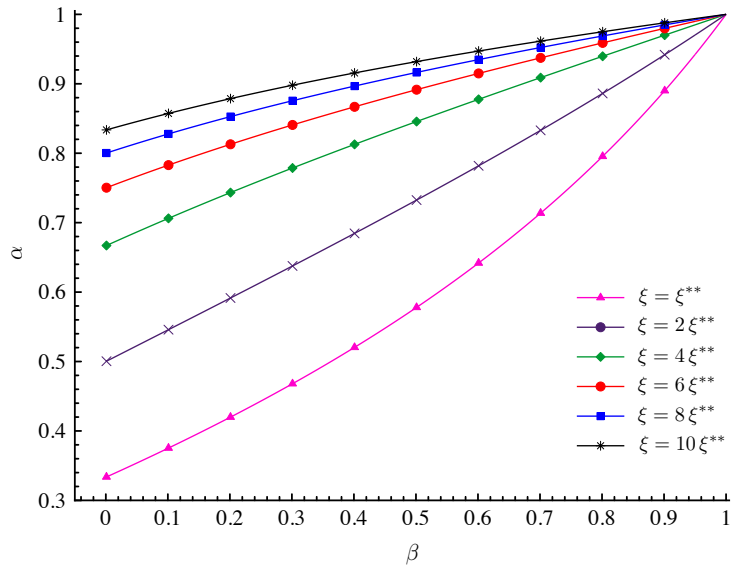

(b)

Figure 4.5 – (a) Ratio between the estimated $\widetilde{\Sigma}_{\mathrm{m}}^{\mathrm{c}}$ and the exact $\Sigma_{\mathrm{m}}^{\mathrm{c}}$ macroscopic hydrostatic tensile strength detailed in Table 4.3 for $\epsilon = +1$ vs β. (b) Exponent α of the heterogeneous velocity field in Eq. (4.23) vs β. Curves obtained for different local-yield-function parameters complying with $(\xi, \beta) \in \mathcal{N}$ (i.e., $\xi \geq \xi^{**}$ and $0 \leq \beta < 1$) and for $f = 1\%$.

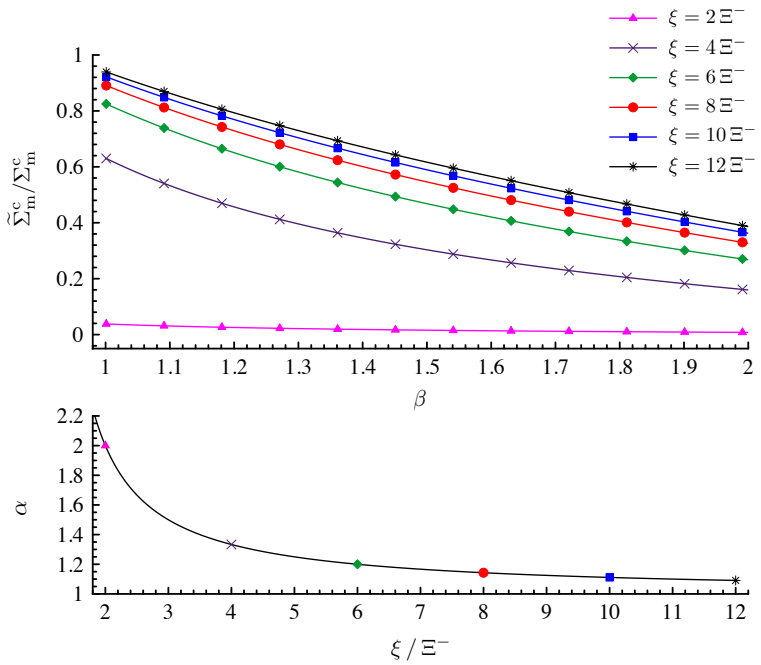

Figure 4.6 – Ratio between the estimated $\widetilde{\Sigma}^{\rm c}_{\rm m}$ and the exact $\Sigma^{\rm c}_{\rm m}$ macroscopic hydrostatic compressive strength detailed in Table 4.3 for $\epsilon = -1$ vs β (top). Exponent α of the heterogeneous velocity field in Eq. (4.23) vs ξ/Ξ^- (bottom). Curves obtained for different local-yield-function parameters complying with $(\xi, \beta) \in \mathcal{O}$ (i.e., $\xi \geq \xi^*$ and $1 \leq \beta \leq 2$, thereby resulting in $\Xi^- > \xi^*$) and for $f = 1\%$.

respect to the case of classical porous materials (i.e., in the limit $\kappa \to 0^+$) is observed when κ increases (namely, when void size $R_{\rm i}$ reduces), for both $\text{TXE}_{\widetilde{\Sigma}}$ and $\text{TXC}_{\widetilde{\Sigma}}$ strength profiles. Such a strengthening effect does not influence the previously-described asymmetries in the macroscopic plastic response. In particular, triaxial-compression and hydrostatic-compressive strength states assume higher values than triaxial-expansion and hydrostatic-tensile ones, irrespective of the void-size parameter κ (see also Fig. 4.10). Nevertheless, void-size effects are proven to affect mainly macroscopic strength states characterized by a negative hydrostatic component, thereby resulting in a significant expansion of $\text{TXE}_{\widetilde{\Sigma}}$ and $\text{TXC}_{\widetilde{\Sigma}}$ strength profiles along the negative hydrostatic axis when κ increases. As shown in Fig. 4.8, this occurrence is clearly evident in the case of a local plastic behaviour with $(\xi, \beta) \in \mathcal{N}$. In this case, the macroscopic hydrostatic tensile strength is affected by the void size less than the compressive one. On the contrary, Fig. 4.9 shows that, when a local yield function with $(\xi, \beta) \in \mathcal{O}$ is considered, a variation in κ induces significant variations of both the predicted hydrostatic tensile and compressive strengths. Furthermore, by comparing strength profiles in Figs. 4.8a and 4.8b (resp., in Figs. 4.9a and 4.9b), void-size effects on macroscopic strength features are proven to be not significantly affected by values assumed for the yield function parameter β.

Finally, the influence of parameter ξ on the macroscopic plastic behaviour under axisymmetric loadings is depicted in Fig. 4.11a (resp., in Fig. 4.11b) for a local yield function with $(\xi, \beta) \in \mathcal{N}$ (resp., $(\xi, \beta) \in \mathcal{O}$) and such that $\beta = 0.5$ (resp., $\beta = 1.5$). Proposed re-

sults highlight that, irrespective of the considered local plastic response, the macroscopic strength domain enclosed by $\mathrm{TXE}_{\widetilde{\Sigma}}$ and $\mathrm{TXC}_{\widetilde{\Sigma}}$ yield profiles tend to overall reduce when ξ increases. Moreover, previously-observed asymmetries between pure deviatoric triaxial-compression and triaxial-expansion stresses, as well as between hydrostatic tensile and compressive strength states are shown to progressively vanish when ξ increases, completely disappearing when a pressure-independent local plastic behaviour is considered (that is, in the limit $\xi \to +\infty$).

4.8 Conclusions

In this Chapter, a general macroscopic yield function for nanoporous materials is analytically derived, by considering a hollow-sphere model with a general isotropic local plastic behaviour and in the case of axisymmetric strain-rate boundary conditions.

Void-size effects on the predicted strength properties have been accounted for via a coherent-imperfect interface model, by prescribing the discontinuity (resp., the continuity) of the stress vector (resp., of the velocity field) across the cavity boundary.

In agreement with physical indications arising from recent Molecular-Dynamics computations on nanosized bulk specimens (Brach et al., 2016a), the material comprising the hollow sphere has been assumed to obey to a pressure-dependent strength criterion, accounting for the influence of stress-Lode-angle effects. More specifically, in the framework of the theoretical approach proposed by Brach et al. (2016b), the local yield function has been defined via a simplified form of the strength criterion provided by Bigoni and Piccolroaz (2004), thereby resulting in a polyhedral yield surface in the space of the Lode coordinates, with linear meridian and multi-sided deviatoric profiles. Therefore, a broad class of local pressure-dependent plastic behaviours, typical of many engineering-relevant porous and nanoporous materials, has been taken into account, allowing for an extreme flexibility in reproducing the stress-Lode-angle effects on solid matrix strength properties.

In the framework of a kinematic limit analysis approach (Gurson, 1977), the velocity field proposed by Brach et al. (2016b), corresponding to the limit state of a Bigoni-like hollow sphere under isotropic boundary conditions, has been adopted to define the heterogeneous part of a suitable trial kinematics. A parametric closed-form estimate for the macroscopic yield function has been obtained as the solution of a KKT inequality-constrained minimization problem, the latter accounting for local plastic admissibility conditions.

Proposed results have shown that, for both pressure-sensitive and pressure-insensitive local yield functions, the macroscopic strength criterion depends on the hydrostatic stress. Moreover, as a result of combined effects of the first and the third-order deviatoric stress invariants on the local plastic behaviour, estimated strength properties have been proven to be hugely affected by the macroscopic stress Lode angle.

Comparative illustrations have been provided in order to highlight the influence of model parameters on the macroscopic strength domain. In detail, the effect induced by local-yield-function coefficients on proposed strength profiles has been clearly established. Furthermore, a consistent description of void-size effects on macroscopic strength states

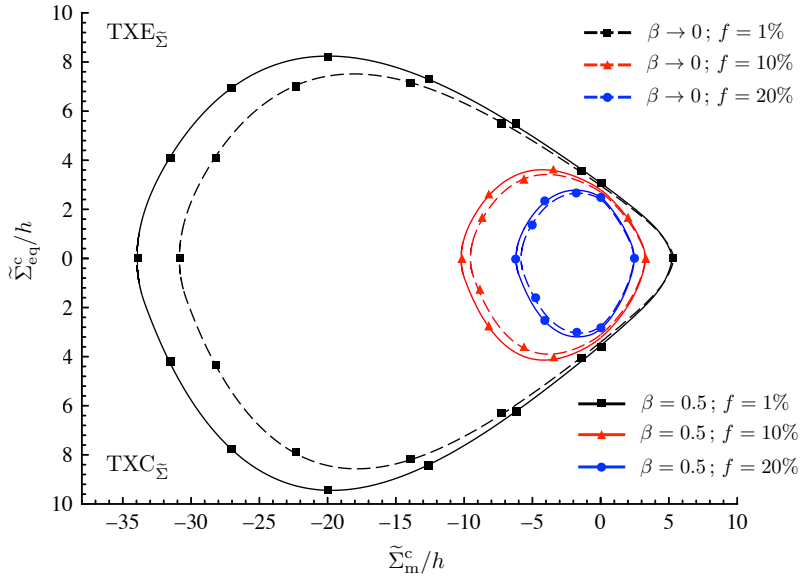

(a)

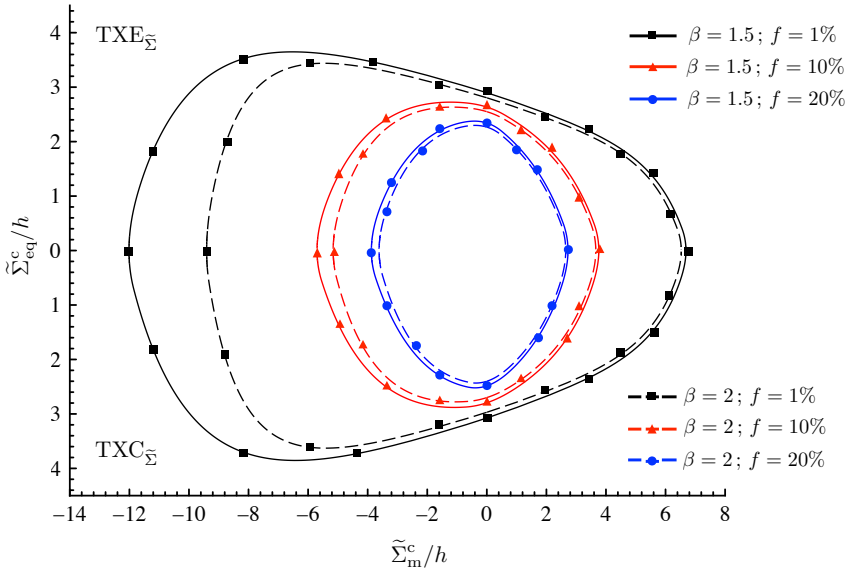

(b)

Figure 4.7 – Hollow-sphere model without interface effects (that is, for $\kappa \to 0^+$). Triaxial-expansion (TXE$_{\widetilde{\Sigma}}$) and triaxial-compression (TXC$_{\widetilde{\Sigma}}$) strength profiles for different values of parameter β and porosity f. Local plastic behaviours complying with: (a) $(\xi, \beta) \in \mathcal{N}$ for $\xi = 2\,\xi^{**}$; (b) $(\xi, \beta) \in \mathcal{O}$ for $\xi = 6\,\Xi^{-}$.

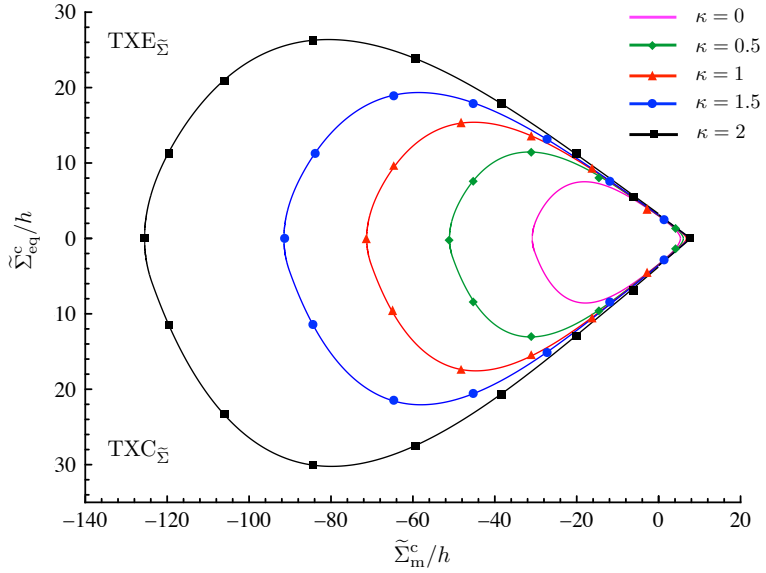

(a)

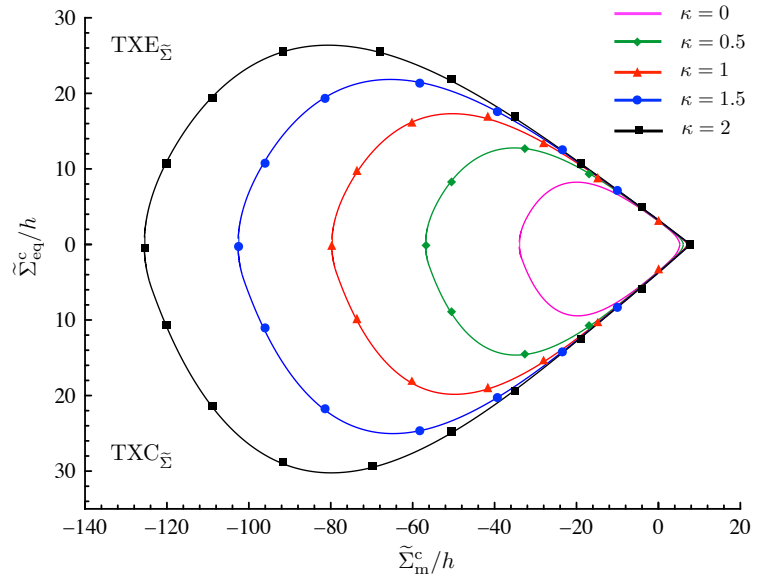

(b)

Figure 4.8 – Hollow-sphere model with interface effects. Triaxial-expansion (TXE$_{\widetilde{\Sigma}}$) and triaxial-compression (TXC$_{\widetilde{\Sigma}}$) strength profiles for different values of the void-size parameter κ, porosity being set equal to $f = 1\%$. Local plastic behaviours complying with: (a) $(\xi, \beta) \in \mathcal{N}$ for $\beta \to 0$ and $\xi = 2\,\xi^{**}$; (b) $(\xi, \beta) \in \mathcal{N}$ for $\beta = 0.5$ and $\xi = 2\,\xi^{**}$.

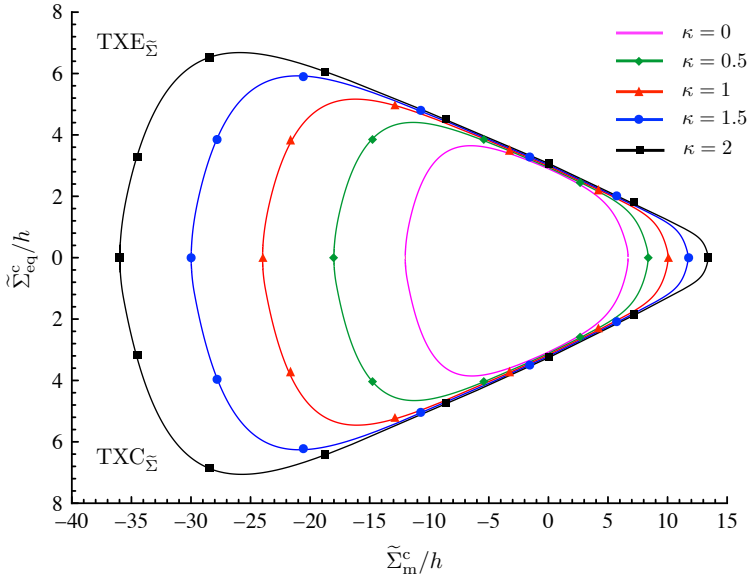

(a)

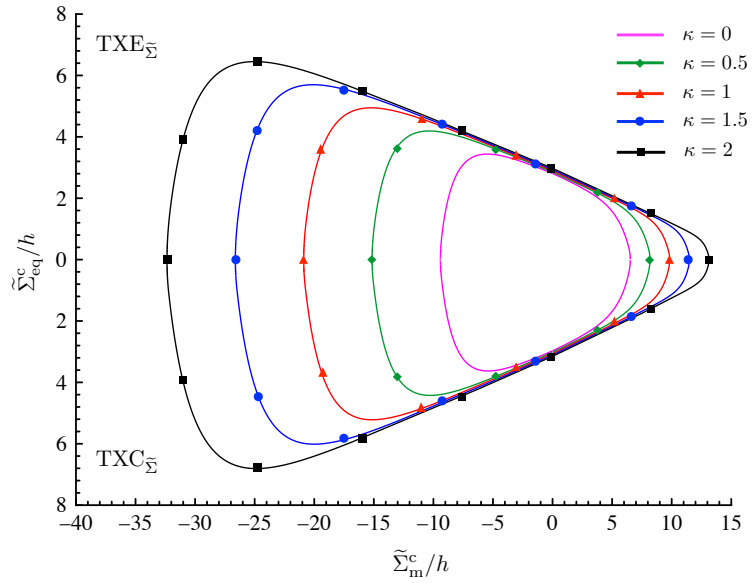

(b)

Figure 4.9 – Hollow-sphere model with interface effects. Triaxial-expansion (TXE$_{\widetilde{\Sigma}}$) and triaxial-compression (TXC$_{\widetilde{\Sigma}}$) strength profiles for different values of the void-size parameter κ, porosity being set equal to $f = 1\%$. Local plastic behaviours complying with: (a) $(\xi, \beta) \in \mathcal{O}$ for $\beta = 1.5$ and $\xi = 6\,\Xi^{-}$; (b) $(\xi, \beta) \in \mathcal{O}$ for $\beta = 2$ and $\xi = 6\,\Xi^{-}$.

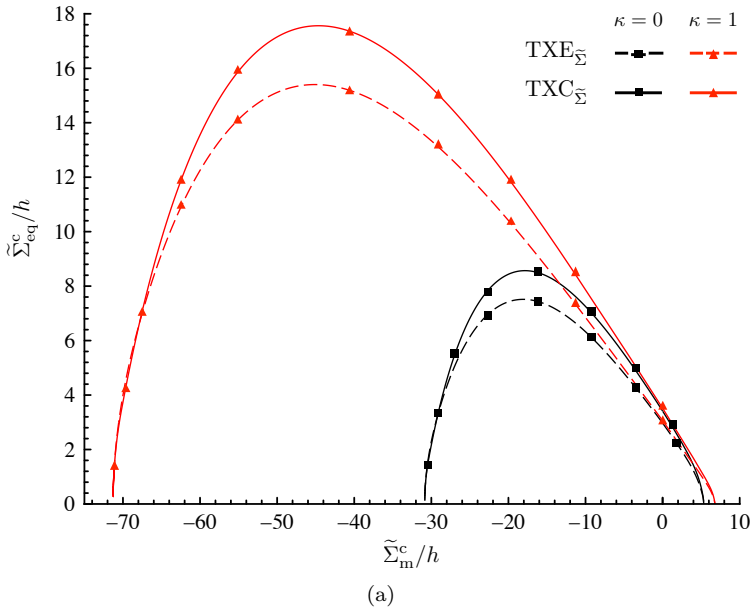

(a)

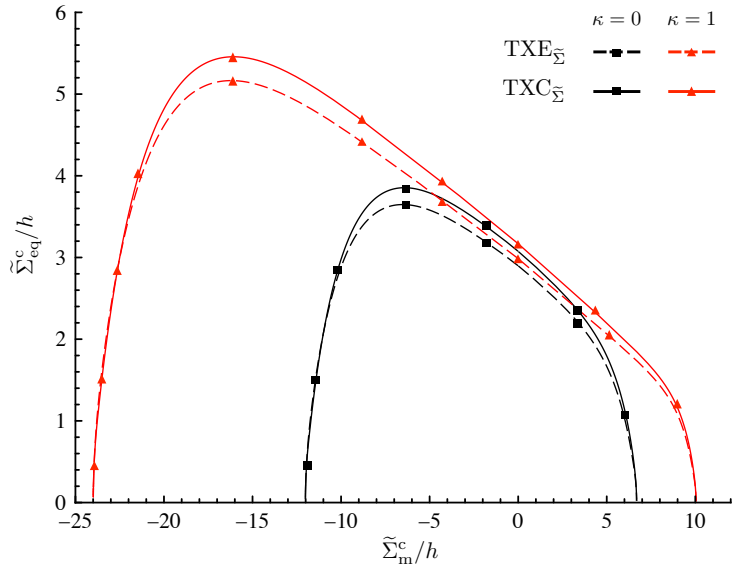

(b)

Figure 4.10 – Hollow-sphere model with interface effects. Asymmetry between triaxial-expansion (TXE$_{\widetilde{\Sigma}}$) and triaxial-compression (TXC$_{\widetilde{\Sigma}}$) strength profiles for different values of the void-size parameter κ, porosity being set equal to $f = 1\%$. Local plastic behaviours complying with: (a) $(\xi, \beta) \in \mathcal{N}$ for $\beta = 0.5$ and $\xi = 2\,\xi^{**}$; (b) $(\xi, \beta) \in \mathcal{O}$ for $\beta = 1.5$ and $\xi = 6\,\Xi^{-}$.

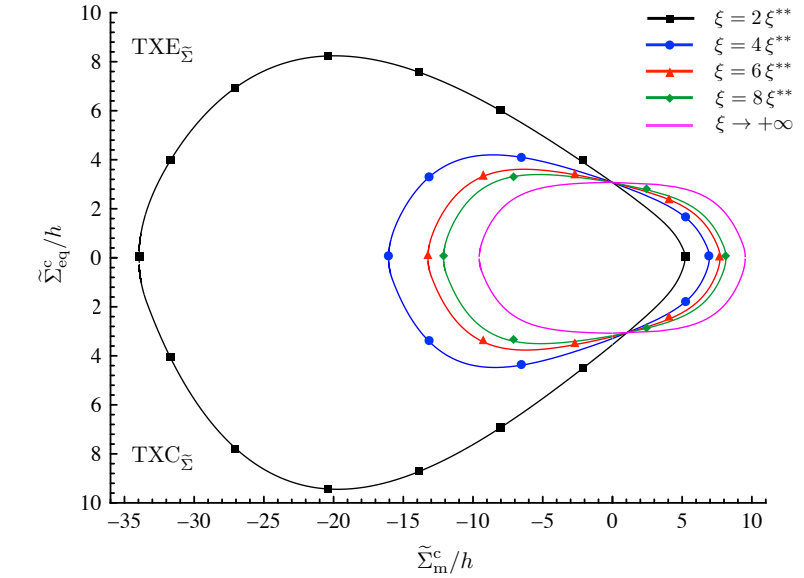

(a)

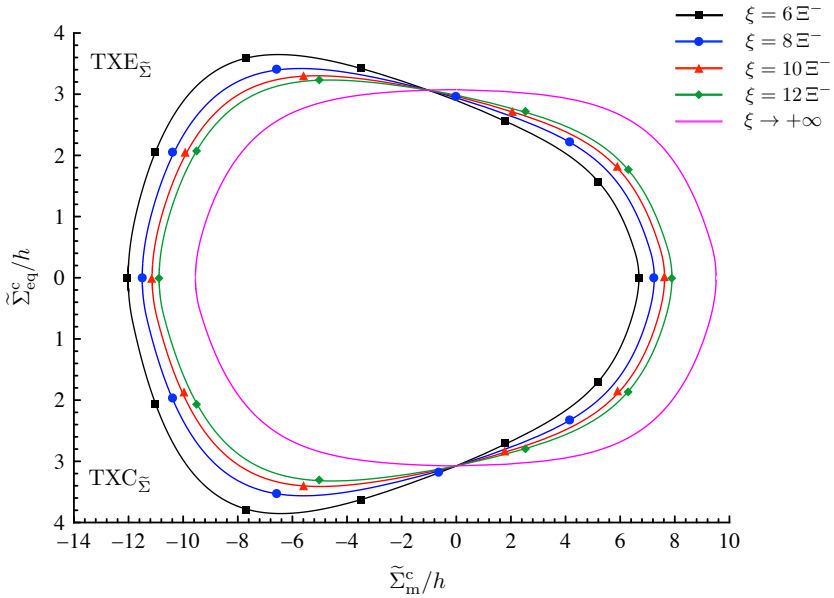

(b)

Figure 4.11 – Hollow-sphere model without interface effects (that is, for $\kappa \to 0^{+}$). Triaxial-expansion (TXE$_{\widetilde{\Sigma}}$) and triaxial-compression (TXC$_{\widetilde{\Sigma}}$) strength profiles for different values of parameter ξ, porosity being set equal to $f = 1\%$. Local plastic behaviours complying with: (a) $(\xi, \beta) \in \mathcal{N}$ for $\beta = 0.5$; (b) $(\xi, \beta) \in \mathcal{O}$ for $\beta = 1.5$.

has been furnished, resulting in an overall expansion of the predicted strength domain when the void radius reduces for a fixed porosity level, qualitatively in agreement with available experimental and numerical indications (Biener et al., 2005, 2006; Brach et al., 2016a; Hakamada and Mabuchi, 2007; Zhao et al., 2009).

As a special case and as a consistency assessment, by properly choosing model parameters and by disregarding interface effects, proposed macroscopic yield function straight recovers relationship provided by Anoukou et al. (2016) in the particular case of a porous material with a Mohr-Coulomb plastic matrix. Moreover, established results fully retrieve analytical expressions of macroscopic hydrostatic strength obtained by Cazacu et al. (2014) and Thoré et al. (2009), by addressing a hollow-sphere model with a Tresca and Mohr-Coulomb local plastic behaviour, respectively.

Finally, for any suitable choice of model parameters complying with model consistency conditions, the proposed approach allows for the straight identification of macroscopic strength properties under axisymmetric loadings for a wide class of porous and nanoporous materials, whose local plastic behaviour can not be properly accounted for by classical yield models.

4.A Closed-form relationships of functions $\mathcal{J}$ and $\mathcal{J}^{\mathcal{I}}$

Depending on the value assumed by macroscopic strain-rate parameters $\epsilon = \operatorname{sgn} C_0$ and $\delta = \operatorname{sgn} J_3^{\mathrm{D}}$, the following cases have to be addressed in order to explicitly determine functions $\mathcal{J}$ and $\mathcal{J}^{\mathcal{I}}$ introduced in Section 4.5.1.

Case A $\mathrm{TXC_D}$ with $C_0 > 0$ (that is, $\epsilon = +1$ and $\delta = -1$).
Owing to Eqs. (4.35) and (4.37), function ι in Eq. (4.77) reads as

$$\iota = 1 + \mathtt{x} + 3\sqrt{1 + \mathtt{x}^2 + 2\mathtt{x}\cos 2\theta} \tag{4.117}$$

yielding the following expression for $\Upsilon(\omega)$

$$\Upsilon(\mathtt{x}) = 5(\mathtt{x}+1) + \frac{3(1-\mathtt{x})^2}{2\sqrt{\mathtt{x}}} \operatorname{arctanh}\left(\frac{2\sqrt{\mathtt{x}}}{1+\mathtt{x}}\right) \tag{4.118}$$

the latter resulting in

$$\mathcal{J}^{\mathcal{I}}(\omega) = \eta_1 \Upsilon(\mathtt{x})\big|_{\mathtt{x}=\omega/f^{\alpha}}, \qquad \forall\, \omega > 0 \tag{4.119}$$

where, since the positiveness of the principal deviatoric strain-rate component $d_{\mathrm{d}1}$ in Eq. (4.35) for any positive value of $\mathtt{x}$, coefficient $\eta_{\pm}$ in Eq. (4.76) reduces to η_1, irrespective of the macroscopic strain-rate triaxiality measure ω.

In agreement with results obtained by Anoukou et al. (2016), function $\mathcal{J}(\omega)$ reads as

$$\mathcal{J}(\omega) = \eta_1 \left[\widetilde{\mathcal{Q}}\left(\frac{\omega}{f^{\alpha}}\right) - \widetilde{\mathcal{Q}}\,(\omega)\right] \tag{4.120}$$

$\widetilde{\mathcal{Q}}$ being the antiderivative with respect to $\mathtt{x}$ of function

$$\mathcal{Q}(\mathtt{x}) = \frac{\Upsilon(\mathtt{x})}{\mathtt{x}^{1+1/\alpha}} \tag{4.121}$$

that is, since Eq. (4.118),

$$\begin{aligned}\widetilde{\mathcal{Q}} = \frac{2\alpha}{\mathtt{x}^{1/\alpha}} \Bigg[&\frac{17\alpha - 10}{(\alpha-2)(3\alpha-2)} + \frac{(9\alpha-5)\mathtt{x}}{(\alpha-1)(3\alpha-2)} - \frac{12\alpha^3\, {}_2\mathrm{F}_1\left(1, -\frac{1}{\alpha}; \frac{\alpha-1}{\alpha}; \mathtt{x}\right)}{(\alpha-2)(\alpha+2)(3\alpha-2)} + \\ &+ \frac{3}{2\sqrt{\mathtt{x}}}\left(\frac{\mathtt{x}^2}{3\alpha-2} - \frac{2\mathtt{x}}{\alpha-2} - \frac{1}{\alpha+2}\right) \operatorname{arctanh}\left(\frac{2\sqrt{\mathtt{x}}}{1+\mathtt{x}}\right)\Bigg]\end{aligned} \tag{4.122}$$

Notation ${}_2\mathrm{F}_1(a, b; c; z)$ is introduced in Eq. (4.122) to indicate the Gauss hypergeometric series

$${}_2\mathrm{F}_1(a, b; c; z) = \sum_{n=0}^{\infty} \frac{(a)_n (b)_n}{(c)_n} \frac{z^n}{n!} \tag{4.123}$$

defined for $|z| < 1$, with $c \notin \{0\} \cup \mathbb{Z}^-$ and $n \in \{0\} \cup \mathbb{Z}^+$, $\mathbb{Z}^-$ and $\mathbb{Z}^+$ being the sets of non-null negative and positive integer numbers, respectively, and where $(\bullet)_n$ is the

Pochhammer symbol denoting the rising factorial $(\bullet)_n = \Gamma(\bullet + n)/\Gamma(\bullet)$, with

$$\Gamma(z) = \int_0^\infty t^{z-1} e^{-t}\, dt \tag{4.124}$$

The hypergeometric function ${}_2\mathrm{F}_1\left(1, -\frac{1}{\alpha}; \frac{\alpha-1}{\alpha}; \mathtt{x}\right)$ in Eq. (4.122) is not defined for $|\mathtt{x}| \geq 1$, thereby leading to a limitation on the range of variation of the strain-rate triaxiality measure ω. However, since the macroscopic yield function in Eq. (4.73) has to be defined for any $\omega > 0$, the analytic continuation formula (e.g., Pearson, 2009)

$$\begin{aligned} {}_2\mathrm{F}_1(a,b;c;z) = {} & (-z)^{-a}\, \frac{\Gamma(c)\Gamma(b-a)}{\Gamma(b)\Gamma(c-a)}\, {}_2\mathrm{F}_1\left(a, a-c+1; a-b+1; \frac{1}{z}\right) + \\ & (-z)^{-b}\, \frac{\Gamma(c)\Gamma(a-b)}{\Gamma(a)\Gamma(c-b)}\, {}_2\mathrm{F}_1\left(b-c+1, b; b-a+1; \frac{1}{z}\right) \end{aligned} \tag{4.125}$$

is used to compute the antiderivative $\widetilde{\mathcal{Q}}(\mathtt{x})$ in Eq. (4.122) for any value of $\mathtt{x}$. Consequently, function $\mathcal{J}(\omega)$ reads as

$$\begin{aligned} \mathcal{J}(\omega) = {} & \frac{2\alpha\,\eta_1}{\omega^{1/\alpha}} \left[\frac{(10-17\alpha)(1-f)}{(\alpha-2)(3\alpha-2)} + \frac{(9\alpha-5)(1-f^{1-\alpha})\omega}{(1-\alpha)(3\alpha-2)} + \right. \\ & \frac{3f^{1-\alpha}}{2\sqrt{\omega f^\alpha}} \left(\frac{\omega^2}{3\alpha-2} - \frac{2\omega f^\alpha}{\alpha-2} - \frac{f^{2\alpha}}{\alpha+2} \right) \operatorname{arctanh}\left(\frac{2\sqrt{\omega f^\alpha}}{\omega + f^\alpha} \right) - \\ & \frac{3}{2\sqrt{\omega}} \left(\frac{\omega^2}{3\alpha-2} - \frac{2\omega}{\alpha-2} - \frac{1}{\alpha+2} \right) \operatorname{arctanh}\left(\frac{2\sqrt{\omega}}{\omega+1} \right) + \\ & \left. \frac{12\alpha^3 \mathcal{A}(\omega)}{(\alpha-2)(\alpha+2)(3\alpha-2)} \right] \end{aligned} \tag{4.126}$$

where $\mathcal{A}(\omega)$ is piece-wise defined as

$$\mathcal{A}(\omega) = \begin{cases} {}_2\mathrm{F}_1\left(1, -\frac{1}{\alpha}; \frac{\alpha-1}{\alpha}; \omega\right) - f\, {}_2\mathrm{F}_1\left(1, -\frac{1}{\alpha}; \frac{\alpha-1}{\alpha}; \frac{\omega}{f^\alpha}\right) & \text{if} \quad 0 < \omega < f^\alpha \\ {}_2\mathrm{F}_1\left(1, -\frac{1}{\alpha}; \frac{\alpha-1}{\alpha}; \omega\right) - \frac{\pi\omega^{1/\alpha}}{\alpha} \cot\left(\frac{\pi}{\alpha}\right) + & \\ \frac{f^{1+\alpha}}{(\alpha+1)\omega}\, {}_2\mathrm{F}_1\left(1, \frac{1+\alpha}{\alpha}; \frac{2\alpha+1}{\alpha}; \frac{f^\alpha}{\omega}\right) & \text{if} \quad f^\alpha < \omega < 1 \\ -\frac{1}{(\alpha+1)\omega} \left[{}_2\mathrm{F}_1\left(1, \frac{1+\alpha}{\alpha}; \frac{2\alpha+1}{\alpha}; \frac{1}{\omega}\right) - \right. & \\ \left. f^{1+\alpha}\, {}_2\mathrm{F}_1\left(1, \frac{1+\alpha}{\alpha}; \frac{2\alpha+1}{\alpha}; \frac{f^\alpha}{\omega}\right) \right] & \text{if} \quad \omega > 1 \end{cases} \tag{4.127}$$

Since both functions $\mathcal{J}^{\mathcal{I}}(\omega)$ in Eq. (4.119) and $\mathcal{J}(\omega)$ in Eq. (4.126) are continuous and continuously differentiable on $\omega \in (0, +\infty)$, solid matrix and interface model functions Ψ_{m}, Ψ_{eq}, $\Psi^{\mathcal{I}}_{\mathrm{m}}$ and $\Psi^{\mathcal{I}}_{\mathrm{eq}}$ are continuous for any value of ω, thereby yielding

$$\ell_{\mathrm{m}} = \ell_{\mathrm{eq}} = \ell^{\mathcal{I}}_{\mathrm{m}} = \ell^{\mathcal{I}}_{\mathrm{eq}} = 0\,, \qquad \forall\, \omega > 0 \tag{4.128}$$

Case B $\mathrm{TXE_D}$ with $C_0 > 0$ (that is, $\epsilon = +1$ and $\delta = +1$).
Owing to Eqs. (4.40) and (4.43), function ι in Eq. (4.77) reads as

$$\iota = \begin{cases} 1 - \mathtt{x} + 3\sqrt{1 + \mathtt{x}^2 - 2\mathtt{x}\cos 2\theta} & \text{if} \quad 0 < \mathtt{x} < \alpha \\ \mathtt{x} - 1 + 3\sqrt{1 + \mathtt{x}^2 - 2\mathtt{x}\cos 2\theta} & \text{if} \quad \alpha < \mathtt{x} < 1 \\ \mathtt{x} - 1 + 3\sqrt{1 + \mathtt{x}^2 - 2\mathtt{x}\cos 2\theta} & \text{if} \quad \mathtt{x} > 1 \end{cases} \tag{4.129}$$

yielding the following relationships for $\Upsilon(\omega)$

$$\Upsilon(\mathtt{x}) = \begin{cases} 5(1 - \mathtt{x}) + \dfrac{3(1+\mathtt{x})^2}{2\sqrt{\mathtt{x}}} \arctan\left(\dfrac{2\sqrt{\mathtt{x}}}{1-\mathtt{x}}\right) & \text{if} \quad 0 < \mathtt{x} < \alpha \\ 1 - \mathtt{x} + \dfrac{3(1+\mathtt{x})^2}{2\sqrt{\mathtt{x}}} \arctan\left(\dfrac{2\sqrt{\mathtt{x}}}{1-\mathtt{x}}\right) & \text{if} \quad \alpha < \mathtt{x} < 1 \\ 5(\mathtt{x} - 1) + \dfrac{3(1+\mathtt{x})^2}{2\sqrt{\mathtt{x}}} \arcsin\left(\dfrac{2\sqrt{\mathtt{x}}}{1+\mathtt{x}}\right) & \text{if} \quad \mathtt{x} > 1 \end{cases} \tag{4.130}$$

the latter resulting in

$$\mathcal{J}^{\mathcal{I}}(\omega) = \begin{cases} \eta_2 \Upsilon(\mathtt{x})\big|_{\mathtt{x}=\omega/f^\alpha} & \text{if} \quad 0 < \omega < \alpha f^\alpha \\ \eta_1 \Upsilon(\mathtt{x})\big|_{\mathtt{x}=\omega/f^\alpha} & \text{if} \quad \alpha f^\alpha < \omega < f^\alpha \\ \eta_1 \Upsilon(\mathtt{x})\big|_{\mathtt{x}=\omega/f^\alpha} & \text{if} \quad \omega > f^\alpha \end{cases} \tag{4.131}$$

where, depending on the sign of the principal deviatoric strain-rate component d_{d1} in Eq. (4.40), coefficient $\eta_\pm$ in Eq. (4.76) reduces to η_1 or to η_2. On the other hand, as regards function $\mathcal{J}(\omega)$, the following expressions are provided by Anoukou et al. (2016)

$$\mathcal{J}(\omega) = \begin{cases} \text{if} \quad 0 < \omega \leq \alpha f^\alpha \ : \\ \eta_2 \left[\tilde{\mathcal{Q}}_1\left(\dfrac{\omega}{f^\alpha}\right) - \tilde{\mathcal{Q}}_1(\omega)\right] \\ \text{if} \quad \alpha f^\alpha \leq \omega < f^\alpha \ : \\ \eta_2 \left[\tilde{\mathcal{Q}}_1(\alpha) - \tilde{\mathcal{Q}}_1(\omega)\right] + \eta_1 \left[\tilde{\mathcal{Q}}_2\left(\dfrac{\omega}{f^\alpha}\right) - \tilde{\mathcal{Q}}_2(\alpha)\right] \\ \text{if} \quad f^\alpha < \omega \leq \alpha \ : \\ \eta_2 \left[\tilde{\mathcal{Q}}_1(\alpha) - \tilde{\mathcal{Q}}_1(\omega)\right] + \eta_1 \left[2\mathcal{B} + \tilde{\mathcal{Q}}_3\left(\dfrac{\omega}{f^\alpha}\right) - \tilde{\mathcal{Q}}_2(\alpha)\right] \\ \text{if} \quad \alpha \leq \omega < 1 \ : \\ \eta_1 \left[2\mathcal{B} + \tilde{\mathcal{Q}}_3\left(\dfrac{\omega}{f^\alpha}\right) - \tilde{\mathcal{Q}}_2(\omega)\right] \\ \text{if} \quad \omega > 1 \ : \\ \eta_1 \left[\tilde{\mathcal{Q}}_3\left(\dfrac{\omega}{f^\alpha}\right) - \tilde{\mathcal{Q}}_3(\omega)\right] \end{cases} \tag{4.132}$$

where, by introducing the polygamma function of order zero $\psi^{(0)} = \Gamma'(z)/\Gamma(z)$, $\mathcal{B}$ is defined as

$$\mathcal{B} = \frac{6\alpha^4}{(\alpha-2)(\alpha-1)(3\alpha-2)} + \frac{\psi^{(0)}\left(\frac{\alpha-1}{2\alpha}\right) - \psi^{(0)}\left(-\frac{1}{2\alpha}\right)}{(\alpha-2)(\alpha+2)(3\alpha-2)} \tag{4.133}$$

and where $\widetilde{\mathcal{Q}}_1$, $\widetilde{\mathcal{Q}}_2$ and $\widetilde{\mathcal{Q}}_3$ are the antiderivatives of functions $\mathcal{Q}_1$, $\mathcal{Q}_2$ and $\mathcal{Q}_3$ obtained by replacing Eqs. (4.130) into Eq. (4.121), that is

$$\begin{aligned}\widetilde{\mathcal{Q}}_1 = \frac{2\alpha}{\mathtt{x}^{1/\alpha}}\Bigg[&\frac{17\alpha-10}{(\alpha-2)(3\alpha-2)} - \frac{(9\alpha-5)\mathtt{x}}{(\alpha-1)(3\alpha-2)} - \frac{12\alpha^3\,{}_2\mathrm{F}_1\left(1,-\frac{1}{\alpha};\frac{\alpha-1}{\alpha};-\mathtt{x}\right)}{(\alpha-2)(\alpha+2)(3\alpha-2)} + \\ &+\frac{3}{2\sqrt{\mathtt{x}}}\left(\frac{\mathtt{x}^2}{3\alpha-2}+\frac{2\mathtt{x}}{\alpha-2}-\frac{1}{\alpha+2}\right)\arctan\left(\frac{2\sqrt{\mathtt{x}}}{1-\mathtt{x}}\right)\Bigg]\end{aligned} \tag{4.134}$$

$$\begin{aligned}\widetilde{\mathcal{Q}}_2 = \frac{2\alpha}{\mathtt{x}^{1/\alpha}}\Bigg[&\frac{(2\alpha-1)(3\alpha+2)}{(\alpha-2)(3\alpha-2)} - \frac{(3\alpha-1)\mathtt{x}}{(\alpha-1)(3\alpha-2)} - \frac{12\alpha^3\,{}_2\mathrm{F}_1\left(1,-\frac{1}{\alpha};\frac{\alpha-1}{\alpha};-\mathtt{x}\right)}{(\alpha-2)(\alpha+2)(3\alpha-2)} + \\ &+\frac{3}{2\sqrt{\mathtt{x}}}\left(\frac{\mathtt{x}^2}{3\alpha-2}+\frac{2\mathtt{x}}{\alpha-2}-\frac{1}{\alpha+2}\right)\arctan\left(\frac{2\sqrt{\mathtt{x}}}{1-\mathtt{x}}\right)\Bigg]\end{aligned} \tag{4.135}$$

$$\begin{aligned}\widetilde{\mathcal{Q}}_3 = \frac{2\alpha}{\mathtt{x}^{1/\alpha}}\Bigg[&\frac{10-17\alpha}{(\alpha-2)(3\alpha-2)} + \frac{(9\alpha-5)\mathtt{x}}{(\alpha-1)(3\alpha-2)} + \frac{12\alpha^3\,{}_2\mathrm{F}_1\left(1,-\frac{1}{\alpha};\frac{\alpha-1}{\alpha};-\mathtt{x}\right)}{(\alpha-2)(\alpha+2)(3\alpha-2)} + \\ &+\frac{3}{2\sqrt{\mathtt{x}}}\left(\frac{\mathtt{x}^2}{3\alpha-2}+\frac{2\mathtt{x}}{\alpha-2}-\frac{1}{\alpha+2}\right)\arcsin\left(\frac{2\sqrt{\mathtt{x}}}{1+\mathtt{x}}\right)\Bigg]\end{aligned} \tag{4.136}$$

It is worth observing that no analytic continuation is needed in Eqs. (4.134), (4.135) and (4.136), since antiderivatives are expressed in terms of the hypergeometric function ${}_2\mathrm{F}_1\left(1,-\frac{1}{\alpha};\frac{\alpha-1}{\alpha};-\mathtt{x}\right)$, which is defined for any $\mathtt{x} > 0$.

In order to ensure the continuity of the macroscopic yield function in Eq. (4.73) for any positive value of the strain-rate triaxiality measure ω, functions $\mathcal{H}^{\mathcal{I}}(\omega)$ and $\mathcal{H}(\omega)$ have to be piece-wise continuously differentiable with respect to C_0 and D_{eq} on intervals defined in Eqs. (4.131) and (4.132), respectively. Accordingly, denoting as $\omega^\star$ an endpoint of one of these subdomains, parameters ℓ_{m}, ℓ_{eq}, $\ell^{\mathcal{I}}_{\mathrm{m}}$ and $\ell^{\mathcal{I}}_{\mathrm{eq}}$ in Eqs. (4.78) are computed by enforcing the continuity of one-sided limits for $\omega \to \omega^{\star-}$ and for $\omega \to \omega^{\star+}$, that is by prescribing

$$\lim_{\omega\to\omega^{\star-}} \frac{\partial\mathcal{H}}{\partial C_0} = \lim_{\omega\to\omega^{\star+}} \frac{\partial\mathcal{H}}{\partial C_0}\,, \qquad \lim_{\omega\to\omega^{\star-}} \frac{\partial\mathcal{H}}{\partial D_{\mathrm{eq}}} = \lim_{\omega\to\omega^{\star+}} \frac{\partial\mathcal{H}}{\partial D_{\mathrm{eq}}} \tag{4.137}$$

$$\lim_{\omega\to\omega^{\star-}} \frac{\partial\mathcal{H}^{\mathcal{I}}}{\partial C_0} = \lim_{\omega\to\omega^{\star+}} \frac{\partial\mathcal{H}^{\mathcal{I}}}{\partial C_0}\,, \qquad \lim_{\omega\to\omega^{\star-}} \frac{\partial\mathcal{H}^{\mathcal{I}}}{\partial D_{\mathrm{eq}}} = \lim_{\omega\to\omega^{\star+}} \frac{\partial\mathcal{H}^{\mathcal{I}}}{\partial D_{\mathrm{eq}}} \tag{4.138}$$

In detail, by computing (4.138) on endpoints $\omega^\star = \alpha f^\alpha$ and $\omega^\star = f^\alpha$ of subdomains in Eqs. (4.131), interface parameters $\ell^{\mathcal{I}}_{\mathrm{m}}$ and $\ell^{\mathcal{I}}_{\mathrm{eq}}$ result equal to zero for any ω belonging to intervals $0 < \omega < \alpha f^\alpha$, $\alpha f^\alpha < \omega < f^\alpha$, and $\omega > f^\alpha$. On the other hand, continuity requirements (4.137) on endpoints $\omega^\star = \alpha f^\alpha$, $\omega^\star = \alpha$, $\omega^\star = f^\alpha$ and $\omega^\star = 1$ of subdomains

in Eqs. (4.132) yield

$$\ell_{\mathrm{m}} = \begin{cases} \text{if} \quad 0 < \omega \leq \alpha f^{\alpha} \quad \text{or} \quad \alpha \leq \omega < 1 \quad \text{or} \quad \omega > 1 : \\ 0 \\ \text{if} \quad \alpha f^{\alpha} \leq \omega < f^{\alpha} \quad \text{or} \quad f^{\alpha} < \omega \leq \alpha : \\ \dfrac{\alpha-1}{\alpha^{\frac{1}{\alpha}-1}}(\eta_1 - 5\eta_2) + \dfrac{3(1+\alpha)^2}{2\alpha^{\frac{1}{\alpha}-\frac{1}{2}}}(\eta_1 - \eta_2)\arctan\left(\dfrac{2\sqrt{\alpha}}{\alpha-1}\right) \end{cases} \tag{4.139}$$

$$\ell_{\mathrm{eq}} = \begin{cases} \text{if} \quad 0 < \omega \leq \alpha f^{\alpha} \quad \text{or} \quad \alpha \leq \omega < 1 \quad \text{or} \quad \omega > 1 : \\ 0 \\ \text{if} \quad \alpha f^{\alpha} \leq \omega < f^{\alpha} \quad \text{or} \quad f^{\alpha} < \omega \leq \alpha : \\ \dfrac{\ell_{\mathrm{m}}}{1-\alpha} \end{cases} \tag{4.140}$$

Case C $\mathrm{TXE_D}$ with $C_0 < 0$ (that is, $\epsilon = -1$ and $\delta = +1$).
Owing to Eqs. (4.45) and (4.47), function ι in Eq. (4.77) reads as

$$\iota = 1 + \mathtt{x} + 3\sqrt{1 + \mathtt{x}^2 + 2\mathtt{x}\cos 2\theta} \tag{4.141}$$

thereby resulting in the same expression of $\Upsilon(\mathtt{x})$ than that provided in Case A, that is Eq. (4.118). By replacing this latter into Eq. (4.76), function $\mathcal{J}^{\mathcal{I}}(\omega)$ results in

$$\mathcal{J}^{\mathcal{I}}(\omega) = \eta_2 \Upsilon(\mathtt{x})\big|_{\mathtt{x}=\omega/f^{\alpha}}, \qquad \forall\, \omega > 0 \tag{4.142}$$

where, since the negativeness of the principal deviatoric strain-rate component d_{d1} in Eq. (4.45) for any positive value of $\mathtt{x}$, coefficient $\eta_{\pm}$ in Eq. (4.76) reduces to η_2 irrespective of the value assumed for ω. As regards function $\mathcal{J}(\omega)$, it has been provided by Anoukou et al. (2016) in the form

$$\mathcal{J}(\omega) = \eta_2 \left[\widetilde{\mathcal{Q}}\left(\frac{\omega}{f^{\alpha}}\right) - \widetilde{\mathcal{Q}}\,(\omega)\right] \tag{4.143}$$

where the antiderivative $\widetilde{\mathcal{Q}}$ reads as in Eq. (4.122). Since this latter is not defined for $|\mathtt{x}| \geq 1$, the analytic continuation formula in Eq. (4.125) is enforced, thereby yielding

$$\begin{aligned} \mathcal{J}(\omega) = \frac{2\alpha\,\eta_2}{\omega^{1/\alpha}} \Bigg[& \frac{(10-17\alpha)(1-f)}{(\alpha-2)(3\alpha-2)} + \frac{(9\alpha-5)(1-f^{1-\alpha})\omega}{(1-\alpha)(3\alpha-2)} + \\ & \frac{3f^{1-\alpha}}{2\sqrt{\omega f^{\alpha}}}\left(\frac{\omega^2}{3\alpha-2} - \frac{2\omega f^{\alpha}}{\alpha-2} - \frac{f^{2\alpha}}{\alpha+2}\right)\operatorname{arctanh}\left(\frac{2\sqrt{\omega f^{\alpha}}}{\omega+f^{\alpha}}\right) - \\ & \frac{3}{2\sqrt{\omega}}\left(\frac{\omega^2}{3\alpha-2} - \frac{2\omega}{\alpha-2} - \frac{1}{\alpha+2}\right)\operatorname{arctanh}\left(\frac{2\sqrt{\omega}}{\omega+1}\right) + \\ & \frac{12\alpha^3\mathcal{A}(\omega)}{(\alpha-2)(\alpha+2)(3\alpha-2)}\Bigg] \end{aligned} \tag{4.144}$$

where function $\mathcal{A}(\omega)$ is piece-wise defined as in Eq. (4.127).

Both $\mathcal{J}^{\mathcal{I}}$ and $\mathcal{J}$ in Eqs. (4.142) and (4.144) are continuous and continuously differentiable in $\omega > 0$, thereby resulting in null values of parameters ℓ_{m}, ℓ_{eq}, $\ell^{\mathcal{I}}_{\mathrm{m}}$, and $\ell^{\mathcal{I}}_{\mathrm{eq}}$.

Case D $\mathrm{TXC_D}$ with $C_0 < 0$ (that is, $\epsilon = -1$ and $\delta = -1$).
Owing to Eqs. (4.48) and (4.50), function ι in Eq. (4.77) reads as

$$\iota = \begin{cases} 1 - \mathtt{x} + 3\sqrt{1 + \mathtt{x}^2 - 2\mathtt{x}\cos 2\theta} & \text{if} \quad 0 < \mathtt{x} < 1 \\ 1 - \mathtt{x} + 3\sqrt{1 + \mathtt{x}^2 - 2\mathtt{x}\cos 2\theta} & \text{if} \quad 1 < \mathtt{x} < \alpha \\ \mathtt{x} - 1 + 3\sqrt{1 + \mathtt{x}^2 - 2\mathtt{x}\cos 2\theta} & \text{if} \quad \mathtt{x} > \alpha \end{cases} \tag{4.145}$$

yielding the following expressions for $\Upsilon(\omega)$

$$\Upsilon(\mathtt{x}) = \begin{cases} 5(1 - \mathtt{x}) + \dfrac{3(1+\mathtt{x})^2}{2\sqrt{\mathtt{x}}} \arctan\left(\dfrac{2\sqrt{\mathtt{x}}}{1-\mathtt{x}}\right) & \text{if} \quad 0 < \mathtt{x} < 1 \\ \mathtt{x} - 1 + \dfrac{3(1+\mathtt{x})^2}{2\sqrt{\mathtt{x}}} \arcsin\left(\dfrac{2\sqrt{\mathtt{x}}}{1+\mathtt{x}}\right) & \text{if} \quad 1 < \mathtt{x} < \alpha \\ 5(\mathtt{x} - 1) + \dfrac{3(1+\mathtt{x})^2}{2\sqrt{\mathtt{x}}} \arcsin\left(\dfrac{2\sqrt{\mathtt{x}}}{1+\mathtt{x}}\right) & \text{if} \quad \mathtt{x} > \alpha \end{cases} \tag{4.146}$$

the latter resulting in

$$\mathcal{J}^{\mathcal{I}}(\omega) = \begin{cases} \eta_1 \Upsilon(\mathtt{x})\big|_{\mathtt{x}=\omega/f^\alpha}, & \text{if} \quad 0 < \omega < f^\alpha \\ \eta_1 \Upsilon(\mathtt{x})\big|_{\mathtt{x}=\omega/f^\alpha}, & \text{if} \quad f^\alpha < \omega < \alpha f^\alpha \\ \eta_2 \Upsilon(\mathtt{x})\big|_{\mathtt{x}=\omega/f^\alpha}, & \text{if} \quad \omega > \alpha f^\alpha \end{cases} \tag{4.147}$$

where, depending on the sign of the principal deviatoric strain-rate component $d_{\mathrm{d}1}$ in Eq. (4.48), coefficient $\eta_\pm$ in Eq. (4.76) reduces to η_1 or to η_2. Moreover, in agreement with results provided by Anoukou et al. (2016), function $\mathcal{J}(\omega)$ is assumed equal to

$$\mathcal{J}(\omega) = \begin{cases} \text{if} \quad 0 < \omega < f^\alpha \ : \\ \eta_1 \left[\widetilde{\mathcal{Q}}_1\left(\dfrac{\omega}{f^\alpha}\right) - \widetilde{\mathcal{Q}}_1(\omega)\right] \\ \text{if} \quad f^\alpha < \omega \leq \alpha f^\alpha \ : \\ \eta_1 \left[2\mathcal{B} + \widetilde{\mathcal{Q}}_2\left(\dfrac{\omega}{f^\alpha}\right) - \widetilde{\mathcal{Q}}_1(\omega)\right] \\ \text{if} \quad \alpha f^\alpha \leq \omega < 1 \ : \\ \eta_2 \left[\widetilde{\mathcal{Q}}_3\left(\dfrac{\omega}{f^\alpha}\right) - \widetilde{\mathcal{Q}}_3(\alpha)\right] + \eta_1 \left[2\mathcal{B} + \widetilde{\mathcal{Q}}_2(\alpha) - \widetilde{\mathcal{Q}}_1(\omega)\right] \\ \text{if} \quad 1 < \omega \leq \alpha \ : \\ \eta_1 \left[\widetilde{\mathcal{Q}}_2(\alpha) - \widetilde{\mathcal{Q}}_2(\omega)\right] + \eta_2 \left[\widetilde{\mathcal{Q}}_3\left(\dfrac{\omega}{f^\alpha}\right) - \widetilde{\mathcal{Q}}_3(\alpha)\right] \\ \text{if} \quad \omega \geq \alpha \ : \\ \eta_2 \left[\widetilde{\mathcal{Q}}_3\left(\dfrac{\omega}{f^\alpha}\right) - \widetilde{\mathcal{Q}}_3(\omega)\right] \end{cases} \tag{4.148}$$

where $\mathcal{B}$ is defined as in Eq. (4.133), and where $\widetilde{\mathcal{Q}}_1$, $\widetilde{\mathcal{Q}}_2$ and $\widetilde{\mathcal{Q}}_3$ are the antiderivatives of functions $\mathcal{Q}_1$, $\mathcal{Q}_2$ and $\mathcal{Q}_3$, obtained by replacing Eqs. (4.146) into Eq. (4.121). In detail, $\widetilde{\mathcal{Q}}_1$ and $\widetilde{\mathcal{Q}}_3$ are expressed as in Eqs. (4.134) and (4.136), respectively, whereas $\widetilde{\mathcal{Q}}_2$ is

$$\widetilde{\mathcal{Q}}_2 = \frac{2\alpha}{\mathtt{x}^{1/\alpha}}\left[-\frac{(2\alpha-1)(3\alpha+2)}{(\alpha-2)(3\alpha-2)} + \frac{(3\alpha-1)\mathtt{x}}{(\alpha-1)(3\alpha-2)} + \frac{12\alpha^3\,{}_2\mathrm{F}_1\left(1,-\frac{1}{\alpha};\frac{\alpha-1}{\alpha};-\mathtt{x}\right)}{(\alpha-2)(\alpha+2)(3\alpha-2)} + \right.$$
$$\left. + \frac{3}{2\sqrt{\mathtt{x}}}\left(\frac{\mathtt{x}^2}{3\alpha-2} + \frac{2\mathtt{x}}{\alpha-2} - \frac{1}{\alpha+2}\right)\arcsin\left(\frac{2\sqrt{\mathtt{x}}}{1+\mathtt{x}}\right)\right] \tag{4.149}$$

for which no analytic continuation is needed, since the Gauss hypergeometric function ${}_2\mathrm{F}_1\left(1,-\frac{1}{\alpha};\frac{\alpha-1}{\alpha};-\mathtt{x}\right)$ is defined for any $\mathtt{x}>0$.

By computing (4.138) at endpoints $\omega^\star = f^\alpha$ and on $\omega^\star = \alpha f^\alpha$ of subdomains in Eqs. (4.147), interface parameters $\ell_{\mathrm{m}}^{\mathcal{I}}$ and $\ell_{\mathrm{eq}}^{\mathcal{I}}$ result equal to zero for any values of ω belonging to intervals $0<\omega<f^\alpha$, $f^\alpha<\omega<\alpha f^\alpha$ and $\omega>\alpha f^\alpha$. On the other hand, by enforcing conditions (4.137) at endpoints $\omega^\star = f^\alpha$, $\omega^\star = \alpha f^\alpha$, $\omega^\star = 1$ and $\omega^\star = \alpha$ of subdomains in Eqs. (4.148), the following expressions result for ℓ_{m} and ℓ_{eq}

$$\ell_{\mathrm{m}} = \begin{cases} \text{if} \quad 0<\omega<f^\alpha \quad \text{or} \quad f^\alpha<\omega\leq\alpha f^\alpha \quad \text{or} \quad \omega\geq\alpha: \\ 0 \\ \text{if} \quad \alpha f^\alpha\leq\omega<1 \quad \text{or} \quad 1<\omega\leq\alpha: \\ \dfrac{\alpha-1}{\alpha^{\frac{1}{\alpha}-1}}(\eta_1-5\eta_2) + \dfrac{3(1+\alpha)^2}{2\alpha^{\frac{1}{\alpha}-\frac{1}{2}}}(\eta_1-\eta_2)\arcsin\left(\dfrac{2\sqrt{\alpha}}{1+\alpha}\right) \end{cases} \tag{4.150}$$

$$\ell_{\mathrm{eq}} = \begin{cases} \text{if} \quad 0<\omega<f^\alpha \quad \text{or} \quad f^\alpha<\omega\leq\alpha f^\alpha \quad \text{or} \quad \omega\geq\alpha: \\ 0 \\ \text{if} \quad \alpha f^\alpha\leq\omega<1 \quad \text{or} \quad 1<\omega\leq\alpha: \\ \dfrac{\ell_{\mathrm{m}}}{1-\alpha} \end{cases} \tag{4.151}$$

References

Anoukou, K., Pastor, F., Dufrenoy, P., & Kondo, D. (2016). Limit analysis and homogenization of porous materials with Mohr–Coulomb matrix. Part I: Theoretical formulation. *Journal of the Mechanics and Physics of Solids*, 91, 145-171.

Benallal, A., Desmorat, R., & Fournage, M. (2014). An assessment of the role of the third stress invariant in the Gurson approach for ductile fracture. *European Journal of Mechanics-A/Solids*, 47, 400-414.

Biener, J., Hodge, A.M., Hamza, A.V., Hsiung, L.M., & Satcher, J.H. (2005). Nanoporous Au: A high yield strength material. *Journal of Applied Physics*, 97, 024301.

Biener, J., Hodge, A.M., Hayes, J.R., Volkert, C.A., Zepeda-Ruiz, L.A., Hamza, A.V., & Abraham, F.F. (2006). Size Effects on the Mechanical Behaviour of Nanoporous Au. *Nano Letters*, 6, 2379-2382.

Bigoni, D., & Piccolroaz, A., (2004). Yield criteria for quasibrittle and frictional materials. *International Journal of Solids and Structures*, 41, 2855-2878.

Bigoni, D. (2012). Nonlinear solid mechanics: bifurcation theory and material instability. Cambridge University Press.

Brach, S., Dormieux, L., Kondo, D., & Vairo, G. (2016). A computational insight into void-size effects on strength properties of nanoporous materials. *Mechanics of Materials*, 101, 102-117.

Brach, S., Dormieux, L., Kondo, D., & Vairo, G. (2016). Nanoporous materials with a general isotropic plastic matrix: exact limit state under isotropic loadings. *International Journal of Plasticity*, DOI: 10.1016/j.ijplas.2016.10.007.

Cazacu, O., Revil-Baudard, B., Chandola, N., & Kondo, D. (2014). New analytical criterion for porous solids with Tresca matrix under axisymmetric loadings. *International Journal of Solids and Structures*, 51, 861-874.

Corigliano, A., Mariani, S., & Orsatti, B. (2000). Identification of Gurson-Tvergaard material model parameters via Kalman filtering technique. I. Theory. *International journal of fracture*, 104, 4, 349-373.

Dormieux, L., & Kondo, D. (2010). An extension of Gurson model incorporating interface stress effects. *International Journal of Engineering Science*, 48, 575-581.

Dormieux, L., & Kondo, D. (2013). Non linear homogenization approach of strength of nanoporous materials with interface effects. *International Journal of Engineering Science*, 71, 102-110.

Duan, H.L., Wang, J., Huang, Z.P., & Luo, Z.Y. (2005). Stress concentration tensors of inhomogeneities with interface effects. *Mechanics of Materials*, 37, 723-736.

Duan, H.L., Wang, J., Huang, Z.P., & Karihaloo, B.L. (2005). Size-dependent effective elastic constants of solids containing nano-inhomogeneities with interface stress. *Journal of the Mechanics and Physics of Solids*, 53, 1574-1596.

Fan, H. L., & Fang, D. N. (2009). Modeling and limits of strength of nanoporous foams. *Materials & Design*, 30, 1441-1444.

Goudarzi, T., Avazmohammadi, R., & Naghdabadi, R. (2010). Surface energy effects on the yield strength of nanoporous materials containing nanoscale cylindrical voids. *Mechanics of Materials*, 42, 852-862.

Guo, T., Faleskog, J., & Shih, C., (2008). Continuum modelling of a porous solid with pressure-sensitive dilatant matrix. *Journal of Mechanics and Physics of Solids*, 56, 2188-2212.

Gurson, A.L. (1977). Continuum theory of ductile rupture by void nucleation and growth: Part I. - Yield criterion and flow rules for porous ductile media. *Journal of Engineering Materials and Technology*, 99, 2-15.

Gurtin, M.E., & Murdoch, A.I. (1975). A continuum theory of elastic material surfaces. *Archive for Rational Mechanics and Analysis*, 57, 291-323.

Hakamada, M., & Mabuchi, M. (2007). Mechanical strength of nanoporous gold fabricated by dealloying. *Scripta Materialia*, 56, 1003-1006.

Hashin, Z., (1962). The elastic moduli of heterogeneous materials. *Journal of Applied Mechanics*, 29, 143-150.

Hodge, A. M., Biener, J., Hayes, J. R., Bythrow, P. M., Volkert, C. A., & Hamza, A. V. (2007). Scaling equation for yield strength of nanoporous open-cell foams. *Acta Materialia*, 55, 1343-1349.

Jenkins, S.B. (2010). Nanoporous Materials: Types, Properties, and Uses. *Nova Science Publishers*, 2010.

Leblond, J. B., Perrin, G., & Suquet, P., (1994). Exact results and approximate models for porous viscoplastic solids. *International Journal of Plasticity*, 10, 213-235.

Le Quang, H., & He, Q. C. (2007). Size-dependent effective thermoelastic properties of nanocomposites with spherically anisotropic phases. *Journal of the Mechanics and Physics of Solids*, 55, 1899-1931.

Le Quang, H., & He, Q. C. (2008). Variational principles and bounds for elastic inhomogeneous materials with coherent imperfect interfaces. *Mechanics of Materials*, 40, 865-884.

Lemarchand, E., Dormieux, L., & Kondo, D. (2015). Lode's angle effect on the definition of the strength criterion of porous media. International *Journal for Numerical and Analytical Methods in Geomechanics*, 39(14), 1506-1526.

Mariani, S., & Corigliano, A. (2001). Anisotropic behaviour of porous, ductile media. *International Journal of Solids and Structures*, 38, 2427-2451.

Mi, C., Buttry, D.A., Sharma, P., & Kouris, D.A. (2011). Atomistic insights into dislocation-based mechanisms of void growth and coalescence. *Journal of the Mechanics and Physics of Solids*, 59, 1858-1871.

Michel, J. C., & Suquet, P., (1992). The constitutive law of nonlinear viscous and porous materials. *Journal of the Mechanics and Physics of Solids*, 40(4), 783-812.

Monchiet, V., & Bonnet, G. (2010). Interfacial models in viscoplastic composites materials. *International Journal of Engineering Science*, 48, 1762-1768.

Monchiet, V., Cazacu, O., Charkaluk, E., & Kondo, D. (2008). Macroscopic yield criteria for plastic anisotropic materials containing spheroidal voids. *International Journal of Plasticity*, 24, 1158-1189.

Monchiet, V., & Kondo, D. (2013). Combined voids size and shape effects on the macroscopic criterion of ductile nanoporous materials. *International Journal of Plasticity*, 43, 20-41.

Moshtaghin, A.F., Naghdabadi, R., & Asghari, M. (2008). Effects of surface residual stress and surface elasticity on the overall yield surfaces of nanoporous materials with cylindrical nanovoids. *Mechanics of Materials*, 51, 74-87.

Needs, R.J., Godfrey, M.J., & Mansfield, M. (1991). Theory of surface stress and surface reconstruction. *Surface Science*, 242, 215-221.

Pastor, J., Francescato, P., Trillat, M., Loute, E., & Rousselier, G. (2004). Ductile failure of cylindrically porous materials. Part II: other cases of symmetry. *European Journal of Mechanics A/Solids*, 23, 191-201.

Pearson, J. (2009). Computation of Hypergeometric Functions. Master's thesis. Worcester College, University of Oxford.

Povstenko, Yu. Z. (1993). Theoretical investigation of phenomena caused by heterogeneous surface tension in solids. *Journal of the Mechanics and Physics of Solids*, 41, 1499-1514.

Rice, J. R. (1971). Inelastic constitutive relations for solids: an internal-variable theory and its application to metal plasticity. *Journal of the Mechanics and Physics of Solids*, 19, 433-455.

Salençon, J., (1983). Calcul à la rupture et analyse limite. *Presses de l'ENPC*.

Sharma, P., & Ganti, S. (2004). Size-dependent Eshelby's tensor for embedded nano-inclusions incorporating surface/interface energies. *Journal of Applied Mechanics*, 71, 663-671.

Suquet, P. (1995). Overall properties of nonlinear composites: a modified secant moduli theory and its link with Ponte Castañeda's non linear variational procedure. *Comptes Rendus Académie de Science de Paris*, II B, 320, 11, 563-571.

Thoré, P., Pastor, F., Pastor, J., & Kondo, D. (2009). Closed-form solutions for the hollow sphere model with Coulomb and Drucker–Prager materials under isotropic loadings. *Comptes Rendus Mécanique*, 337(5), 260-267.

Thoré, P., Pastor, F., & Pastor, J., (2011). Hollow sphere models, conic programming and third stress invariant. *European Journal of Mechanics A/Solids*, 30, 63-71.

Traiviratana, S., Bringa, E.M., Benson, D.J., & Meyers, M.A. (2008). Void growth in metals: Atomistic calculations. *Acta Materialia*, 56, 3874-3886.

Tvergaard, V. (1982). On localization in ductile materials containing spherical voids. *International Journal of Fracture*, 18, 237-252.

Tvergaard, V., & Needleman, A. (1984). Analysis of the cup-cone fracture in a round tensile bar. *Acta metallurgica*, 32, 157-169.

Wang, J., Huang, Z., Duan, H., Yu, S., Feng, X., Wang, G., Zhang, W., & Wang, T. (2011). Surface stress effect in mechanics of nanostructured materials. *Acta Mechanica Solida Sinica*, 52-82.

Weissmüller, J., Newman, R. C., Jin, H. J., Hodge, A. M., & Kysar, J. W. (2009). Nanoporous metals by alloy corrosion: formation and mechanical properties. *Mrs Bulletin*, 34, 577-586.

Zhang, W., & Wang, T.J. (2007). Effect of surface energy on the yield strength of nanoporous materials. *Applied Physics Letters*, 90, 063104.

Zhang, W., Wang, T.J., & Chen, X. (2008). Effect of surface stress on the asymmetric yield strength of nanowires. *Journal of Applied Physics*, 103, 123527.

Zhang, W., Wang, T.J., & Chen, X. (2010). Effect of surface/interface stress on the plastic deformation of nanoporous materials and nanocomposites. *International Journal of Plasticity*, 26, 957-975.

Zhao, K.J., Chen, C.Q., Shen, Y.P., & Lu, T.J. (2009). Molecular dynamics study on the nano-void growth in face-centered cubic single crystal copper. *Computational Materials Science*, 46, 749-754.

Conclusions and future perspectives

Concluding remarks

In this thesis, strength properties of nanoporous materials have been investigated via theoretical approaches and Molecular Dynamics computations, establishing engineering-oriented analytical models and numerical benchmarking evidence.

As a first modelling strategy and motived by recent numerical findings by Morin et al. (2015), a non-linear homogenization approach based on a 3-layered description has been proposed in Chapter 1, yielding a closed-form macroscopic strength criterion for nanoporous materials. Referring to available benchmarking evidence (Morin et al., 2015) and with the aim to enhance the non-linear homogenization model latterly provided by (Dormieux and Kondo, 2013), a representative volume element containing isotropically-distributed spherical voids and comprising a von Mises plastic matrix has been considered. In agreement with the modified secant method (Suquet, 1995) and with the multiphase modelling technique proposed by Herve and Zaoui (1993), the non-linear homogenization problem has been solved by considering a four-phases linear comparison composite material, the latter consisting in 3-layered composite spheres confocal to nanovoids and embedded into a homogeneous solid matrix. Nanovoids-induced surface stresses at the cavities boundary (e.g., Needs et al., 1991) have been modelled by introducing an imperfect-coherent interface. As a result, a macroscopic strength criterion accounting for void-size effects has been analytically derived, recovering, as a consistency assessment and for a proper choice of model parameters, previously-established non-linear variational homogenization estimates for both porous (Ponte Castañeda, 1991) and nanoporous (Dormieux and Kondo, 2013) materials. Qualitatively in agreement with experimental evidence, a physically-consistent description of void-size effects has been provided, predicting a significant strengthening effect as the void radius reduces. Comparative illustrations have proven the accuracy of the proposed yield surface with respect to available numerical benchmarking data (Morin et al., 2015; Trillat and Pastor, 2005), resulting in a substantial enhancement of previously-established strength criteria (Dormieux and Kondo, 2013; Ponte Castañeda, 1991), especially at high stress-triaxiality regimes.

However, despite their practical interest, available finite-elements based results on strength properties of nanoporous materials can not be properly considered as an exhaustive reference. As a matter of fact, since size-related effects on macroscopic features arise at the nanoscale, a sufficiently rich description of both atomic-level phenomena and

material characteristic length-scales has to be ensured. Therefore, among various simulation techniques addressing sub-micron scales, Molecular Dynamics can be considered as one of the most promising numerical approaches for providing strongly physics-based insights into nanoporous materials. Nevertheless, although atomistic failure mechanisms underlying void-growth and coalescence have been extensively analysed in literature (e.g., Farrissey et al., 2000; Lubarda et al., 2004; Lubarda, 2011; Marian et al., 2004, 2005; Pogorelko and Mayer, 2016; Ruestes et al., 2013; Tang et al., 2010; Traiviratana et al., 2008), a proper characterization of the three-dimensional strength domain of nanoporous materials has not been proposed yet, available strength estimates being computed under specific loading conditions only (see for instance Mi et al., 2011; Traiviratana et al., 2008; Zhao et al., 2009).

Accordingly, as compared with previously-established studies and aiming to give novel contributions in this context, a Molecular-Dynamics computational model addressing more comprehensive loading cases has been proposed in Chapter 2. In detail, numerical calculations have been carried out on in-silico nanoporous aluminium samples undergoing triaxial-expansion, triaxial-compression and shear strain-rate boundary conditions. For each deformation scenario, a wide range of triaxiality regimes has been considered, describing deformation paths ranging from pure deviatoric to pure hydrostatic strain states. Although more complex geometries could be considered in order to properly represent realistic experimental samples, the herein-adopted periodic microstructure, based on a representative single-crystal cell embedding a single spherical void, enables to limit as much as possible any coupling phenomenon (such as those associated to voids shape and interactions), focusing on dominant mechanisms related to the nanosize of voids. Effective strength properties of both bulk and nanoporous specimens have been computed, resulting in meridian and deviatoric strength profiles hugely dependent on the three Haigh-Westergaard stress invariants. The size-related strengthening effect observed in experimental tests for a fixed porosity level (Biener et al., 2005, 2006; Hakamada and Mabuchi, 2007; Fan and Fang, 2009) has been consistently recovered, resulting in an overall expansion of computed strength domains when the void radius reduces. Moreover, both the occurrence and the amount of void-size effects have been proven to strongly depend on the Lode angle, leading to a shape-transition of deviatoric strength profiles when the void radius is varied.

Physical indications arising from Molecular-Dynamics computations clearly suggest the need of improving available strength models for nanoporous materials by considering a richer description of the matrix plastic behaviour. To this aim, and opening towards a limit analysis approach, the starting point has consisted in exactly solving the limit-state problem in the case of isotropic loading conditions, as detailed in Chapter 3. A hollow-sphere model with an imperfect-coherent interface at the cavity boundary, representative of a particular microstructure for nanoporous materials, has been considered. Aiming to account for a broad class of pressure-sensitive limit responses, as well as to allow for an extreme flexibility in reproducing stress-Lode-angle effects, both the solid matrix and the interface have been assumed to obey to a general isotropic yield function, defined

as a simplified form of the criterion proposed by Bigoni and Piccolroaz (2004). Closed-form relationships for local strain-rate, velocity and stress fields have been determined, identifying the exact limit state for the hollow-sphere model in the case of both negligible (i.e., for porous materials) and significant (i.e., for nanoporous materials) interface effects. Since the high flexibility and the general form of the adopted strength criterion, the present approach has allowed to identify the exact limit state for a wide range of local plastic behaviours, possibly-affected by all the three isotropic stress invariants, and that may not be properly described via classical yield models. As special cases and as a consistency assessment, obtained relationships have been proven to exactly recover, for a suitable choice of model parameters, available analytical expressions (Cazacu et al., 2014; Gurson, 1977; Thoré et al., 2009) deduced in the case of negligible interface effects, and associated to classical local strength criteria.

Finally, a general macroscopic strength criterion accounting for void-size effects has been analytically derived in Chapter 4, by referring to a hollow-sphere model with an imperfect-coherent interface at the void surface, and in the case of axisymmetric strain-rate boundary conditions. Both the solid matrix and the interface have been assumed to obey to a particular form of the local yield function introduced in Chapter 3, describing a polyhedral yield surface in the space of the Lode coordinates with linear meridian and multi-sided deviatoric yield profiles. The corresponding local support function and plastic admissibility condition provided in Chapter 3 have been considered. In the framework of a kinematic limit-analysis approach, and following the modelling strategy proposed by Gurson (1977) and successively adopted in a number of theoretical models (e.g., Anoukou et al., 2016; Cazacu et al., 2014; Dormieux and Kondo, 2010; Guo et al., 2008), a trial velocity field has been defined as the superposition of a suitable homogeneous term and of the velocity determined in Chapter 3. Taking advantage of the theoretical procedure established by Anoukou et al. (2016), a parametric closed-form relationship for the macroscopic yield function has been obtained as the solution of a Karush-Kuhn-Tucker inequality-constrained minimization problem, this latter accounting for local plastic admissibility conditions. Predicted macroscopic strength properties have been proven to be hugely affected by all the three isotropic stress invariants, resulting in pressure-sensitive strength profiles exhibiting significant stress-Lode-angle effects. Comparative illustrations have clearly shown the influence of the local plastic behaviour on the macroscopic one, thereby highlighting a great flexibility in describing a wide class of porous and nanoporous materials, generally not properly represented via classical yield models. An effective description of void-size effects on macroscopic yield stress states has been furnished, resulting in an overall expansion of the predicted strength domain when the void radius reduces. As a particular case and as a consistency assessment, proposed macroscopic yield function has been proven to recover the relationship provided by (Anoukou et al., 2016) for a Mohr-Coulomb local plastic behaviour. Moreover, expressions obtained by Thoré et al. (2009) and Cazacu et al. (2014) for the exact hydrostatic strength of Mohr-Coulomb and Tresca plastic porous materials have been fully retrieved, via a suitable calibration of local-yield-function parameters and in the case of negligible interface effects.

Future research directions

The present thesis leaves a number of challenging open issues, which it would be interesting to address in future studies. Specifically, as regards both theoretical and numerical modelling approaches, the following research directions are traced.

Combined effects of void size and void shape Since the wide range of structural geometries characterising nanoporous materials in current engineering applications, an important research aspect consists in investigating combined effects of void size and void shape on effective strength properties.

A first attempt in this direction has been recently provided by Monchiet and Kondo (2013), in the framework of a kinematic limit-analysis approach and by considering the trial velocity field previously-introduced by Gologanu et al. (1993), Gologanu et al. (1994), and Gologanu et al. (1997). Specifically, in order to derive a macroscopic strength criterion accounting for both void-size and void-shape effects, a hollow-spheroid model with a confocal spheroidal cavity has been considered, by introducing an imperfect-coherent interface at the void boundary. The material comprising the solid matrix being assumed to obey to a von Mises yield function, a richer description of the local plastic behaviour could be addressed, for instance via the general criterion introduced in Chapter 3.

On the other hand, a limited number of computational studies has been devoted to the numerical investigation of combined effects of void size and void shape on the constitutive plastic response of nanoporous materials. Therefore, aiming to furnish novel contributions in this context, a possible modelling strategy could be represented by the Molecular Dynamics procedure established in Chapter 2. In particular, by considering the reference geometry adopted in the afore-mentioned theoretical model, numerical simulations may be carried out on computational domains embedding prolate or oblate spheroidal nanocavities, thereby allowing for a parametric analysis of the computed strength domains as dependent on both the size and the shape of voids.

Physics-based modelling of void-size effects In all the theoretical models proposed in this thesis, the dependence of strength properties on the size of voids, for a nanoporous material with a fixed value of porosity, has been addressed by describing cavities boundary via an imperfect-coherent interface stress model. Specifically, in agreement with a number of previously-established approaches (e.g., Fan and Fang, 2009; Needs et al., 1991; Povstenko and Yu, 1993; Weissmüller et al., 2009) the stress vector has been prescribed to undergo a discontinuity across the interface, in order to account for self-equilibrated surface stresses induced by the nanosize of voids. However, although such a modelling description has been extensively adopted in the available literature for both elastic (Brisard et al., 2010a,b; Duan et al., 2005a,b; Le Quang and He, 2007; Sharma et al., 2003; Sharma and Ganti, 2004) and plastic (Dormieux and Kondo, 2010, 2013; Monchiet and Kondo, 2013; Goudarzi et al., 2010; Moshtaghin et al., 2012; Zhang and Wang, 2007; Zhang et al., 2008, 2010) regimes, its physical basis still needs to be more documented.

Accordingly, a possible research direction could consist in analysing the local perturbation induced by the presence of a nanovoid into an otherwise perfect atomic arrangement. As shown in Fig. 2.4, this directly impacts on the number of neighbouring atoms, thereby resulting in significantly different values of total energy as compared to the case of a bulk sample. Moreover, and as a preliminary observation, the high strain-rate gradient related to the dislocations accumulation depicted in Fig. 2.5 may result in a strengthening of the material comprising the cavity surface. The Molecular Dynamics procedure proposed in Chapter 2 may allow for a more comprehensive understanding of nanoscale mechanisms underlying the occurrence of size-related effects, thereby opening towards both the assessment of interface stress models and the definition of novel physics-based theoretical descriptions. Alternatively, following the approach proposed by Yvonnet et al. (2012) for investigating surface elasticity, ab-initio calculations may be performed in order to furnish insightful indications on nano-cavities physics.

Combined effects of void size and crystallographic anisotropy Anisotropic effects in nanoporous materials, with particular reference to those related to the crystalline texture of the solid matrix, have not been addressed in the present thesis. Nevertheless, the combined influence of void size and crystallographic anisotropy on the effective material mechanical response still represents a promising research topic. As a matter of fact, existing theoretical and numerical models mainly refer to crystals containing macro-sized cavities. Mention is made to approaches recently proposed by Han et al. (2013), Mbiakop et al. (2015) and Paux et al. (2015), highlighting the great interest in considering anisotropy effects for estimating effective strength properties of porous single-crystals.

In this context, possible novel modelling strategies could consist in:

- characterizing combined effects of void size and crystallographic anisotropy on the material plastic response via Molecular Dynamics computations. To this end, results provided in Chapter 2 for a FCC nanoporous single-crystal could be enhanced by considering crystallographic arrangements for which anisotropy effects are expected to be particularly evident (such as BCC and HCP atomic structures). Consequently, comparative analyses may be furnished to depict the occurrence and the amount of both void-size (for a given crystallographic texture and porosity level) and anisotropy (for fixed values of void size and porosity) effects on predicted strength domains.

- extending the macroscopic general strength criterion derived in Chapter 4 to the case of nanoporous materials with an anisotropic plastic solid matrix. To this aim, representation theorems (e.g., Boehler, 1987) based on the introduction of a suitable structural anisotropy tensor, may be used to extend the herein adopted Bigoni-like isotropic yield function to local structural plastic anisotropy.

Numerical implementation of the proposed general strength criterion The numerical implementation in engineering-oriented numerical codes of the macroscopic general yield function for nanoporous materials derived in Chapter 4 may represent a challeng-

ing research task, opening towards the definition of powerful homogenization toolboxes for structural applications. Nevertheless, as a supplement of the general macroscopic strength criterion, two theoretical issues should be preliminary addressed, consisting in the explicit determination of:

- the macroscopic flow rule, that is the constitutive relationship between the predicted strength estimate and the macroscopic strain-rate state. Owing to a classical result established by Rice (1971), the normality property of the local flow rule is expected to be preserved in the homogenization procedure, thereby resulting in a plastic normality law at the macroscopic level.

- evolution laws providing the actual value of both porosity and void size at each stage of the deformation process. To this aim, a careful attention should be paid to the pressure-sensitivity of the considered local plastic behaviour, resulting in a plastic compressibility of the material comprising the solid matrix.

APPENDIX A

Deviatoric strength of nanoporous materials: A limit analysis approach

Abstract

In this Appendix, deviatoric strength properties of nanoporous materials are investigated by addressing the limit state of a hollow sphere undergoing axisymmetric deviatoric strain-rate based loading conditions. The hollow sphere is assumed to be comprised of a rigid ideal-plastic matrix obeying to a von Mises strength criterion. Void-size effects are consistently described by introducing a coherent-imperfect homogeneous interface at the cavity boundary. In the framework of a kinematic approach, the limit-analysis problem on the hollow sphere is solved by referring to a particular trial velocity field, expressed in terms of some free model parameters, chosen as a result of an optimization strategy. A closed-form expression for estimating the macroscopic deviatoric strength is obtained and successfully compared with available benchmarking data.

Present Appendix corresponds to the published research paper (Brach et al., 2016e) [Springer Series in Solid and Structural Mechanics; DOI: 10.1007/978-3-319-48884-4 (2016)].
A self-consistent notation is adopted.

Keywords: Nanoporous materials, void-size effects, deviatoric strength, kinematic limit analysis, trial velocity field.

A.1 Introduction

Nanoporous materials have been characterised by a fast-growing development in the last two decades, attracting a world-wide interest in both industrial and academic domains Arico et al. (2005); Jenkins (2010); Lu et al. (2004). As a matter of fact, owing to their good properties in terms of stiffness and strength, nanoporous materials open towards groundbreaking applications in several technical fields, involving ultra-high performance devices and challenging multifunctional uses. In order to fulfil to these promising applications, one of the most fundamental aspects consists in describing, into an effective engineering design framework, strength properties of these materials as dependent on the size of voids. Recent nano-mechanical experiments (e.g., Biener et al., 2005, 2006; Hakamada and Mabuchi, 2007) have shown that, for a fixed porosity value, a reduction in the length-scale of nanovoids induces an increase in the material yield strength. Similarly, Molecular-Dynamics simulations carried out on in-silico nanoporous samples Brach et al. (2016a); Mi et al. (2011); Traiviratana et al. (2008); Zhao et al. (2009) have proven that the predicted strength decreases towards asymptotic values when the size of voids increases. The physical origin of such a phenomenon has been related by Needs et al. (1991) to the presence of self-equilibrated surface stresses at the cavity surface, induced by a local perturbation in the atomic arrangement close to the nanovoids and usually negligible for classical porous materials. In the framework of a continuum approach, void-size effects have been generally addressed by introducing coherent-imperfect interface laws at the cavity boundaries (e.g., Duan et al., 2005a,b; Gurtin and Murdoch, 1975, 1978; Povstenko and Yu, 1993), that is accounting for surface stresses by prescribing the discontinuity of the stress vector across the interface.

Strength models for classical porous materials Gurson (1977); Ponte Castañeda (1991) are able to account for porosity effects only, thereby resulting in void-size independent yield functions. Void-size dependent strength criteria have been recently proposed in Brach et al. (2016b); Dormieux and Kondo (2013); Goudarzi et al. (2010); Moshtaghin et al. (2012); Zhang and Wang (2007); Zhang et al. (2008, 2010), by referring to non-linear homogenization techniques. As regards limit analysis approaches, the well-established criterion proposed by Gurson (1977) for porous media has been extended to nanoporous materials in Dormieux and Kondo (2010), via a plastic generalization of interface stress models Monchiet and Bonnet (2010). However, as it will be also shown in the following, the novel strength criterion proposed in Dormieux and Kondo (2010) overrates available numerical evidence Trillat and Pastor (2005). In this light, and with reference to deviatoric axisymmetric states only, present Appendix aims to furnish a more effective estimate for the macroscopic deviatoric strength of nanoporous materials, properly accounting for void-size effects. In detail, the limit analysis problem on a hollow sphere domain is solved by referring to the parametric trial velocity field introduced in Budiansky et al. (1982) (see also Zhu and Zbib, 1993), allowing for an optimization procedure.

The Appendix is organized as follows. In Section A.2 basic elements of the limit-analysis theoretical framework are presented. In Section A.3 the adopted trial velocity field is introduced. The estimate of the macroscopic strength of a hollow sphere with

interface effects and undergoing an axisymmetric deviatoric loading is determined in Section A.4, discussing effectiveness and accuracy of the proposed model. Finally, some conclusions are traced in Section A.5.

A.2 Problem statement

Let the hollow sphere in Fig. A.1 be considered, whose internal and external radii are denoted as R_i and R_e, respectively. Moreover, let $\partial\Omega_\mathrm{i}$ and $\partial\Omega_\mathrm{e}$ be the corresponding internal and external surfaces, the total boundary of the system resulting in $\partial\Omega = \partial\Omega_\mathrm{i} \cup \partial\Omega_\mathrm{e}$. Denoting as $|\Omega_\mathrm{s}|$ and $|\Omega_\mathrm{v}|$ the volume measures of the solid region (namely, Ω_s) and of the spherical void (Ω_v), respectively, the total volume of the system (namely, $\Omega = \Omega_\mathrm{s} \cup \Omega_\mathrm{v}$) is $|\Omega| = |\Omega_\mathrm{s}| + |\Omega_\mathrm{v}|$, and the porosity p is equal to $p = |\Omega_\mathrm{v}|/|\Omega|$. The solid matrix Ω_s is assumed to be homogeneous and comprised of an isotropic material with a rigid ideal-plastic behaviour.

In agreement with continuum-based descriptions Duan et al. (2005a); Gurtin and Murdoch (1975, 1978); Wang et al. (2011) and strength models for nanoporous materials Dormieux and Kondo (2010, 2013), the influence of non-negligible surface stresses induced by the presence of a possibly-nanosized void is herein addressed by introducing a coherent and imperfect homogeneous interface $\mathcal{I}$ at the void boundary $\partial\Omega_\mathrm{i}$ (Fig. A.1). In particular, the velocity field (resp., the stress vector) is prescribed to be continuous (resp., discontinuous) through $\partial\Omega_\mathrm{i}$. In the framework of a plastic generalization of the Gurtin-Murdoch stress-interface model Gurtin and Murdoch (1975), the material comprising the homogeneous interface is assumed to be itself isotropic and rigid ideal-plastic.

Let the Cartesian reference system $(\mathbf{e}_\mathrm{x}, \mathbf{e}_\mathrm{y}, \mathbf{e}_\mathrm{z})$ be introduced, with the origin O at the sphere center. For what follows, and referring to the notation in Fig. A.1, it is useful to consider the spherical coordinate system (r, θ, φ) and the local orthonormal basis $(\mathbf{e}_\mathrm{r}, \mathbf{e}_\theta, \mathbf{e}_\varphi)$, r being the radial coordinate, $\theta \in [0, \pi]$ and $\varphi \in [0, 2\pi]$ the zenith and the azimuth angular coordinates, respectively. Accordingly, the position of a point in Ω (resp., at the interface $\mathcal{I}$ and at the exterior boundary $\partial\Omega_\mathrm{e}$) with respect to O is identified by $\mathbf{r} = r\,\mathbf{e}_\mathrm{r}(\theta, \varphi)$ (resp., $\mathbf{r}_\mathrm{i} = R_\mathrm{i}\,\mathbf{e}_\mathrm{r}(\theta, \varphi)$ and $\mathbf{r}_\mathrm{e} = R_\mathrm{e}\,\mathbf{e}_\mathrm{r}(\theta, \varphi)$).

As a notation rule, vector and second-order tensor quantities are denoted by bold letters; symbols $\cdot$, $:$, and $\otimes$ indicate inner, double-dot, and tensor product operators, respectively; ∇ and $\nabla^{\mathcal{I}}$ are the nabla operators in Ω_s and along the interface, $\widetilde{\nabla}$ and $\widetilde{\nabla}^{\mathcal{I}}$ identifying the symmetric parts of the corresponding gradient operators. Notation $\mathcal{B}(r^*)$ is also introduced to indicate the spherical surface identified by the radial coordinate $r = r^*$.

Let the fourth-order projector tensor $\mathbb{T} = \mathbf{P}\overline{\otimes}\mathbf{P}$ be introduced, where the operator $\overline{\otimes}$ is component-wise defined by $\mathbb{T}_{ijkl} = (P_{ik}P_{jl} + P_{il}P_{jk})/2$, and where the second-order tensor $\mathbf{P}$ is defined as $\mathbf{P} = (\mathbf{1} - \mathbf{e}_\mathrm{r} \otimes \mathbf{e}_\mathrm{r})$ with $\mathbf{1}$ the identity tensor. Accordingly, $\mathbf{A}_\mathbb{T} = \mathbb{T} : \mathbf{A}$ identifies the projection on planes orthogonal to $\mathbf{e}_\mathrm{r}$ of a second-order tensor $\mathbf{A}$. In the following, $\mathbf{A}$ is referred to as a planar tensor if $\mathbf{A} = \mathbf{A}_\mathbb{T}$.

Neglecting the influence of body forces, sets of statically-admissible ($\mathcal{S}_\sigma$) and plastically-admissible ($\mathcal{P}_\sigma$) stress fields are introduced as

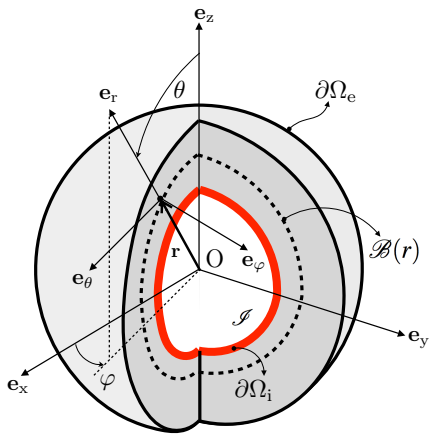

Figure A.1 – Problem statement. Notation.

$$\mathcal{S}_\sigma = \left\{ (\boldsymbol{\sigma}, \boldsymbol{\tau}) \quad \text{s.t.} \quad \begin{array}{l} \nabla \cdot \boldsymbol{\sigma} = \mathbf{0} \quad \text{in } \Omega_s\,, \\ (\boldsymbol{\sigma}^+ - \boldsymbol{\sigma}^-) \cdot \mathbf{e}_r + (\boldsymbol{\tau} : \mathbf{K})\mathbf{e}_r = \nabla^{\mathcal{I}} \cdot \boldsymbol{\tau} \quad \text{on } \partial\Omega_i \end{array} \right\} \tag{A.1a}$$

$$\mathcal{P}_\sigma = \left\{ (\boldsymbol{\sigma}, \boldsymbol{\tau}) \quad \text{s.t.} \quad f^s(\boldsymbol{\sigma}) = 0 \quad \text{in } \Omega_s \quad \text{and} \quad f^{\mathcal{I}}(\boldsymbol{\tau}) = 0 \quad \text{on } \partial\Omega_i \right\} \tag{A.1b}$$

where $\boldsymbol{\sigma}$ (resp., $\boldsymbol{\tau}$) denotes the microscopic second-order stress tensor (resp., the planar surface stress tensor at $\mathcal{I}$), f^s (resp., $f^{\mathcal{I}}$) indicates the yield function of the solid matrix (resp., of the interface), $\mathbf{K}$ is the curvature tensor, and $\boldsymbol{\sigma}^\pm = \boldsymbol{\sigma}(r \to R_i^\pm)$. It is worth pointing out that the equilibrium equation at $\mathcal{I}$ in Eq. (A.1a) is expressed via a generalized form of the Young-Laplace equation Gurtin and Murdoch (1975); Duan et al. (2005b), and set $\mathcal{P}_\sigma$ prescribes that the material is everywhere yielding.

The exterior boundary $\partial\Omega_e$ of the system is assumed to undergo to strain rate-based conditions, expressed in terms of the following second-order axisymmetric deviatoric tensor:

$$\mathbf{D} = \widetilde{D}\left[\frac{1}{2}\left(\mathbf{e}_x \otimes \mathbf{e}_x + \mathbf{e}_y \otimes \mathbf{e}_y\right) - \mathbf{e}_z \otimes \mathbf{e}_z\right] \tag{A.2}$$

$\widetilde{D}$ being a constant strain-rate parameter, and whose second-order deviatoric and third-order deviatoric stress invariants are denoted as $J_2^d = \mathrm{tr}(\mathbf{D}^2)/2$ and $J_3^d = \mathrm{tr}(\mathbf{D}^3)/3$, respectively. The strain-rate deviatoric measure D_{eq}, as well as the strain-rate Lode angle θ_D are also introduced

$$D_{eq} = 2\sqrt{\frac{J_2^d}{3}}\,, \qquad \theta_D = \frac{1}{3}\arccos\frac{3\sqrt{3}J_3^d}{2(J_2^d)^{3/2}} \tag{A.3}$$

The set of kinematically-admissible ($\mathcal{K}_d$) strain-rate fields is defined as:

$$\mathcal{K}_d = \left\{ \begin{array}{ll} & \mathbf{d} = \widetilde{\nabla}\mathbf{v} \quad \text{in } \Omega_\mathrm{s}\,, \\ (\mathbf{d}, \mathbf{d}^\mathcal{I}) \quad \text{s.t.} & \mathbf{d}^\mathcal{I} = \mathbf{d}(\mathbf{r}_\mathrm{i}) \quad \text{on } \partial\Omega_\mathrm{i}\,, \\ & \text{with } \mathbf{v} = \mathbf{D}\cdot\mathbf{r} \quad \text{on } \partial\Omega_\mathrm{e} \end{array} \right\} \tag{A.4}$$

with $\mathbf{d}$ (resp., $\mathbf{d}^\mathcal{I}$) denoting the microscopic second-order strain-rate tensor in Ω_s (resp., on $\partial\Omega_\mathrm{i}$), and where $\mathbf{v}$ is the local velocity field.

When statically-admissible stress (i.e., $(\boldsymbol{\sigma}, \boldsymbol{\tau}) \in \mathcal{S}_\sigma$) and kinematically-admissible strain-rate (i.e., $(\mathbf{d}, \mathbf{d}^\mathcal{I}) \in \mathcal{K}_\mathrm{d}$) local fields are considered, the Hill's theorem holds (e.g., Salençon, 1983)

$$|\Omega|\boldsymbol{\Sigma} : \mathbf{D} = \int_{\Omega^\mathrm{s}} \boldsymbol{\sigma} : \mathbf{d}\, d\Omega + \int_{\partial\Omega_\mathrm{i}} \boldsymbol{\tau} : \mathbf{d}^\mathcal{I}_\mathbb{T}\, dA \tag{A.5}$$

the macroscopic stress tensor $\boldsymbol{\Sigma}$ and the macroscopic strain-rate tensor $\mathbf{D}$ having to comply with relationships $\boldsymbol{\Sigma} = \overline{\boldsymbol{\sigma}}$ and $\mathbf{D} = \overline{\mathbf{d}}$, respectively, where $\overline{\mathbf{a}}$ identifies the Ω-based average of a certain space-dependent field $\mathbf{a}(\mathbf{r})$ (i.e., $\overline{\mathbf{a}} = |\Omega|^{-1}\int_\Omega \mathbf{a}\, d\Omega$). The exterior power has to be lower or at the most equal to the maximum plastic dissipation $\mathcal{P}_\mathrm{rm}$ that can be afforded in Ω

$$|\Omega|\boldsymbol{\Sigma} : \mathbf{D} \leq \mathcal{P}_\mathrm{rm}\,, \quad \text{with} \quad \mathcal{P}_\mathrm{rm}(\mathbf{d}) = \int_{\Omega_\mathrm{s}} \pi^\mathrm{s}(\mathbf{d})\, d\Omega + \int_{\partial\Omega_\mathrm{i}} \pi^\mathcal{I}(\mathbf{d}^\mathcal{I})\, dA\,, \tag{A.6}$$

where

$$\pi^\mathrm{s}(\mathbf{d}) = \sup_{\boldsymbol{\sigma}\in\mathcal{G}^\mathrm{s}} (\boldsymbol{\sigma} : \mathbf{d}), \qquad \text{with} \qquad \mathcal{G}^\mathrm{s} = \{\boldsymbol{\sigma} \quad \text{s.t.} \quad f^\mathrm{s}(\boldsymbol{\sigma}) \leq 0\} \tag{A.7}$$

$$\pi^\mathcal{I}(\mathbf{d}^\mathcal{I}) = \sup_{\boldsymbol{\tau}\in\mathcal{G}^\mathcal{I}} (\boldsymbol{\tau} : \mathbf{d}^\mathcal{I}_\mathbb{T}), \qquad \text{with} \qquad \mathcal{G}^\mathcal{I} = \left\{\boldsymbol{\tau} \quad \text{s.t.} \quad f^\mathcal{I}(\boldsymbol{\tau}) \leq 0\right\} \tag{A.8}$$

with $\mathbf{d}^\mathcal{I}_\mathbb{T} = \mathbb{T} : \mathbf{d}^\mathcal{I}$, and where the equality sign in Eq. (A.6) holds at the limit state. Function π^s (resp., $\pi^\mathcal{I}$) is the support function for the local strength domain $\mathcal{G}^\mathrm{s}$ (resp., $\mathcal{G}^\mathcal{I}$). It has the meaning of the maximum volume (resp., surface) density of the resisting power that can be locally achieved by the material, when the local strain-rate field $\mathbf{d}$ (resp., $\mathbf{d}^\mathcal{I}$) is considered.

Accordingly, the macroscopic limit stress $\boldsymbol{\Sigma}^\ell$ results from

$$\boldsymbol{\Sigma}^\ell = \frac{\partial \Pi_\mathrm{hom}(\mathbf{D})}{\partial \mathbf{D}} \tag{A.9}$$

where $\Pi_\mathrm{hom}(\mathbf{D})$ is the macroscopic support function, defined as Dormieux and Kondo (2010)

$$\Pi_\mathrm{hom}(\mathbf{D}) = \inf_{(\mathbf{d},\mathbf{d}^\mathcal{I})\in\mathcal{K}_d} \left\{\Pi^\mathrm{s}_\mathrm{hom}(\mathbf{d}) + \Pi^\mathcal{I}_\mathrm{hom}(\mathbf{d}^\mathcal{I})\right\} \tag{A.10}$$

with

$$\Pi^\mathrm{s}_\mathrm{hom} = \overline{\pi^\mathrm{s}(\mathbf{d})}\,, \qquad \Pi^\mathcal{I}_\mathrm{hom} = \frac{1}{|\Omega|}\int_{\partial\Omega_\mathrm{i}} \pi^\mathcal{I}(\mathbf{d}^\mathcal{I})\, dA \tag{A.11}$$

In the case of an isotropic local plastic behaviour and since for the case under inves-

tigation $\mathrm{tr}(\mathbf{D}) = 0$, the macroscopic support function Π_{hom} in Eq. (A.10) is expressed in terms of the isotropic strain-rate invariants D_{eq} and θ_{D} only, resulting in the macroscopic limit deviatoric stress tensor

$$\boldsymbol{\Sigma}^{\ell} = \frac{2}{3D_{\mathrm{eq}}}\frac{\partial \Pi_{\mathrm{hom}}}{\partial D_{\mathrm{eq}}}\mathbf{D} + \frac{\partial \Pi_{\mathrm{hom}}}{\partial \theta_{\mathrm{D}}}\frac{\partial \theta_{\mathrm{D}}}{\partial \mathbf{D}} \tag{A.12}$$

Correspondingly, the deviatoric strength measure $\Sigma^{\ell}_{\mathrm{eq}} = \sqrt{3J_2^{\sigma}}$ is introduced, with $J_2^{\sigma} = \mathrm{tr}\left(\boldsymbol{\Sigma}^{\ell}\right)^2/2$.

In the following, instead of seeking the infimum in Eq. (A.10) over all the kinematically-admissible strain-rate states, a particular microscopic velocity field $\widehat{\mathbf{v}}$, such that $\widehat{\mathbf{v}} = \mathbf{D}\cdot\mathbf{r}$ on $\partial\Omega_{\mathrm{e}}$ and yielding to the local strain-rate fields $(\widehat{\mathbf{d}}, \widehat{\mathbf{d}}^{\mathcal{I}}) \in \mathcal{K}_{\mathrm{d}}$, is chosen furnishing an estimate of the macroscopic support function and thereby an upper bound of the macroscopic limit stress.

A.3 Trial velocity field

In agreement with the strategy originally derived in Budiansky et al. (1982) and also adopted in Zhu and Zbib (1993), the local kinematics at the collapse state is estimated by assuming a trial velocity field $\widehat{\mathbf{v}} = \widehat{v}_{\mathrm{r}}\,\mathbf{e}_{\mathrm{r}} + \widehat{v}_{\theta}\,\mathbf{e}_{\theta} + \widehat{v}_{\varphi}\,\mathbf{e}_{\varphi}$ in the form

$$\begin{aligned}
\widehat{v}_{\mathrm{r}} &= -\frac{1}{r^2\sin\theta}\frac{\partial}{\partial\theta}\left[\zeta(r,\theta)\sin\theta\right] \\
\widehat{v}_{\theta} &= \frac{1}{r}\frac{\partial}{\partial r}\left[\zeta(r,\theta)\right] \\
\widehat{v}_{\varphi} &= 0
\end{aligned} \tag{A.13}$$

where function $\zeta(r,\theta)$ is defined by

$$\zeta(r,\theta) = D_{\mathrm{eq}}\left[\frac{r^3}{4} + \chi(r)\right]\sin(2\theta) \tag{A.14}$$

$\chi(r)$ being a regular function such that

$$\chi(R_{\mathrm{e}}) = \chi^{I}(R_{\mathrm{e}}) = 0 \tag{A.15}$$

where Roman numerals are used to indicate derivatives with respect to r. Relationships (A.15) allow the velocity field in Eq. (A.13) to comply with the strain-rate boundary condition expressed in Eq. (A.4), and thereby resulting in a kinematically-admissible strain-rate field $(\widehat{\mathbf{d}}, \widehat{\mathbf{d}}^{\mathcal{I}}) \in \mathcal{K}_{\mathrm{d}}$. In detail, it is simple to prove that the adopted trial velocity field under the constrain (A.15) satisfies the boundary requirement $\widehat{\mathbf{v}} = \mathbf{D}\cdot\mathbf{r}$ on $\partial\Omega_{\mathrm{e}}$, that is

$$\begin{aligned}
\widehat{v}_{\mathrm{r}}(\mathbf{r}_{\mathrm{e}}) &= -D_{\mathrm{eq}}\frac{R_{\mathrm{e}}}{4}\left[1 + 3\cos(2\theta)\right] \\
\widehat{v}_{\theta}(\mathbf{r}_{\mathrm{e}}) &= D_{\mathrm{eq}}\frac{3}{4}R_{\mathrm{e}}\sin(2\theta) \\
\widehat{v}_{\varphi}(\mathbf{r}_{\mathrm{e}}) &= 0
\end{aligned} \tag{A.16}$$

It is worth observing that condition $\chi(r) = 0$ straight yields the velocity field classically adopted in kinematic limit-analysis approaches Dormieux and Kondo (2010); Gurson (1977). Furthermore, assumptions (A.13) and (A.14) correspond to a local strain-rate field verifying the incompressibility condition

$$\operatorname{tr}\widehat{\mathbf{d}} = \frac{\partial}{\partial r}\big(r^2\widehat{v}_r\sin\theta\big) + \frac{\partial}{\partial\theta}\big(r\widehat{v}_\theta\sin\theta\big) = 0 \tag{A.17}$$

everywhere in the hollow sphere, irrespective of the particular form assumed for $\chi(r)$.

A.4 Strength estimate

The solid matrix Ω_s and the interface $\mathcal{I}$ are assumed to obey to a von Mises strength criterion, whose yield (f^s and $f^\mathcal{I}$) and support (π^s and $\pi^\mathcal{I}$) functions are respectively expressed as Salençon (1983)

$$f^\mathrm{s}(\boldsymbol{\sigma}) = \frac{3}{2}\boldsymbol{\sigma}_\mathrm{d} : \boldsymbol{\sigma}_\mathrm{d} - \sigma_0^2 \tag{A.18a}$$

$$f^\mathcal{I}(\boldsymbol{\tau}) = \frac{3}{2}\boldsymbol{\tau}_\mathrm{d} : \boldsymbol{\tau}_\mathrm{d} - k_\mathcal{I}^2 \tag{A.18b}$$

$$\pi^\mathrm{s}(\mathbf{d}) = \begin{cases} \sigma_0\sqrt{\frac{2}{3}\mathbf{d}:\mathbf{d}} & \text{if} \quad \operatorname{tr}\mathbf{d} = 0 \\ +\infty & \text{if} \quad \operatorname{tr}\mathbf{d} \neq 0 \end{cases} \tag{A.18c}$$

$$\pi^\mathcal{I}(\mathbf{d}^\mathcal{I}) = \begin{cases} k_\mathcal{I}\sqrt{\frac{2}{3}\mathbf{d}^\mathcal{I}:\mathbf{d}^\mathcal{I}} & \text{if} \quad \operatorname{tr}\mathbf{d}^\mathcal{I} = 0 \\ +\infty & \text{if} \quad \operatorname{tr}\mathbf{d}^\mathcal{I} \neq 0 \end{cases} \tag{A.18d}$$

where $\boldsymbol{\sigma}_\mathrm{d} = \boldsymbol{\sigma} - (\operatorname{tr}\boldsymbol{\sigma}/3)\mathbf{1}$ is the deviatoric part of the stress tensor $\boldsymbol{\sigma}$ in Ω_s, $\boldsymbol{\tau}_\mathrm{d} = \boldsymbol{\tau} - (\operatorname{tr}\boldsymbol{\tau}/3)\mathbf{1}$ is the deviatoric part of the planar stress tensor $\boldsymbol{\tau}$ at $\mathcal{I}$, with $\mathbf{1}$ the second-order identity tensor, and where σ_0 and $k_\mathcal{I}$ are the deviatoric strength parameters of the solid matrix and the interface, respectively, the latter having the dimensions of a membrane stress (namely, a force per unit length).

Kinematically-admissible strain-rate fields $(\widehat{\mathbf{d}}, \widehat{\mathbf{d}}^\mathcal{I}) \in \mathcal{K}_\mathrm{d}$, computed via the velocity field $\widehat{\mathbf{v}}$ introduced in Section A.3, allows to determine, through Eqs. (A.18c) and (A.18d), the following estimate for the macroscopic support function introduced in Eq. (A.11)

$$\widehat{\Pi}_\mathrm{hom}(D_\mathrm{eq}, \theta_\mathrm{D}) = \sqrt{\frac{2}{3}}\frac{\sigma_0}{|\Omega|}\left[\int_{\Omega_\mathrm{s}}\sqrt{\widehat{\mathbf{d}}:\widehat{\mathbf{d}}}\,d\Omega + \kappa R_\mathrm{i}\int_{\partial\Omega_\mathrm{i}}\sqrt{\widehat{\mathbf{d}}^\mathcal{I}:\widehat{\mathbf{d}}^\mathcal{I}}\,dA\right] \tag{A.19}$$

where the dimensionless parameter

$$\kappa = \frac{k_\mathcal{I}}{R_\mathrm{i}\sigma_0} \tag{A.20}$$

is introduced aiming to account for the influence of void-size effects. As a matter of fact, when strength values for the interface (namely, $k_\mathcal{I}$) and for the solid matrix (σ_0) are considered as fixed, a reduction in the void size R_i corresponds to increase κ. The case of porous materials comprising cavities with large values of R_i is thereby recovered simply

by considering $\kappa = 0$, namely by assuming as negligible surface-induced effects.

In order to obtain an explicit analytical estimate of Π_{hom}, the Cauchy-Schwartz inequality leads:

$$\int_{\mathcal{B}(r)} \sqrt{\widehat{\mathbf{d}} : \widehat{\mathbf{d}}}\, dA \leq \sqrt{4\pi r^2} \sqrt{\int_{\mathcal{B}(r)} \widehat{\mathbf{d}} : \widehat{\mathbf{d}}\, dA} \tag{A.21}$$

and therefore, it results in

$$\widehat{\Pi}_{\mathrm{hom}}(D_{\mathrm{eq}}, \theta_{\mathrm{D}}) \leq \breve{\Pi}_{\mathrm{hom}}(D_{\mathrm{eq}}) \tag{A.22}$$

with

$$\breve{\Pi}_{\mathrm{hom}}(D_{\mathrm{eq}}) = \sqrt{\frac{2}{3}} \frac{\sigma_0}{|\Omega|} \left[\int_{R_{\mathrm{i}}}^{R_{\mathrm{e}}} \left(\sqrt{4\pi r^2} \sqrt{\int_{\mathcal{B}(r)} \widehat{\mathbf{d}} : \widehat{\mathbf{d}}\, dA} \right) dr + 3\kappa p |\Omega| \sqrt{\lambda_{\mathcal{I}}} \right] \tag{A.23}$$

where

$$\lambda_{\mathcal{I}} = \frac{1}{4\pi R_{\mathrm{i}}^2} \int_{\partial\Omega_{\mathrm{i}}} \widehat{\mathbf{d}}^{\mathcal{I}} : \widehat{\mathbf{d}}^{\mathcal{I}}\, dA \tag{A.24}$$

A further use of the Cauchy-Schwartz inequality for the radial-coordinate integral in Eq. (A.22) produces

$$\breve{\Pi}_{\mathrm{hom}}(D_{\mathrm{eq}}) \leq \widetilde{\Pi}_{\mathrm{hom}}(D_{\mathrm{eq}}) \tag{A.25}$$

with

$$\widetilde{\Pi}_{\mathrm{hom}}(D_{\mathrm{eq}}) = \sqrt{\frac{2}{3}} \sigma_0 \left[(1-p) \sqrt{\lambda_{\mathrm{s}}} + 3\kappa p \sqrt{\lambda_{\mathcal{I}}} \right] \tag{A.26}$$

and where

$$\lambda_{\mathrm{s}} = \frac{1}{|\Omega_{\mathrm{s}}|} \int_{\Omega_{\mathrm{s}}} \widehat{\mathbf{d}} : \widehat{\mathbf{d}}\, d\Omega \tag{A.27}$$

It is worth observing that both λ_{s} and $\lambda_{\mathcal{I}}$ depend on the choice of function $\chi(r)$. Moreover, as proven in Gurson (1977), $\breve{\Pi}_{\mathrm{hom}}$ and thereby $\widetilde{\Pi}_{\mathrm{hom}}$ do not depend on the strain-rate Lode angle θ_{D}. Accordingly, the corresponding macroscopic stress estimate results in (see Eq. (A.12))

$$\widetilde{\boldsymbol{\Sigma}}^{\ell} = \frac{2}{3} \frac{1}{D_{\mathrm{eq}}} \frac{\partial \widetilde{\Pi}_{\mathrm{hom}}}{\partial D_{\mathrm{eq}}} \mathbf{D} = \frac{2}{3} \frac{1}{D_{\mathrm{eq}}} \widetilde{\Sigma}_{\mathrm{eq}}^{\ell}\, \mathbf{D} \tag{A.28}$$

where $\widetilde{\Sigma}_{\mathrm{eq}}^{\ell}$ is an upper-bound deviatoric macroscopic strength measure.

Aiming to furnish a consistent and effective estimate for the macroscopic support function in Eq. (A.10), function $\chi(r)$ has to minimise $\lambda_{\mathrm{s}}(\chi)$ and $\lambda_{\mathcal{I}}(\chi)$, as well as it has to comply with kinematic admissibility conditions (A.15). The first requirement results in a standard problem of variational calculus and leads to the following differential equation

$$\chi^{IV}(r) - \frac{12}{r^2} \chi^{II}(r) + \frac{24}{r^3} \chi^{I}(r) = 0 \tag{A.29}$$

whose solution is:

$$\chi(r) = C_1 + C_2 \frac{R_{\mathrm{e}}^2}{r^2} + C_3 \frac{r^3}{R_{\mathrm{e}}^3} + C_4 \frac{r^5}{R_{\mathrm{e}}^5} \tag{A.30}$$

where C_1, C_2, C_3 and C_4 are some integration constants. These latter, due to the kinematic admissibility in Eq. (A.15), have to satisfy

$$C_1 = -\frac{1}{2}(5C_3 + 7C_4), \qquad C_2 = \frac{1}{2}(3C_3 + 5C_4) \tag{A.31}$$

Therefore, C_3 and C_4 can be considered as free model parameters to employ for seeking the best possible estimate for the infimum in Eq. (A.10). In detail, by replacing Eqs. (A.30) and (A.31) into Eq. (A.26), function $\widetilde{\Pi}_{\mathrm{hom}} = \widetilde{\Pi}_{\mathrm{hom}}(C_3, C_4)$ can be minimized with respect to C_3 and C_4.

It is worth remarking that such an optimization strategy can not be performed with classical trial velocity fields, which result to be completely defined via strain-rate boundary conditions only, such the one proposed by Gurson (1977) and used in Dormieux and Kondo (2010) (namely, Eq. (A.13) with $\chi(r) = 0$).

Accordingly, the optimal values C_3^{opt} and C_4^{opt} are obtained as

$$\begin{aligned} C_3^{\mathrm{opt}} &= -R_{\mathrm{i}}^3 \frac{100 - 84p^{2/3} + 19p^{7/3}}{2\Delta} \\ C_4^{\mathrm{opt}} &= 30R_{\mathrm{i}}^3 \frac{1 - p^{2/3}}{\Delta} \end{aligned} \tag{A.32}$$

where $\Delta = 48 + 225p^{2/3} - 336p^{5/3} + 200p + 38p^{10/3}$.

By replacing Eqs. (A.32) into Eq. (A.28) and in the framework of small values of p, the following closed-form upper bound of the macroscopic deviatoric strength measure (denoted as BDKV) is obtained

$$\begin{aligned} \frac{\widetilde{\Sigma}_{\mathrm{eq}}^{\ell}}{\sigma_0} = 1 &- \left(\frac{4}{3} - \kappa\sqrt{15}\right)p + \left(\frac{41}{12} - \frac{25}{6}\kappa\sqrt{15}\right)p^2 + \\ &- \left(\frac{35}{6} - \frac{28}{3}\kappa\sqrt{15}\right)p^{8/3} + \mathrm{O}(p^3) \end{aligned} \tag{A.33}$$

With reference to the proposed result, the following observations can be stated:

- By enforcing $\chi = 0$ in the estimate $\breve{\Pi}_{\mathrm{hom}}$ of Eq. (A.22), the upper-bound strength measure proposed by Dormieux and Kondo (2010) (denoted in the following as DK) is recovered, resulting in

$$\frac{\Sigma_{\mathrm{eq}}^{\mathrm{DK}}}{\sigma_0} = 1 - \left(1 - \frac{3\sqrt{15}}{5}\kappa\right)p \tag{A.34}$$

  that, in the case of negligible interface effects (namely, $\kappa = 0$) corresponds to the Gurson's description Gurson (1977);

- Equation (A.33), truncated at the first order in p and for $\kappa = 0$, recovers the strength estimate obtained via a variational procedure by Ponte Castañeda (1991).

Model sensitivity to porosity p and void-size effect parameter κ is addressed in Figs. A.2 and A.3. As expected, results shown in Fig. A.2 highlight that the macroscopic deviatoric

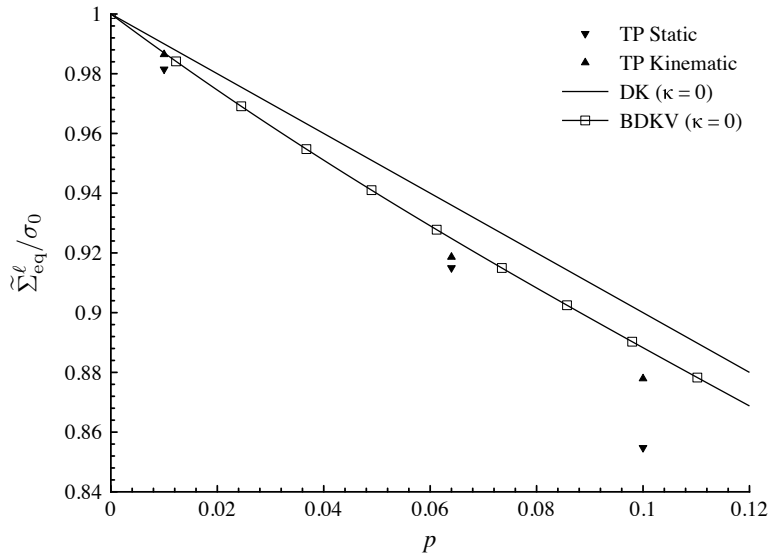

(a)

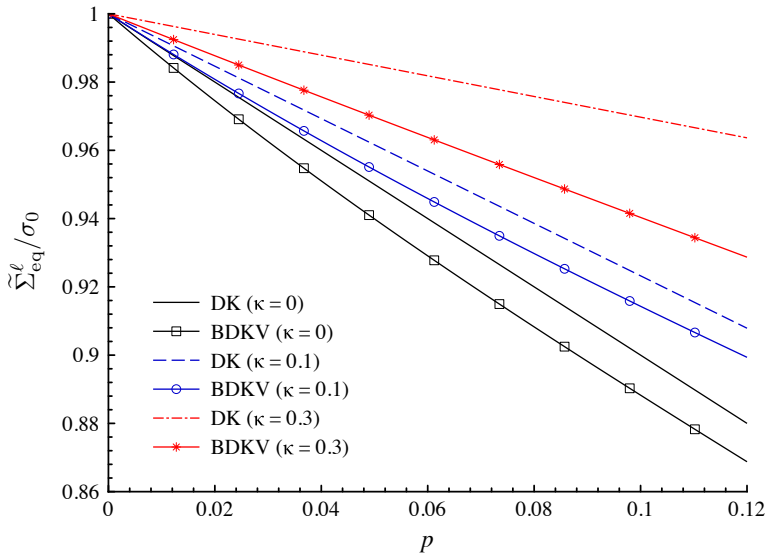

(b)

Figure A.2 – Normalised deviatoric strength estimate $\widetilde{\Sigma}^{\ell}_{\mathrm{eq}}/\sigma_0$ as a function of the porosity p for different values of κ. (a) Assessment with respect to ($\kappa = 0$): static and kinematic numerical bounds (TP Trillat and Pastor (2005)); DK model Dormieux and Kondo (2010); Gurson (1977). (b) Void-size effects and comparison with respect to the DK model.

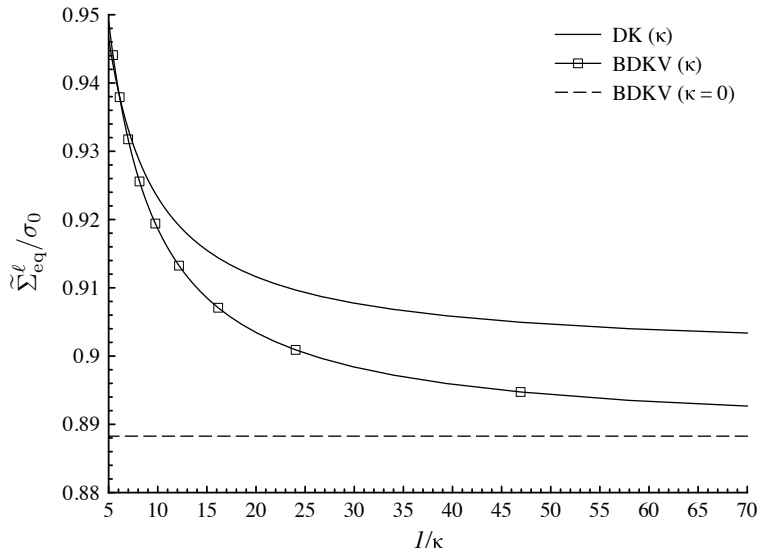

Figure A.3 – Normalised deviatoric strength estimate $\widetilde{\Sigma}^{\ell}_{\mathrm{eq}}/\sigma_0$ as a function of the void-size parameter κ ($1/\kappa$ resulting proportional to the void radius R_{i}) for $p = 0.1$. Comparison with respect to the DK model Dormieux and Kondo (2010); Gurson (1977).

strength estimate reduces when p increases. The influence of void-size effects is addressed in Figs. A.2b and A.3, resulting in an improvement of the material strength when the size of void reduces (that is, for large values of κ). Such an occurrence is qualitatively in agreement with well-established experimental Biener et al. (2005, 2006); Hakamada and Mabuchi (2007) and numerical (e.g., Brach et al., 2016a; Zhao et al., 2009) evidence.

Aiming to assess the effectiveness of the proposed strength estimate, comparisons with both theoretical and numerical benchmarks are also provided for different values of parameters p and κ. In detail, reference is made to the theoretical predictions obtained via Eq. (A.34) Dormieux and Kondo (2010); Gurson (1977) and to finite-element-based static and kinematic limit-analysis computations provided in Trillat and Pastor (2005) (these latter, available only in the case of $\kappa = 0$ and denoted as TP data). It is observed that, although the proposed deviatoric strength is an upper bound of the exact one, BDKV-based results improve the DK estimate, resulting in lower values and thereby in a more accurate estimate of deviatoric strength properties for porous ($\kappa = 0$) and nanoporous ($\kappa > 0$) materials.

A.5 Concluding remarks

In this Appendix, an upper-bound estimate of the macroscopic deviatoric strength of a hollow sphere, representative of a particular microstructure for porous and nanoporous materials, has been determined in the case of an axisymmetric deviatoric strain-rate condition and via a kinematic limit analysis approach. The hollow sphere has been assumed to be comprised of a rigid ideal-plastic material, obeying to a von Mises strength criterion. Void-size effects associated to the possible void nanoscale Biener et al. (2005, 2006);

Hakamada and Mabuchi (2007) have been accounted for via a coherent and imperfect homogeneous interface at the cavity boundary. The local kinematics at the limit state has been estimated by introducing a suitable trial velocity field, in agreement with findings in Budiansky et al. (1982) (see also Zhu and Zbib, 1993) and allowing for an optimization procedure.

With respect to the current state-of-the-art, proposed results furnish the following novel and original contributions:

- an effective description of void-size effects, resulting in an increase of the predicted macroscopic deviatoric strength as the void radius decreases, qualitatively in agreement with available experimental Biener et al. (2005, 2006); Hakamada and Mabuchi (2007) and numerical Brach et al. (2016a); Zhao et al. (2009) evidence;
- an improvement of limit-analysis based estimates Dormieux and Kondo (2010); Gurson (1977), resulting in a more effective description of the macroscopic deviatoric strength for porous and nanoporous materials.

References

Arico, A.S., Bruce, P., Scrosati, B., Tarascon, J.M., & Van Schalkwijk, W. (2005). Nanostructured materials for advanced energy conversion and storage devices. *Nature materials*, 4, 366-377.

Biener, J., Hodge, A.M., Hamza, A.V., Hsiung, L.M., & Satcher, J.H. (2005). Nanoporous Au: A high yield strength material. *Journal of Applied Physics*, 97, 024301.

Biener, J., Hodge, A.M., Hayes, J.R., Volkert, C.A., Zepeda-Ruiz, L.A., Hamza, A.V., & Abraham, F.F. (2006). Size Effects on the Mechanical Behaviour of Nanoporous Au. *Nano Letters*, 6, 2379-2382.

Brach, S., Dormieux, L., Kondo, D., & Vairo, G. (2016). A computational insight into void-size effects on strength properties of nanoporous materials. *Mechanics of Materials*, 101, 102-117.

Brach, S., Dormieux, L., Kondo, D., & Vairo, G. (2016). Strength properties of nanoporous materials: a 3-layered based non-linear homogenization approach with interface effects. Submitted.

Brach, S., Dormieux, L., Kondo, D., & Vairo, G. (2016). Deviatoric Strength of nanoporous materials: a limit analysis approach. In: Frémond, M., Maceri, F., Vairo, G. (Eds.), *Models, Simulation, and Experimental Issues in Structural Mechanics*, Springer Series in Solid and Structural Mechanics, DOI: 10.1007/978-3-319-48884-4.

Budiansky, B., Hutchinson, J. W., & Slutsky, S. (1982). Void growth and collapse in viscous solids. In: Hopkins, H.G., Sewell, M.J. (Eds.), *Mechanics of Solids*, The Rodney Hill 60th Anniversary Volume, pp. 13–45. Oxford: Pergamon Press.

Dormieux, L., & Kondo, D. (2010). An extension of Gurson model incorporating interface stress effects. *International Journal of Engineering Science*, 48, 575-581.

Dormieux, L., & Kondo, D. (2013). Non linear homogenization approach of strength of nanoporous materials with interface effects. *International Journal of Engineering Science*, 71, 102-110.

Duan, H.L., Wang, J., Huang, Z.P., & Luo, Z.Y. (2005). Stress concentration tensors of inhomogeneities with interface effects. *Mechanics of Materials*, 37, 723-736.

Duan, H.L., Wang, J., Huang, Z.P., & Karihaloo, B.L. (2005). Size-dependent effective elastic constants of solids containing nano-inhomogeneities with interface stress. *Journal of the Mechanics and Physics of Solids*, 53, 1574-1596.

Goudarzi, T., Avazmohammadi, R., & Naghdabadi, R. (2010). Surface energy effects on the yield strength of nanoporous materials containing nanoscale cylindrical voids. *Mechanics of Materials*, 42, 852-862.

Gurson, A.L. (1977). Continuum theory of ductile rupture by void nucleation and growth: Part I. - Yield criterion and flow rules for porous ductile media. *Journal of Engineering Materials and Technology*, 99, 2-15.

Gurtin, M.E., & Murdoch, A.I. (1975). A continuum theory of elastic material surfaces. *Archive for Rational Mechanics and Analysis*, 57, 291-323.

Gurtin, M.E., & Murdoch, A.I. (1978). Surface stress in solids. *International Journal of Solids and Structures*, 14, 431-440.

Hakamada, M., & Mabuchi, M. (2007). Mechanical strength of nanoporous gold fabricated by dealloying. *Scripta Materialia*, 56, 1003-1006.

Jenkins, S.B. (2010). Nanoporous Materials: Types, Properties, and Uses. *Nova Science Publishers*.

Lu, G.Q., Zhao, X.S., & Wei, T.K. (2004). Nanoporous materials: science and engineering. *Imperial College Press*.

Mi, C., Buttry, D.A., Sharma, P., & Kouris, D.A. (2011). Atomistic insights into dislocation-based mechanisms of void growth and coalescence. *Journal of the Mechanics and Physics of Solids*, 59, 1858-1871.

Monchiet, V., & Bonnet, G. (2010). Interfacial models in viscoplastic composites materials. *International Journal of Engineering Science*, 48, 1762-1768.

Moshtaghin, A.F., Naghdabadi, R., & Asghari, M. (2008). Effects of surface residual stress and surface elasticity on the overall yield surfaces of nanoporous materials with cylindrical nanovoids. *Mechanics of Materials*, 51, 74-87.

Needs, R.J., Godfrey, M.J., & Mansfield, M. (1991). Theory of surface stress and surface reconstruction. *Surface Science*, 242, 215-221.

Ponte Castañeda, P. (1991). The effective mechanical properties of nonlinear isotropic composites. *Journal of the Mechanics and Physics of Solids*, 39, 45-71.

Povstenko, Yu. Z. (1993). Theoretical investigation of phenomena caused by heterogeneous surface tension in solids. *Journal of the Mechanics and Physics of Solids*, 41, 1499-1514.

Salençon, J., (1983). Calcul à la rupture et analyse limite. *Presses de l'ENPC*.

Trillat, M., & Pastor, J. (2005). Limit analysis and Gurson's model. *European Journal of Mechanics A/Solids*, 24, 800-819.

Traiviratana, S., Bringa, E.M., Benson, D.J., & Meyers, M.A. (2008). Void growth in metals: Atomistic calculations. *Acta Materialia*, 56, 3874-3886.

Wang, J., Huang, Z., Duan, H., Yu, S., Feng, X., Wang, G., Zhang, W., & Wang, T. (2011). Surface stress effect in mechanics of nanostructured materials. *Acta Mechanica Solida Sinica*, 52-82.

Zhang, W., & Wang, T.J. (2007). Effect of surface energy on the yield strength of nanoporous materials. *Applied Physics Letters*, 90, 063104.

Zhang, W., Wang, T.J., & Chen, X. (2008). Effect of surface stress on the asymmetric yield strength of nanowires. *Journal of Applied Physics*, 103, 123527.

Zhang, W., Wang, T.J., & Chen, X. (2010). Effect of surface/interface stress on the plastic deformation of nanoporous materials and nanocomposites. *International Journal of Plasticity*, 26, 957-975.

Zhao, K.J., Chen, C.Q., Shen, Y.P., & Lu, T.J. (2009). Molecular dynamics study on the nano-void growth in face-centered cubic single crystal copper. *Computational Materials Science*, 46, 749-754.

Zhu, H.T., & Zbib, H.M. (1993). A continuum model for flow strength of metal-matrix composites. *Scripta Metallurgica et Materialia*, 28, 1323-1328.

General Bibliography

Adiga, S. P., Jin, C., Curtiss, L. A., Monteiro-Riviere, N. A., & Narayan, R. J. (2009). Nanoporous membranes for medical and biological applications. *Wiley Interdisciplinary Reviews: Nanomedicine and Nanobiotechnology*, 1, 568-581.

Allen, M.P., & Tildesley, D.J. (1991). *Computer Simulation of Liquids*. Clarendon Press Oxford.

Amelang, J.S., & Kochmann, D.M. (2015). Surface effects in nanoscale structures investigated by a fully-nonlocal energy-based quasicontinuum method. *Mechanics of Materials*, 90, 166-184.

Anoukou, K., Pastor, F., Dufrenoy, P., & Kondo, D. (2016). Limit analysis and homogenization of porous materials with Mohr–Coulomb matrix. Part I: Theoretical formulation. *Journal of the Mechanics and Physics of Solids*, 91, 145-171.

Arico, A. S., Bruce, P., Scrosati, B., Tarascon, J. M., & Van Schalkwijk, W. (2005). Nanostructured materials for advanced energy conversion and storage devices. *Nature materials*, 4, 366-377.

Benallal, A., Desmorat, R., & Fournage, M. (2014). An assessment of the role of the third stress invariant in the Gurson approach for ductile fracture. *European Journal of Mechanics-A/Solids*, 47, 400-414.

Biener, J., Hodge, A.M., Hamza, A.V., Hsiung, L.M., & Satcher, J.H. (2005). Nanoporous Au: A high yield strength material. *Journal of Applied Physics*, 97, 024301.

Biener, J., Hodge, A.M., Hayes, J.R., Volkert, C.A., Zepeda-Ruiz, L.A., Hamza, A.V., & Abraham, F.F. (2006). Size Effects on the Mechanical Behaviour of Nanoporous Au. *Nano Letters*, 6, 2379-2382.

Bigoni, D. (2012). Nonlinear solid mechanics: bifurcation theory and material instability. Cambridge University Press.

Bigoni, D., & Piccolroaz, A., (2004). Yield criteria for quasibrittle and frictional materials. *International Journal of Solids and Structures*, 41, 2855-2878.

Bilger, N., Auslender, F., Bornert, M., & Masson, R. (2002). New bounds and estimates for porous media with rigid perectly plastic matrix. *Compte Rendu Mécanique*, 330, 127-132.

Boehler, J. P. (Ed.). (1987). *Applications of tensor functions in solid mechanics*, Springer.

Borg, U., Niordson, C.F., & Kysar, J.W. (2008). Size effects on void growth in single crystals with distributed voids. *International Journal of Plasticity*, 24, 688-701.

Brach, S., Dormieux, L., Kondo, D., & Vairo, G. (2016). Strength properties of nanoporous materials: a 3-layered based non-linear homogenization approach with interface effects. Submitted.

Brach, S., Dormieux, L., Kondo, D., & Vairo, G. (2016). A computational insight into void-size effects on strength properties of nanoporous materials. *Mechanics of Materials*, 101, 102-117.

Brach, S., Dormieux, L., Kondo, D., & Vairo, G. (2016). Nanoporous materials with a general isotropic plastic matrix: exact limit state under isotropic loadings. *International Journal of Plasticity*, DOI: 10.1016/j.ijplas.2016.10.007.

Brach, S., Anoukou, K., Kondo, D., & Vairo, G. (2016). Nanoporous materials with a general isotropic plastic matrix: Limit analysis and homogenization under axisymmetric loadings. Submitted.

Brach, S., Dormieux, L., Kondo, D., & Vairo, G. (2016). Deviatoric Strength of nanoporous materials: a limit analysis approach. In: Frémond, M., Maceri, F., Vairo, G. (Eds.), *Models, Simulation, and Experimental Issues in Structural Mechanics*, Springer Series in Solid and Structural Mechanics, DOI: 10.1007/978-3-319-48884-4.

Bringa, E.M., Traiviratana, S., & Meyers, M.A. (2010). Void initiation in fcc metals: Effects of loading orientation and nanocrystalline effects. *Acta Materialia*, 58, 4458-4477.

Brisard, S., Dormieux, L., & Kondo, D. (2010). Hashin-Shtrikman bounds on the bulk modulus of a nanocomposite with spherical inclusions and interface effects. *Computational Materials Science*, 48, 589-596.

Brisard, S., Dormieux, L., & Kondo, D. (2010). Hashin-Shtrikman bounds on the shear modulus of a nanocomposite with spherical inclusions and interface effects. *Computational Materials Science*, 50, 403-410.

Buryachenko, V. (1993). Effective strength properties of elastic physically nonlinear composites. *Mecamat*, 93, 567-578.

Budiansky, B., Hutchinson, J. W., & Slutsky, S. (1982). Void growth and collapse in viscous solids. In: Hopkins, H.G., Sewell, M.J. (Eds.), *Mechanics of Solids*, The Rodney Hill 60th Anniversary Volume, pp. 13–45. Oxford: Pergamon Press.

Cammarata, R.C. (1994). Surface and interface stress effects in thin films. *Progress in Surface Science*, 46, 1-38.

Cazacu, O., Revil-Baudard, B., Chandola, N., & Kondo, D. (2014). New analytical criterion for porous solids with Tresca matrix under axisymmetric loadings. *International Journal of Solids and Structures*, 51, 861-874.

Chen, Y., Gerald, J. F., Chadderton, L. T., & Chaffron, L. (1999). Nanoporous carbon produced by ball milling. *Applied physics letters*, 74, 2782-2784.

Cheng, I. C., & Hodge, A. M. (2013). Strength scale behavior of nanoporous Ag, Pd and Cu foams. *Scripta Materialia*, 69, 295-298.

Corigliano, A., Mariani, S., & Orsatti, B. (2000). Identification of Gurson-Tvergaard material model parameters via Kalman filtering technique. I. Theory. *International journal of fracture*, 104, 4, 349-373.

Dai, Z., & Ju, H. (2012). Bioanalysis based on nanoporous materials. *Trends in Analytical Chemistry*, 39, 149-162.

Daw, M.S., & Baskes, M.I. (1984). Embedded-atom method: derivation and application to impurities, surfaces and other defects in metals. *Physical Review B*, 29, 6443-6453.

de Buhan, P. (1986). Approach fondamentale du calcul à la rupture des ouvrages en sols renforcés. Thèse d'État. Paris VI.

Ding, Y., & Zhang, Z. (2016). Nanoporous Metals for Advanced Energy Technologies. *Springer*.

Dormieux, L., & Kondo, D. (2010). An extension of Gurson model incorporating interface stress effects. *International Journal of Engineering Science*, 48, 575-581.

Dormieux, L., & Kondo, D. (2013). Non linear homogenization approach of strength of nanoporous materials with interface effects. *International Journal of Engineering Science*, 71, 102-110.

Dormieux, L., Kondo, D., & Ulm, F.-J. (2006). *Microporomechanics*. Chichester: J. Wiley & Sons.

Drucker, D.C., Prager, W., & Greenberg, H.J., (1952). Extended limit design theorems for continuous media. *The Quarterly of Applied Mathematics*, 9, 381-389.

Duan, H.L., Wang, J., Huang, Z.P., & Luo, Z.Y. (2005). Stress concentration tensors of inhomogeneities with interface effects. *Mechanics of Materials*, 37, 723-736.

Duan, H.L., Wang, J., Huang, Z.P., & Karihaloo, B.L. (2005). Size-dependent effective elastic constants of solids containing nano-inhomogeneities with interface stress. *Journal of the Mechanics and Physics of Solids*, 53, 1574-1596.

Erb, U., El-Sherik, A. M., Palumbo, G., & Aust, K. T. (1993). Synthesis, structure and properties of electroplated nanocrystalline materials. *Nanostructured Materials*, 2, 383-390.

Fan, H. L., & Fang, D. N. (2009). Modeling and limits of strength of nanoporous foams. *Materials & Design*, 30, 1441-1444.

Farrissey, L., Ludwig, M., McHugh, P.E., & Schmauder, S., (2000). An atomistic study of void growth in single crystalline copper. *Computational Materials Science*, 18, 102-117.

Feng, G., Cheng, Y., Wang, S. Y., Hsu, L. C., Feliz, Y., Borca-Tasciuc, D. A., & Moraru, C. I. (2014). Alumina surfaces with nanoscale topography reduce attachment and biofilm formation by Escherichia coli and Listeria spp. *Biofouling*, 30, 1253-1268.

Fritzen, F., Forest, S., Böhlke, T., Kondo, D., & Kanit, T. (2012). Computational homogenization of elasto-plastic porous metals. *International Journal of Plasticity*, 29, 102-119.

Gibbs, J W. (1906). *The scientific papers of J. Willard Gibbs* (Vol.1). London, New York & Bombay: Longmans, Green and Company.

Gleiter, H. (2000). Nanostructured materials: basic concepts and microstructure. *Acta materialia*, 48, 1-29.

Gologanu, M., Leblond, J.-B., & Devaux, J., (1993). Approximate models for ductile metals containing non-spherical voids - case of axisymmetric prolate ellipsoidal cavities. *Journal of the Mechanics Physics and Solids*, 41, 1723-1754.

Gologanu, M., Leblond, J.B., Perrin, G., & Devaux, J., (1994). Approximate models for ductile metals containing non-spherical voids - case of axisymmetric oblate ellipsoidal cavities. *Journal of Engineering Materials and Technology*, 116, 290-297.

Gologanu, M., Leblond, J.B., Perrin, G., & Devaux, J., (1997). Recent extensions of Gurson's model for porous ductile metals. In: Suquet, P. (Ed.), *Continuum Micromechanics*. Springer-Verlag.

Goudarzi, T., Avazmohammadi, R., & Naghdabadi, R. (2010). Surface energy effects on the yield strength of nanoporous materials containing nanoscale cylindrical voids. *Mechanics of Materials*, 42, 852-862.

Guo, T., Faleskog, J., & Shih, C., (2008). Continuum modelling of a porous solid with pressure-sensitive dilatant matrix. *Journal of Mechanics and Physics of Solids*, 56, 2188-2212.

Gurson, A.L. (1977). Continuum theory of ductile rupture by void nucleation and growth: Part I. - Yield criterion and flow rules for porous ductile media. *Journal of Engineering Materials and Technology*, 99, 2-15.

Gurtin, M.E., & Murdoch, A.I. (1975). A continuum theory of elastic material surfaces. *Archive for Rational Mechanics and Analysis*, 57, 291-323.

Gurtin, M.E., & Murdoch, A.I. (1978). Surface stress in solids. *International Journal of Solids and Structures*, 14, 431-440.

Hakamada, M., & Mabuchi, M. (2007). Mechanical strength of nanoporous gold fabricated by dealloying. *Scripta Materialia*, 56, 1003-1006.

Han, X., Besson, J., Forest, S., Tanguy, B., & Bugat, S. (2013). A yield function for single crystals containing voids. *International Journal of Solids and Structures*, 50, 2115-2131.

Hashin, Z. (1962). The elastic moduli of heterogeneous materials. *Journal of Applied Mechanics*, 29, 143-150.

Haythornthwaite, R.M. (1985). A family of smooth yield surfaces. *Mechanics research communications*, 12(2), 87-91.

Herve, E., & Zaoui, A. (1993). n-Layered inclusion-based micromechanical modelling. *International Journal of Engineering Science*, 31, 1-10.

Higginbotham, A., Bringa, E.M., Marian, J., Park, N., Suggit, M., & Wark, J.S. (2011). Simulations of copper single crystals subjected to rapid shear. *Journal of Applied Physics*, 109, 063530.

Hill, R. (1948). A theory of the yielding and plastic flow of anisotropic metals. *In Proceedings of the Royal Society of London A: Mathematical, Physical and Engineering Sciences*, 193, 281-297.

Hodge, A. M., Biener, J., Hayes, J. R., Bythrow, P. M., Volkert, C. A., & Hamza, A. V. (2007). Scaling equation for yield strength of nanoporous open-cell foams. *Acta Materialia*, 55, 1343-1349.

Honeycutt, J.D., & Andemen, H.C. (1987). Molecular Dynamics Study of Melting and Freezing of Small Lennard-Jones Clusters. *The Journal of Physical Chemistry*, 91, 4950-4963.

Horstemeyer, M.F., Baskes, M.I., & Plimpton, S.J. (2001). Length scale and time scale effects on the plastic flow of FCC metals. *Acta Materalia*, 49, 4363-4374.

Huang, M., Li, Z., & Wang, C. (2005). Coupling effects of void size and void shape on the growth of prolate ellipsoidal microvoid. *Acta Mechanica Sinica*, 21, 272-277.

Hull, D., & Bacon, D.J. (2001). *Introduction to Dislocations*. Butterworth-Heinemann.

Jenkins, S.B. (2010). Nanoporous Materials: Types, Properties, and Uses. *Nova Science Publishers*, 2010.

Kärger, J., Ruthven, D. M., & Theodorou, D. N. (2012). Diffusion in nanoporous materials. *John Wiley & Sons*.

Kelchner, C.L., Plimpton, S.J., & Hamilton, J.C. (1998). Dislocation nucleation and defect structure during surface indentation. *Physical Review B*, 58, 11085.

Khan, A.S., & Huang, S., (1995). *Continuum Theory of Plasticity*. John Wiley & Sons, New York.

Koch, C. C., & Cho, Y. S. (1992). Nanocrystals by high energy ball milling. *Nanostructured Materials*, 1, 207-212.

Kreher, W. (1990). Residual stresses and stored elastic energy of composites and polycrystals. *Journal of the Mechanics and Physics of Solids*, 38, 115-128.

Kumeria, T., Rahman, M. M., Santos, A., Ferré-Borrull, J., Marsal, L. F., & Losic, D. (2014). Nanoporous anodic alumina rugate filters for sensing of ionic mercury: Toward environmental point-of-analysis systems. *ACS applied materials & interfaces*, 6, 12971-12978.

Kustandi, T. S., Loh, W. W., Gao, H., & Low, H. Y. (2010). Wafer-scale near-perfect ordered porous alumina on substrates by step and flash imprint lithography. *American Chemical Society nano*, 4, 2561-2568.

Lang, X., Hirata, A., Fujita, T., & Chen, M. (2011). Nanoporous metal/oxide hybrid electrodes for electrochemical supercapacitors. *Nature Nanotechnology*, 6, 232-236.

Lee, J. H. (2009). Gas sensors using hierarchical and hollow oxide nanostructures: overview. *Sensors and Actuators B: Chemical*, 140, 319-336.

Le Quang, H., & He, Q. C. (2007). Size-dependent effective thermoelastic properties of nanocomposites with spherically anisotropic phases. *Journal of the Mechanics and Physics of Solids*, 55, 1899-1931.

Le Quang, H., & He, Q. C. (2008). Variational principles and bounds for elastic inhomogeneous materials with coherent imperfect interfaces. *Mechanics of Materials*, 40, 865-884.

Leblond, J.-B., Perrin, G., & Suquet, P. (1994). Exact results and approximate models for porous viscoplastic solids. *International Journal of Plasticity*, 10, 213-235.

Lemarchand, E., Dormieux, L., & Kondo, D. (2015). Lode's angle effect on the definition of the strength criterion of porous media. *International Journal for Numerical and Analytical Methods in Geomechanics*, 39(14), 1506-1526.

Levenberg, K. (1944). A Method for the Solution of Certain Problems in Least-Squares. *Quarterly of Applied Mathematics*, 2, 164-168.

Li, Z., & Huang, M. (2005). Combined effects of void shape and void size-oblate spheroidal microvoid embedded in infinite non-linear solid. *International Journal of Plasticity*, 21, 625-650.

Lu, G. Q., & Zhao, X. S. (2004). Nanoporous materials: science and engineering. *World Scientific*.

Lubarda, V.A., (2011). Emission of dislocations from nanovoids under combined loading. *International Journal of Plasticity*, 27, 181-200.

Lubarda, V.A., Schneider, M.S., Kalantar, D.H., Remington, B.A., & Meyers, M.A., 2004. Void growth by dislocation emission. *Acta Materialia*, 52, 1397-1408.

Lubliner, J. (2008). *Plasticity Theory*. Dover Publications Inc., Mineola, New York.

Luton, M. J., Jayanth, C. S., Disko, M. M., Matras, S., & Vallone, J. (1988). Cryomilling of nano-phase dispersion strengthened aluminum. *MRS Proceedings*, 132, 79.

Marian, J., Knap, J., & Ortiz, M., (2004). Nanovoid Cavitation by Dislocation Emission in Aluminum. *Physical Review*, 93.

Marian, J., Knap, J., & Ortiz, M., (2005). Nanovoid deformation in aluminum under simple shear. *Acta Materialia*, 53, 2893-2900.

Mariani, S., & Corigliano, A. (2001). Anisotropic behaviour of porous, ductile media. *International Journal of Solids and Structures*, 38, 2427-2451.

Marquardt, D. (1963). An Algorithm for Least-Squares Estimation of Nonlinear Parameters. *SIAM Journal on Applied Mathematics*, 11, 431-441.

Mbiakop, A., Constantinescu, A., & Danas, K. (2015). An analytical model for porous single crystals with ellipsoidal voids. *Journal of the Mechanics and Physics of Solids*, 84, 436-467.

Menetrey, P.H., & Willam, K.J. (1995). Triaxial Failure Criterion for Concrete and Its Generalization. *ACI Structural Journal*, 92, 311-318.

Mi, C., Buttry, D.A., Sharma, P., & Kouris, D.A. (2011). Atomistic insights into dislocation-based mechanisms of void growth and coalescence. *Journal of the Mechanics and Physics of Solids*, 59, 1858-1871.

Michel, J.C., & Suquet, P. (1992). The constitutive law of nonlinear viscous and porous materials. *Journal of the Mechanics and Physics of Solids*, 40(4), 783-812.

Mishin, Y., Farkas, D., Mehl, M.J., & Papaconstantopoulos D.A. (1999). Interatomic potentials for monoatomic metals from experimental data and ab initio calculations. *Physical Review B*, 59, 3393.

Monchiet, V., & Bonnet, G. (2010). Interfacial models in viscoplastic composites materials. *International Journal of Engineering Science*, 48, 1762-1768.

Monchiet, V., Cazacu, O., Charkaluk, E., & Kondo, D. (2008). Macroscopic yield criteria for plastic anisotropic materials containing spheroidal voids. *International Journal of Plasticity*, 24, 1158-1189.

Monchiet, V., & Kondo, D. (2012). Exact solution of a plastic hollow sphere with a Mises-Schleicher matrix. *International Journal of Engineering Science*, 51, 168-178.

Monchiet, V., & Kondo, D. (2013). Combined voids size and shape effects on the macroscopic criterion of ductile nanoporous materials. *International Journal of Plasticity*, 43, 20-41.

Morin, L., Kondo, D., & Leblond, J.-B. (2015). Numerical assessment, implementation and application of an extended Gurson model accounting for void size effects. *European Journal of Mechanics A/Solids*, 51, 183-192.

Moshtaghin, A.F., Naghdabadi, R., & Asghari, M. (2008). Effects of surface residual stress and surface elasticity on the overall yield surfaces of nanoporous materials with cylindrical nanovoids. *Mechanics of Materials*, 51, 74-87.

Murr, L.E. (1975). *Interfacial Phenomena in Metals and Alloys*. London: Addison-Wesley.

Needs, R.J., Godfrey, M.J., & Mansfield, M. (1991). Theory of surface stress and surface reconstruction. *Surface Science*, 242, 215-221.

Oliveira, B.F., da Cunda, L.A., Öchsner, A., & Creus, G.J. (2010). Computational Analysis of Loading–Unloading and Non-homogeneity Effects in Metallic Hollow Sphere Structures. *In Materials with Complex Behaviour*, 83-97.

Orowan, E. (1970). Surface energy and surface tension in solids and liquids. *Proceedings of the Royal Society of London A*, 316, 473-491.

Ozdemir, S., & Gole, J. L. (2007). The potential of porous silicon gas sensors. *Current Opinion in Solid State and Materials Science*, 11, 92-100.

Paux, J., Morin, L., Brenner, R., & Kondo, D. (2015). An approximate yield criterion for porous single crystals. *European Journal of Mechanics-A/Solids*, 51, 1-10.

Pearson, J. (2009). Computation of Hypergeometric Functions. Master's thesis. Worcester College, University of Oxford.

Perrin, G. (1992). Contribution à l'étude théorique et numérique de la rupture ductile des métaux. Thèse de doctorat, Ecole Polytechnique.

Pinnavaia, T. J., & Thorpe, M. F. (2006). Access in nanoporous materials. *Springer Science & Business Media*.

Plimpton, S.J. (1995). Fast parallel algorithms for short-range molecular dynamics. *Journal of Computational Physics*, 117, 1-19.

Podgórski, J. (1985). Limit state condition and the dissipation function for isotropic materials. *Archives of Mechanics*, 36, 322-342.

Podgórski, J. (1985). General failure criterion for isotropic media. *Journal of Engineering Mechanics*, 111, 188-201.

Pogorelko, V.V., & Mayer, A.E. (2016). Influence of titanium and magnesium nanoinclusions on the strength of aluminum at high-rate tension: Molecular dynamics simulations. *Materials Science and Engineering: A*, 662, 227-240.

Ponte Castañeda, P. (1991). The effective mechanical properties of nonlinear isotropic composites. *Journal of the Mechanics and Physics of Solids*, 39, 45-71.

Ponte Castañeda, P., & Suquet, P. (1998). Nonlinear Composites. *Advances in Applied Mechanics*, 34, 171-302.

Povstenko, Yu. Z. (1993). Theoretical investigation of phenomena caused by heterogeneous surface tension in solids. *Journal of the Mechanics and Physics of Solids*, 41, 1499-1514.

Rahman, S., Atkins, G. J., Findlay, D. M., & Losic, D. (2015). Nanoengineered drug releasing aluminium wire implants: a model study for localized bone therapy. *Journal of Materials Chemistry B*, 3, 3288-3296.

Rice, J. R. (1971). Inelastic constitutive relations for solids: an internal-variable theory and its application to metal plasticity. *Journal of the Mechanics and Physics of Solids*, 19, 433-455.

Rittel, D., Ravichandran, G., & Venkert, A. (2006). The mechanical response of pure iron at high strain rates under dominant shear. *Materials Science and Engineering: A*, 432, 191-201.

Roque-Malherbe, R. M. (2007). Adsorption and diffusion in nanoporous materials. *CRC press.*

Ruestes, C.J., Bringa, E.M., Stukowski, A., Rodriguez Nieva, J.F., Bertolino, G., Tang, Y., & Meyers, M.A. (2013). Atomistic simulation of the mechanical response of a nanoporous body-centered cubic metal. *Scripta Materialia*, 68, 817-820.

Rice, J.R. (1971). Inelastic constitutive relations for solids: an internal-variable theory and its application to metal plasticity. *Journal of the Mechanics and Physics of Solids*, 19, 433-455.

Salençon, J. (1983). Calcul à la rupture et analyse limite, *Presses de l'ENPC.*

Senior, N. A., & Newman, R. C. (2006). Synthesis of tough nanoporous metals by controlled electrolytic dealloying. *Nanotechnology*, 17, 2311.

Seppala, E.T., Belak, J., & Rudd, R.E. (2004). Effect of stress triaxiality on void growth in dynamic fracture of metals: A molecular dynamics study. *Physical Review B*, 69, 134101.

Shabib, I., & Miller, R.E. (2009). Deformation characteristics and stress-strain response of nanotwinned copper via molecular dynamics simulation. *Acta Materialia*, 57, 4364-4373.

Sharma, P., Ganti, S., & Bhate, N. (2003). Effect of surfaces on the size-dependent elastic states of nano-inhomogeneities. *Applied Physics Letters*, 82, 535-537.

Sharma, P., & Ganti, S. (2004). Size-Dependent Eshelby's Tensor for Embedded Nano-Inclusions Incorporating Surface/Interface Energies. *Journal of Applied Mechanics*, 71, 663-671.

Shen, W. Q., Shao, J. F., Kondo, D., & Gatmiri, B. (2012). A micro–macro model for clayey rocks with a plastic compressible porous matrix. *International Journal of Plasticity*, 36, 64-85.

Shin, H. C., Dong, J., & Liu, M. (2003). Nanoporous structures prepared by an electrochemical deposition process. *Advanced Materials*, 15, 1610-1614.

Shuttleworth, R. (1950). The surface tension of solids. *Proceedings of the Physical Society A*, 63, 444-457.

Sotiropoulou, S., Vamvakaki, V., & Chaniotakis, N. A. (2005). Stabilization of enzymes in nanoporous materials for biosensor applications. *Biosensors and Bioelectronics*, 20, 1674-1679.

Stukowski, A. (2010). Visualization and analysis of atomistic simulation data with OVITO-the Open Visualization Tool. *Modelling and Simulation in Materials Science and Engineering*, 18, 015012.

Stukowski, A. (2012). Structure identification methods for atomistic simulations of crystalline materials. *Modelling and Simulation in Materials Science and Engineering*, 20, 4.

Subramaniyan, A.K., & Sun, C. (2008). Continuum interpretation of virial stress in molecular simulations. *International Journal of Solids and Structures*, 45, 4340-4346.

Sun, L., Chien, C. L., & Searson, P. C. (2004). Fabrication of nanoporous nickel by electrochemical dealloying. *Chemistry of materials*, 16, 3125-3129.

Suquet, P. (1995). Overall properties of nonlinear composites: a modified secant moduli theory and its link with Ponte Castañeda's non linear variational procedure. *Comptes Rendus Académie de Science de Paris*, II B, 320, 11, 563-571.

Suquet, P. (1997). *Continuum micromechanics*. New York: Springer-Verlag.

Tang, T., Kim S., & Horstemeyer, M.F. (2010). Molecular dynamics simulations of void growth and coalescence in single crystal magnesium. *Acta Materalia*, 58, 4742-4759.

Thoré, P., Pastor, F., Pastor, J., & Kondo, D. (2009). Closed-form solutions for the hollow sphere model with Coulomb and Drucker–Prager materials under isotropic loadings. *Comptes Rendus Mécanique*, 337(5), 260-267.

Thoré, P., Pastor, F., & Pastor, J., (2011). Hollow sphere models, conic programming and third stress invariant. *European Journal of Mechanics A/Solids*, 30, 63-71.

Traiviratana, S., Bringa, E.M., Benson, D.J., & Meyers, M.A. (2008). Void growth in metals: Atomistic calculations. *Acta Materialia*, 56, 3874-3886.

Trillat, M., & Pastor, J. (2005). Limit analysis and Gurson's model. *European Journal of Mechanics A/Solids*, 24, 800-819.

Tvergaard, V. (1982). On localization in ductile materials containing spherical voids. *International Journal of Fracture*, 18, 237-252.

Tvergaard, V., & Needleman, A. (1984). Analysis of the cup-cone fracture in a round tensile bar. *Acta metallurgica*, 32, 157-169.

Valiev, R. Z., Zhilyaev, A. P., & Langdon, T. G. (2013). Bulk nanostructured materials: fundamentals and applications. *John Wiley & Sons*.

Verlet, L. (1967). Computer "Experiments" on Classical Fluids. I. Thermodynamical Properties of Lennard-Jones Molecules. *Physical Review*, 159, 98.

Vincent, P.-G., Monerie, Y., & Suquet, P. (2009). Porous materials with two populations of voids under internal pressure: I. instantaneous constitutive relations. *International Journal of Solids and Structures*, 46, 480-506.

Wang, J., Huang, Z., Duan, H., Yu, S., Feng, X., Wang, G., Zhang, W., & Wang, T. (2011). Surface stress effect in mechanics of nanostructured materials. *Acta Mechanica Solida Sinica*, 52-82.

Weck, A., Wilkinson, D. S., Toda, H., & Maire, E. (2006). 2D and 3D Visualization of Ductile Fracture. *Advanced Engineering Materials*, 8: 469-472.

Weissmüller, J., Newman, R. C., Jin, H. J., Hodge, A. M., & Kysar, J. W. (2009). Nanoporous metals by alloy corrosion: formation and mechanical properties. *Mrs Bulletin*, 34, 577-586.

Witkin, D. B., & Lavernia, E. J. (2006). Synthesis and mechanical behavior of nanostructured materials via cryomilling. *Progress in Materials Science*, 51, 1-60.

Yvonnet, J., Mitrushchenkov, A., Chambaud, G., He, Q. C., & Gu, S. T. (2012). Characterization of surface and nonlinear elasticity in wurtzite ZnO nanowires. *Journal of Applied Physics*, 111, 124305.

Zehetbauer, M. J., & Zhu, Y. T. (2009). Bulk nanostructured materials. *John Wiley & Sons*.

Zhai, J., Luo, T., Gao, X., Graham, S. M., Baral, M., Korkolis, Y. P., & Knudsen, E. (2016). Modeling the ductile damage process in commercially pure titanium. *International Journal of Solids and Structures*, 91, 26-45.

Zhang, W., & Wang, T.J. (2007). Effect of surface energy on the yield strength of nanoporous materials. *Applied Physics Letters*, 90, 063104.

Zhang, W., Wang, T.J., & Chen, X. (2008). Effect of surface stress on the asymmetric yield strength of nanowires. *Journal of Applied Physics*, 103, 123527.

Zhang, W., Wang, T.J., & Chen, X. (2010). Effect of surface/interface stress on the plastic deformation of nanoporous materials and nanocomposites. *International Journal of Plasticity*, 26, 957-975.

Zhao, K.J., Chen, C.Q., Shen, Y.P., & Lu, T.J. (2009). Molecular dynamics study on the nano-void growth in face-centered cubic single crystal copper. *Computational Materials Science*, 46, 749-754.

Zhu, H.T., & Zbib, H.M. (1993). A continuum model for flow strength of metal-matrix composites. *Scripta Metallurgica et Materialia*, 28, 1323-1328.